Diversity of Lithologic Components at Meridiani Planum, Mars: Insights from Mössbauer Spectroscopic Investigations

Dissertation zur Erlangung des Grades
„Doktor der Naturwissenschaften“
am Fachbereich Physik, Mathematik und Informatik
der Johannes Gutenberg-Universität
in Mainz

Iris Fleischer
geboren in Fulda

Mainz, den 23.08.2010

Datum der mündlichen Prüfung: 10.11.2010

D77 – Dissertation Universität Mainz

Abstract (English): Diversity of Lithologic Components at Meridiani Planum, Mars: Insights from Mössbauer Spectroscopic Investigations

The two Mars Exploration Rovers (MER), Spirit and Opportunity, landed on the Martian surface in January 2004 and have since collected a wealth of information about their landing sites. As part of their payload, the miniaturised Mössbauer spectrometer MIMOS II contributes to the success of the mission by identifying Iron-bearing minerals and by determining Iron oxidation states in them. The basis of this work is the data set obtained at Opportunity's landing site at Meridiani Planum. A portion of this data set is evaluated with different methods, with the aim to thoroughly characterize lithologic components at Meridiani Planum and possible relations between them.

MIMOS II is able to measure Mössbauer spectra at different energies simultaneously, bearing information from different sampling depths of the investigated target. The ability of depth-selective Mössbauer spectroscopy to characterize weathered surface layers is illustrated through its application to two suitable rock targets that were investigated on Mars. In both cases, an enhanced concentration of Iron oxides at the rock surface was detected, pointing to a low degree of aqueous alteration.

The mineral hematite (α-Fe_2O_3) is present in the matrix of outcrop rocks and in spherules weathering from the outcrop. Simultaneous fitting of Mössbauer spectra was applied to data sets obtained on both target types to characterize the hematite component in detail. This approach reveals that two hematite populations are present, both in the outcrop matrix as well as in spherules. The hematite component with a comparably high degree of crystallinity and/or chemical purity is present in the outcrop matrix. The investigation of hematite at Meridiani Planum has shown that simultaneous fitting is a suitable and useful method to evaluate a large, correlated set of Mössbauer spectra.

Opportunity encountered loose, cm-sized rocks along its traverse. Based on their composition and texture, these "cobbles" can be divided into three different groups. Outcrop fragments are impact-derived ejecta from local outcrop rocks. Cobbles of meteoritic origin contain the minerals kamacite (Fe,Ni) and troilite (FeS) and exhibit high Ni contents. Melt-bearing impact breccias bear similarities to local outcrop rocks and basaltic soil, with a phase composition and texture consistent with a formation scenario involving partial melting and inclusion of small, bright outcrop clasts.

Iron meteorites on the Martian surface experience weathering through the presence of even trace amounts of water due to their metallic nature. Opportunity encountered and investigated four Iron meteorites, which exhibit evidence for physical and chemical weathering. Discontinuous coatings contain Iron oxides, pointing to the influence of limited amounts of water.

A terrestrial analogue site for Meridiani Planum is the Rio Tinto basin in south-west Spain. With its deposits of sulfate- and iron-oxide-bearing minerals, the region provides an adequate test bed for instrumentation for future Mars missions. In-situ investigations at Rio Tinto were carried out with a special focus on the combined use of Mössbauer spectroscopy with MIMOS II and Raman spectroscopy with a field-portable instrument. The results demonstrate that the two instruments provide complementary information about investigated samples.

Abstract (Deutsch): Diversity of Lithologic Components at Meridiani Planum, Mars: Insights from Mössbauer Spectroscopic Investigations

Die beiden Mars Exploration Rover (MER), Spirit und Opportunity, haben seit ihrer Landung auf dem Mars im Januar 2004 eine enorme Menge Daten über ihre Landestellen gesammelt. Teil ihrer Nutzlast ist das miniaturisierte Mössbauer-Spektrometer MIMOS II, das zum Erfolg der Mission beiträgt, indem es eisenhaltige Minerale identifiziert und Eisen-Oxidationszustände in ihnen nachweist. Grundlage dieser Arbeit ist der Datensatz, der an Opportunitys Landestelle in Meridiani Planum aufgenommen wurde. Ein Teil dieses Datensatzes wird ausgewertet mit dem Ziel, die lithologischen Komponenten und mögliche Zusammenhänge zwischen ihnen zu charakterisieren.
Mit MIMOS II können Mössbauer-Spektren bei verschiedenen Energien simultan gemessen werden, die dann Informationen aus verschiedenen Probentiefen enthalten. Mittels dieser tiefenselektiven Mössbauer-Spektroskopie können verwitterte Oberflächenschichten charakterisiert werden. Dies wird anhand zweier geeigneter Proben gezeigt, die auf dem Mars untersucht wurden. In beiden Fällen ist die Konzentration von Eisenoxiden an der Oberfläche erhöht, was auf einen geringen Grad wasserbedingter Verwitterung hindeutet.
Das Mineral Hämatit (α-Fe_2O_3) kommt sowohl in der Matrix von Aufschlussgestein als auch in Globulen vor, die aus dem Aufschlussgestein herauswittern. Um die Hämatit-Komponente eingehend zu charakterisieren, wurden Mössbauer-Datensätze von beiden Probentypen mittels simultanen Fittens ausgewertet. Diese Vorgehensweise zeigt, dass jeweils zwei Hämatit-Populationen in der Matrix von Aufschlussgestein und in den Globulen vorkommen. Die Hämatitkomponente mit einem vergleichsweise hohen Grad an Kristallinität und/oder chemischer Reinheit liegt in der Gesteinsmatrix vor. Die Untersuchung von Hämatit in Meridiani Planum hat ebenfalls gezeigt, dass simultanes Fitten eine geeignete und hilfreiche Methode ist, um einen großen, korrelierten Satz von Mössbauer-Spektren auszuwerten.
Opportunity stieß entlang der Traverse wiederholt auf lose Steine mit wenigen Zentimetern Durchmesser. Aufgrund ihrer Zusammensetzung und Textur können diese in drei Gruppen unterteilt werden. Fragmente von Aufschlussgestein sind durch Impakte verursachte Auswürfe des lokalen Grundgesteins. Steine meteoritischen Ursprungs enthalten die Minerale Kamazit (Fe,Ni) und Troilit (FeS) und weisen hohe Ni-Gehalte auf. Schmelzhaltige Impakt-Brekzien zeigen Ähnlichkeiten zu lokalem Aufschlussgestein und basaltischem Sand. Ihre Zusammensetzung und Textur steht im Einklang mit einer Bildung aus partiell aufgeschmolzenem Material mit Einschlüssen des Aufschlussgesteins.
Eisenmeteorite auf der Marsoberfläche zeigen aufgrund ihrer metallischen Natur bereits bei minimalem Einfluss von Wasser Verwitterungserscheinungen. Die vier von Opportunity gefundenen Eisenmeteoriten tragen Anzeichen für physikalische und chemische Verwitterung. Diskontinuierliche Oberflächenschichten enthalten Eisenoxide, die auf den Einfluss begrenzter Wassermengen hindeuten.
Ein terrestrisches Analog-Gebiet zu Meridiani Planum ist das Rio-Tinto-Becken in Südwest-Spanien. Mit seinen Vorkommen an Sulfat- und Eisenoxid-haltigen Mineralen bietet es eine angemessene Testumgebung für Instrumente für zukünftige Marsmissionen. In-situ Untersuchungen wurden durchgeführt mit dem Augenmerk auf der kombinierten Verwendung von Mössbauer-Spektroskopie mit MIMOS II und Raman-Spektroskopie mit einem portablen Instrument. Die Ergebnisse zeigen, dass die beiden Instrumente komplementäre Informationen über untersuchte Proben liefern.

Contents

1 Introduction

The two Mars Exploration Rovers (MER), Spirit and Opportunity, landed on the Martian surface in January 2004. The rovers were designed to last for 90 sols (a sol is a Martian day with a duration of 24 hours and 37 minutes). At the time of writing, more than six years - or 2000 sols - after their landing, both rovers are still operational and continue to record and transmit scientific data to Earth.
Spirit landed on the plains of 160 km diameter Gusev crater, and Opportunity landed at Meridiani Planum. The primary objective of their mission was defined to be the exploration of these two sites on the Martian surface, where water may once have been present, and to assess past environmental conditions at those sites and their suitability for life [*Squyres et al.*, 2003]. Both rovers carry mast-mounted remote sensing instruments and in situ instruments mounted on a 5 degree-of-freedom instrument deployment device (IDD). As part of their payload, the miniaturised Mössbauer spectrometer MIMOS II [*Klingelhöfer et al.*, 2003] contributes to the success of the mission by identifying Iron-bearing minerals and by determining Iron oxidation states in them. To date, Mössbauer spectra are available from 159 separate targets at Gusev crater and from 137 targets at Meridiani Planum.

The basis of this work is the data set obtained at Opportunity's landing site. A portion of this data set is evaluated with the aim to thoroughly characterize lithologic components at Meridiani Planum and possible relations between them. The landing site is characterized by sulfate-rich sedimentary outcrop rock, covered with basaltic sand and a lag deposit of hematite-rich, mm-sized spherules weathering from the outcrop [e.g., *Squyres et al.*, 2006]. The outcrop and spherules formed more than 3.5 Ga ago [e.g., *McLennan et al.*, 2005] and thus bear information on the environmental conditions at Meridiani Planum in this distant past. In more recent episodes, impacts have also shaped the area, as evidenced from numerous craters with diameters from a few meters to a few kilometers. Occasionally, Opportunity encountered loose rocks related to impact events, including impact-ejecta and iron meteorites as well as a number of cm-sized rocks referred to as "cobbles".
Different approaches are applied to evaluate Mössbauer spectra obtained at Meridiani Planum. Complementary information is provided through data from other MER instruments as well as through laboratory investigations and analogue in-situ studies at Rio Tinto, Spain.

Mössbauer spectra obtained at different energies (i. e., corresponding to transitions between different nuclear or atomic energy levels) on the same sample bear information from different sampling depths. The MIMOS II instruments are able to measure Mössbauer spectra at 14.4 keV and 6.4 keV simultaneously and have been commanded to do so for all targets measured with Opportunity's instrument and for all targets through sol 561 with Spirit's instrument. The comparison of 14.4 keV spectra and 6.4 keV spectra may reveal the presence and composition of layers, which may form through aqueous alteration. Calculations, results from laboratory measurements and examples from the MER mission are presented in chapter 3.

On both rovers, Mössbauer spectra are acquired over the Martian diurnal temperature range (~180 K to ~290 K) in up to 13 temperature windows each 10 K wide. So far, publications discussing the MER Mössbauer data set are largely based on 14.4 keV spectra summed over the available temperature range to improve counting statistics [e.g., *Klingelhöfer et al.*, 2004, 2005; *Morris et al.*, 2004, 2006a, 2006b, 2008]. Separate fits of single spectra from different temperature windows hinted at the possible presence of

distinct hematite populations, but did not allow determining their characteristics. Simultaneous fitting (simfitting) is applied to a set of spectra obtained on outcrop targets at Eagle crater and to a set of spectra obtained on spherule-rich targets. This approach allows establishing target- and temperature-related characteristics between separate spectra. Thereby, Mössbauer parameters are preserved for spectra from single temperature windows, with tighter constraints on Mössbauer parameters compared to uncorrelated fits of single spectra, and more detailed information about material properties can be obtained. Results for the hematite component in Meridiani outcrop rocks and spherules are presented in chapter 4 and compared to low-temperature measurements carried out with a laboratory version of the MIMOS II instrument on hematite-bearing analogue samples.

Cobbles are present along Opportunity's >20 km traverse. Compared to outcrop and basaltic sand, cobbles are rare. They are often observed in clusters in the vicinity of impact craters and apparently not connected to the ubiquitous outcrop rocks. Whenever mission constraints allowed, a science campaign was carried out to investigate one or several adjacent cobbles with the rover's instruments, ideally with the whole instrument suite. This way, complementary information about their elemental composition (Alpha Particle X-ray spectrometer, APXS), iron-bearing mineral phases (MIMOS II) and texture (Microscopic Imager, MI) was obtained. The analysis of related data products from different instruments is necessary to detect and interpret relations between different cobbles, their connection to Meridiani Planum and their possible origins. Results from investigations of 15 cobbles encountered between sols 106 and 1974 are described in chapter 5.

Four Iron meteorites were encountered by Opportunity, three of them located within a range of ~1 km, encountered between sols 1961 and 2034, and separated by ~10 km from the fourth specimen encountered on sol 350. Due to their metallic nature, Iron meteorites experience weathering through the presence of even trace amounts of water. The detailed study of Iron meteorites on the Martian surface can therefore reveal information not only about the meteorites themselves, but also about the climate and weathering conditions at their current site since the time of their impact. Iron meteorites with similar compositions also impact Earth. Many of them have been characterized in detail and are available for further laboratory studies [e.g., *Lovering,* 1956; *Wasson and Goldstein,* 1967; *Vdovykin,* 1972; *Weinke,* 1977; *Al-Kathiri et al.*, 2006]. Thus, the Mössbauer spectra of the Meridiani Iron meteorites are compared with data from five analogue Iron meteorite specimens, analysed with MIMOS II laboratory setups. Results are discussed in chapter 6.

The Rio Tinto basin in southwest Spain is an analogue site for Meridiani Planum. Rio Tinto exhibits a nearly constant, acidic pH value of ~2.3 along its ~100 km long course. Depending on the exact environmental conditions, numerous Iron-bearing oxide-, oxyhydroxide- and sulfate-minerals precipitate in the acidic water and close to the water margin, including hematite (α-Fe_2O_3) and jarosite ($(K,Na)Fe^{3+}_3(SO_4)_2(OH)_6$) [e.g., *Fernandez-Remolar et al.*, 2003, 2004, 2005]. Both minerals are also abundant at Meridiani Planum [e.g., *Klingelhöfer et al.*, 2004]. Rio Tinto offers an opportunity to study the formation of sulfate-minerals in-situ, as well as their alteration and connection to primary minerals. As a Martian analogue site, Rio Tinto also provides a test bed for instruments that are available or under development for future Mars missions. Therefore, in-situ investigations at Rio Tinto were carried out with a special focus on the combined use of Mössbauer spectroscopy with MIMOS II and Raman spectroscopy with a field-portable Raman spectrometer. Results are reported in chapter 7.

2 Mössbauer spectroscopy with MIMOS II

2.1 Basic Principles of Mössbauer Spectrocopy

The Mössbauer effect, i. e., the recoilless absorption and emission of γ-rays by nuclei of certain isotopes bound in a solid, was first observed by R. L. Mössbauer in 1958 in experiments with ^{191}Ir [*Mössbauer,* 1958a, 1958b, 2000]. For his discovery, he received the Nobel Prize in 1961. First applications of Mössbauer spectroscopy in mineralogical studies were described in the following years [e.g. *Pollak et al.*, 1962; *de Coster et al*., 1963] and the first studies of extraterrestrial (i.e., meteoritic) material were performed soon after [e.g., *Sprenkel-Segel and Hanna,* 1964; *Bailey and Duncan,* 1967]. The Mössbauer effect has been observed for many different isotopes from more than 40 elements, but the most common isotope used in Mössbauer studies is ^{57}Fe, which occurs with a relative abundance of ~2.2 % in natural iron. Numerous publications provide extensive reviews of Mössbauer spectroscopy [e.g., *Wegener,* 1966; *Gonser,* 1975; *Gütlich,* 1978, *Hawthorne*, 1988] and its applications in mineralogy and geochemistry [e.g., *Mitra,* 1992; *Murad and Cashion,* 2004].

2.1.1 The Mössbauer Effect

When the nucleus of a free atom decays from an excited state to the ground state with an energy difference E_0, thereby emitting a γ-ray with energy $E_\gamma = E_0 - E_R$, it experiences a recoil of energy E_R:

$$E_R = \frac{E_\gamma^2}{2Mc^2} \quad , \tag{2.1}$$

where M is the mass of the nucleus and c the velocity of light. Similarly, in an absorption process, the line will be shifted to $E_\gamma = E_0 + E_R$. For example, the excited state of ^{57}Fe with nuclear spin *I=3/2* is separated from the ground state with *I=1/2* by E_0 = 14.4 keV, resulting in a recoil energy $E_R \approx 10^{-3}$ eV, which is six orders of magnitude larger than the natural line width ($\Gamma = 4{,}67 \cdot 10^{-9} eV$). Thus, γ-rays emitted by free atoms are usually off resonance and will not be absorbed by atoms of the same sort.
However, if both atoms are bound in a crystal lattice, the crystal as a whole takes up the recoil energy, which is transferred to the lattice by phonon excitations. With a certain probability, a γ-ray absorption occurs without phonon excitation and the emission or absorption process occurs without recoil. This recoil free fraction *f* can be expressed as:

$$f = \exp\left(-k^2 < x^2 >\right), \tag{2.2}$$

where *k* is the wave vector of the γ-ray and $<x^2>$ is the mean vibrational amplitude of the nucleus. The recoil free fraction is also referred to as the "Lamb-Mössbauer factor" or "Debye-Waller-factor" [e.g. *Wegener,* 1966; *Gütlich et al.*, 1978; *Mössbauer,* 2000; *Murad and Cashion,* 2004]. Depending on the absorbing compound, *f* takes up values between ~0.4 and ~0.9 and is generally larger for ferric (Fe^{3+}-bearing) than for ferrous (Fe^{2+}-bearing) compounds [e.g., *de Grave and van Alboom,* 1991].

2.1.2 Experimental Setup of a Mössbauer Experiment

To measure the Mössbauer resonance spectrum of a sample, the sample is irradiated with a source emitting γ-radiation of the required energy. Generally, source and sample will be different compounds. As the chemical environment influences nuclear energy levels, resonance lines will be shifted against each other. This shift can be compensated for by moving the source relative to the sample, using the Doppler Effect to shift the energy of emitted γ-rays. A velocity v results in a Doppler shift of:

$$E_D = \frac{v}{c} E_\gamma . \tag{2.3}$$

The positions of resonance lines are usually referred to by their Doppler velocity relative to a standard absorber (metallic α-Iron in this work). The Doppler velocity is used to label the x-axis, usually in a scale of mm/s. A suitable source for Mössbauer spectroscopy with ^{57}Fe is ^{57}Co, which decays by electron capture with a half-life of 270 days to ^{57}Fe. With a certain probability, the decay occurs via the excited state of ^{57}Fe (*I=3/2*), which decays to the ground state (*I=1/2*), thereby emitting the desired 14.4 keV γ-rays. Typically, the drive velocity range for Mössbauer spectroscopy with ^{57}Fe is on the order of magnitude of ±10 mm/s, corresponding to an energy shift on the order of ~10^{-8} eV.
A detector may be arranged in two different measurement geometries, both shown in Figure 2.1. In transmission geometry, thin slices or small amounts of a powdered sample are placed between source and detector. This configuration requires samples to be prepared adequately, in order to fulfill both the requirement of sufficient absorption and transparency, and to keep thickness effects small at the same time. Resulting Mössbauer spectra show transmission minima. In backscattering geometry, source and detector are placed on the same side of the sample. The detector then records re-emitted radiation, the recorded spectra show reflection maxima. The main advantage of this setup is that sample preparation is not necessary, a sample of complex geometry may be analysed by simply placing it in contact with the instrument.

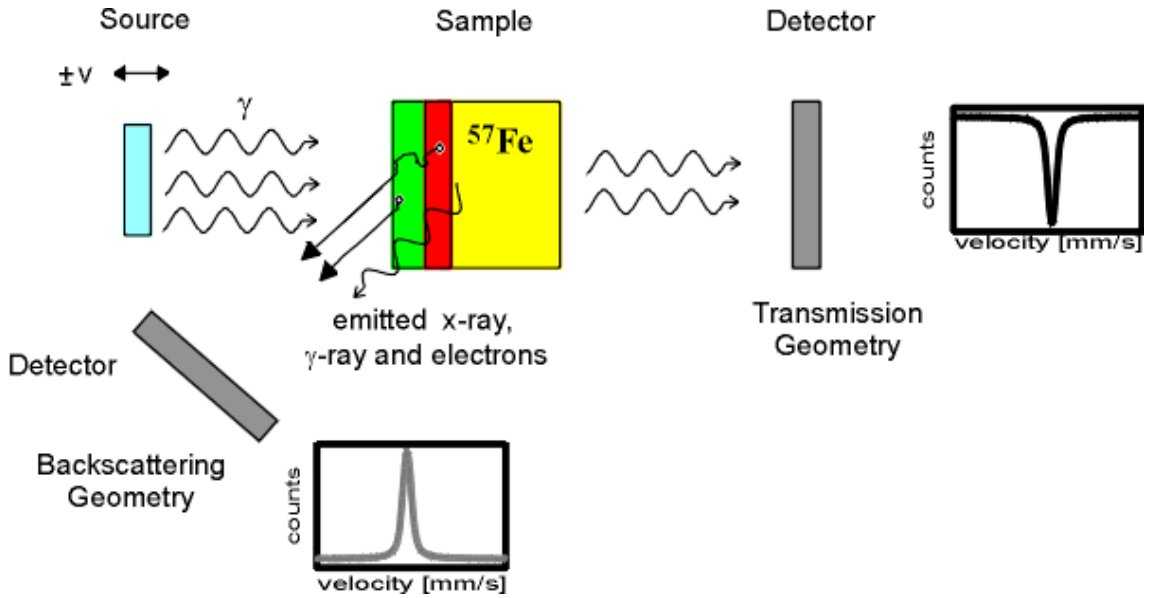

Figure 2.1: A Mössbauer experiment may be set up in transmission geometry or backscattering geometry. Either way, a sample resonantly absorbs γ-rays from a source. A detector placed in line with source and sample measures transmission minima; a detector placed on the same side of the sample as the source measures reflection maxima from re-emitted radiation.

In addition to reemitted 14.4 keV γ-rays, radiation emitted in competing de-excitation processes may also be detected, including X-rays, conversion electrons and Auger electrons, as indicated in Figure 2.2. The simultaneous detection of γ-rays, X-rays and electrons constitutes a depth-selective Mössbauer experiment, as described in more detail in chapter 3.

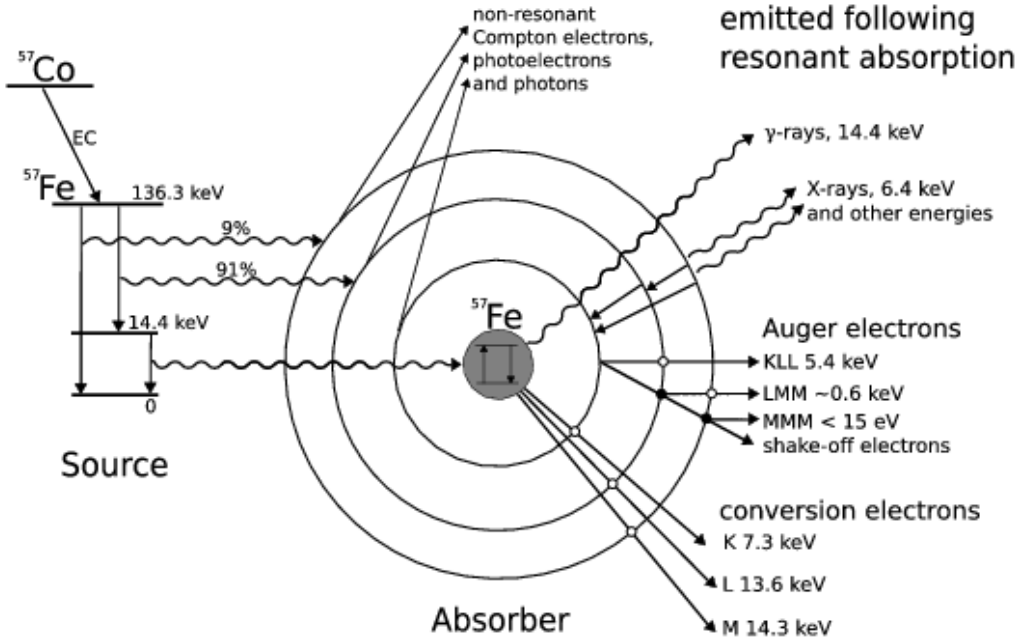

Figure 2.2 : Emission processes during the decay of ^{57}Co to ^{57}Fe and de-excitation of ^{57}Fe (modified from [*de Grave et al.,* 2005]).

2.1.3 Observed Parameters in Mössbauer Spectra

The nuclear energy levels in a nucleus are affected by the interactions of the nucleus with its chemical environment. The positions of resonant lines in Mössbauer spectra reflect these energy levels and may thus be used to characterize the investigated compound. Three parameters, resulting from different interactions, are relevant to fully characterise a Mössbauer spectrum. These are the center shift (δ), the electric quadrupole splitting (ΔE_Q), and the magnetic hyperfine field B_{hf}. Hyperfine splittings in ^{57}Fe and possible transitions from the excited to the ground state are shown in Figure 2.3.
Many different compounds can be identified through a comparison of catalogued parameters [e.g., *Stevens et al.*, 2002] with parameters determined from measured spectra.

2.1.3.1 Center Shift

The center shift δ is the shift of the centroid of a spectrum against a zero reference point of the Doppler velocity, measured relative to a reference absorber, such as α-Iron in this work. The center shift is comprised of the temperature-independent isomer shift and the temperature-dependent second-order Doppler shift: $\delta = \delta_I + \delta_{SOD}$. The isomer shift δ_I results from the Coulomb interaction of the positive nuclear charge distribution over a finite radius R and the electron charge density at the nucleus. It can be expressed as:

$$\delta_I = \frac{4}{5}\pi \cdot Z \cdot e^2 \cdot \frac{\delta R}{R} \cdot R^2 \cdot \left\{ \left|\Psi(0)\right|_A^2 - \left|\Psi(0)\right|_S^2 \right\}, \qquad (2.4)$$

where $Z \cdot e$ is the nuclear charge, $\delta R/R$ is the relative change of nuclear radius between excited state and ground state and $|\Psi(0)|_A^2$ and $|\Psi(0)|_S^2$ are the electron densities at the nucleus of the absorber (A) or the source (S), respectively.
The second-order Doppler shift δ_{SOD} is a small thermal shift resulting from lattice vibrations that is observed if the temperature of the source and the absorber are different.
In the case of the miniaturised Mössbauer spectrometer used for this work (see section 2.2), the complete experimental setup is kept at the same temperature, so that δ_{SOD} can not be observed. The center shift is equivalent to the isomer shift and not temperature-dependent.
The isomer shift is influenced by the oxidation state. For ^{57}Fe, the ratio $\delta R/R$ is negative, implying that an increasing electron density at the nucleus results in a more negative value of δ. Oxidation of metallic iron to Fe^{2+} occurs through the removal of two 4s electrons. Not considering relativistic effects, only s-electrons have a finite electron density inside the nucleus, so that $|\Psi(0)|^2$ decreases and δ values for ferrous compounds increase compared to metallic iron. Further oxidation to Fe^{3+} occurs through the removal of a 3d electron, so that the shielding of 3s electrons from the nuclear charge by 3d electrons is reduced. Thus, $|\Psi(0)|^2$ increases and δ values for ferric compounds decrease compared to ferrous compounds [e.g., *Gütlich,* 1978]. Typical values for the isomer shifts measured at room temperature for iron bound to oxygen in silicates, sulfates or carbonates range from ~0.75 mm/s to ~1.3 mm/s for Fe^{2+}, and from ~0.15 mm/s to ~0.5 mm/s for Fe^{3+} [e.g., *Burns,* 1993; *McCammon,* 1995; *Stevens et al.*, 2002].

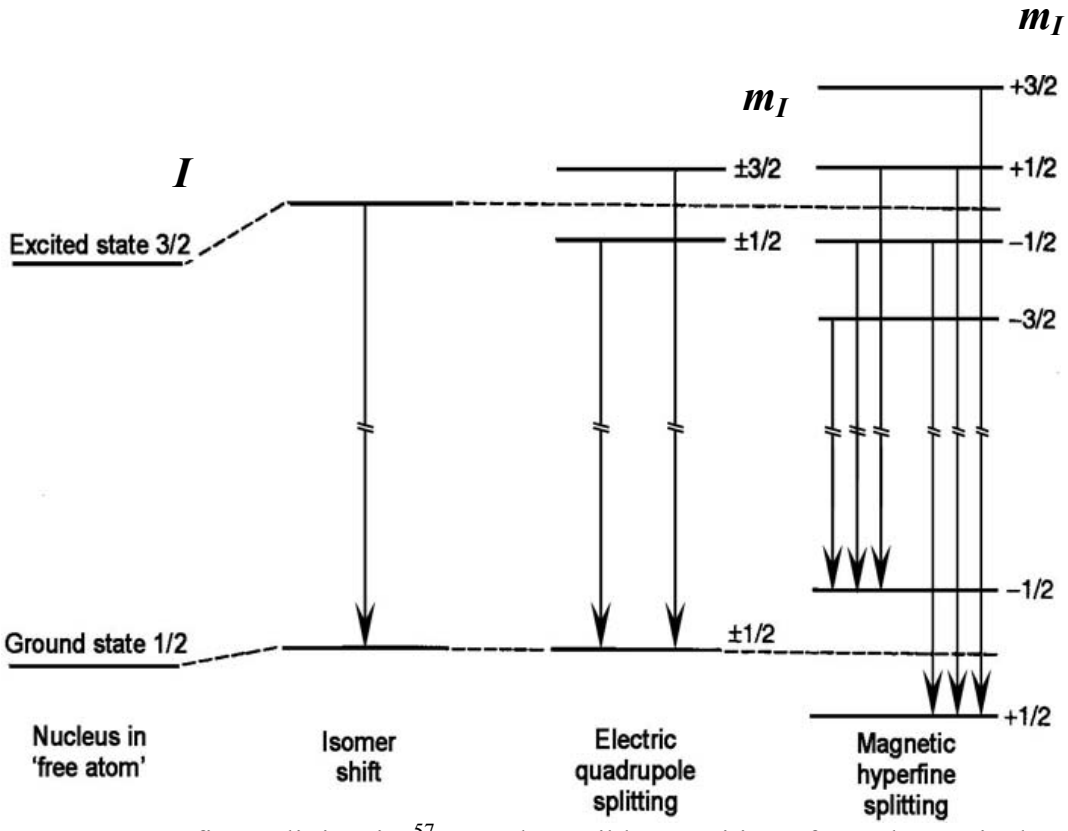

Figure 2.3: Hyperfine splitting in ^{57}Fe and possible transitions from the excited to the ground state for pure electric quadrupole splitting or pure magnetic hyperfine splitting; the combined case of electric quadrupole and magnetic dipole interaction is neglected.

2.1.3.2 Quadrupole Splitting

The Quadrupole splitting ΔE_Q results from electric quadrupole interaction. It arises from the interaction between the nuclear quadrupole moment and the electric field gradient. A nuclear quadrupole moment exists when the nucleus has a non-spherical shape. An electric field gradient is typically present for local lattice symmetries other than cubic. Nuclear states are characterized by the nuclear spin quantum number *I* and nuclear magnetic spin quantum number $m_I = (I, I-1, ..., -I)$. The electric quadrupole interaction causes a splitting of the nuclear states into substates $\left| I,\ m_I \right\rangle$. For ^{57}Fe, the excited state (*I = 3/2*) is split into two levels with $m_I = \pm 3/2$ and $m_I = \pm 1/2$. The difference between both states is given by:

$$\Delta E_Q = E_Q(\pm 3/2) - E_Q(\pm 1/2) = eQV_{ZZ}/2, \tag{2.5}$$

where e is the electron charge, Q is the nuclear quadrupole moment and V_{zz} is the main component of the electric field gradient. Transitions to the ground state (*I = 1/2*) occur from both (*I = 3/2*) states, the Mössbauer spectrum shows a two line pattern ("doublet"). The separation of the two line centers is equal to ΔE_Q. In the case of combined electric monopole and quadrupole interaction, the center shift is defined by the position of the center between both lines. The electric field gradient results from different coordination environments of the nucleus as well as different electronic configurations (i.e., different oxidation states). Values for ΔE_Q are generally larger for ferrous compounds than for ferric compounds [e.g., *Burns,* 1993; *McCammon,* 1995; *Stevens et al.*, 2002].

2.1.3.3 Magnetic Hyperfine Field

The magnetic dipole moment of the nucleus interacts with a magnetic field present at the nucleus, which can either be intrinsic or externally applied. The magnetic field removes the degeneracy of the nuclear energy states, which are split into substates $\left| I,\ m_I \right\rangle$ with energies:

$$E_M(m_I) = -g_N \mu_N B_{hf} m_I, \tag{2.6}$$

where g_N is the nuclear Landé g-factor, μ_N is the nuclear dipole moment and B_{hf} is the magnetic hyperfine field. For ^{57}Fe, the excited state is split into four levels, while the ground state is split into two levels. Six transitions are allowed, as indicated in Figure 2.3, following the selection rule for magnetic dipole transitions ($\Delta I = 1,\ \Delta m_I = 0, \pm 1$). Thus, a six line pattern (sextet) is observed in Mössbauer spectra. B_{hf} can be extracted from the separation of the two outermost lines, which is given by:

$$\Delta E_M = \left(-\frac{3}{2} g_e + \frac{1}{2} g_g\right) \mu_N B_{hf}, \tag{2.7}$$

where g_e and g_g are the respective Landé g-factors of the excited and ground states. In the case of combined electric monopole interaction, electric quadrupole interaction and magnetic dipole interaction, the center shift is given by the position of the barycenter of the sextet. As long as $B_{hf} >> \Delta E_Q$, the electric quadrupole interaction can be treated as a perturbation to the magnetic dipole interaction and the quadrupole splitting can be calculated from the position of the six lines:

$$\Delta E_Q = \frac{1}{2}\left[\left(v_6 - v_5\right) - \left(v_2 - v_1\right)\right], \tag{2.8}$$

where the lines are numbered from lower to higher velocity. This approach is applicable to ^{57}Fe Mössbauer spectroscopy in many cases.

The lines of a Mössbauer sextet are generally not of equal intensity, because the transition probabilities are dependent on the angle between the direction of the magnetic field at the nucleus and the propagation direction of the γ-radiation. For a sample in which the magnetic domains are randomly oriented, the intensity ratios are 3:2:1:1:2:3 [e.g., *Bancroft*, 1973; *Hawthorne,* 1988].
A magnetic hyperfine splitting is observed for magnetically ordered compounds. These are characterized by exchange interactions between nearest neighbor magnetic moments, which cause the direction of the moment of one atom to influence the directions of the moments of its neighbors. The material becomes ordered below an ordering temperature (referred to as the Néel temperature or Curie temperature for ferromagnetic materials), when the sum of the energy of the magnetic exchange interactions becomes comparable to the thermal energy. In ferromagnetic materials, the magnetic moments are aligned in one direction. In antiferromagnetic materials, the magnetic moments are in an antiparallel alignment. For an antiferromagnet, the net magnetization for all the atoms must sum to zero. In a ferrimagnetic material, an antiferromagnetic alignment (e.g., of two or more types of magnetic atoms) will not lead to complete cancellation [e.g., *Murad and Cashion,* 2004].
The magnetic polarization of paramagnetic samples is changing due to spin-spin and spin-lattice relaxation effects. These changes occur fast compared to the life time of the ^{57}Fe excited state, so that the magnetic field sensed by the nucleus of the Mössbauer isotope is zero on average and no magnetic splitting is observed. If a magnetically ordered sample is composed of particles with sizes in the range of the magnetically ordered domains, the magnetic hyperfine splitting may not be observed. Thermal excitations may cause fluctuations of the magnetization direction of such one-domain particles. If the relaxation time is smaller than the lifetime of the excited nuclear state, the magnetic field sensed by the nucleus of the Mössbauer isotope is zero on average and the particles become superparamagnetic. For a number of iron oxides considered in this work, this effect is observed at room temperature for nanocrystalline particles (<30 nm). To restore the magnetic hyperfine splitting, the relaxation time must be increased by lowering the temperature of the sample during the measurement [e.g., *Hawthorne,* 1988; *Murad and Cashion,* 2004].

2.1.4 Spectral Line Shapes and Widths

The resonant spectral lines in a Mössbauer spectrum exhibit a Lorentzian shape:

$$I(E) = \frac{\Gamma/2\pi}{\left(E - E_0\right)^2 + \left(\Gamma/2\right)^2}, \tag{2.9}$$

where I is the intensity, E_0 is the resonant energy and Γ is the natural line width, which is related to the lifetime τ of the excited state via Heisenberg's uncertainty principle: $\Gamma \cdot \tau \geq \hbar$, where $\hbar$ is Planck's constant divided by 2π. For ^{57}Fe, $E_0 = 14.4$ *keV*, $\tau = 10^{-7}$ *s*, and $\Gamma = 4.67 \cdot 10^{-7}$ *eV* [e.g., *Bancroft,* 1973; *Gütlich,* 1978].

Lines may broaden and deviate from Lorentzian shapes through the influence of various effects. For broadened lines, a more adequate fit is obtained by using a convolution of Lorentzian and Gaussian line shapes (i.e., a Voigt-profile). The line width depends on the effective absorber thickness t_A:

$$t_a = f n \beta \sigma_0 d \tag{2.10}$$

where f is the recoil-free fraction, n is the number of atoms per volume, β is the abundance of atoms which can absorb resonantly, σ_0 is the absorption cross section at resonance and d is the thickness of the sample. A Mössbauer sextet related to a well defined site of a thin absorber has equal widths for all lines. As the thickness of the sample increases, the line shapes begin to deviate from Lorentzian shapes due to saturation effects [*Margulies and Ehrmann,* 1961].
The geometry of the experimental setup may also have an influence on line widths. Photons emitted with an angle θ with respect to the drive axis do not gain the full Doppler energy, but a fraction:

$$\Delta E = \frac{v_r}{c} E_\gamma \cos\theta , \tag{2.11}$$

where E_γ is the photon energy and v_r is the relative velocity between source and sample. This so-called *cosine-smearing effect* leads to broadened lines with asymmetric line shapes and shifts line centers outwards, particularly at higher velocities [e.g., *Riesenman et al.*, 1969; *Aramu and Maxia,* 1969].
If a sample is not perfectly ordered and homogeneous, hyperfine field distributions may arise. Particle size distributions, inter-particle interactions, surface effects and other interactions may also broaden the spectral lines and alter their shapes [e.g., *Vandenberghe et al.*, 2000]. The resulting asymmetrical line shapes are often observed for small particle systems. If a distribution of closely related sites is present, a model with Lorentzian line shapes broadening from inner to outer lines as Γ+2d, Γ+d, Γ, Γ, Γ+d, Γ+2d, with a broadening parameter d, may be appropriate. Asymmetric spectral line shapes may be approximated with skewed Lorentzian lines, composed of two half-Lorentzians joined at their midline, the left one with a half-width of ½Γ (1–k) and the right one with a half-width of ½ Γ (1+k). The skew parameter k has the same absolute value for all six lines of a sextet, being positive for lines 1-3 and negative for lines 4-6 [e.g., *Morris et al.*, 1989].

2.2 MIMOS II on the Mars Exploration Rover Mission

The miniaturised Mössbauer spectrometer MIMOS II was specifically developed to meet the requirements for planetary missions. Besides low mass and volume, these include low power consumption and a design to withstand acceleration forces and shocks during launch and landing, temperature stability over the Martian diurnal cycle and cosmic radiation. The instrument measures in backscattering geometry to avoid complicated sample preparation. It is simply placed in contact with samples. MIMOS II was deployed successfully on the surface of another planet for the first time in the framework of the NASA Mars Exploration Rover Mission. A detailed description of the MER instrument is given in [*Klingelhöfer et al.*, 2003].
Both MER rovers are equipped with the Athena Science payload [*Squyres et al.*, 2003], including two remote sensing instruments (a *Panoramic Camera (Pancam)* and a *Miniature Thermal Emission Spectrometer (Mini-TES)*, both integrated in the Pancam Mast Assembly), and four contact instruments mounted on the Instrument Deployment Device (IDD), including a *Rock Abrasion Tool (RAT)*, a *Microscopic Imager (MI)*, an

Alpha Particle X-ray Spectrometer (APXS), and the *miniaturised Mössbauer spectrometer MIMOS II*. The science package also includes navigational cameras (Navcams), hazard assessment cameras (Hazcams) and a set of magnets to collect sand and dust particles. A MER rover in a virtual Martian landscape is shown in Figure 2.4, along with a Pancam image of Opportunity's MIMOS II instrument.

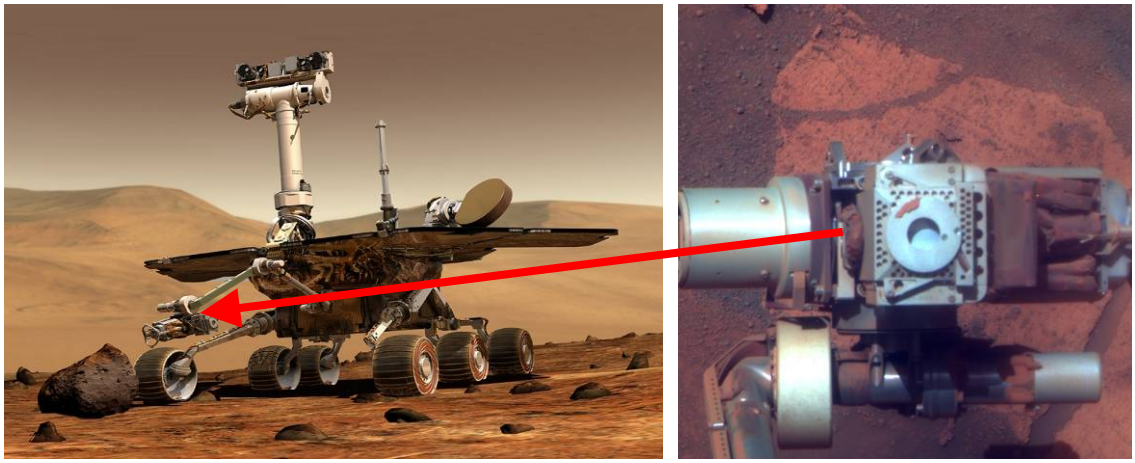

Figure 2.4: A Mars Exploration Rover in a virtual Martian landscape (left), the arrow points to the instrument assemblage on the Instrument Deployment Device. Right: MIMOS II captured by Opportunity's Panoramic Camera on Sol 1399.

Pancam comprises two separate cameras to provide stereo imaging capability, each equipped with an eight position filter wheel. 13 of the 16 filter slots are occupied by "geology" filters for multispectral imaging in the range from 434 to 1009 nm [*Bell et al.*, 2003]. Two filters are designed for direct imaging of the sun. The remaining filter slot is empty to maximize sensitivity for low-light imaging conditions. *Mini-TES* is a Fourier transform interferometer/spectrometer and covers the wavelength region from 5 to 29.5 µm [*Christensen et al.*, 2003]. Mounted inside the rover body at the base of the PMA, the instrument views the rover surroundings using the PMA as a periscope. Remote sensing data from both instruments provide information on the composition of rocks and soils, often preceding an analysis campaign with the contact instruments.

The *Rock Abrasion Tool (RAT)* was designed to expose fresh rock surfaces for study with other instruments by grinding away the rock surface and by brushing away soil covering the rock [*Gorevan et al.*, 2003]. A RAT grind or brush has a diameter of 45 mm, with a desired excavation depth of typically ~5 mm. The motor currents measured during a grinding operation serve as a measure of rock density and hardness.

The *Microscopic Imager (MI)* is a fixed-focus camera with a field of view of 32 by 32 mm. With a resolution of ~30 µm/pixel, MI images provide important information about the texture of a sample [*Herkenhoff et al.*, 2003]. The focus position is changed by moving the IDD in steps of a few mm, acquiring an image after each step. Completely focused images of targets with irregular surfaces are obtained by combining multiple images taken from various distances. Elemental analysis is carried out with the *Alpha Particle X-ray Spectrometer (APXS)* [*Rieder et al.*, 2003]. The instrument uses a ^{244}Cm source for X-ray excitation. Two excitation mechanisms cause the emission of X-rays from the sample: X-ray fluorescence (XRF) and particle induced X-ray emission (PIXE). This combination results in good sensitivities for the elements ranging from sodium (atomic number = 11) up to bromine (atomic number = 35). Emitted X-rays are registered by an X-ray detector inside the sensor head and accumulated in an X-ray energy spectrum. Elements can be identified by their peaks at characteristic energies; elemental abundances can be derived from the peak areas.

In this framework, MIMOS II provides information on the presence of Iron-bearing phases, Iron oxidation states and the distribution of Iron among them. Whenever possible, a sample is investigated with the whole instrument suite to establish a strong correlation between different data sets. When reconciling mineralogy determined from Mössbauer data with composition determined from APXS measurements, the different fields of view (~15 mm for MIMOS II, ~38 mm for the APXS) and sampling depths (~200 µm for MIMOS II, ~1 – 20 µm for the APXS) of both instruments have to be taken into account.

2.2.1 Instrument Configuration

MIMOS II has two major components: the electronics board is situated in the Warm Electronics Box (WEB) inside the rover body, which is kept at temperatures over -40°C, and includes power supplies, a dedicated central processing unit, memory, and associated support electronics. The sensor head is mounted on the rovers' Instrument Deployment Device (IDD), as shown in Figure 2.4. A schematic drawing of the sensor head components and an image of a sensor head with an opened chassis is shown in Figure 2.5 [from *Klingelhöfer et al.*, 2003].

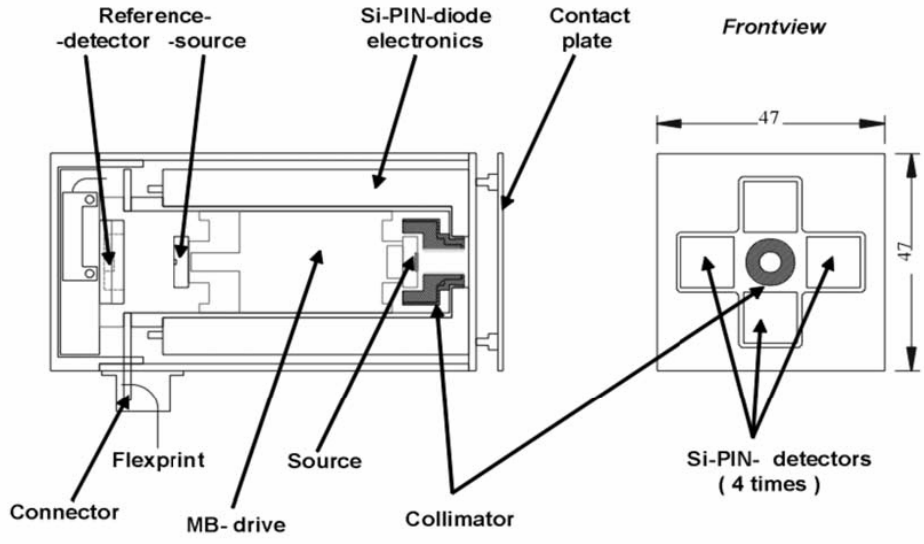

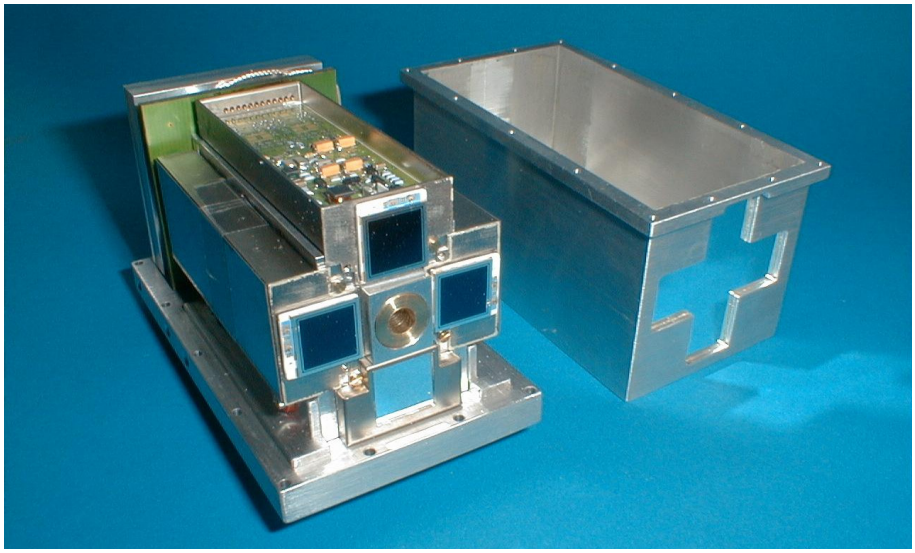

Figure 2.5: Above: Schematic drawing of the main components of the MIMOS II sensorhead [from *Klingelhöfer et al.*, 2003]. Below: A sensor head with opened chassis; the four Si-PIN detectors centered around the collimator as well as one of the amplifier boards are visible.

The central drive unit is surrounded by circuit boards with amplifier and discriminator electronics. The collimator and four detectors are visible at the front of the sensor head. Two ^{57}Co in Rh matrix Mössbauer sources, manufactured as thin foils with ~4 mm diameter, are mounted at opposite ends of the velocity transducer. A weaker source (typically ~15 – 20 mCi), a reference absorber and –detector are configured in transmission geometry internal to the instrument to obtain calibration spectra in transmission geometry simultaneously to the spectra obtained on surface targets. The stronger source, typically ~30 – 150 mCi, is mounted in the direction of the sample and enclosed in a collimator, a graded shield consisting of concentric tubes of brass, tantalum, and lead.
Four Si-PIN detectors are placed around the collimator, each with an area of 10 by 10 mm² and a thickness of 500 µm. The collimator opening determines the diameter of the irradiated target area. With increasing diameter, a larger sample spot is irradiated, minimizing the integration time. However, a large collimator diameter compromises the quality of the spectra because geometric effects such as cosine smearing become more relevant. Considering these two opposed effects, a collimator with an inner diameter of 5.6 mm was chosen for MIMOS II [*Schröder,* 2006]. With this setup, the irradiated sample spot has a diameter of 15 mm. The detector system has to be shielded against direct radiation from the source. This is partly achieved by the collimator design and partly by tantalum plates with 500 µm thickness on the backside of the detectors. An aluminized kapton foil in the outer shell of the chassis shields the detectors from dust and external light. The optimum distance between sensor head and sample is sensed by the closing of two switches on a contact plate. With a chassis made of aluminum, the sensor head weighs 400 g and measures 50 by 50 by 90 mm³. The energy consumption is ~2 W.

2.2.2 Operational Modes

Five counters with 512 channels each are available to store the data obtained with the four main detectors plus the reference detector on MIMOS II. One counter is reserved to store the reference spectrum, which is measured in transmission geometry and thus with 14.4 keV γ-rays. The other four counters can be set to collect either 14.4 keV γ-rays or 6.4 keV X-rays only or 14.4 keV γ-rays and 6.4 keV X-rays simultaneously. In the latter case, data from two specific detectors have to be binned and stored in one counter, so that two counters each collect 14.4 keV γ-rays or 6.4 keV X-rays, respectively. The analysis of 14.4 keV and 6.4 keV spectra yields depth selective information about the investigated sample, as will be described in more detail in chapter 3. However, the binning of data does not allow singling out a faulty detector.
The Martian diurnal temperature cycle covers the range from below 180 K during a winter night to above 290 K on a summer day. The Mössbauer parameters of many minerals are temperature dependent and MIMOS II instrument characteristics may also be influenced by temperature variations. Spectra are thus stored in 13 temperature windows 10 K wide between 180 K and 290 K (m2 – m12), as well as below 180 K (m1) and above 290 K (m13). The temperature is measured with three individual sensors, one located on the electronics board in the rover body, one near the reference target inside the sensor head and one on the contact plate. The sensor at the contact plate measures the temperature closest to the sample and is read out periodically for binning into temperature windows. A temperature independent mode is available for laboratory room temperature measurements. An energy mode is available to obtain pulse-height analysis spectra to determine and improve discriminator settings for Mössbauer measurements.

2.2.3 Calibration

Velocity calibration for MER Mössbauer spectra is primarily carried out by evaluating reference spectra obtained in transmission geometry. Reference spectra are obtained simultaneously with each backscatter measurement, so that the drive velocity can be determined for each temperature window of the measurement. The reference absorbers of the two MER instruments are composed of metallic α-iron, hematite (α-Fe_2O_3) and magnetite (Fe_3O_4). An example spectrum is shown in Figure 2.6a. The temperature dependence of the hyperfine parameters of these phases over the Martian diurnal temperature range was measured prior to the mission, as described in [*Schröder,* 2006].
Additionally, a "compositional calibration target" (CCT) is mounted on the rovers. The CCT was measured several times during the mission to confirm the calibration based on internal calibration measurements. An example spectrum is shown in Figure 2.6b.

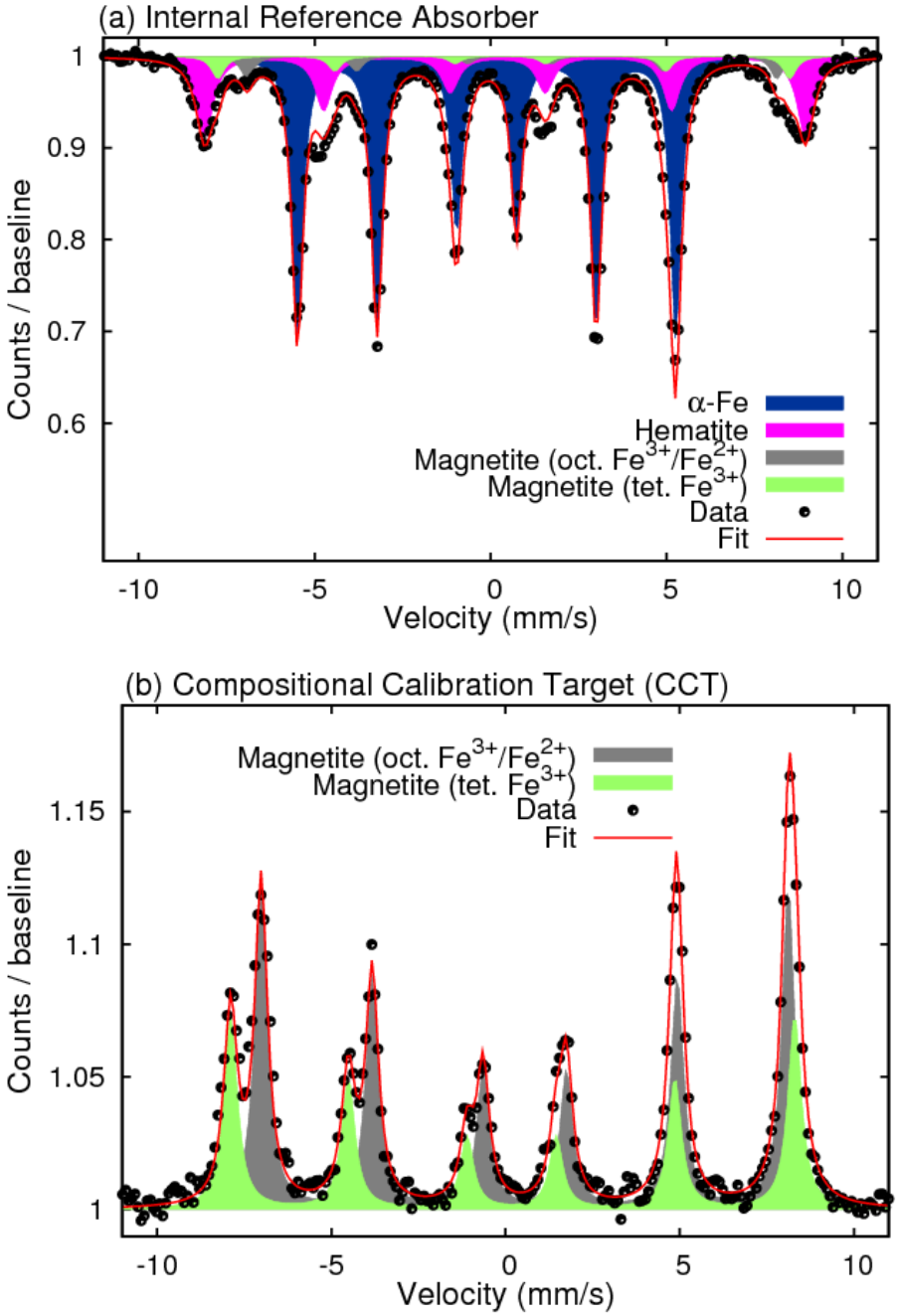

Figure 2.6: Example spectra obtained with Spirit's MIMOS II instrument (a) on the internal reference absorber on sol 14 and (b) on the rover's compositional calibration target on sol 213 (oct = octahedrally coordinated; tet = tetrahedrally coordinated).

2.2.4 Terrestrial Applications

Straight-forward laboratory measurements with copies of the MER instruments include analyses of Martian analogues, such as pure minerals, igneous rocks of diverse origins and with different degrees of weathering, and a range of meteorites. In addition to measurements at room temperature, these samples can also be measured at Mars-equivalent temperatures in a climate chamber cooled with liquid nitrogen. MIMOS II is field-portable and has been involved in field tests at Mars analogue sites such as Rio Tinto, Spain [e.g., *Fleischer et al*., 2010a] and Mauna Kea, Hawaii [e.g., *Schröder et al.*, 2010a].
A field-portable Mössbauer instrument is also of interest for a range of terrestrial applications. MIMOS II has been used in the monitoring of Iron ore production, to provide detailed quantitative insight into the reaction products present at different stages of the Iron ore processing [e.g., *Klingelhöfer et al.*, 1998]. A special experimental setup was developed for in-field monitoring of hydromorphic soils and the formation of the green-rust mineral fougerite [e.g., *Rodionov et al.*, 2006]. For air pollution studies, MIMOS II was installed in an airborne particle sampler [*de Souza,* 2000]. The instrument configuration in backscattering geometry also allows non-destructive analyses of rare and precious materials, such as archaeological artefacts [e.g., *Klingelhöfer et al.*, 2002a, 2002b; *de Souza et al.*, 2003].

2.2.5 Future Developments: MIMOS IIA

MIMOS IIA is an advanced version of the MER-type instrument. The most significant change is the implementation of silicon drift detectors (SDDs) instead of Si PIN diodes. Thereby, a much better energy resolution is provided, on the order of ~300 eV for SDDs compared to ~1 keV for Si PIN diodes at room temperature. The thus significantly improved signal-to-noise ratio allows a reduction of measurement times.
The higher resolution of the new detector system also enables the additional acquisition of X-ray fluorescence (XRF) spectra for elemental analysis. The 14.4 keV, 122 keV and 136 keV radiation from the Mössbauer source acts as excitation source for X-ray emission. The collimator was optimized for 14.4 keV radiation, but is less effective for higher energies. Consequently, the instrument field of view is larger in the XRF mode than in the Mössbauer mode. The combination of both modes in a single, field-portable instrument enables the simultaneous acquisition of elemental chemistry and Fe-mineralogical data on the same sample spot in a non-destructive way [*Klingelhöfer et al.*, 2010; *Blumers et al.*, 2010].

3 Depth selective Mössbauer spectroscopy

This chapter is partly based on the following publication:
I. Fleischer, G. Klingelhöfer, C. Schröder, R. V. Morris, M. Hahn, D. Rodionov, R. Gellert and P. A. de Souza (2008), *Depth selective Mossbauer spectroscopy: Analysis and simulation of 6.4 keV and 14.4 keV spectra obtained from rocks at Gusev Crater, Mars, and layered laboratory samples.* Journal of Geophysical Research - Planets, 113, E6.

3.1 Introduction

Natural rock samples often exhibit a surface layer, such as a weathering rind or biological rock varnish, or a layer of soil adhering to the rock. The investigation of such surface layers is of interest because their thickness and composition depend on the weathering history of the rock.
MIMOS II measures resonant 14.4 keV γ-rays and resonant 6.4 keV X-rays simultaneously. The analysis of both 6.4 keV and 14.4 keV Mössbauer spectra provides depth selective information about the mineralogical composition of both layers, because photon penetration depths are energy-dependent [*Klingelhöfer et al.*, 2002a, 2003; *de Souza,* 2004; *Fleischer,* 2006; *Fleischer et al.*, 2008a, 2008b]. The spectra derived from the less energetic 6.4 keV X-rays stem from shallower depths and contain more information about the near-surface part of a sample than do the more energetic 14.4 keV γ-rays, as shown schematically in Figure 3.1. Depending on the exact sample density and composition, especially its Fe content, photons in the keV-range have a sampling depth of up to a few hundred μm. A surface layer leads to significant differences between 6.4 keV and 14.4 keV spectra if it has a thickness of at least a few μm, but is thin enough to allow 14.4 keV radiation to reach the sample bulk.

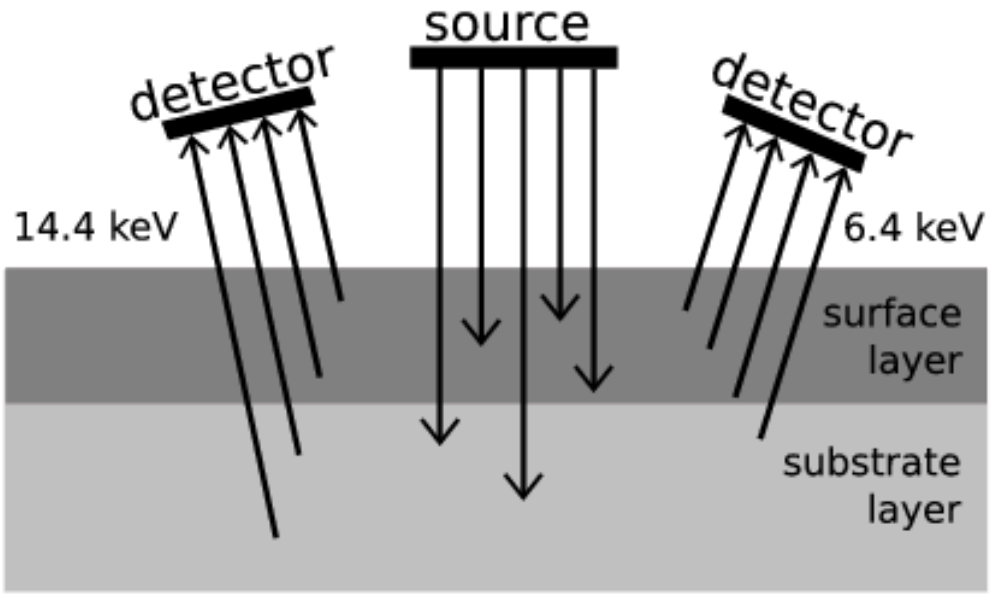

Figure 3.1: A hypothetical sample with a bulk region and a distinct surface layer. The 6.4 keV radiation bears more information from the near-surface part of the sample.

Very thin surface layers can be investigated with Conversion Electron Mössbauer Spectroscopy (CEMS), which makes use of conversion electrons with energies of up to 14.3 keV, resulting in sensitivity to the first ~0.2 µm of a sample [*Salvat and Parellada*, 1984; *Gellert et al.*, 1993]. Low-energy electron Mössbauer spectroscopy (LEEMS) utilizes Auger- and shake-off-electrons with energies of <15 eV, which have a sampling depth of ~0.005 µm [*Vandenberghe et al.*, 1998; *Klingelhöfer and Kankeleit,* 1990; *Klingelhöfer et al.*, 1992; *de Grave et al.*, 2005].

3.2 The Maximum Thickness of a Surface Layer

The maximum thickness of a surface layer can be defined as the thickness that allows the detection of a substrate in Mössbauer spectra, at least at the detection limit of ~2 % of the total subspectral area (i.e., equal to the typical uncertainty of subspectral areas for well-resolved spectra [e.g. *Morris et al.*, 2006a, 2006b, 2008]). This maximum thickness increases with decreasing Fe-content and decreasing density. While the penetration depth in a given surface layer does of course not change, the visibility of the substrate depends on the Fe content. With decreasing Fe content, it becomes harder to detect or is not visible at all.

If a γ-ray with incident intensity I_0 penetrates a sample with thickness x, its intensity $I(x)$ after passing through the sample is given by:

$$I(x) = I_0 \cdot e^{-\mu \cdot x} \,. \tag{3.1}$$

The absorption coefficient µ can be calculated from atomic cross sections σ_i for the different photon interaction processes i:

$$\mu = \frac{N_A}{A} \rho \sum_i \sigma_i w_i \,, \tag{3.2}$$

where N_A is the Avogadro constant, A is the atomic mass number, ρ is the density of the sample and w_i represents the weight percentages of different elements. The total absorption cross section is composed of the cross sections for the different processes:

$$\sigma_{total} = \sigma_{resonant} + \sigma_{photo} + \sigma_{Compton} + \sigma_{Rayleigh} \,. \tag{3.3}$$

The absorption cross section for resonant absorption is determined by:

$$\sigma_{res}(E_\gamma) = f\beta\sigma_0 \frac{\Gamma^2}{4} \sum_i \left(\frac{1}{(E_\gamma - E_{res,i})^2 + \frac{\Gamma^2}{4}} \right), \tag{3.4}$$

where β is the isotopic fraction of ^{57}Fe (2.2 %), σ_0 is the maximum resonant cross section, Γ is the natural line width of the source, E_γ is the energy of the emitted photon and E_{res} the energy at resonance [e.g., *Wegener*, 1966].

For Fe, non-resonant absorption coefficients are rather similar for 6.4 keV and 14.4 keV radiation because of the presence of the Fe K-edge at 7.1 keV, but can be an order of magnitude larger for 6.4 keV for other elements (e.g. Si). Some examples for common rock forming elements are displayed in Figure 3.2. Equation (3.1) can be used to calculate the γ-ray intensity after passing through a layer, using absorption coefficients for 14.4-keV γ-rays from the X-Com tables [*Berger,* 2010].

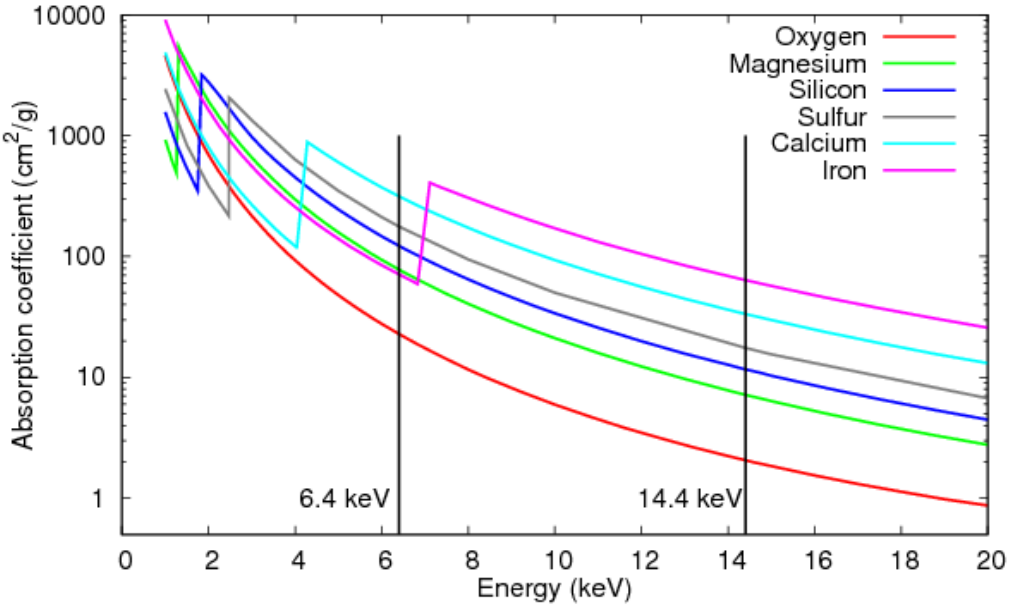

Figure 3.2: Energy dependence of non-resonant absorption coefficients for common elements.

In a measurement in backscattering geometry, as is the case for MIMOS II, photons pass the surface layer twice before reaching the detectors (i.e., on their way into and out of the sample). Attenuation processes must be taken into account for both passages, and it has to be considered that resonant 6.4 keV X-rays are emitted after resonant absorption of 14.4 keV γ-rays in the sample.

The calculated intensity after passing through 50 µm metallic Fe foil is 0.78 % for 14.4 keV γ-rays and 0.60 % for 6.4 keV X-rays. Measurements on a layered sample composed of 50 µm Fe foil on top of a hematite substrate yield subspectral areas of hematite of 1 % in the 6.4 keV spectrum and 3 % in the 14.4 keV spectrum. A layer of metallic Fe foil with a thickness of ~50 µm, corresponding to ~0.04 g/cm² Iron, can therefore be regarded as having the maximum thickness which allows the substrate to be resolved in Mössbauer spectra. The calculated values can be used to estimate the maximum thickness of surface layers with other compositions.

For a surface layer composed of hematite (Fe_2O_3) with a density of 5.3 g/cm³, maximum thicknesses of ~100 µm for 14.4 keV γ-rays, and of ~90 µm for 6.4 keV X-rays were calculated. For a surface layer of basaltic composition, a simplified model of 20 wt% FeO and 80 wt% SiO_2 with a density of 3 g/cm³ was used [e.g., *Gellert et al.*, 2004], yielding calculated maximum thicknesses of ~530 µm for 14.4 keV γ-rays and ~130 µm for 6.4 keV X-rays. These values are consistent with earlier results [*Morris et al.*, 2000a; *Klingelhöfer et al.*, 2003], where a different definition of the maximum sampling depth is used: a layer with maximum sampling depth is defined as a layer absorbing 95 % of the incident radiation, taking into account an experimental setup in backscattering geometry as described above. With this approach, *Morris et al.* [2000a] calculate a maximum sampling depth of ~200 µm (14.4 keV γ-rays) for a sample of basaltic composition.

The calculations described above are in agreement with results obtained from laboratory measurements: Figure 3.3 shows spectra obtained on samples composed of layers of basalt from Ortenberg, Vogelsberg with thicknesses of 100 and 500 µm on top of 50 µm Fe foil. With a basaltic surface layer of 100 µm thickness, metallic Fe shows subspectral areas of 42 % in the 14.4 keV spectrum, and 4 % in the 6.4 keV spectrum. With a basaltic surface layer of 100 µm thickness, metallic Fe shows subspectral areas of 42 % in the 14.4 keV spectrum, and 4 % in the 6.4 keV spectrum. With a basaltic surface layer of 500 µm

thickness, a spectral signature of metallic Fe is clearly present in the 14.4 keV spectrum (area percentage 4 %), but not detectable in the 6.4 keV spectrum.

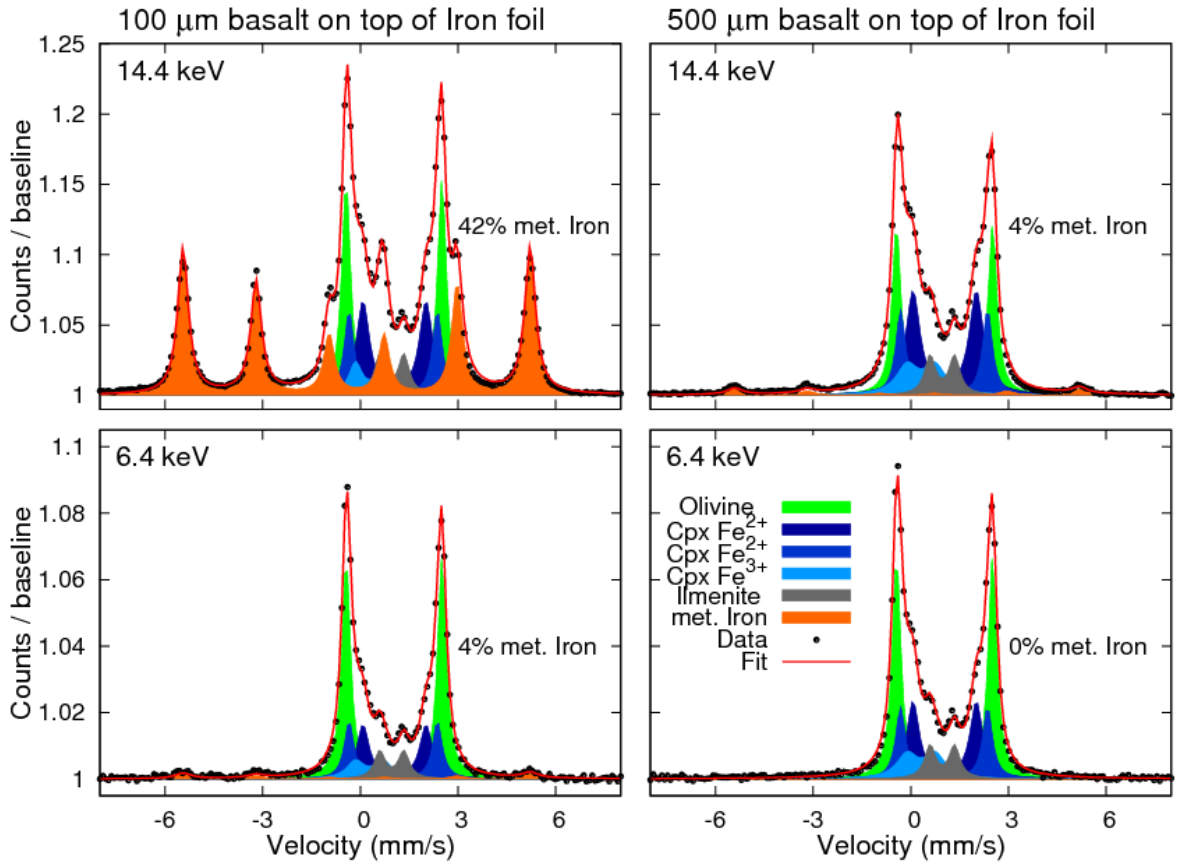

Figure 3.3: Spectra obtained on stacked samples of Ortenberg basalt on top of Fe foil.

3.3 Surface Weathering on Mazatzal and Bounce Rock

The MIMOS II instruments on the MER rovers have collected 6.4 keV X-ray and 14.4 keV γ-ray spectra for all targets through sol 461 for Spirit, and for all targets to date for Opportunity. With the higher level of background noise in 6.4 keV spectra, only measurements obtained early in the mission (while the source was still comparably strong) have a high enough statistical quality to allow a depth-selective analysis from separate fits of 6.4 keV and 14.4 keV spectra. The two rocks *Mazatzal* and *Bounce Rock* were found to show definite, depth-related differences between 6.4 keV and 14.4 keV spectra.

Mazatzal (Figure 3.4a) was encountered by Spirit on the basaltic plains of Gusev crater and belongs to the *Adirondack class* of weakly weathered basaltic rocks [*Morris et al.*, 2006a]. The mineralogy of this rock class is dominated by olivine and pyroxene, along with the weathering product nanophase ferric oxide as well as minor hematite and magnetite. Nanophase ferric oxide (npOx) is a generic name for Fe oxides or oxyhydroxides with particle sizes in the nanometer range that are superparamagnetic at the temperature of observation, e.g. hematite (α-Fe_2O_3), maghemite (γ-Fe_2O_3) or goethite (α-FeOOH).

Figure 3.4b shows a microscopic image obtained on the rock after a partial RAT grind, with a dark surface layer covering the brighter rock interior. The surface layer was removed practically completely during a second RAT grind. The fraction of npOx is largest in the 6.4 keV spectra obtained on the undisturbed or brushed surface, and reduced in spectra obtained after grinding. Mössbauer spectra obtained on the brushed surface are shown in Figure 3.4c and Figure 3.4d, with 47 % npOx in the 6.4 keV spectrum and 29 % npOx in the 14.4 keV spectrum, with an uncertainty of 2 % (absolute). Mössbauer

parameters and uncertainties are listed in Table 3.1. As described in detail in [*Fleischer,* 2006] and [*Fleischer et al.*, 2008b], *Mazatzal* spectra were Monte Carlo simulated to estimate the composition and thickness of the surface layer. A layer with a composition of mainly npOx with minor contributions from hematite and magnetite and with a thickness of ~10 µm was found to be in good agreement with measured spectra.

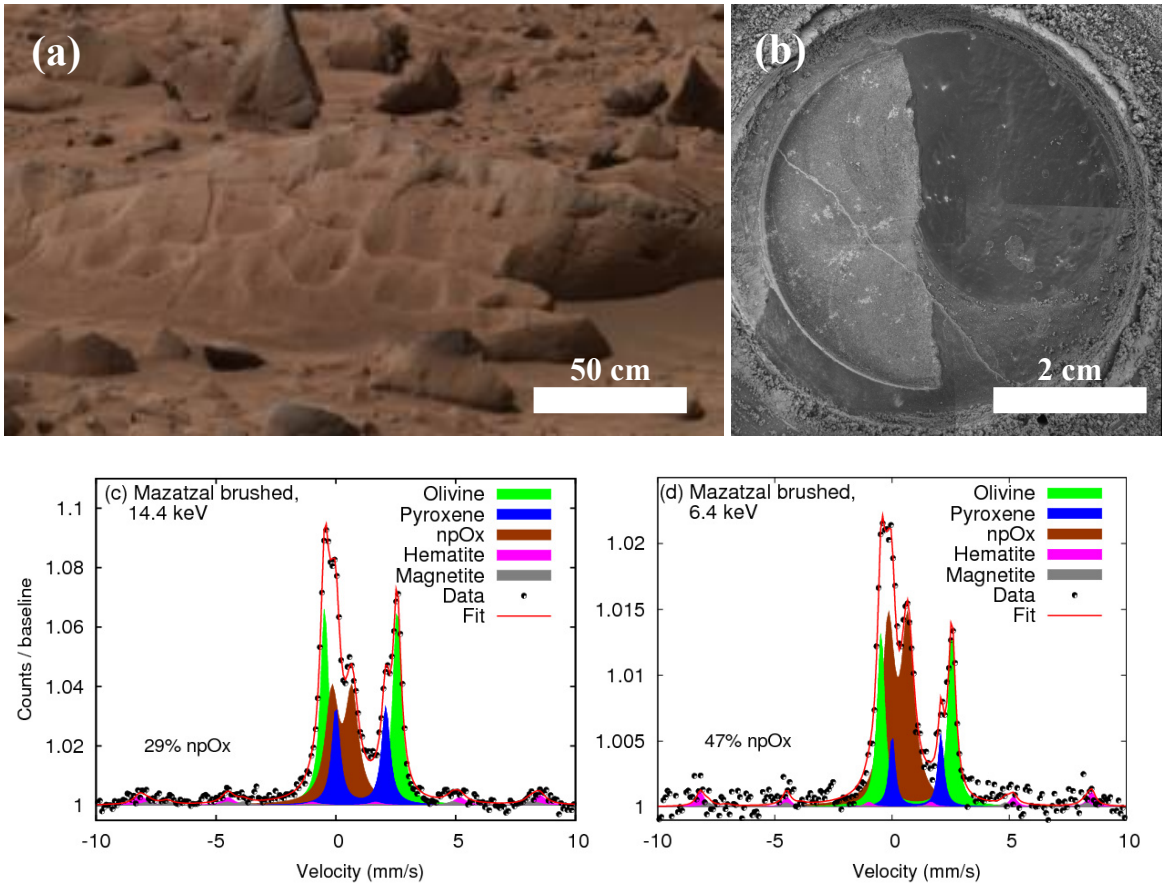

Figure 3.4: On the rock *Mazatzal* ((a), Pancam image), a dark coating was detected ((b), microscopic image, partially abraded spot with 45 mm diameter). The comparison of Mössbauer spectra ((c), 14.4 keV and (d), 6.4 keV) shows a larger fraction of npOx in the 6.4 keV spectrum than in the 14.4 keV spectrum.

Table 3.1: Mössbauer parameters for *Mazatzal* and *Bounce Rock*.

	Mazatzal			Bounce Rock	
Mineral Phase	**δ (mm/s)**	**ΔE_Q (mm/s)**	**B_{hf} (T)**	**δ (mm/s)**	**ΔE_Q (mm/s)**
Olivine	1.16	3.02	-	-	-
Pyroxene	1.16	2.08	-	1.17	2.78
Pyroxene	-	-	-	1.15	2.07
npOx	0.37	0.83	-	0.49	0.75
Hematite	0.37	-0.17	51.8	-	-
Magnetite[1]	0.31	-0.06	50.1	-	-
Magnetite[2]	0.64	0	46.9	-	-

Uncertainties are ±0.02 mm/s for δ and ΔE_Q and ±0.8 T for B_{hf}.
[1]tetrahedrally coordinated Fe^{3+}
[2]octahedrally coordinated Fe^{3+}/Fe^{2+}

Bounce Rock was encountered by Opportunity close to the rim of Eagle crater on sol 63. This ~30 cm diameter rock is chemically and mineralogically similar to the martian SNC meteorites (named for the three type meteorites Shergotty, Nakhla, and Chassigny) [*Zipfel et al.*, 2010; *Meyer,* 2010], but distinct from any other material at Opportunity's landing site and was most likely delivered to its current location as secondary impact ejecta [*Zipfel et al.*, 2010]. Spectra obtained on the abraded surface of *Bounce Rock* are shown in Figure 3.5, Mössbauer parameters and uncertainties are listed in Table 3.1. They reveal two pyroxene phases with small amounts of npOx present. With less than 1 % in the 14.4 keV spectrum and 2 % in the 6.4 keV spectrum, and an uncertainty of 2 %, these values are within uncertainty of zero. Three spots were investigated on the undisturbed surface. They show slightly larger amounts of npOx, up to 3 % in 14.4 keV spectra; and up to 5 % in 6.4 keV spectra. Mössbauer parameters are different from those of the npOx phase measured in surrounding soil, suggesting oxidation of the surface rather than npOx from surface dust contamination [Table 3.1; *Zipfel et al.*, 2010].

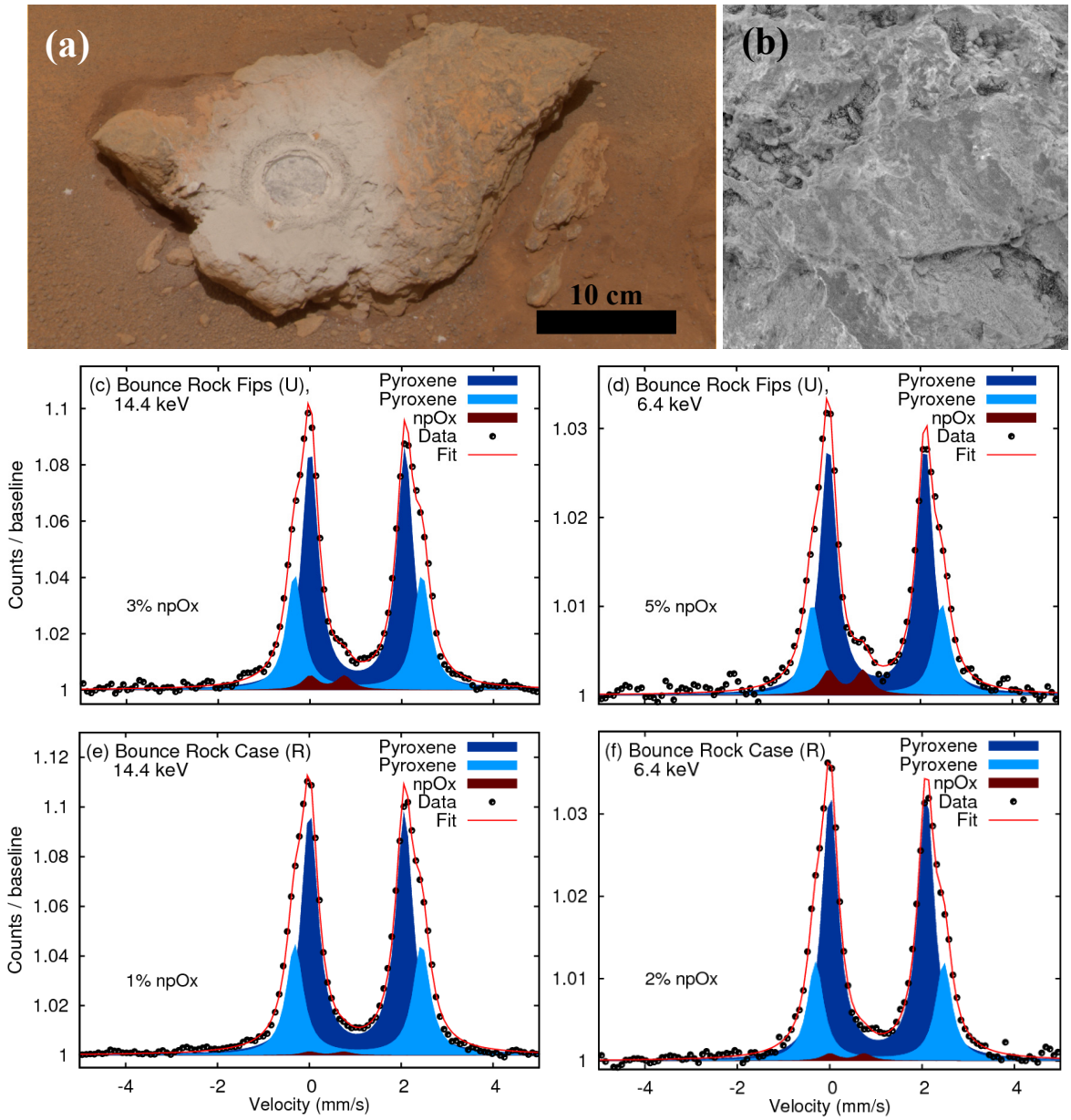

Figure 3.5: Pancam (a) and microscopic (b) images of *Bounce Rock*. Spectra obtained on the undisturbed ("U") surface spot *Fips* ((c) and (d)) show larger portions of nanophase ferric oxide (npOx) than spectra obtained on the RAT-abraded ("R") surface spot *Case* ((e) and (f)).

3.4 The Effect of Viewing Geometry: Meridiani Spherules

With Opportunity's Mössbauer spectrometer, several measurements were carried out on hematite-rich spherules weathering out of the outcrop rock. Ten different spherule-bearing targets were analysed, microscopic images are shown in Figure 3.6. Spherule distributions range from a few large (~5 mm diameter) spherules on top of soil or outcrop rock to spots of soil covered entirely with small (~2 mm diameter) spherules. The first case is represented by the target *Berry Survey* measured between sols 222 and 228, the second case by the target *Ripple Crest* measured between sols 368 and 370. Both cases were set up as analogue laboratory experiments (Figure 3.6k and Figure 3.6l). For both configurations, hematite-rich spherules were placed on top of coarse basaltic sand (grain size <0.5 mm). Two measurements were made before and after covering the spherules with fine basaltic sand (grain size <0.1 mm). Four large (~5 mm diameter) spherules were measured in the first experiment, and enough small (~1 – 1.5 mm diameter) spherules to cover the field of view were measured in the second experiment. Fine sand did not adhere to the spherules, but rather accumulated in the gaps between them, comparable to what can be observed for both Meridiani samples.

With the laboratory setup, spherules and basaltic sand were measured separately to determine Mössbauer parameters and relative subspectral areas of mineral phases. In the combined measurements of spherules and sand, all parameters were fixed to these previously determined values. Figure 3.7 shows a collection of spectra obtained on the two Meridiani targets *Berry Survey* and *Ripple Crest* and on the analogue setups with a basaltic sand cover. The left column shows fits of the 14.4 keV spectra; the right column shows a comparison of the 14.4 keV and 6.4 keV spectra obtained on each target. For Meridiani spherules, the basaltic component includes olivine, pyroxene, magnetite and nanophase ferric oxide (npOx). The hematite in spherules was modeled with two components, discussed in detail in chapter 4. The analogue spherules were found to have a magnetically ordered component in addition to hematite, potentially maghemite. The basaltic sand used for the analogue setups contains olivine, pyroxene, magnetite and a ferric phase. In Figure 3.7, it is apparent that differences between the 14.4 keV spectrum and the 6.4 keV spectrum are larger for the two setups with four large spherules.

Subspectral areas for all investigated targets are given in Table 3.2, with respect to components related to spherules and basaltic material in the field of view. Representative Mössbauer parameters are listed in Table A1 in the appendix.

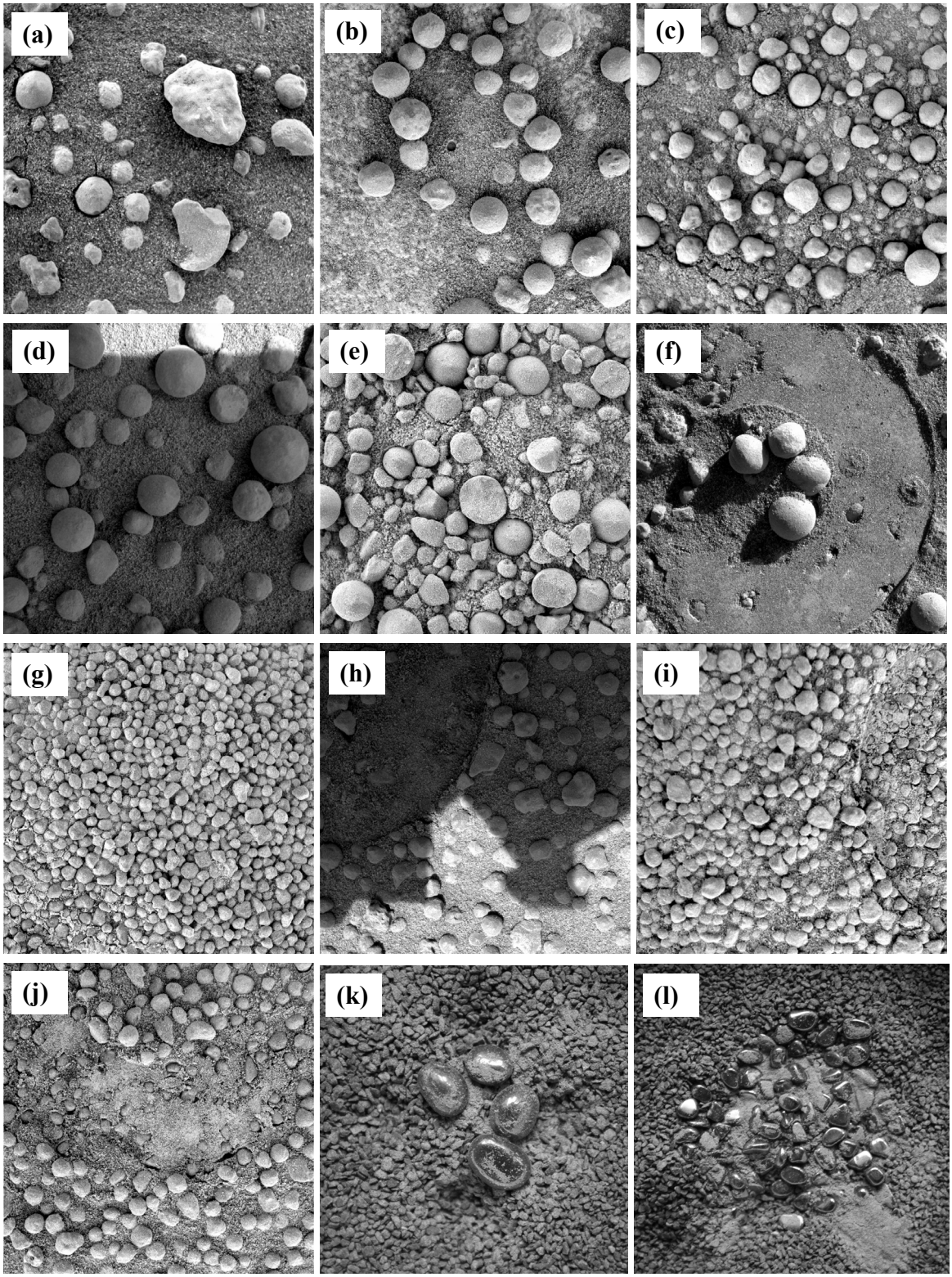

Figure 3.6: (a)-(j): Microscopic images of spherule-rich Meridiani targets, with a basaltic substrate and basaltic dust accumulated between them. The targets are: (a) *Hema2*, Sol 23. (b) *Berry Bowl*, Sol 48. (c) *Panaluu*, Sol 52. (d) *Aegean Crest*, Sol 73. (e) *Leah's Choice*, Sols 97-99. (f) *Berry Survey*, Sols 222-228. (g) *Ripple Crest*, Sol 368-370. (h) *Mobarak*, Sol 415. (i) *MayBeRooz*, Sol 420. (j) *Cure*, Sol 445. (k), (l): Analogue setup with four large (k) or many small spherules (l), respectively. Spherule diameters vary between ~1 mm (e.g., (g)) and ~5 mm (e.g., (f)).

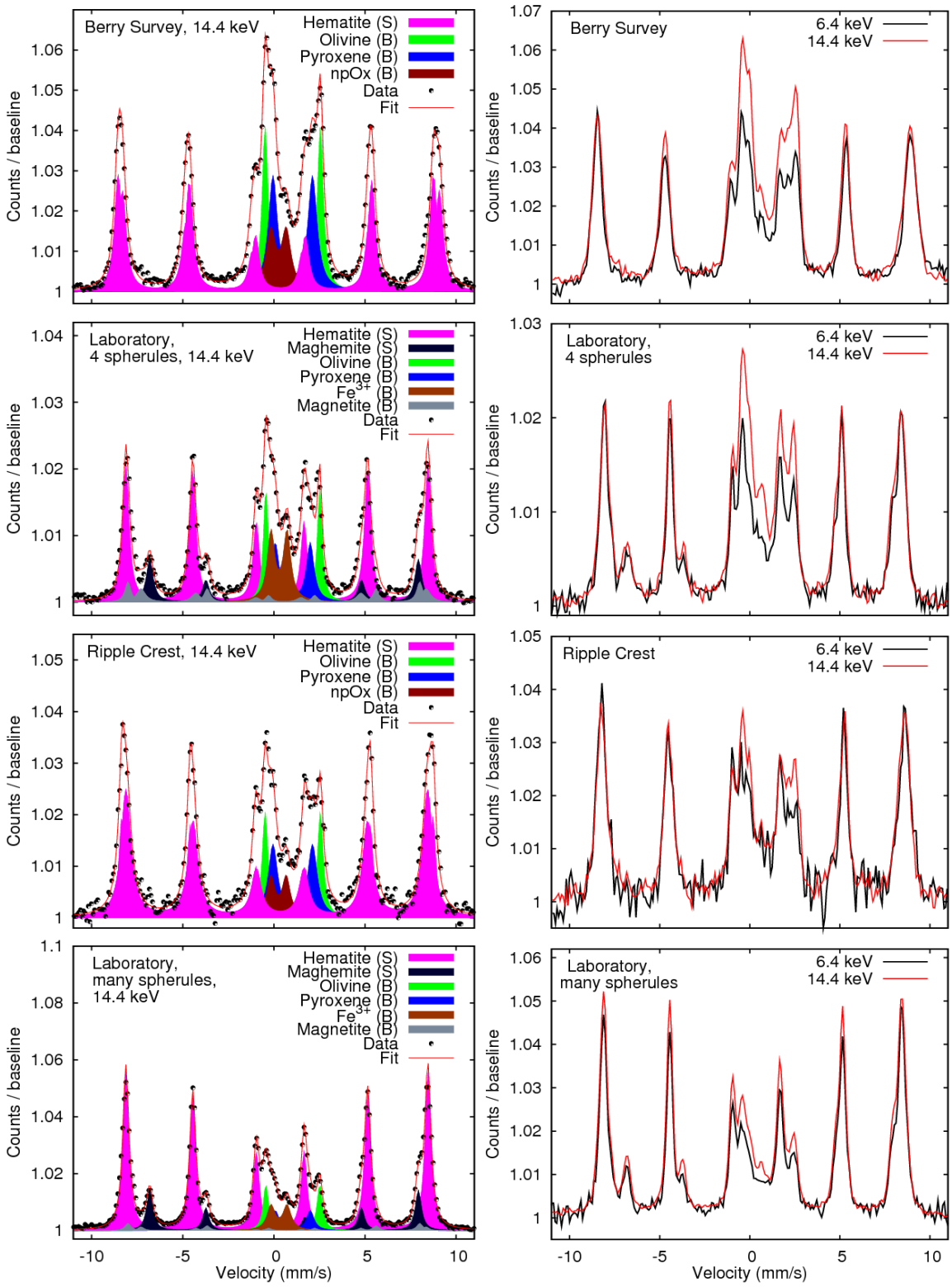

Figure 3.7: Spectra obtained on the two Martian targets *Ripple Crest* and *Berry Survey* and on the laboratory analogue setups. The left column shows fits of the 14.4 keV spectra (S: spherules; B: basaltic component). The right column shows a direct comparison of 14.4 keV and 6.4 keV spectra for each target. Greater differences between both spectra occur for the measurements with four spherules.

Table 3.2: Subspectral area fractions of basaltic components and spherules, and subspectral area ratios of both components for Meridiani Planum and analogue measurements.

Sample	Sol	Subspectral Area (%)				Area Ratio Basalt/Spherules	
		Basaltic component		Spherules			
		14.4 keV	6.4 keV	14.4 keV	6.4 keV	14.4 keV	6.4 keV
(a) Hema2	23	72	69	28	31	2.6	2.2
(b) BerryBowl	48	38	31	62	69	0.6	0.4
(c) Panaluu	52	27	20	73	80	0.4	0.3
(d) AegeanCrest	73	24	18	76	82	0.3	0.2
(e) LeahsChoice	97-99	47	39	53	61	0.9	0.6
(f) BerrySurvey	222-228	43	36	56	64	0.8	0.6
(g) RippleCrest	368-370	30	24	70	77	0.4	0.3
(h) Mobarak	415-418	49	42	51	58	1.0	0.7
(i) MayBeRooz	420-421	45	45	55	55	0.8	0.8
(j) Cure	445	46	40	53	60	0.9	0.7
Four spherules without cover	n. a.	34	45	66	55	0.5	0.8
(k) Four spherules with cover	n. a.	45	36	55	64	0.8	0.6
Many spherules without cover	n. a.	0	0	100	100	0	0
(l) Many spherules with cover	n. a.	23	21	77	79	0.3	0.3

Different targets can be compared based on the subspectral area ratio of basaltic components and spherules.
Subspectral areas and ratios are very similar for the target *Berry Survey* and the laboratory setup with four sand-covered spherules; and for the target *Ripple Crest* and the laboratory setup with many sand-covered spherules, demonstrating that both analogue setups are reasonable approximations of the Meridiani samples. As spherules and basaltic sand could be measured separately for the laboratory setup, it can be excluded that the observed differences result from an inhomogeneous composition of the spherules. Instead, the differences must be attributed to energy-dependent penetration depths associated with the uneven nature of the target surfaces, causing varying amounts of soil to be visible in the spectra. Generally, the ratio becomes smaller with increasing area coverage by spherules. In practically all cases, the ratio is smaller for the 6.4 keV spectrum, corresponding to a larger subspectral area of the spherule component. These results can be explained taking into account the viewing geometry of the setup: a smaller number of spherules covers a smaller area, so that more basaltic material will be visible in the instrument field of view. A flat surface is approximated if the field of view is covered with many small spherules, and the viewing geometry will be more similar for the two different energies. More basaltic material is visible in 14.4 keV spectra because the higher energy radiation is more likely to reach the soil accumulated between spherules.
The spectra obtained on Meridiani spherules demonstrate that differences between 14.4 keV and 6.4 keV spectra cannot always be attributed to compositional variations with depth in a sample, but rather to viewing geometry in some cases. The spectra from Meridiani spherules are in agreement with a spherule composition of pure hematite, and a soil signature from substrate and soil accumulated between spherules, in agreement with other Meridiani spherule studies [e.g., *Jolliff et al.*, 2007].

3.5 Measurements on Homogeneous Samples

Identical subspectral areas (within statistical errors) would be expected from 6.4 keV and 14.4 keV spectra for homogeneous samples, such as well-mixed soils or clean, smooth rock surfaces. Laboratory measurements were performed on basaltic rock samples and powdered samples. Two rock specimens were sampled at Bauersberg, Rhön and Ortenberg, Vogelsberg, respectively. Three Martian analogue samples (AREF108, AREF135 and AREF149) were chosen from the Athena Reference catalogue [*C. Schröder,* 2003, unpublished material]. Powdered samples include Ortenberg basalt and two sieve fractions (<0.1 mm and <0.5 mm) of a commercially available basalt ("Kremer Basalt") as well as mixtures of olivine and pyroxene powders (sieve fraction <45 µm) with mixing ratios of 1:1, 1:3, 3:1 and 9:1 by weight.

Measurements of Martian soil for 10 targets from Gusev crater and 15 targets from Meridiani Planum were included, as well as measurements from 15 RAT abraded rock targets from Gusev crater. The bulk of soil grains are resolved in MI images, so that a size range of 50-150 µm can be inferred [*Soderblom et al.*, 2004]. Many MI images obtained on abraded rock targets show single grains embedded in a matrix of grains too fine to be resolved by the MI [*Herkenhoff et al.*, 2006]. Four example spectra are shown in Figure 3.8, the spectrum of Ortenberg basalt is shown in Figure 3.3. Mössbauer parameters are compiled in Table A2 in the appendix.

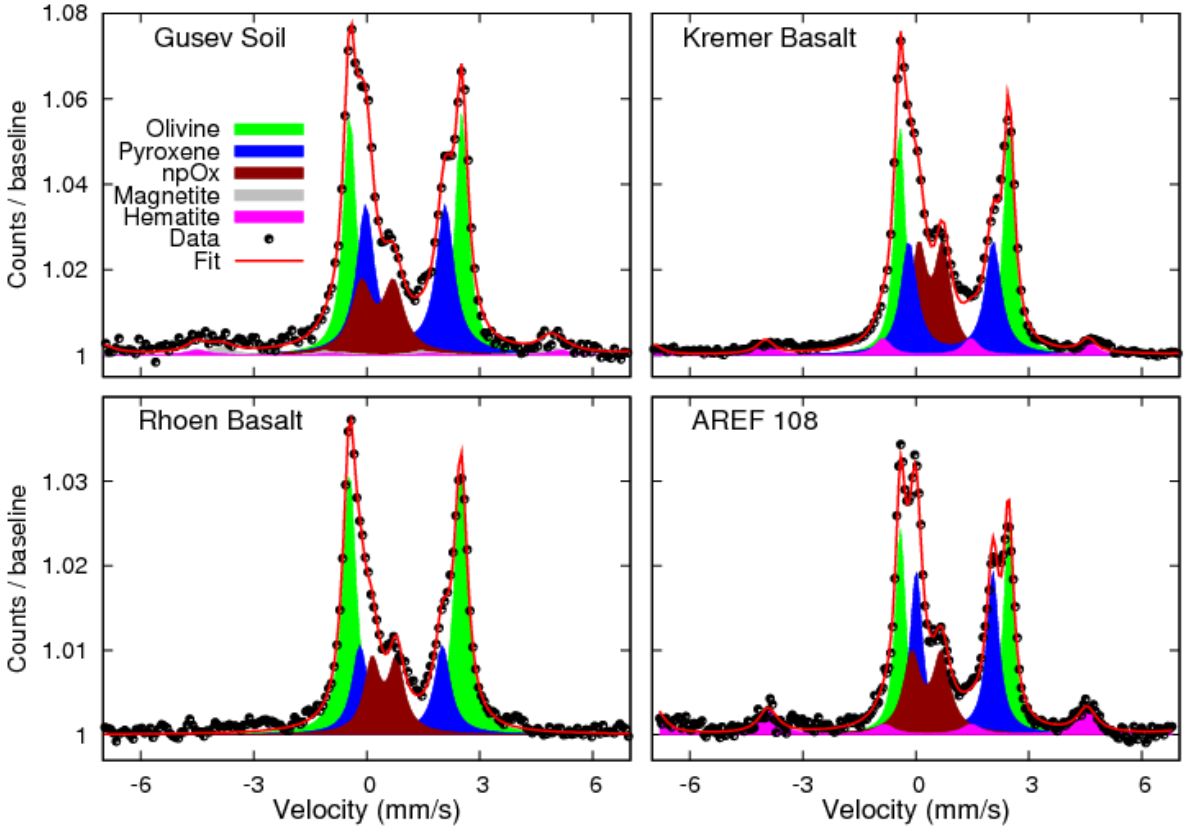

Figure 3.8: Example spectra (14.4 keV) obtained on Gusev Soil and three basaltic analogue samples. All spectra (including those not shown here) are dominated by olivine and pyroxene with nanophase ferric oxide (npOx), hematite and magnetite.

Subspectral areas for olivine, pyroxene, nanophase ferric oxide (npOx), hematite and magnetite from 14.4 keV spectra of this data set were plotted against the areas of the corresponding phase from 6.4 keV spectra, as shown in Figure 3.9. Mineral phases with identical subspectral areas in 14.4 keV and 6.4 keV spectra are located on a line through the origin with slope 1. This behaviour would be expected for the aforementioned homogeneous targets, with margins defined by the subspectral area uncertainty of ±2 %. Surprisingly, ~80 % of all measurements from Martian targets show a larger fraction of olivine and npOx in 6.4 keV spectra, along with a smaller fraction of pyroxene in ~70 % of all 6.4 keV spectra. Hematite and magnetite plot approximately along the line. Subspectral areas from analogue measurements fall closer to the line, but most of them also show slightly larger olivine subspectral areas in 6.4 keV spectra.

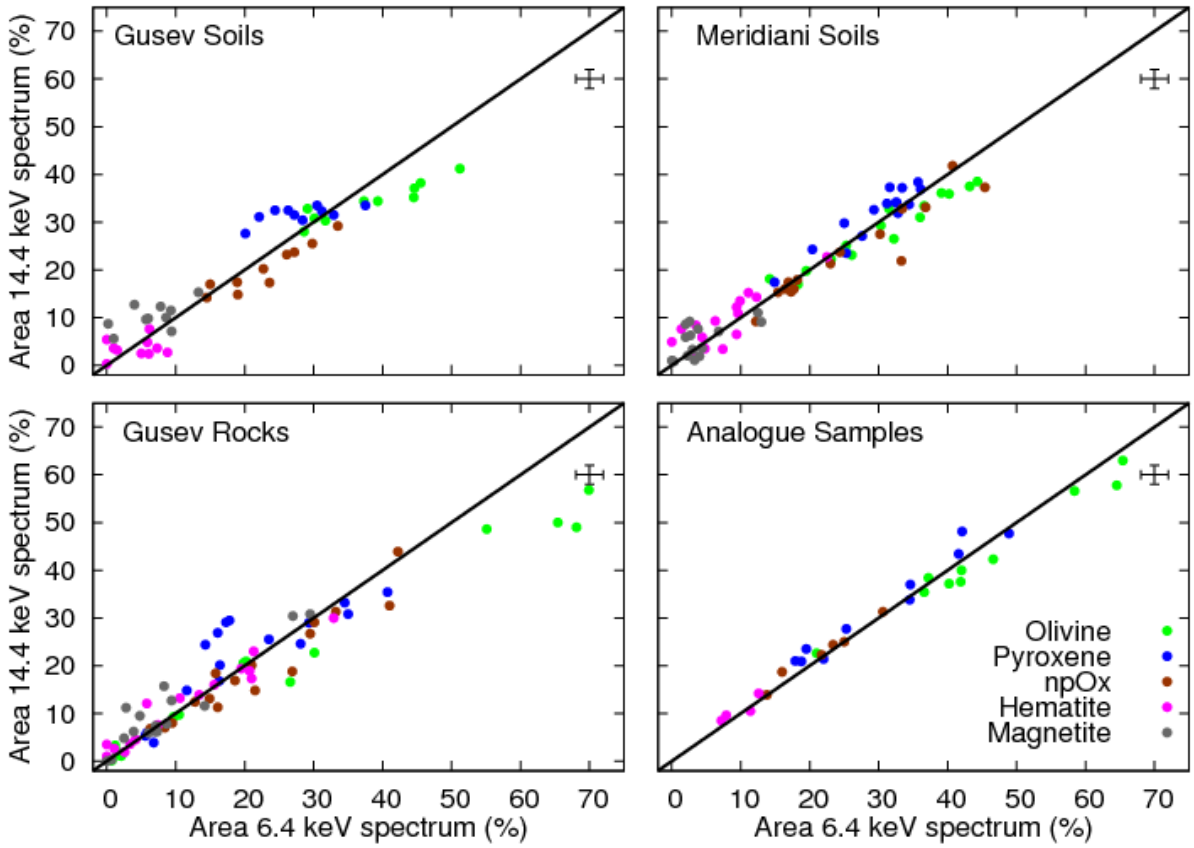

Figure 3.9: Comparison of 6.4 keV and 14.4 keV subspectral areas for basaltic soils from both landing sites, basaltic rocks from Gusev crater and analogue samples. The line represents equal subspectral areas in 14.4 keV and 6.4 keV spectra. In many cases, subspectral areas for olivine and nanophase ferric oxide (npOx) are larger in 6.4 keV spectra. Representative uncertainties are indicated (2 % absolute).

Larger npOx subspectral areas in 6.4 keV spectra are expected if weathered surface layers exist on rock targets, but potentially also on single soil grains. However, such surface layers are unlikely to be enriched in olivine, because olivine is the mineral most susceptible to weathering [e.g. *Morris et al.*, 2006a]. An olivine-enriched surface layer can also be excluded for the analogue samples. *Gunnlaugsson et al.* [2006] speculated that pyroxene crystals may be preferentially removed by RAT abrasion operations, while olivine crystals are cut and thus remain at the sample surface. However, this does not explain the observations from soil targets.

In many samples discussed here, olivine is the phase with the largest subspectral area. Energy dependent geometry- or thickness-effects could contribute to an overestimation of olivine subspectral areas in 6.4 keV spectra. Depending on the available integration time, 6.4 keV spectra may not be as well-resolved as 14.4 keV because of the generally higher noise level. This is usually not an issue for laboratory spectra, but may have a considerable effect on spectra measured on Mars and may thus be another contributing factor. Different subspectral areas for 6.4 keV and 14.4 keV spectra are observed independent of the employed spectrometer, so that an instrumental influence appears unlikely.
While the origin of the increased olivine content in 6.4 keV spectra remains unresolved, this observation shows that differences between subspectral areas from 14.4 keV and 6.4 keV spectra on the order of several percent cannot automatically be attributed to the presence of compositional variation with depth in a sample.

3.6 Conclusions

Depth selective Mössbauer spectroscopy has successfully been applied to some suitable rock targets encountered by both Mars Exploration Rovers. The method has proven helpful to detect and characterize weathering layers on rocks.
Differences between 6.4 keV and 14.4 keV spectra are dependent on the thickness, density and composition of the investigated surface layer and the underlying substrate. Based on laboratory experiments and reinforced by calculations, a substrate can be detected in Mössbauer spectra if the thickness of the overlying surface layer does not exceed 50 µm in the case of metallic iron and up to 500 µm for a basaltic composition.
Soil samples with a considerable contribution of mm-sized spherules encountered at Meridiani Planum show substantial differences between 6.4 keV and 14.4 keV spectra. Laboratory experiments with analogue setups confirm that the complex sample geometry is the origin of the observed differences, rather than inhomogeneities in the spherules themselves.
The investigation of well mixed soil samples and rock samples with fine grained matrices shows that differences between 6.4 keV and 14.4 keV spectra on the order of a few percent may also arise for apparently homogeneous samples and cannot automatically be attributed to the existence of layering in a sample.

4 Distinct Hematite Populations at Meridiani Planum

This chapter is based on the following publication:
I. Fleischer, D. G. Agresti, G. Klingelhöfer and R. V. Morris (2010), *Distinct hematite populations from simultaneous fitting of Mössbauer spectra from Meridiani Planum, Mars.* Journal of Geophysical Research (in print).

4.1 Introduction

Opportunity's Meridiani Planum landing site is characterized as a bright, sulfate-rich outcrop overlain by basaltic soil, a lag of hematite spherules and their fragments that were weathered from the outcrop. Observations suggest that the outcrop and spherules formed under the influence of substantial amounts of water. Occasional occurrences of loose rocks include crater ejecta and meteorites [*Squyres et al.*, 2004, 2006; *Klingelhöfer et al.*, 2004; *Christensen et al.*, 2004; *Clark et al*., 2005; *McLennan et al.*, 2005 ; *Morris et al*., 2006b; *Calvin et al.*, 2008]. Hematite in the sulfate-rich outcrop is present both as the ~5 mm diameter spherules and in the outcrop matrix as particles whose diameters are below the resolution limit of the MI (~30 μm/pixel) [*Klingelhöfer et al.*, 2004; *Morris et al.*, 2006].
Figure 4.1a shows an image obtained with the rover's Panoramic camera at the landing site in Eagle crater. Figure 4.1b shows a portion of the outcrop rock (partly covered with basaltic soil) with accumulated spherules and a brushed, nearly spherule-free area. Figure 4.1c shows the soil target *Berry Survey*, where a cluster of four large spherules was investigated.
The approach taken in previous analyses of Meridiani Planum Mössbauer spectra was to model the hematite component with a single sextet, using sums of individual spectra acquired in temperature windows 10 K wide from 180 K to 290 K [*Klingelhöfer et al.*, 2004; *Morris et al.*, 2006b]. Because some spectra were acquired mostly during daytime hours and some were acquired mostly during nighttime hours and because daytime and nighttime temperatures varied from season to season, the average temperature of summed spectra in general varies from spectrum to spectrum. The range in average temperatures for summed spectra is the explanation for the range in values for the quadrupole splitting (ΔE_Q) and the magnetic hyperfine field (B_{hf}) for hematite that were obtained from single-sextet least squares fits [*Morris et al.*, 2006b]. This variation, which contributed to the identification of the sextet as hematite, was attributed to the Morin transition of hematite which occurs within the Martian diurnal temperature range.
The approach taken here is to analyze the Mössbauer spectra in each temperature window for outcrop and spherule lag deposit spectra for the purpose of characterizing the temperature dependence of the Morin transition. Focus is given to outcrop spectra obtained at Eagle crater between sol 16 and sol 51 and on lag deposit spectra obtained between sol 48 and sol 446. It is challenging to infer specific intrinsic properties from such data because of uniqueness issues, as also stated by *Dang et al.* [1998] and *Vandenberghe et al.* [2000], but it will be shown that the data provide constraints on intrinsic properties and permit identification of different hematite populations within the outcrop.
For comparison with Meridiani hematite spectra, eight terrestrial hematite analogue samples were measured at Mars-equivalent temperatures with a laboratory setup of the MIMOS II spectrometer that is equivalent to Opportunity's instrument.

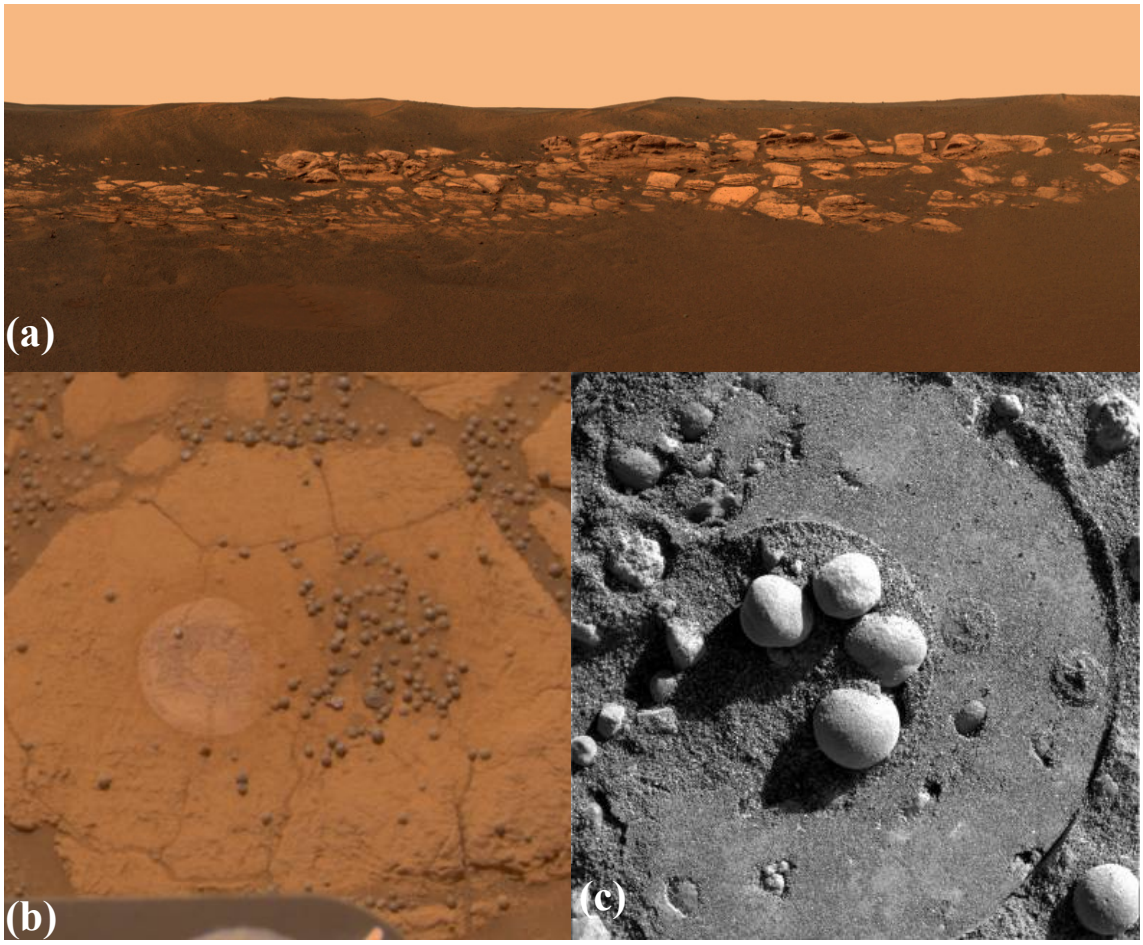

Figure 4.1: (a) Pancam image of the outcrop in the rim of Eagle crater. (b) Pancam image of the target "Berry Bowl", where brushed outcrop (round spot, ~45 mm diameter) and a spherule accumulation were investigated. (c) Microscopic image of the soil target "Berry survey" with four large (~5 mm) spherules. Image credit: NASA/JPL/Pancam/MI

4.2 The Hematite Morin Transition

Hematite (α-Fe_2O_3) has a rhombohedral crystal structure and is isostructural with corundum, (α-Al_2O_3). Crystals are uniaxial along the c-axis, which is perpendicular to the basal plane. The Morin temperature (T_M) for well-crystalline and chemically pure hematite is approximately 264 K [e.g., *Amin and Arajs,* 1987]. At temperatures higher than T_M but below the Néel temperature (~956 K), hematite is in a weakly ferromagnetic (WFM) state resulting from a slight misalignment of the antiferromagnetically ordered lattices with respect to the basal plane. The spins are canted with a canting angle of 0.1°. At temperatures lower than T_M, hematite is in an antiferromagnetic state (AFM) with the electron spins making an angle of 7° with the c-axis [e.g., *Nagata,* 1961]. The values of both ΔE_Q and B_{hf} change over a narrow temperature interval (ΔT_M ~4 K). With decreasing temperature, ΔE_Q changes magnitude and sign from ~ -0.2 mm/s for the WFM to ~0.4 mm/s for the AFM state, and B_{hf} increases in magnitude by ~0.8 T from its value of ~51.8 T for the WFM state [e.g., *Greenwood and Gibb,* 1971; *Long,* 1986; *Murad and Cashion,* 2004]. A temperature variation of the center shift δ caused by the temperature dependence of the second-order Doppler shift is observed by a number of authors [e.g., *Long,* 1986; *de Grave et al.*, 1983; *de Grave and Vandenberghe,* 1990].

The values of B_{hf}, T_M and ΔT_M are influenced by a variety of often interdependent factors including particle diameter and morphology, crystallinity, substitutional impurities, and structural features. Both the WFM and AFM phases can coexist over ΔT_M in response to finite distributions in these intrinsic properties [e.g., *Vandenberghe et al*., 2000; *Murad and*

Cashion, 2004]. Given the number of ways the temperature dependence of the Morin transition can be influenced in natural systems, *Dang et al*. [1998] and *Vandenberghe et al.* [2000] caution that intrinsic properties inferred from values of T_M and ΔT_M derived from Mössbauer measurements are equivocal. However, if T_M is above 250 K, the hematite is likely a pure phase and devoid of deleterious structural defects [e.g., *Murad and Cashion*, 2004].

4.2.1 Influence of Particle Size

A significant lowering of T_M is observed for particle sizes of ~50 nm [*Schroeer and Nininger,* 1967]. These particles were found to have $T_M = 166 \pm 10$ K, while a value of $T_M = 258 \pm 2$ K was observed for a bulk sample. *Nininger and Schroeer* [1978] investigated bulk hematite samples and microcrystalline hematite with particle sizes ranging from 5 nm to 75 nm. Lowering of T_M was observed from ~260 K for bulk samples to values from ~175 – 200 K for samples with particle sizes of 35 – 50 nm. Below a limiting particle size (~20 nm), the Morin transition is completely suppressed. Hematite will then remain in the weakly ferromagnetic state even at ~4 K, presumably because of lattice expansion throughout the whole microcrystal [e.g., *Kündig and Bömmel,* 1965; *Schroeer and Nininger,* 1967; *Nininger and Schroeer,* 1978; *de Grave and Vandenberghe,* 1990].

If a distribution of particle diameters is present, WFM and AFM phases may coexist over a range of temperatures even in well-crystallized hematite. *Nininger and Schroeer* [1978] observed a transition width of 40 K for particle sizes of 35 nm. *Amin and Arajs* [1986] annealed samples to remove strains, inhomogeneities and absorbed water. After this procedure, T_M was significantly higher, e.g. by 55 K for a sample with particle sizes of 620 nm, indicating that these factors were indeed causing a depression of T_M.

4.2.2 Influence of Cation Substitution

Cation substitution for Fe often reduces T_M and broadens the Morin transition width. Geologically relevant impurities (Al, Ti, Cr, Mn, H_2O and OH^-) lower T_M and increase ΔT_M [*Flanders and Remeika,* 1965; *Srivastava and Sharma,* 1972; *de Grave et al*., 1982, 1983, 2005; *Fysh and Clark,* 1982; *Ericsson et al.*, 1986; *Amin and Araj*s, 1986; *de Grave and Vandenberghe,* 1990; *Dang et al.,* 1998]. *Flanders and Remeika* [1965] found Sn and Ti to have a particularly pronounced effect. *Dang et al*. [1998] discuss the influence of molecular H_2O, structural hydroxide, and adsorbed sulfate on the Morin transition. The Morin transition is completely suppressed (i.e., not detected down to ~4 K) for values of the molar ratio M/(M+Fe) equal to ~0.10 for M = Al, ~0.04 for M = Cr, and ~0.038 for M = Ti [*de Grave et al.*, 1982; *Cornell and Schwertmann,* 1996, and references therein]. Diamagnetic substitutional impurities like Al^{3+} also reduce the magnitude of B_{hf} and produce asymmetric line shapes [e.g., *de Grave et al*., 1982, 1983, 2005; *Srivastava and Sharma,* 1972].

Instead of an abrupt transition, a continuous decrease of ΔE_Q with increasing temperature was observed for Al-substituted hematite [*de Grave et al.*, 1982, 1983, 2005; *Srivastava and Sharma,* 1972]. This behaviour was explained by *de Grave et al.*, [1983] through the existence of a gradual rotation of the spins towards the basal plane with rising temperature over the width of the Morin transition. *Srivastava and Sharma* [1972] also observed an increase of the transition width with increasing Al content.

Table 4.1: Overview of hematite analogue samples.

Sample	Fe_2O_3[a] (wt.%)	Hematite Content[b] (%)	Sieve Fraction (µm)	Comment (References)[c]
HMCM1		100	<250	Well-crystalline, fibrous texture, Cleator Moore, England. (1)
HMMG1	98.87	100	150-500	Well-crystalline; Minas Gerais, Brazil. (2)
HMMG1-FP	98.87	100	<150	
HMRE2		100	<500	Microplaty hematite, schistose texture. Republic, MI. (2)
HWMK745R-SC		91	10-100	Spherule concentrate from a clastic volcanic breccia, Mauna Kea, Hawaii. (3)
HWMK30	12.21	85	<1000	Phyllosilicate-bearing tephra, Mauna Kea, Hawaii. (4, 5)
HWMK11	12.18	69	<1000	Heated and oxidized tephra, Mauna Kea, Hawaii (5, 6, 7)
HWMK20	11.67	42	<1000	Tephra, Mauna Kea, Hawaii. (7)

[a]Bulk chemical concentrations from XRF analysis with all Fe calculated as Fe_2O_3.
[b]The hematite content is the subspectral area (not f-factor corrected).
[c]References: 1 = *Morris et al*., [2000b]; 2 = *Lane et al.*, [2002]; 3 = *Morris et al*., [2005]; 4 = *Morris et al.*, [1997] ; 5 = *Hamilton et al.*, [2008]; 6 = *Golden et al.*, [1993]; 7 = *Morris et al.*, [2000a].

4.3 Mössbauer Spectroscopic Analysis of Analogue Samples

The investigation of eight hematite-bearing analogue samples (Table 4.1) is discussed first because these samples provide a framework of Mössbauer measurements for samples that have been previously studied as terrestrial analogues for Mars on the basis of visible and near-infrared spectra, thermal emission spectra, and/or magnetic properties. The four samples HMCM1, HMMG1, HMMG1-FP and HMRE2 are powders derived by grinding and sieving of hand specimens of hematite rock. HMCM1 is from Cleator Moore, England, and is well-crystalline with fibrous texture [*Morris et al.*, 2000a]. HMMG1 and HMMG1-FP are powders of well-crystalline material and each particle (equant in shape) is a hematite single crystal [*Lane et al.*, 2002]. HMRE2 is microplaty hematite with schistose texture from Republic, MI [*Lane et al.*, 2002]. Three samples (HWMK11, HWMK20, and HWMK30) are size fractions of hematite-bearing volcanic tephra from Mauna Kea, Hawaii [*Golden et al.*, 1993; *Morris et al*., 1997; 2000b; *Hamilton et al.*, 2008]. HWMK745R-SC is a hematite spherule concentrate from a clastic volcanic rock [*Morris et al.*, 2005; *Golden et al.*, 2008].All measurements were carried out in a climate chamber cooled with liquid nitrogen and a MIMOS II instrument equivalent to the spectrometer on board the Opportunity rover. Both sensor head and sample were mounted inside the chamber. The sample and the α-Fe foil used for velocity calibration were thus approximately at the same temperature, with a temperature offset of 10 K or less. Measurements were performed under a dry nitrogen atmosphere at ~10 mbar pressure.

The room temperature Mössbauer spectra for the analogue samples are shown in Figure 4.2, Mössbauer parameters are listed in Tables A3 and A4 in the appendix. Only samples HMCM1, HMMG1, HMMG1-FP and HMRE2 are pure hematite with respect to Iron-bearing phases, the Mössbauer spectra of all other samples exhibit doublets corresponding to other Iron-bearing phases.

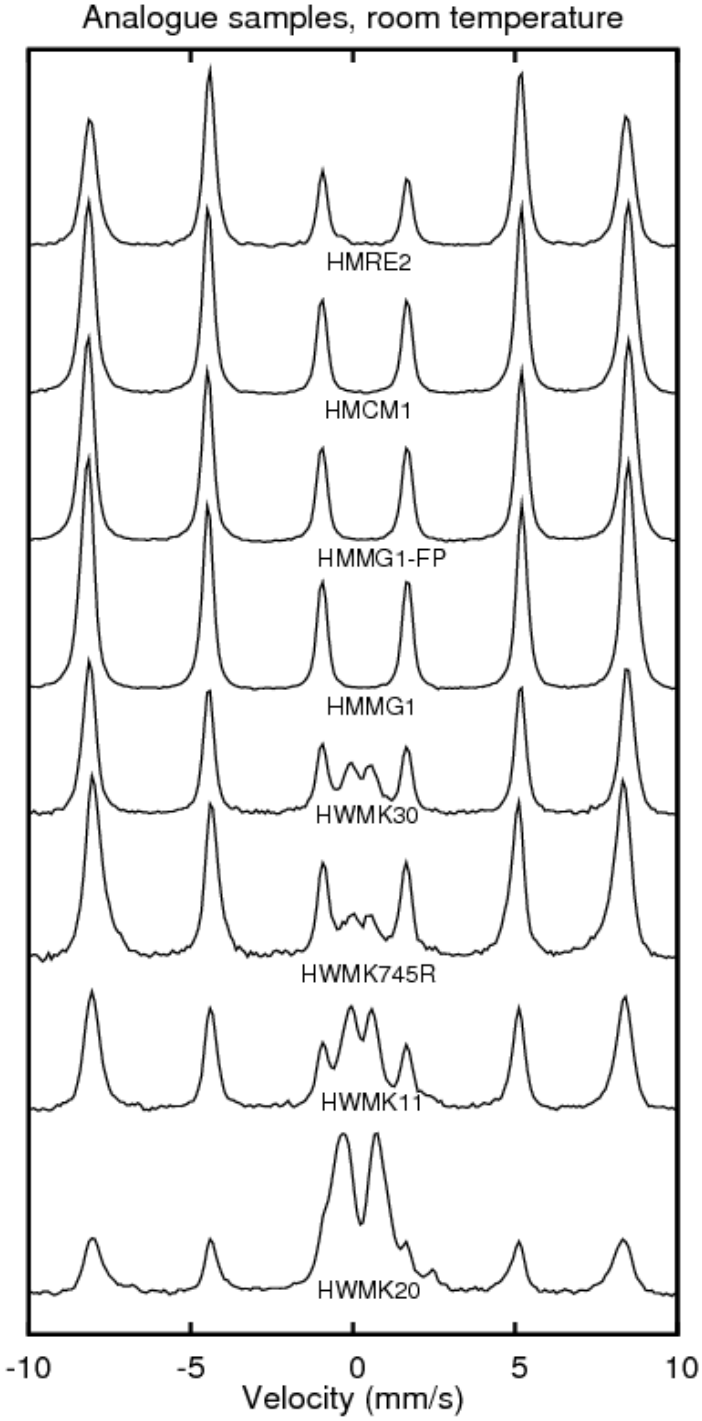

Figure 4.2: Mössbauer spectra of analogue samples (Table 4.1), obtained at room temperature. Samples HMRE2, HMCM1, HMMG1-FP and HMMG1 show only a hematite sextet. Samples HWMK30, HWMK745R, HWMK11, and HWMK20 have additional Iron-bearing phases.

The spectra were analyzed by a least-squares fitting procedure where doublet lines were constrained to have equal areas and widths and line pairs of sextets were constrained to have equal areas. All lines of the hematite sextet were modeled with equal widths. Two hematite sextets (corresponding to coexisting AFM and WFM phases) were not required to model the sextet at temperatures near T_M.
The temperature trends for the Mössbauer parameters δ, ΔE_Q, B_{hf} and line widths Γ are shown in the plots in Figure 4.3. Based on the presence or absence of a Morin transition,

indicated by the temperature dependence of ΔE_Q, the samples can be divided into two groups. The first column has results for samples with a Morin transition (HMCM1, HMMG1, HMMG1-FP and HWMK30) as indicated by the positive values of ΔE_Q at the lowest temperatures. The second column has results for the four samples (HWMK11, HWMK20, HWMK745R-SC, and HMRE2) that do not have a detectable Morin transition above ~200 K, indicated by ΔE_Q ~ -0.20 mm/s at all measurement temperatures. The factors that contribute to suppression of the Morin transition to below 200 K are uncertain, but microbeam analysis of hematite particles in samples HWMK11 and HWMK745R-SC [*Golden et al.*, 1993; *Morris et al.*, 2005] show impurity levels for Ti and Al, respectively, to lower T_M significantly below 200 K.

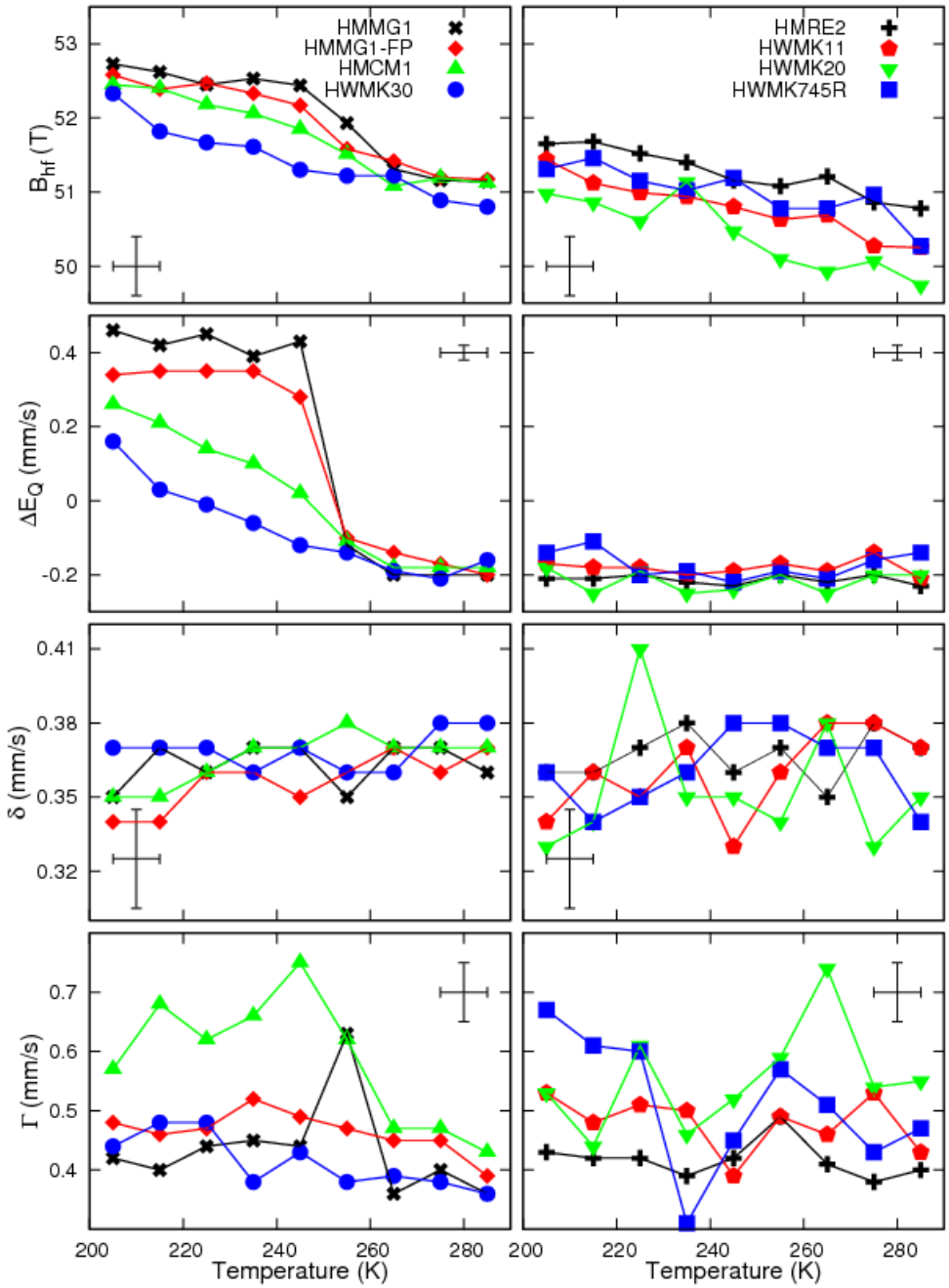

Figure 4.3: Temperature dependence of Mössbauer parameters for hematite-bearing Martian analogue samples. Representative error bars are indicated in each plot. Samples for which the Morin transition is observed are displayed in the left column. Parameter uncertainties are 0.4 T for B_{hf}, 0.02 mm/s for δ and ΔE_Q and 0.05 mm/s for line widths Γ. In this and all following plots, lines have no physical meaning but help guide the eye.

The behavior of the Morin transition with respect to temperature for both size fractions of sample HMMG1 is a good example of what is expected for coarse grained, well-crystalline, and chemically pure hematite (see section 4.2). The transition occurs abruptly at ~250 K (ΔT_M < 10K) with ΔE_Q ~ -0.20 mm/s for T > T_M and ΔE_Q ~0.40 mm/s for T < T_M. For HMCM1 and HWMK30, T_M occurs at lower temperatures (~240 K and ~220 K, respectively, where ΔE_Q ~0.0 mm/s). Their ΔT_M values are greater than 25 K, but cannot be determined without Mössbauer measurements at lower temperatures.

The magnetic hyperfine field B_{hf} is clearly temperature dependent for all samples, decreasing continuously with increasing temperature (Figure 4.3) following the temperature dependence of the magnetization (Brillouin function, e.g., [*Greenwood and Gibb,* 1971]). The temperature trend is generally more pronounced and offset to higher values of B_{hf} for those samples where a Morin transition is present. The samples with and without a Morin transition have average values of B_{hf} equal to ~52.5 T and 51.3 T, respectively, at 205 K. The corresponding values at 285 K are 51.0 T and 50.2 T. For HMMG1 and HMMG1-FP, a ~0.6 T change in the value of B_{hf} at ~250 K is present, in accordance with their abrupt transition from AFM to WFM states.

The center shift δ and line width Γ have no detectable temperature dependence within error for any sample (Figure 4.3), except that the line widths for sample HMCM1 are larger for temperatures below 260 K (i.e., ~0.65 mm/s below 260 K compared to ~0.45 mm/s at higher temperatures). On average, the line widths for the samples with a Morin transition are somewhat smaller than those without a Morin transition.

In Figure 4.4, a direct comparison of the Mössbauer spectra for sample HMMG1 in its AFM and WFM states is shown. The sextet corresponding to the AFM state at 205 K is characterized by δ=0.35 mm/s; ΔE_Q=0.46 mm/s and B_{hf}= 52.7 T; the sextet corresponding to the WFM state at 285 K has δ=0.36 mm/s; ΔE_Q=-0.20 mm/s and B_{hf}=51.1 T. Note that the values of the center shift and the velocity axis in Figure 3 are referenced to the center point of the spectrum of metallic Fe foil at the measurement temperature. Based on values derived from the least-squares fitting procedure, parameter uncertainties are estimated to be ±0.4 T for B_{hf}, ±0.02 mm/s for δ and ΔE_Q and ±0.05 mm/s for line widths Γ.

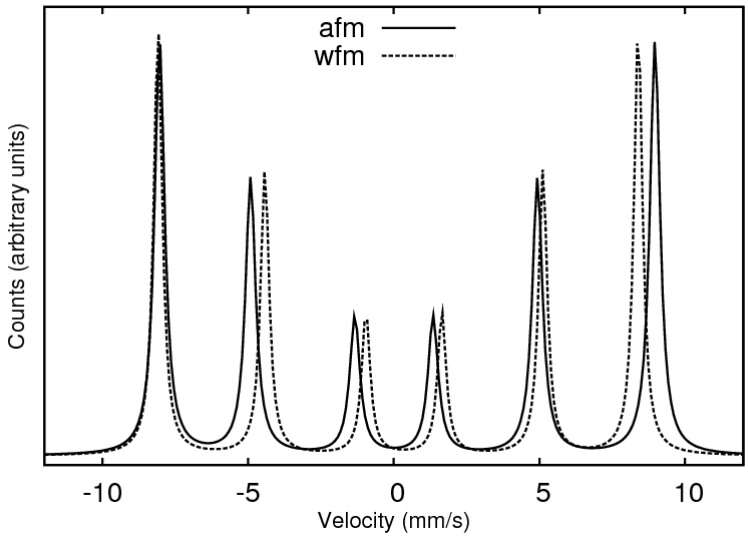

Figure 4.4: Direct comparison of the AFM (205 K) and WFM (285 K) sextets for sample HMMG1.

4.4 MER Mössbauer Data Analysis by Simultaneous Fitting

On Mars, integration time available to the Mössbauer instrument is limited, so that Mössbauer spectra for a given temperature window often have counting statistics that are too low to permit analysis by least-squares fitting without imposing constraints (fixing values) on a large number of parameters (e.g., all line centers and widths). *Morris et al.* [2006a, 2006b, 2008] reduced this problem by summing the spectra from all available temperature windows, which improved the counting statistics but resulted in a loss of temperature-dependent information. In this work, simultaneous fitting ("simfitting") [*Agresti et al.*, 1967, 1969; *Bent et al.*, 1969] of multiple Mössbauer spectra is applied to overcome issues associated with low counting statistics but still retain the ability to determine the values of the Mössbauer parameters δ, ΔE_Q, and B_{hf} as a function of temperature. The requirement for simfitting spectra is that the individual spectra are mixtures in different proportions of the same subspectral components. This requirement is reasonably met for all outcrop spectra and for all spherule lag deposit spectra [*Morris et al*., 2006b]. Preliminary simfitting results for Meridiani Planum Mössbauer spectra are reported by *Agresti and Gerakines* [2008], *Fleischer et al.* [2009] and *Agresti et al*. [2010].

The MER Mössbauer spectra of outcrop and spherule targets (Table 4.1) were extracted from raw data, calibrated, and fold-summed using *MERView* [*Agresti et al.*, 2005, 2006a, 2006b], and non-linear least-squares simfits were performed with *MERFit* [*Agresti and Gerakines*, 2008, 2009]. Written in Lahey-Fujitsu Fortran, both programs are Windows-based, enabling data entry and control through dialog boxes, with graphical display of spectra that can change as parameter values are adjusted.

The essential first step in simfitting is to establish relations among parameters, either as single-spectrum or multi-spectrum constraints. Typical single-spectrum constraints, which apply to all individual spectra in the simfit set, are: equating line widths or areas of the two components of a doublet; relating sextet line widths (e.g., equal or according to a distribution as discussed earlier); and holding area ratios of the lines of a sextet constant (e.g., to 3:2:1:1:2:3). Examples of multi-spectrum constraints include: setting hyperfine parameters equal for spectra taken at the same temperature; and equating area ratios of sites in spectra of a given target taken at different temperatures. Compared with single-spectrum fits, multi-spectrum fits result in reduced correlations among parameters because parameters in different spectra are held in fixed relations (e.g. equal) during a fit. As a result, fitted parameter values are automatically consistent among all spectra in the simfit set, whereas repeated single-spectrum fits might otherwise be required to arrive at compatible parameter values. Thus, fewer (or no) parameters have to be constrained to fixed values, and the resulting fits provide tighter trends of Mössbauer parameters as function of an environmental variable such as temperature.

In a preliminary simfit analysis of outcrop spectra [*Fleischer et al.*, 2009], spectra from different targets acquired in a given temperature window were grouped together, and each temperature group was subjected to a separate simfit while holding all sextet hyperfine parameters equal for all targets within the group. Hyperfine values for each temperature window were obtained, but there was no attempt to account for relations among parameters that are present in different temperature groups, for example doublet parameters and site area ratios that are expected to be independent of temperature of a given target, such an application of simfitting is referred to as "one-dimensional" because relations are established for one environmental parameter (e.g., temperature), while others (different outcrop targets in this case) are not related.

For this work, a full "two dimensional" simfit analysis is employed by establishing parameter relations for both variables (temperature and target) in the same simfit [cf. *Agresti et al.*, 2010]. A set of 60 Eagle crater outcrop spectra (60 spectra from individual temperature windows of 10 different outcrop targets) is analyzed, and a set of 46 spectra obtained on 10 spherule-rich lag deposits (Table 4.2). Each distinct simfit includes all

spectra with appropriate parameter constraints, and thus is sufficient by itself to define all parameter values for a given spectral model for all sols (i.e., targets) and temperatures of all spectra in the simfit set. The model for Iron-bearing phases was the same as that employed by *Morris et al.* [2006b] except that two hematite sextets were used.

Table 4.2: Eagle crater outcrop and spherule targets used for simfit modeling.

Sol[a]	Target	Type[b]	% Hm[c]	T (K)		Sol[a]	Target	Type[b]	% Hm[c]	T (K)
Eagle Outcrop data set						*Spherule data set*				
16	RobertE	RU	40	200-260		48	BerryBowl	RU	63	200-280
29	McKittrick	RU	31	210-280		52	Panaluu	SU	65	250-270
30	Guadalupe	RU	45	200-280		73	AegeanCrest	SU	65	250-270
32	McKittrick	RR	39	200-270		97	Leah'sChoice	SU	47	240-250
35	Guadalupe	RR	36	200-280		222-228	BerrySurvey	SU	54	200-260
43	Mojo	RU	32	260-280		368-370	RippleCrest	SU	68	250-280
45	Mojo	RR	38	200-270		415-418	Mobarak	SU	48	190-290
46	BerryBowlEmpty	RU	36	240-280		419	Norooz	SU	53	260-290
49	Rasberry_Newton	RU	36	240-270		420	MaybeRooz	SU	55	260-290
51	RealSharksTooth	RU	54	200-280		445-446	RecoverySoil_Cure	SD	50	190-290

[a] Separate targets are identified by the first sol of the integration.
[b] Target types are: undisturbed rock (RU); abraded rock (RR); undisturbed soil (SU); disturbed soil (SD).
[c] The hematite content is the temperature-independent value from a fit with a one-sextet model [*Morris et al.*, 2006b].

Two-dimensional simfitting is illustrated for the outcrop spectra in Table 4.3, where sol number and temperature are listed for the 60 outcrop spectra, along with their sequence numbers in the simfit set, total number of spectra per sol (N_S) and total number of spectra per temperature window (N_T). For any Mössbauer parameter (e.g., B_{hf}) with no relations defined, there are 60 distinct places (variables) in a 60-element B_{hf} array. To assure that B_{hf} has a unique value at a given temperature (e.g., 235 K), the elements of this array for the spectra identified by the 7 sequence numbers in the column labeled "235" are held equal in the simfit. Equating B_{hf} for the other columns reduces to 8 the number of distinct values of B_{hf} in the array, one for each temperature group.

Table 4.3: 60 Eagle crater outcrop spectra.

	Temperature (K)								
Sol	**205**	**215**	**225**	**235**	**245**	**255**	**265**	**275**	**N_S**
16	1	2	3	4	5	6			**6**
29		7	8	9	10	11	12	13	**7**
30	14	15	16	17	18	19	20	21	**8**
32	22	23	24	25	26	27	28		**7**
35	29	30	31	32	33	34	35	36	**8**
43							37	38	**2**
45	39	40	41	42	43	44	45		**7**
46					46	47	48	49	**4**
49					50	51	52		**3**
51	53	54	55	56	57	58	59	60	**8**
N_T	**6**	**7**	**7**	**7**	**9**	**9**	**9**	**6**	**60**

At the same time, parameter relations are established among spectra acquired at different temperatures for the same sol. For example, if the relative content of olivine (Ol) and pyroxene (Px) shall be independent of temperature for a given target (i.e., their relative subspectral areas do not depend on temperature), the ratio, Area(Px)/Area(Ol), is constrained to be equal for all temperatures of the selected target (i.e. sol). Thus, for sol 49 the three Ol areas for spectra 50, 51 and 52 are allowed to be variable in the simfit, as well as the Px area for spectrum 50. Then, for each iteration of the simfit, the Px areas for spectra 51 and 52 are defined to maintain the same Px/Ol area ratio as for spectrum 50.

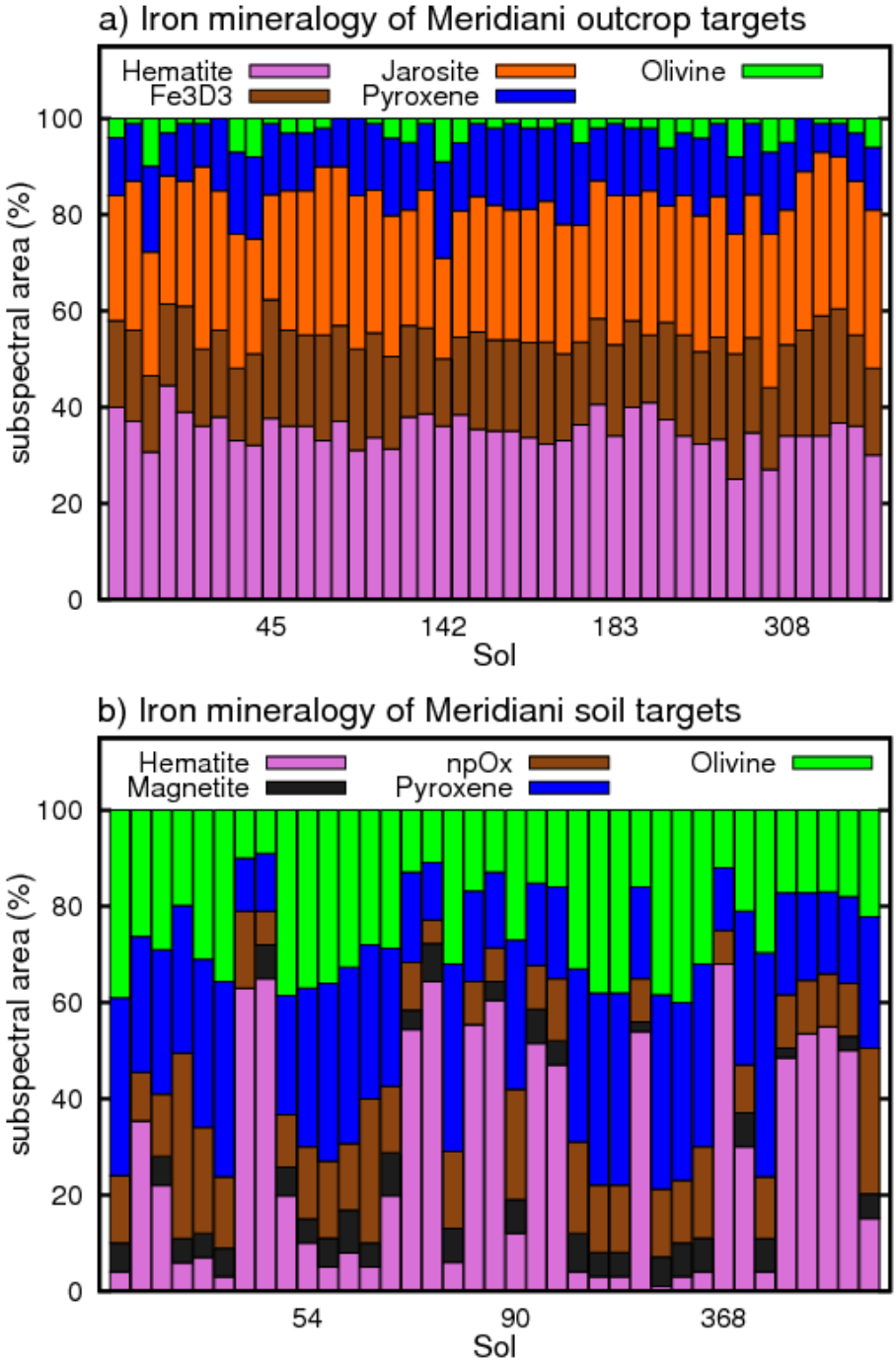

Figure 4.5: (a) Mineralogy of outcrop targets investigated along Opportunity's traverse through sol 1461. Outcrop spectra show only minor iron-mineralogical variations. (b) Mineralogy of soil targets investigated through sol 1642. The large variation of the hematite content reflects the presence or absence of spherules; high hematite content corresponds to spherule-rich targets.

4.5 Analysis of Meridiani Hematite Spectra

Simfitting was performed with two groups of Mössbauer spectra acquired on 10 sulfate-rich outcrop targets (total of 60 spectra) and on 10 targets (total of 46 spectra) with high concentrations of hematite-rich spherules and their fragments (Table 4.2). The outcrop targets are all from Eagle crater. The spherule-rich targets are primarily lag deposits of spherules and their fragments intermixed with basaltic soil.

With the assumption that all samples within each data set (i.e., outcrop and lag deposits) contain the same Iron-bearing phases in different proportions (a prerequisite for simfitting), the simfit results are used to compare four distinct temperature-dependent models all of which employ two Lorentzian sextets for hematite. The sextet with the larger value of B_{hf} is referred to as "S1" and the sextet with the smaller value of B_{hf} is referred to as "S2". All other Iron-bearing phases are modeled identically within each data set.

Figure 4.5 shows the distribution of Iron minerals along Opportunity's traverse based on results from single-sextet fits [*Morris et al.*, 2006b]. Outcrop measurements reveal a homogeneous composition, as shown in Figure 4.5a. The large variation of the hematite content in soil spectra (Figure 4.5b) reflects variable proportions of hematite-rich spherules and their fragments in the field of view. While focus is given to a manageable data set for simfitting, these two diagrams show that the interpretations are also relevant for other outcrop and spherule-rich targets from the Meridiani Planum data set. Mössbauer parameters derived from simfits of the outcrop and spherule data sets are listed in the appendix in Tables A5 and A6, respectively.

4.5.1 Simultaneous Fitting of Meridiani Planum Outcrop Spectra

All Iron-bearing components in the outcrop except hematite were modeled in the same way as described by *Morris et al.* [2006b], i.e. one symmetric Lorentzian doublet each for Fe in olivine, pyroxene, jarosite, and an unassigned doublet phase (Fe3D3). The average values of δ, ΔE_Q, and Γ for these phases are compiled in Table 4.4. The parameters were constrained to these values for all spectra during the simfitting procedure, because this resulted in greater consistency among the sextet parameters. Widths and areas were paired equal for any given doublet as a single-spectrum constraint, and doublet area ratios were held equal for all spectra for a given target as a multi-spectrum constraint.

Table 4.4: Mössbauer parameters for all phases except hematite for outcrop and spherule simfits.

Mineral Phase	**δ (mm/s)**	**ΔE_Q (mm/s)**	**B_{hf} (T)**	**Γ (mm/s)**		**δ (mm/s)**	**ΔE_Q (mm/s)**	**B_{hf} (T)**	**Γ (mm/s)**
	Outcrop targets					*Spherule-rich targets*			
Olivine	1.15	3.00	-	0.41		1.15	3.03	-	0.39
Pyroxene	1.14	2.12	-	0.57		1.15	2.17	-	0.59
Fe3D3	0.38	0.67	-	0.46		-	-	-	-
Jarosite	0.37	1.24	-	0.42		-	-	-	-
npOx	-	-	-	-		0.37	0.85	-	0.77
Magnetite Fe^{3+}	-	-	-	-		0.31	0.06	50.1	0.46
Magnetite Fe^{3+}/Fe^{2+}	-	-	-	-		0.64	0	46.9	0.68

Doublet hyperfine and width parameters from [*Morris et al.*, 2006b]. For spherules, magnetite parameters are from a fit of the Gusev crater rock target Peace [*Morris et al.*, 2006a]. Values listed here were held fixed during all simfits.

The two hematite sextets were modeled in four different ways, giving four different simfit models that differ with regard to line widths and line shapes (Table 4.5). For all models, the center shift (δ) was constrained to a value of 0.37 mm/s for both sextets. Without this

constraint, values for δ from the two sextets follow the same trend, but sometimes δ(S1) is larger and sometimes δ(S2) is larger, indicating that they cannot be distinguished in the simfit. Both sextets were modeled with line intensity ratios of 3:2:1:1:2:3 as a single-spectrum constraint. Because all outcrop targets are assumed to contain the same hematite, the sextet parameters and area ratios are constrained equal for a given temperature as multi-spectrum constraints.

Table 4.5. Overview of models used for the Outcrop and spherule simfits.

		Sextet S1		Sextet S2					Sextet S1		Sextet S2	
No.	**Model[a]**	**Widths**	**Skew**	**Widths**	**Skew**		**No.**	**Model[a]**	**Widths**	**Skew**	**Widths**	**Skew**
	Outcrop targets						*Spherule-rich targets*					
1	S1eS2e	equal	no	equal	no		1	S1eS2e	equal	no	equal	no
2	S1eS2b	equal	no	broadened	no		2	S1eS2b	equal	no	broadened	no
3	S1eS2ek	equal	no	equal	yes		3	S1eS2ek	equal	no	equal	yes
4	S1eS2bk	equal	no	broadened	yes		4	S1eS2bk	equal	no	broadened	yes

[a]S1 = hematite sextet S1; S2 = hematite sextet S2;
e = equal line widths; d = widths broadened outward from the center as Γ+2d, Γ +d, Γ, Γ, Γ +d, Γ +2d;
k = skewed line shapes.

Both symmetrical and asymmetrical Lorentzian line shapes were used. To model lines broadened outward according to a distribution in B_{hf} or because of thickness effects, the full widths at half maximum intensity (Γ) for the sextet lines were defined by Γ+2d for lines 1 and 6, Γ+d for lines 2 and 5, and Γ for lines 3 and 4, where d is a broadening parameter. Asymmetrical Lorentzian line shapes are composed of two half-Lorentzians joined at their midline, as described in section 2.1.4.
Preliminary simfitting with skewed Lorentzian line shapes for sextet S1 resulted in small skew parameters (<0.1), so that S1 was always modeled with symmetric Lorentzian line shapes. This was not the case for sextet S2, so both symmetric and skewed Lorentzian line shapes were used. Simfitting S1 with line widths broadened outward generally led to a small broadening parameter, so S1 was modeled with equal line widths. All simfits converge to similar partial χ^2-values (the χ^2-value associated with each single spectrum in a simfit set). A simfit with model S1eS2b of the spectrum of outcrop target *McKittrick* for the temperature interval 210 K to 220 K is shown in Figure 4.6a as a typical result of the procedure.

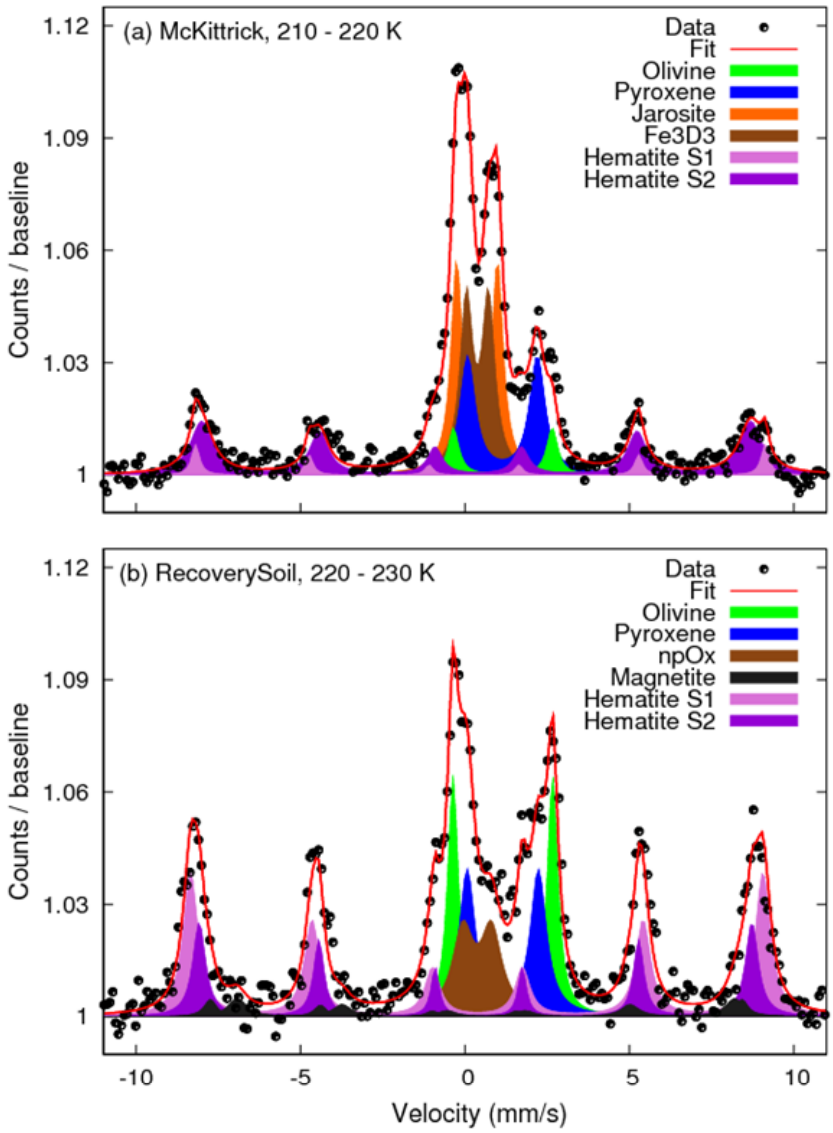

Figure 4.6: (a) Typical outcrop spectrum obtained on the target *McKittrick* in the temperature range between 210 K and 220 K. (b) Spectrum obtained on the spherule rich target *RecoverySoil_Cure* between 220 K and 230 K. Both fits are based on simfit model S1eS2b.

The temperature dependences of B_{hf} and ΔE_Q for the two hematite sextets are shown in Figure 4.7 for each of the four simfit models (Table 4.5). The temperature dependences for Γ and for the fraction of total hematite subspectral area associated with the S1 sextet are shown in Figure 4.8a and Figure 4.8b and in Figure 4.9a, respectively. It is obvious from these figures that the values of the Mössbauer parameters and their temperature dependence do not depend on the choice of simfit model within parameter uncertainty. The observation that the relative intensity of the S1 sextet does not rapidly change (around the Morin transition) at the expense of the S2 sextet (the subspectral areas are temperature independent) is best explained by two different populations of hematite particles as opposed to coexisting WFM and AFM phases of the same population.
The hematite S1 sextet is subordinate in abundance (~16 – 18 %) to the S2 sextet (Figure 4.9a), but it does have a Morin transition at T_M ~260 K (defined at $\Delta E_Q = 0$) and values of B_{hf} at low temperatures (~53.8 T; Figure 4.7a); that are characteristic of well-crystalline and chemically pure hematite in its AFM state (cf. HMMG1, Figure 4.3).

However, the absence of an abrupt change in ΔE_Q at T_M and ΔE_Q ~0.20 mm/s at ~205 K (instead of ~0.40 mm/s) preclude the presence of hematite that is both well-crystalline and chemically pure. The temperature dependence of ΔE_Q for the outcrop S1 sextet is similar to that for the hematite in analogue sample HMCM1, but the magnitude of B_{hf} for the Martian sextet is significantly higher (~1 T) at all temperatures (Figure 4.3, Figure 4.7a).
The hematite S2 sextet accounts for most of the hematite in the outcrop (~82 – 84 %). In contrast to the S1 sextet, the S2 sextet has no Morin transition down to ~205 K, has values of B_{hf} (51 – 52 T) that are systematically 1 – 2 T less than the values for S1 (Figure 4.7b), and has line widths (~0.7 mm/s) that are systematically broader by ~0.3 mm/s compared to S1 line widths (Figure 4.8b). These differences point to a population of hematite particles that has some unknown combination of reduced average particle diameter, reduced crystallinity, and enhanced concentration of chemical impurities compared to the hematite population represented by sextet S1. Irrespective of the actual controlling factor(s), there are two populations of hematite particles in the outcrop represented by the S1 and S2 sextets. Two hematite populations can occur as separate populations of discrete particles having different intrinsic properties or they can occur as one population of discrete particles whose individuals have non-constant internal intrinsic properties.
The results are consistent for the different models, with tight temperature trends for B_{hf} and ΔE_Q, and support the presence of slightly skewed lines (with the skew parameter k rising from ~0.10 at 205 K to ~0.23 at 275 K), as well as some outward broadening for S2. To obtain parameter uncertainties, a straight line was least-squares fit to all 32 values for each sextet parameter (8 temperature windows, 4 simfits). Two separate lines were fit to ΔE_Q(S1) and B_{hf}(S1) data points, respectively, reflecting the presence of the Morin transition. Parameter scatter (shown as error bars on Figure 4.7, Figure 4.8, and Figure 4.9) is then defined as the standard deviation of the residuals from the linear (or bi-linear) fit. To obtain parameter uncertainties, results are compared from other simfits performed on the 60-spectrum outcrop data set, including those with relaxed parameter constraints with respect to the current models. Based on this, estimated parameter uncertainties are: ±0.04 mm/s for ΔE_Q(S1) and ΔE_Q(S2); ±0.3 T for B_{hf}(S1); ±0.4 T for B_{hf}(S2); ±0.05 mm/s for Γ(S1); ±0.08 mm/s for Γ(S2); ±3 % (absolute) for subspectral areas; and ±0.1 for the skew parameter. Comparably large uncertainties for line widths and subspectral areas reflect the strong overlap of both sextets.

4.5.2 Simultaneous Fitting of Meridiani Planum Spherule Spectra

The procedure for simfitting spherule-rich spectra paralleled that for simfitting outcrop spectra. Olivine, pyroxene, and nanophase ferric oxide (npOx) were modeled with symmetric Lorentzian doublets, and magnetite was modeled with two symmetric Lorentzian sextets, both with intensity ratios 3:2:1:1:2:3. As single spectrum constraints, all doublet widths and areas were paired equal and the values of δ and ΔE_Q for all doublets were constrained to the values in Table 4.4. Because of the low subspectral area for magnetite, δ, ΔE_Q, B_{hf}, Γ, and relative sextet subspectral areas were fixed to values obtained for the magnetite-rich rock target *Peace* at Gusev crater [*Morris et al.*, 2006a]. The area ratio was found to be $A(Fe^{3+}/Fe^{2.5+})=0.66$.
As multi spectrum constraints, subspectral area ratios for olivine, pyroxene and npOx were constrained equal for all spectra for a given target. To constrain magnetite areas to reasonable values for spectra with low counting statistics, the area ratio of olivine and magnetite was constrained equal for all spectra in a simfit. The two hematite sextets were modeled in nearly the same way and with the same parameter constraints as for outcrop spectra, giving four models for simfit analysis (Table 4.5). For spherule simfits, symmetrical Lorentzian line shapes were always used, and both sextets have two models with broadened widths. A simfit with model S1eS2b of the spectrum of the spherule-rich

lag deposit *RecoverySoil_Cure* for the temperature interval 220 K to 230 K is shown in Figure 4.6b. Compared to outcrop spectra, the relative contribution of hematite to the spectrum is significantly larger. Partial χ^2-values are very similar for all models.

The results for the four spherule simfit models are very similar, perhaps owing to the high proportion of Fe as hematite in these targets. The temperature dependences of ΔE_Q and B_{hf} for the spherule-rich targets are shown in Figure 4.10. Corresponding data for the line width and the relative area of sextet S1 are plotted in Figure 4.8c and Figure 4.8d and Figure 4.9b, respectively. Like outcrop hematite, spherule hematite is not both well-crystalline and chemically pure; this is indicated by the absence of an abrupt Morin transition as observed for analogue sample HMMG1 (Figure 4.3).

The ΔE_Q data suggest a possible Morin transition at T_M ~200 – 220 K (defined where ΔE_Q = 0.0 mm/s) with ΔT_M larger than the measurement interval, but measurements at lower temperature would be needed for confirmation. The sextet with the larger B_{hf} (S1) accounts for most of the spherule hematite (~65 % independent of temperature). The temperature dependences of B_{hf} for the S1 and S2 hematite sextets are approximately the same, but the values for S1 are systematically larger by ~2 T (~54.3 T compared to ~52.3 T). Although there is considerable scatter in the data for S2, ΔE_Q decreases with increasing temperature for both sextets. For S2, ΔE_Q is always negative, so that T_M is not determined at the measurement temperatures. The line widths range between ~0.42 mm/s and 0.60 mm/s for S1 and between ~0.32 mm/s and 0.55 mm/s for S2 with no systematic dependence on temperature. The spherule Mössbauer data thus indicate two distinct hematite populations that are represented by the S1 and S2 sextets. This can happen if the hematite within individual spherules is heterogeneous with respect to intrinsic properties or if the intrinsic properties of the spherules vary from spherule to spherule.

The temperature trends for B_{hf} and ΔE_Q are very tight (except ΔE_Q(S2)) and almost identical for the different models (Figure 4.10). The results support a model with symmetric lines for both sextets, with either equal line widths for each sextet or broadening from inner to outer lines to some extent. Parameter scatter is shown as error bars on Figure 4.8, Figure 4.9 and Figure 4.10. Parameter uncertainties were derived based on the method described for the outcrop data set, resulting in: ±0.02 mm/s for ΔE_Q(S1); ±0.03 mm/s for ΔE_Q(S2); ±0.2 T for B_{hf}(S1) and B_{hf}(S2); ±0.1 mm/s for Γ(S1) and Γ(S2); and ±3 % (absolute) for subspectral areas.

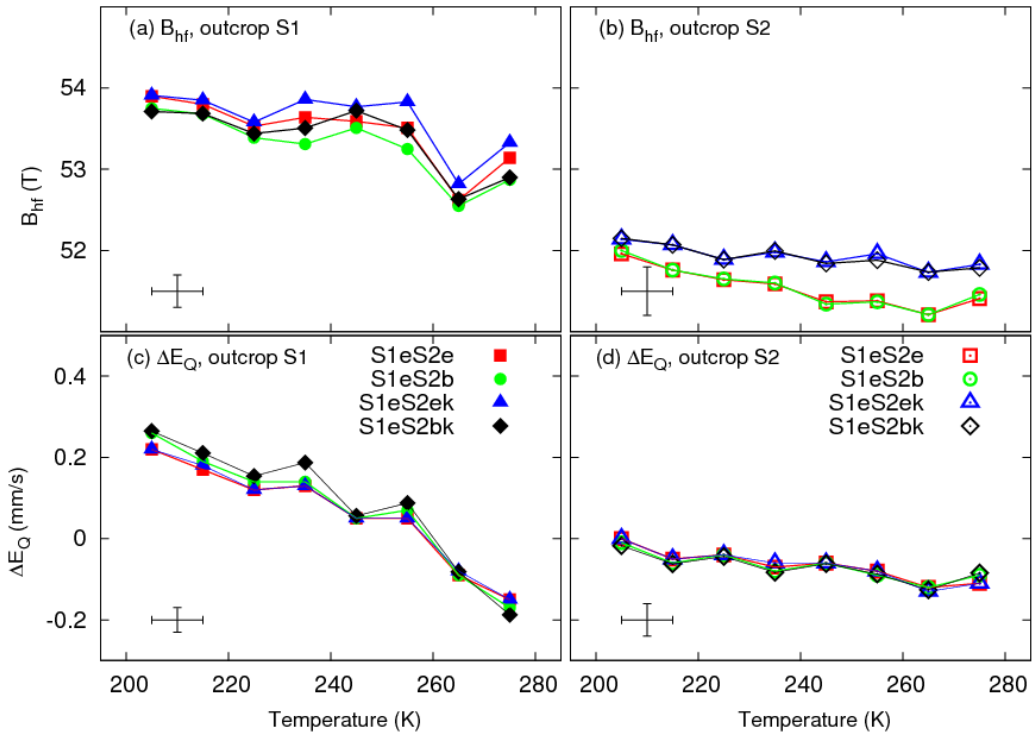

Figure 4.7: Temperature dependence of Mössbauer parameters for outcrop from the four different models described in the text. B_{hf}(S1) drops by ~0.5-1 T at 260 K, and ΔE_Q drops below zero in the same temperature range. The two trend lines for B_{hf}(S2) result from absence or presence of skew. The error bars indicate parameter scatter based on linear or bi-linear fits to the displayed data (±0.03 mm/s for ΔE_Q(S1); ±0.04 mm/s for ΔE_Q(S2); ±0.2 T for B_{hf}(S1); ±0.3 T for B_{hf}(S2)).

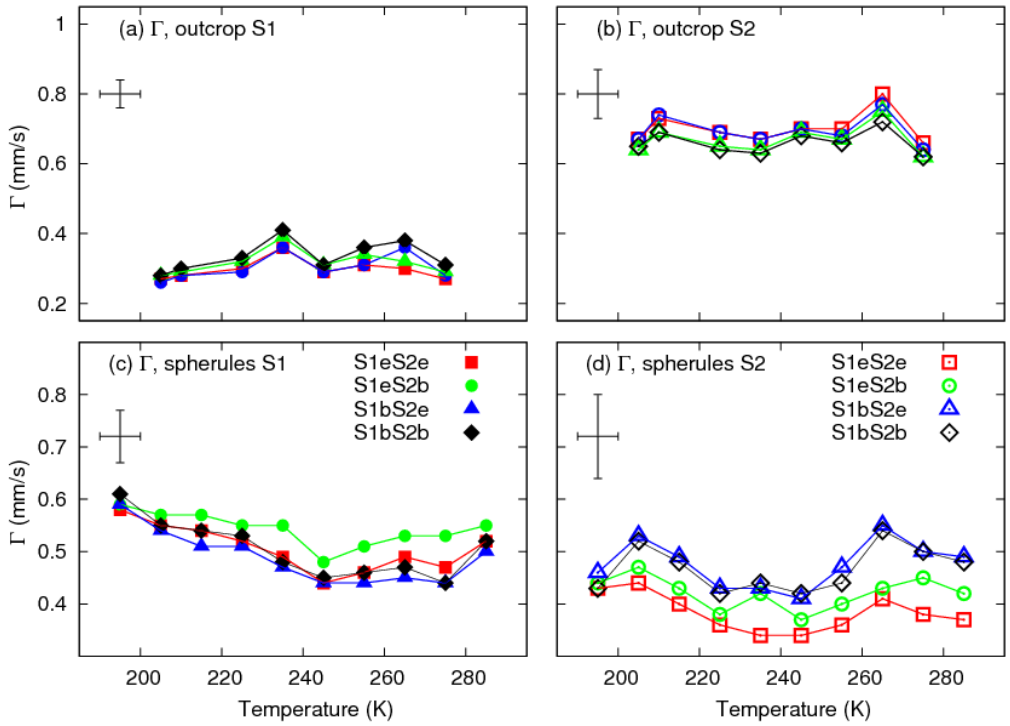

Figure 4.8: Line widths for sextets S1 and S2 from outcrop (a, b) and spherules (c, d) with error bars representing parameter scatter (±0.04 mm/s for outcrop S1; ±0.07 mm/s for outcrop S2; ±0.05 mm/s for spherules S1; and ±0.08 mm/s for spherules S2). For models with broadened lines, the widths for the line 2 and line 5 pair are given.

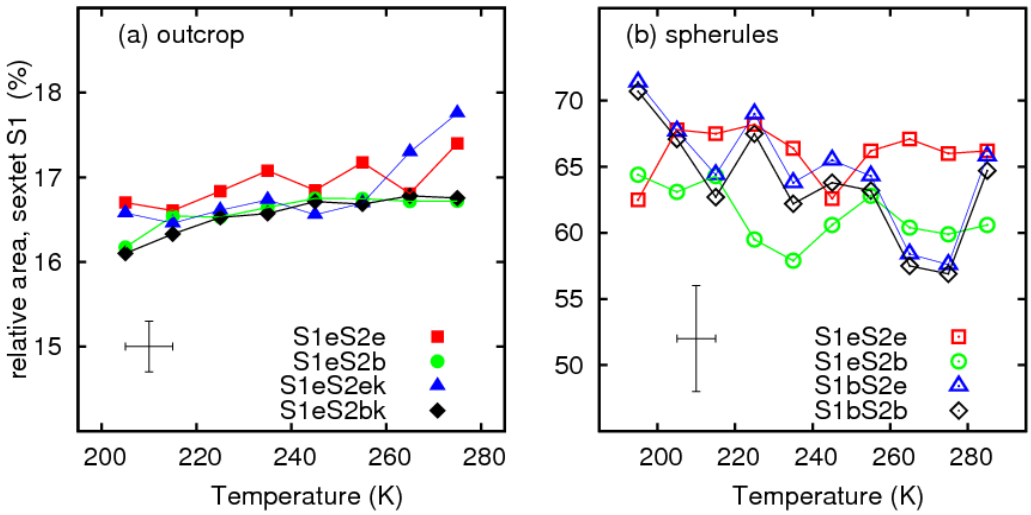

Figure 4.9: Hematite area fraction of S1 for (a) outcrop and (b) spherules with error bars representing parameter scatter (±0.3 % for outcrop; ±4 % for spherules). Note the difference in y-scales. S1 is a minor component in outcrop spectra with less than 20 %; and the dominant phase in spherule spectra with ~60 – 70 %.

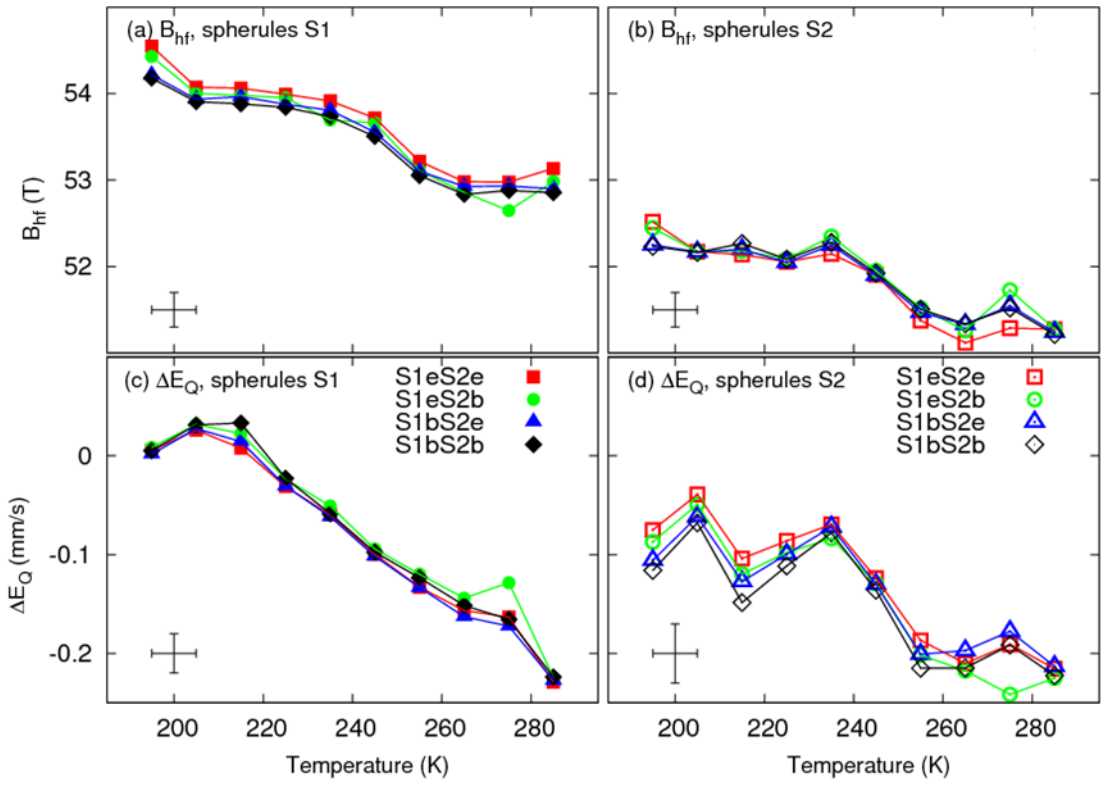

Figure 4.10: Temperature dependence of B_{hf} and ΔE_Q for spherule-rich targets from the four different models described in the text with error bars representing parameter scatter (±0.02 mm/s for ΔE_Q(S1); ±0.03 mm/s for ΔE_Q(S2); ±0.2 T for B_{hf}(S1) and B_{hf}(S2)). B_{hf}(S1) is significantly larger than B_{hf}(S2) by ~2 T. For both sextets, ΔE_Q is approximately zero or negative.

4.6 Identification of Distinct Hematite Populations

In this section, Mössbauer results from single-sextet fits of hematite-bearing analogue samples, the two-sextet simfits of outcrop and spherule-rich targets, and the corresponding one-sextet fits reported by *Morris et al.* [2006b] are summarized and discussed. The one- and two-sextet fits for outcrop and spherule hematite are compared in a plot of B_{hf} versus ΔE_Q (Figure 4.11a). The advantage of this plot is that non-representative temperature measurements are not a factor.

Simfit parameters for outcrop and spherules are from the S1eS2b model. Parameters for B_{hf} and ΔE_Q for outcrop S2 hematite plot within the range for the parameters reported by *Morris et al.* [2006b] for single-sextet fits of hematite. This is the expected result, because the outcrop S2 sextet is dominant with ~83 % of the total hematite subspectral area (Figure 4.9a). The values of B_{hf} and ΔE_Q for one-sextet fits of spherule hematite plot intermediate to the corresponding data for the two-sextet simfits. Again, this is the expected result as the spherule S2 sextet is ~35 % of the total hematite subspectral area (Figure 4.9b).

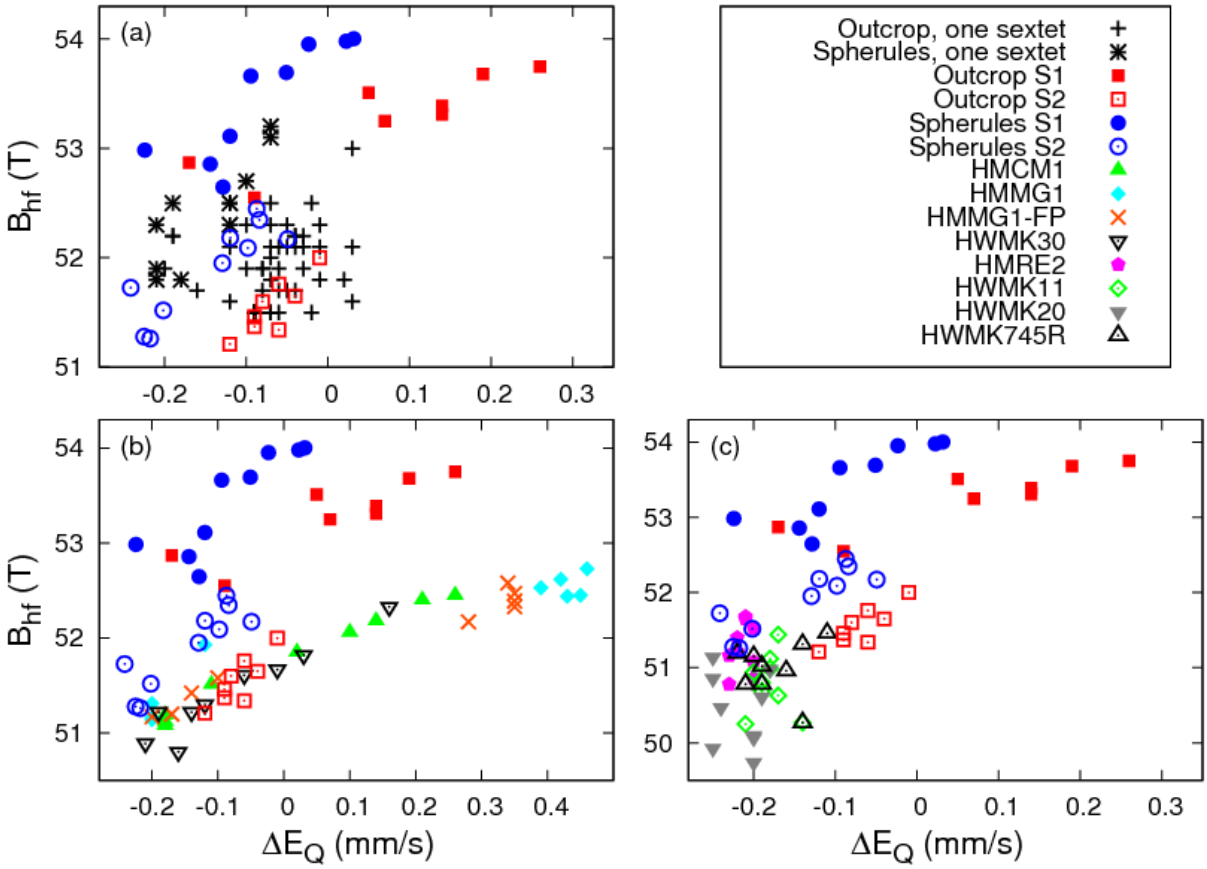

Figure 4.11: B_{hf} versus ΔE_Q plots for hematite. Parameters labeled "Outcrop, one sextet" and "Spherules, one sextet" are from [*Morris et al.*, 2006b]. Simfit parameters for outcrop and spherules are from fits with model S1eS2b at all temperatures. Parameters for analogue samples are from a one-sextet fit. (a) Meridiani Planum one-sextet fits compared to simfit results. (b) Simfit results compared to analogue samples with Morin transition. Note the extended ΔE_Q scale for this plot. (c) Simfit results compared to analogue samples without Morin transition.

As discussed in previous sections, the outcrop and spherule hematite each have two distinct hematite populations on the basis of derived Mössbauer parameters B_{hf} and ΔE_Q. This result is apparent in Figure 4.11a because the data points for each of the four sextets cluster in a different region of the plot. With respect to abundance, sextet S2 is dominant for outcrop hematite, and sextet S1 is dominant for spherule hematite. The mm-sized spherules are embedded in the outcrop matrix (Figure 4.1b), but were not included in the field of view of the Mössbauer instrument during outcrop measurements.

The outcrop and spherule hematite are compared with corresponding B_{hf} and ΔE_Q values for analogue samples (from Figure 4.2) in Figure 4.11b and Figure 4.11c. From literature data [*de Grave and Vandenberghe*, 1990], the WFM state for well-crystalline and chemically-pure bulk hematite (coarse grained with T_M ~264 K) with (ΔE_Q, B_{hf}) ~ (-0.20 mm/s, 51.8 T) at room temperature, plots at the lower left corner of this diagram, and the AFM state, with (ΔE_Q, B_{hf}) ~ (0.42 mm/s, 54.2 T) at ~4 K, plots at the upper right corner. For a hematite with a mean crystallite diameter of ~48 nm and T_M = 225 K, the WFM state has (ΔE_Q, B_{hf}) ~ (-0.20 mm/s, 51.7 T) at 270 K and ~ (-0.14 mm/s, 52.3 T) at 200 K; and the AFM state has (ΔE_Q, B_{hf}) ~ (0.33 mm/s, 52.8 T) at 230 K, ~ (0.36 mm/s, 53.1 T) at 200 K, and ~ (0.37 mm/s, 53.8 T) at 80 K. All of the values for the AFM state of this sample have B_{hf} >52.8 T and ΔE_Q ~0.33 mm/s at 200 K and thus also plot in the upper right corner of Figure 4.11.

On the basis of Figure 4.11, the Meridiani hematite most like well-crystalline and chemically pure hematite is the hematite represented by outcrop sextet S1. It has a discernible Morin transition with T_M ~260 K and a positive ΔE_Q (i.e., AFM-like) at the lowest measurement temperature. The S2 sextet for the outcrop has no discernible Morin transition and a negative ΔE_Q (i.e., WFM-like) at the lowest measurement temperature. Without direct measurement of the intrinsic properties of S1 hematite (e.g., particle or crystallite diameter, substitutional impurities like Al^{3+} or OH^-, etc.), it cannot be meaningfully distinguished which property or combination of properties is most important.

Because hematite accounts for approximately one third of the total Fe in the outcrop and because the total Fe concentration in the outcrop is ~20 wt% Fe as Fe_2O_3 [*Rieder et al.*, 2004; *Morris et al.,* 2006b], based on chemical data from Opportunity's Alpha Particle X-Ray Spectrometer (APXS), it is unlikely that the combination of Mössbauer and APXS data can be used to identify and constrain the concentration of chemical impurities in outcrop hematite.

Possible relations between hematite abundance and the concentrations of elements which may influence the Morin transition, including Al, Ti, Mn, and Cr were examined. The correlations for outcrop for all four elements are shown in Figure 4.12a. With correlation coefficients of R^2=0.09 for Al, R^2=0.15 for Ti, R^2=0.03 for Mn, and R^2=0.18 for Cr, the correlations are too weak to infer any information on possible elemental substitution in the outcrop hematite. For spherules, the correlations are stronger, as shown in Figure 4.12b, with correlation coefficients of R^2=0.66 for Al, R^2=0.60 for Ti, R^2=0.76 for Mn, and R^2=0.49 for Cr. However, all correlations for spherules are negative with increasing hematite content and thus do not point to elemental substitutions. Instead, they are mixing lines between basaltic soil and dusty spherules [*Jolliff et al.*, 2007].

For the spherule-rich targets, the near zero value of ΔE_Q for sextet S1 at the lowest measurement temperature is suggestive of a Morin transition at lower temperatures (T_M < 205 K). Like the S2 sextet for outcrop hematite, the spherule S2 sextet has no discernable Morin temperature and even more negative values of ΔE_Q. As just discussed, the Mössbauer data alone cannot constrain intrinsic properties for this hematite. Because the spherule targets have a higher proportion of total Iron associated with hematite and a higher total Fe concentration than outcrop targets [*Rieder et al.*, 2004; *Morris et al.,* 2006b; *Brückner et al.*, 2008], *Morris et al.* [2006b] calculated that the spherules contained

~0.3 wt.% Ni. However, the values of B_{hf} and ΔE_Q for hematite are not dependent on the Ni content for concentrations as high as 5.3 mol% [e.g., *Saragovi et al.*, 2004].
One might consider that size effects are not a consideration for the spherules because of their macroscopic size (~5 mm). However, a large particle can be polycrystalline with crystallite sizes (X-ray domains) small enough to affect the Morin temperature. Polycrystalline behavior with a fibrous radial morphology is likely for the Meridiani spherules based on the laboratory experiments of *Golden et al*. [2008].

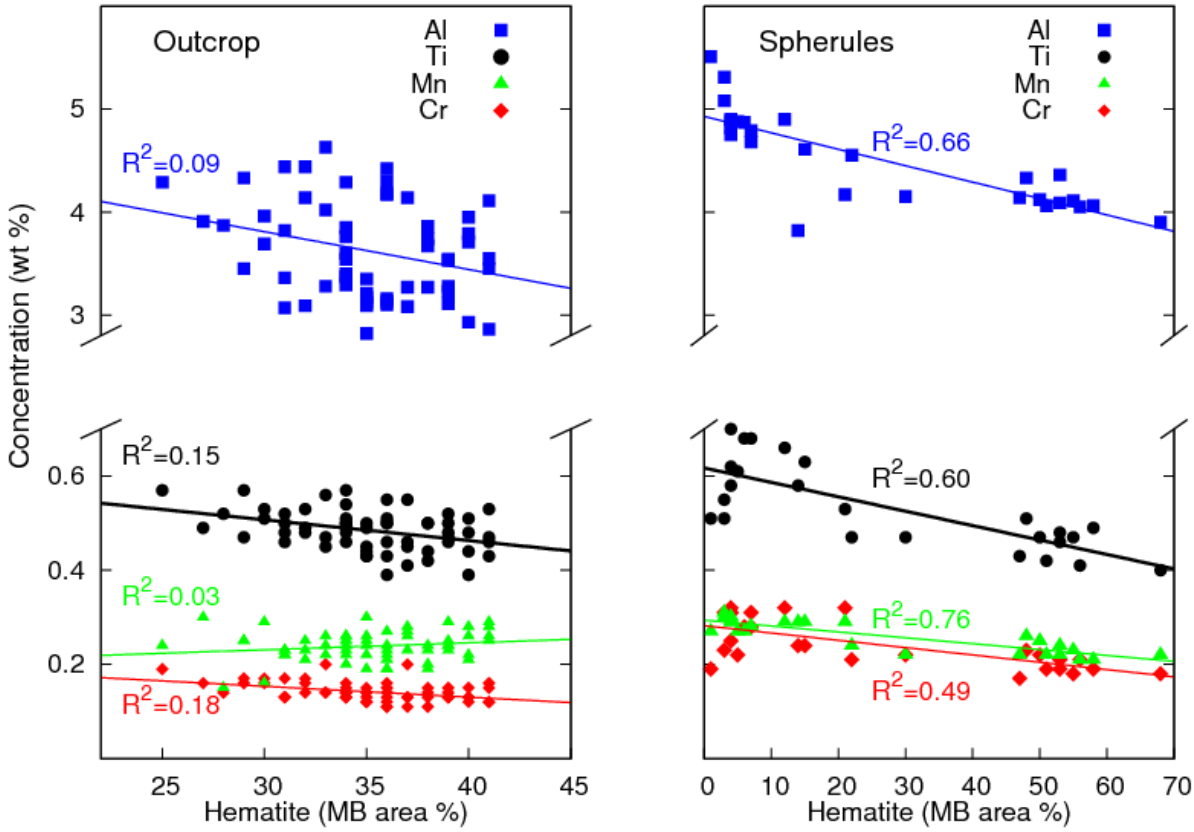

Figure 4.12: Correlations of Al, Ti, Mn and Cr with hematite. Values for hematite are area fractions from Mössbauer spectra (Figure 5). Note the different scales for hematite abundances.

4.7 Summary and Conclusions

Simultaneous fitting (simfitting) is an effective method to systematically fit a large number of MER Mössbauer spectra. Summing of spectra to improve counting statistics is avoided, fewer parameters are held fixed, and target-related quantities can be established. The temperature dependence of parameters can be studied and different models can be compared without the need to repeat countless single spectrum fits.
Simfitting was applied to two data sets of Meridiani Mössbauer spectra: 60 separate spectra from 10 Eagle crater outcrop targets, and 46 separate spectra from 10 different spherule targets. This approach provides additional information on the nature of hematite in the outcrop and spherules compared to a one-sextet model [*Morris et al.*, 2006b]: by modeling the hematite component with two sextets, two separate hematite populations can be resolved for both target types.
For outcrop targets, hematite sextet S1 has narrower lines and larger B_{hf} compared to hematite sextet S2. With increasing temperature, the presence of a Morin transition for S1 is indicated by a drop in B_{hf}, and a steadily decreasing ΔE_Q that changes sign at ~260 K, rather close to the value for well-crystallized and chemically pure hematite (~264 K). For

sextet S2, $\Delta E_Q < 0$ at all temperatures; i.e. it represents weakly ferromagnetic hematite with no Morin transition. With relative subspectral areas of ~83 %, S2 is the dominating hematite phase. The two hematite populations can occur as any combination of separate populations of (I) particles covering a narrow size range and with different properties such as compositions and degrees of crystallinity; and (II) particles with similar intrinsic properties covering a wider size range.

For spherule-rich targets, S1 has larger B_{hf} and slightly broader lines than S2. Both sextets have symmetric lines and ΔE_Q at or less than zero at all temperatures, indicating WFM hematite with no Morin transition. S1 is the dominating hematite phase in spherule spectra with relative subspectral areas of ~65 %. Two hematite phases can occur if the hematite within individual spherules is heterogeneous with respect to intrinsic properties or if intrinsic properties vary from spherule to spherule. Hematite particle size effects can occur in macroscopic particles like the spherules if they are polycrystalline with small crystallite (domain) sizes.

Without additional information concerning the intrinsic properties of outcrop and spherule hematite, it is not possible to distinguish among particle size, substitutional impurities like Al^{3+}, and other factors as the property responsible for the temperature dependences of B_{hf} and ΔE_Q in association with the Morin transition. If a range of particle sizes is present in the outcrop hematite, there may be a continuous size distribution of hematite particles ranging from largest (the S1 sextet), to intermediate (the S2 sextet), to smallest, where the Fe3D3 doublet in outcrop Mössbauer spectra is interpreted as superparamagnetic hematite. Because the largest particles are not detected by the MER Microscopic Imager (MI), the upper size limit corresponds to the resolution of the MI of ~30 μm/pixel [*Herkenhoff et al.*, 2003]. The presence of different hematite populations in Meridiani outcrop and spherules implies more than one hematite-forming process or episode, as discussed by *Morris et al.* [2005]. *McLennan et al.* [2005] identified at least two episodes of cementation, and at least four episodes of groundwater recharge in the outcrop. For spherules, they propose a formation scenario through a rapid process, likely involving breakdown and/or oxidation of preexisting ferrous sulfate minerals. The hematite populations in the outcrop matrix may have formed during different episodes, their different particle sizes may reflect different environmental conditions.

5 Cobbles at Meridiani Planum

This chapter is based on the following publication:
I. Fleischer, J. Brückner, C. Schröder, W. Farrand, E. Tréguier, R.V. Morris, G. Klingelhöfer, K. Herkenhoff, D. Mittlefehldt, J. Ashley, M. Golombek, J. R. Johnson, B. Jolliff, S. W. Squyres, C. Weitz, R. Gellert, P. A. de Souza and B. Cohen (2010), *Mineralogy and Chemistry of Cobbles at Meridiani Planum, Mars.* Journal of Geophysical Research (in print).

5.1 Introduction

The Meridiani plains are covered with basaltic sand, with frequent exposures of sulfate-rich outcrop rock and a lag deposit of hematite-rich spherules [e.g., *Squyres et al.*, 2006]. Opportunity investigated the Meridiani lithologic components at numerous locations on the plains and in the inner walls of a number of craters, the largest being Victoria with a diameter of ~800 m [*Squyres et al.*, 2009]. Occasionally, loose rocks with no apparent connection to the ubiquitous outcrop were encountered. Typically, these rocks have dimensions of several centimeters or more. On the Krumbein φ scale [*Krumbein and Sloss,* 1963], this makes them pebble (4 - 64 mm) to cobble (64 – 256 mm) size, but for the sake of simplicity, these rocks are referred to as "cobbles". Cobbles are comparably rare and clusters are observed preferentially near craters. Their investigation is of interest for a number of reasons: cobbles may represent impact ejecta from deeper or more distant geologic units, providing access to materials otherwise inaccessible to the Opportunity rover. Cobbles may also represent meteoritic material. Presumably, such materials were delivered to their present location through impact events, either as impactors or as secondary impact ejecta. A good example is *Bounce Rock*, a single rock without related fragments, whose composition is similar to basaltic shergottites, a subgroup of meteorites whose origin is believed to be Mars [*Zipfel et al.*, 2010]. Meteoritic materials often include metallic Iron and are thus very sensitive to the presence of water during and subsequent to their arrival [*Ashley et al.*, 2010b]. In this chapter, possible relations between cobbles scattered over a range of several kilometers are investigated.

5.2 Cobble Classification

The 15 cobbles listed in Table 5.1 were investigated with Opportunity's contact instruments at 12 different locations between April 2004 and September 2009. Cobbles are divided into three groups, referred to as the "Arkansas Group" and the "Barberton Group", after the first specimen of each that was encountered by Opportunity, and "Outcrop Fragments". Pancam images of some representative cobbles are shown in Figure 5.1. The distribution of cobbles along Opportunity's traverse is shown in Figure 5.2; the distribution of the meteorites among those cobbles is discussed in more detail by *Schröder et al.* [2010b]. Two large boulders named *Bounce Rock* and *Marquette Island* and four Iron meteorites, informally named *Heat Shield Rock*, *Block Island*, *Shelter Island* and *Mackinac Island*, are not further considered here because they are significantly larger than cobbles. *Bounce Rock* was found to be a Martian basalt similar to some basaltic shergottites, a subgroup of the SNC meteorites (named for the three type meteorites Shergotty, Nakhla, and Chassigny) whose origin is believed to be Mars, and is probably crater ejecta [*Zipfel et al.*, 2010]. *Marquette Island* is probably also crater ejecta but not related to meteorites from Mars [*Mittlefehldt et al.*, 2010]. *Heat Shield Rock* was classified as a IAB complex Iron meteorite and given the approved official name "Meridiani Planum" after the location of its find [*Connolly et al.*, 2006]. It has been described in detail by *Schröder et al.* [2008] and *Fleischer et al.* [2010c]. The complete suite of Iron meteorites is discussed elsewhere [Ashley et al., 2009a, 2010a].

Table 5.1: Overview of cobbles discussed in this work in order of discovery.

#	Name[a]	Sol[b]	Diameter (cm)	Classification
1	Lion Stone	106	30 by 10	Outcrop fragment
2	Barberton	122	4	Barberton group
3	Russett	381	13 by 15	Outcrop fragment
4	Arkansas	551	5	Arkansas group
5	Perseverance	554	3	Arkansas group
6	Antistasi	642	6	Arkansas group
7	JosephMcCoy	886	<2	Arkansas group
8	Haiwassee	890	<2	Arkansas group
9	Santa Catarina	1045	12	Barberton group
10	Santorini	1741	10	Barberton group
11	Kos	1880	<2	Arkansas group
12	Tilos	1880	<2	Arkansas group
13	Rhodes	1882	3	Arkansas group
14	Kasos	1886	8	Barberton group
15	Vail Beach	1974	2	Arkansas group

[a] Names are informal and not officially approved by the International Astronomical Union.
[b] The sol indicates the beginning of investigations with contact instruments.

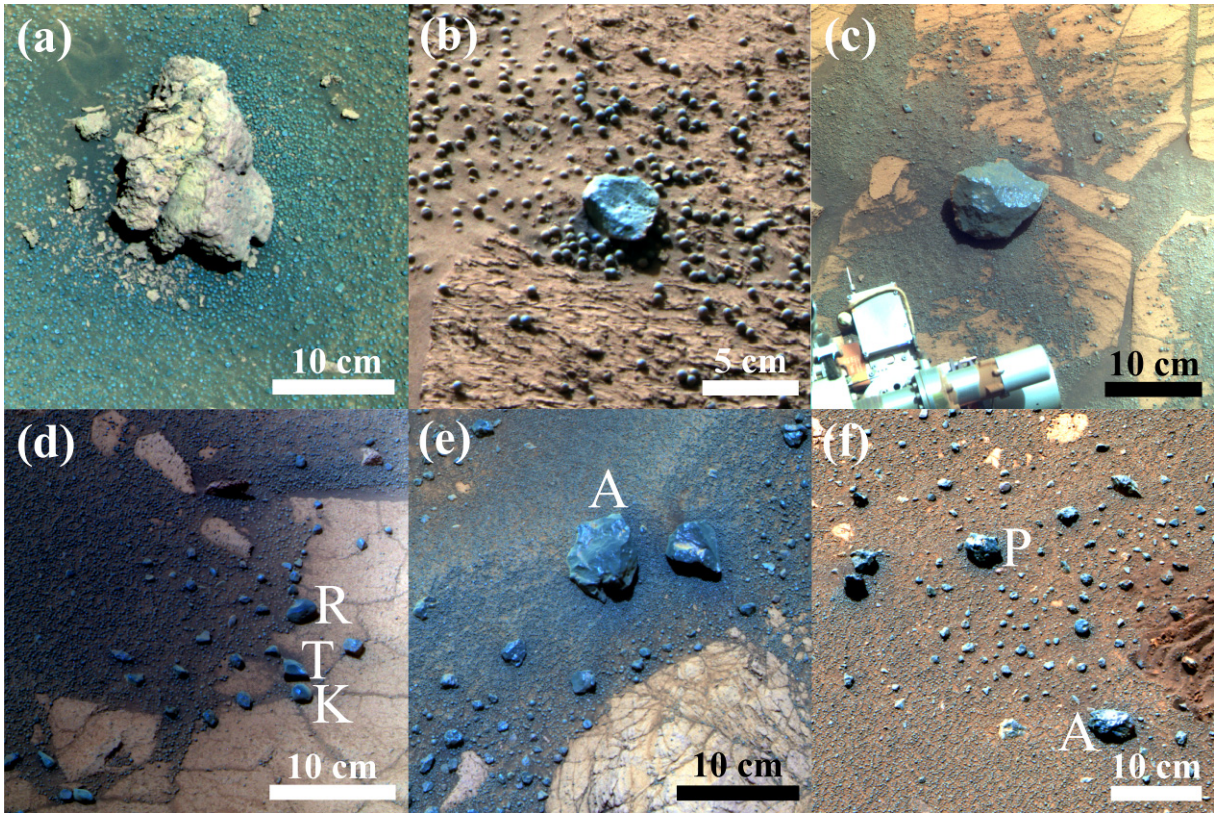

Figure 5.1: Representative false-color Pancam images of Meridiani cobbles. (a) *Russett*; (b) *Barberton*; (c) *Santorini*; (d) *Rhodes* ("R"), *Tilos* ("T") and *Kos* ("K"); (e) *Antistasi* ("A"); (f) *Perseverance* ("P") and *Arkansas* ("A"). Locations included in Table 5.1. Image credit: NASA/JPL/Pancam.

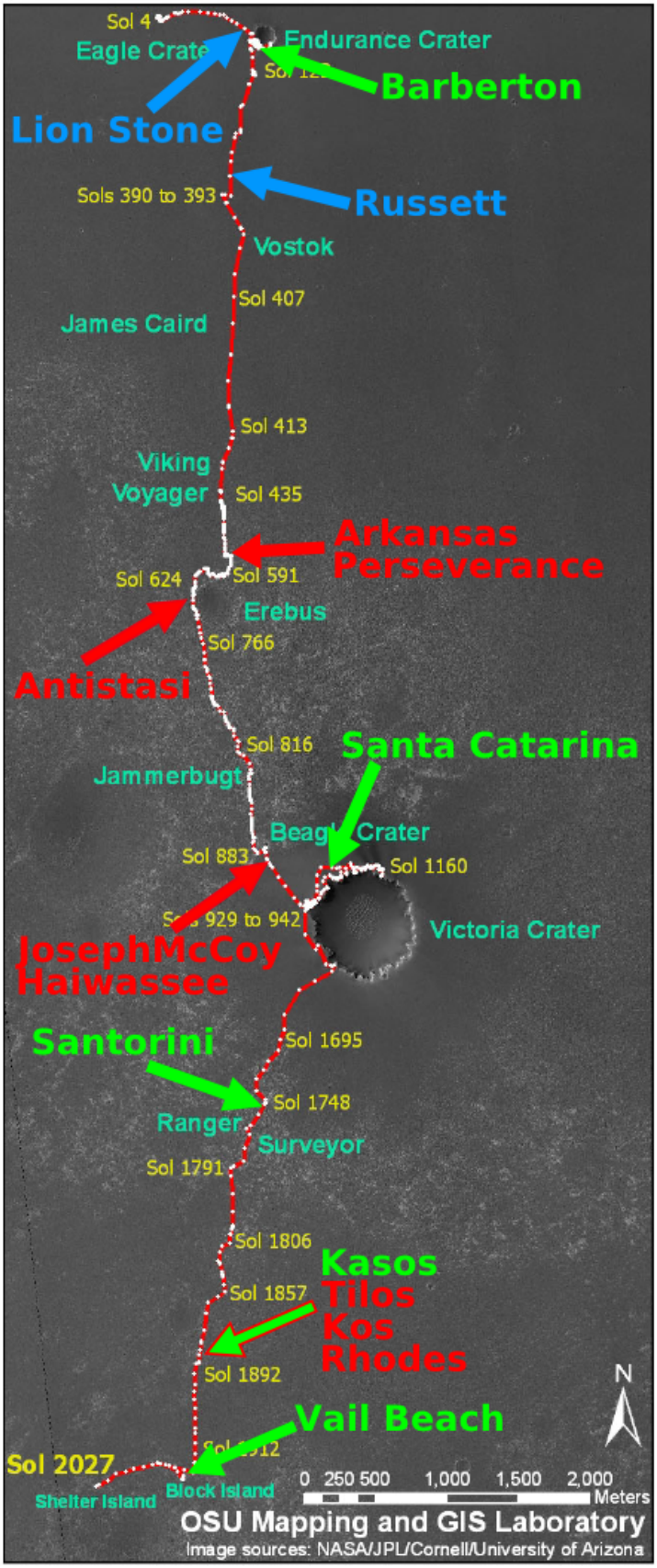

Figure 5.2: The locations of cobbles along Opportunity's traverse, with blue labels for outcrop fragments, green labels for Barberton group cobbles and red labels for Arkansas group cobbles. The locations of craters and two of the Iron meteorites (*Shelter Island* and *Block Island*) are shown in dark green.

Pancam 13-filter spectra were obtained for a much larger number of cobbles than those few investigated with the IDD instruments. Data from more than 200 loose rocks were assembled in a database [*Nuding and Cohen*, 2009]. Spectral parameters from 13-filter spectra indicate systematic differences in spectral properties that are very useful for revealing differences among cobbles [e.g., *Farrand et al.*, 2008]. Pancam multispectral imaging has proven vital to distinguishing cobbles from outcrop materials, and to selecting which cobbles will be subjected for IDD investigations. However, it is challenging to directly relate data obtained with Pancam and the contact instruments: the instruments have different fields of views and penetration depths, so that results may especially be influenced by clasts and/or discontinuous surface coatings observed in some cobble MI images. Viewing and lighting geometries have a notable effect on Pancam spectra. Figure 5.3 shows Pancam decorrelation stretches of *Russett* (outcrop fragment), *Antistasi* (Arkansas group) and *Santa Catarina* (Barberton group) that are representative of their type. Figure 5.4 shows Pancam 13-filter spectra obtained on the three cobbles, where R* is a Pancam reflectance parameter defined as "the brightness of the surface divided by the brightness of Radiometric Calibration Target scaled to its equivalent Lambert reflectance" (i.e., assuming the luminance of the surface is isotropic) [*Bell et al.*, 2006].

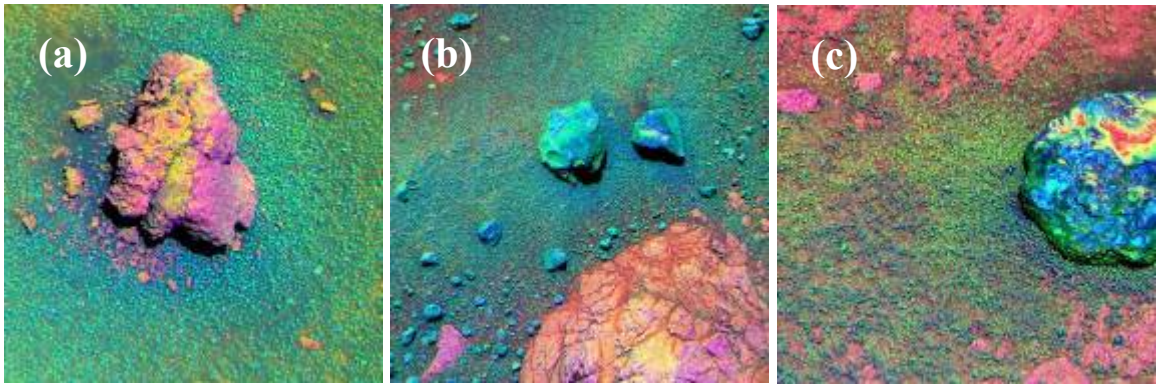

Figure 5.3: Decorrelation stretches showing the outcrop fragment *Russett* (a), Arkansas group cobble *Antistasi* (b) and Barberton group cobble *Santa Catarina* (c).

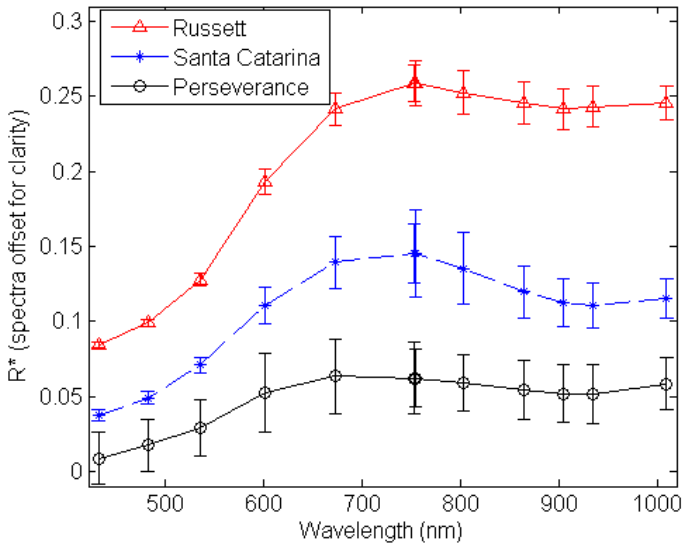

Figure 5.4: Pancam 13-filter spectra for the three cobbles shown in Figure 5.3.

The outcrop fragment *Russett* has spectral properties commensurate with those of Meridiani outcrop. Namely, it is bright compared to soil and appears buff-yellow and purple in a stretched composite (left camera filter numbers 3, 5 and 7; 673, 535, and 432 nm; Figure 5.3a). Also, it has a higher blue-to-red slope and higher 535 nm band depth than the darker cobbles. In contrast, the darker cobbles are lower in overall reflectance than outcrop (though relatively brighter at the shortest wavelength 432 nm L7 and 436 nm R1 filters). In stretched L357 composites, these cobbles appear blue. In decorrelation stretch (DCS) versions of these images, the cleanest surfaces of the cobbles are blue, those with some dust contamination appear blue-green (Figure 5.3b) and surfaces with accumulations of airfall dust are yellow to red (Figure 5.3c). The cobbles have a low to sometimes negative 535 nm band depth and generally display a positive 900 nm band depth. Chemically and mineralogically, the dark cobbles are subdivided into two groups, as will be discussed in detail in the following sections. The geochemical differences that distinguish the cobble groups are not overtly manifested in the Pancam multispectral data although there are differences between dark cobbles. *Arkansas*, *Perseverance* and other cobbles in the vicinity have a shallow and broad long-wavelength absorption centered in some spectra in the R5 904 nm band, and others in the 934 nm R6 band, with a relative reflectance maximum at 673 nm (Figure 5.4). In the *Jesse Chisholm* area cobbles (i.e., close to Erebus crater), the relative reflectance maximum shifts to 754 nm and the long wavelength absorption band minimum is more uniform in the 934 nm band. In the *Tilos, Kos*, and *Rhodes* spectra, the relative reflectance maximum is at 803 nm with a narrower long wavelength absorption centered at 934 nm.

The cobbles clustering in a cobble field near *Santa Catarina* (close to the rim of Victoria crater) share a low overall reflectance, low 535 nm band depth, a relative reflectance maximum at 754 nm, and a long wavelength absorption with a band minimum at 934 nm (Figure 5.4). However, there are differences in the width of the long wavelength absorption band which can be characterized by the slope from the 754 to 864 nm bands. *Weitz et al.* [2010] provide more information on Pancam spectral parameters of cobbles.

Based on chemical (APXS) and mineralogical (MB) data, three different cobble groups can be identified. The first group comprises two bright rocks (*Lion Stone* and *Russett*) which are compositionally indistinguishable from outcrop rocks and are thus identified as "outcrop fragments". Dark cobbles can be subdivided into the "Barberton group" and "Arkansas group", respectively, named after the first cobble of each group analyzed by Opportunity. Figure 5.5 and Figure 5.6 show plots for elemental abundances for all cobble groups in comparison with soils, Meridiani outcrop rocks, and SNC meteorites. Generally, the data for each cobble group form distinct clusters that do not overlap with each other or with soil or outcrop data. An exception is the outcrop fragments, which overlap with data for outcrop rocks. The elemental compositions of cobbles discussed in this work are summarized in Table 5.2 [*R. Gellert*, personal communication].

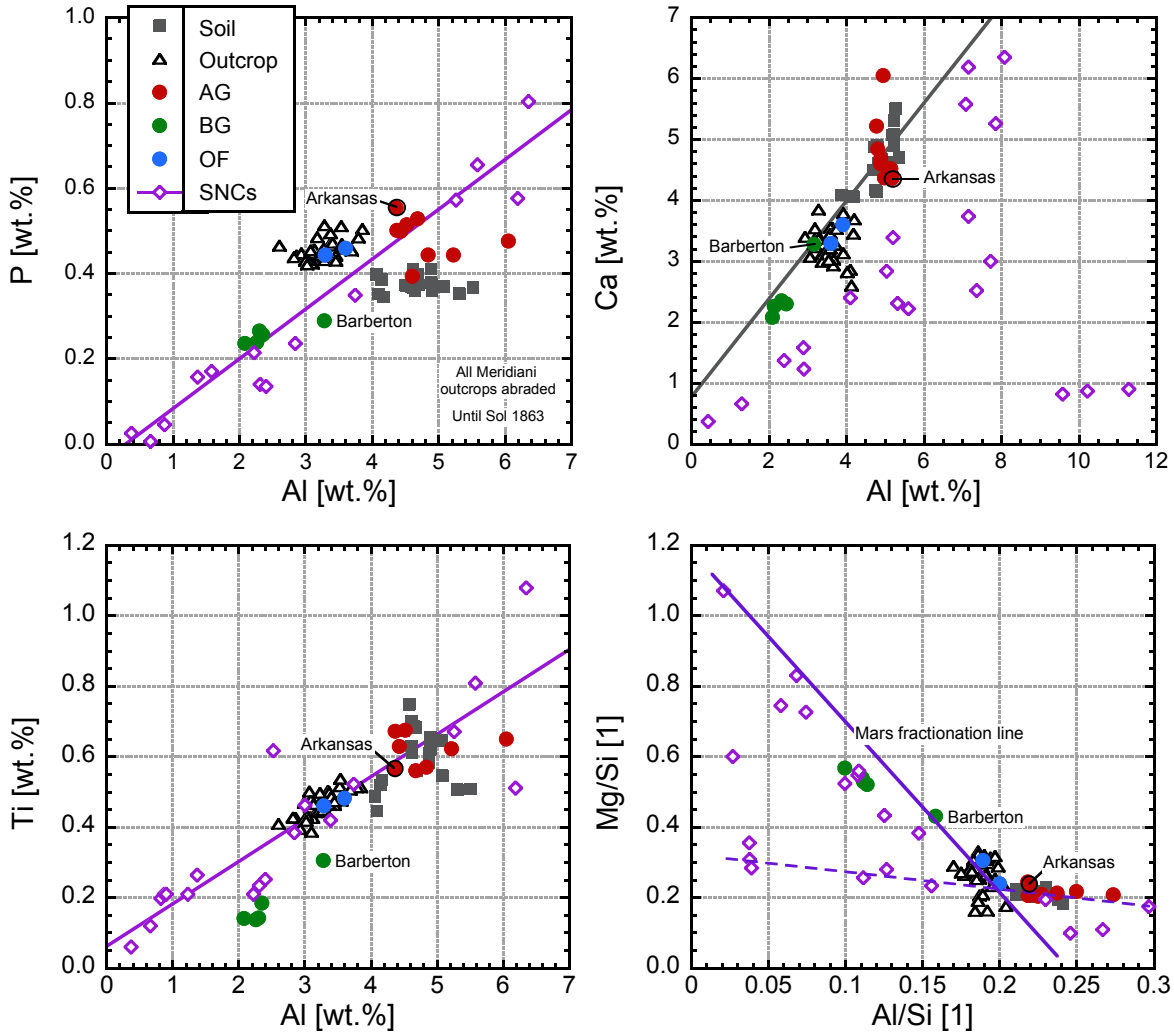

Figure 5.5: Composition of cobbles compared to Meridiani outcrop, soil, and SNC meteorites for P vs. Al, Ca vs. Al, Ti vs. Al, and Mg/Si vs. Al/Si. Outcrop fragments (OF) are indistinguishable from other outcrop rocks; Barberton group cobbles (BG) are clearly different from any other material; Arkansas group cobbles (AG) appear compositionally close to soil for a number of elements. For the P-Al and Ti-Al plots, correlation lines are calculated for the SNC samples. In the Ca-Al plot, a trend line is derived from soil samples.

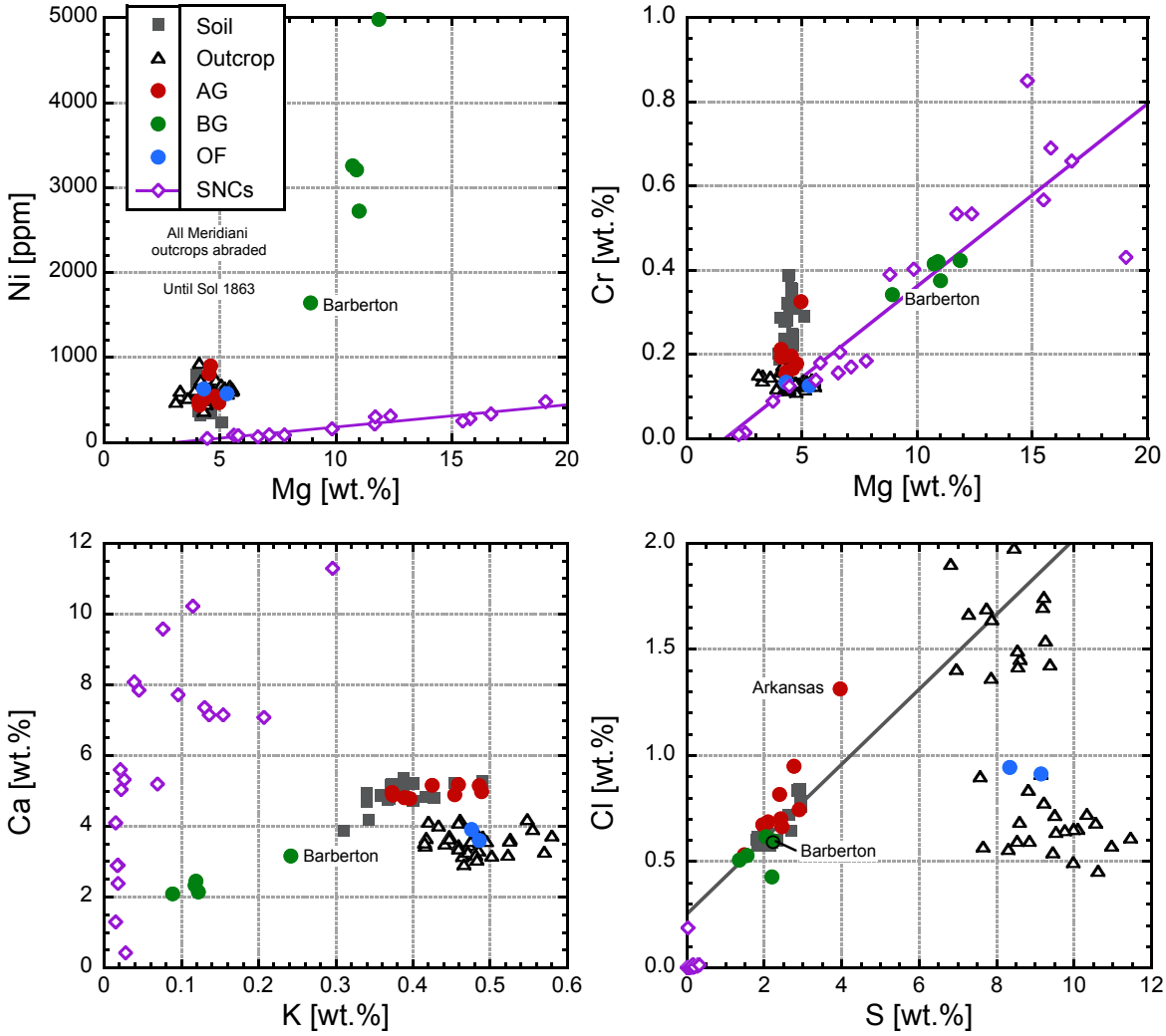

Figure 5.6: Composition of cobbles compared to outcrop, soil and SNC meteorites for Ni and Cr vs. Mg, with correlation lines for the SNCs. No trend line was found for the Ca-K plot. In the Cl-S plot, a trend line is derived based on the Meridiani soil samples. Some outcrop rocks scatter around this line, while others show a strong depletion in Cl compared to S. See Figure 5 caption for abbreviations.

Table 5.2: Elemental composition of cobbles

Sol	Cobble	Na	SE	Mg	SE	Al	SE	Si	SE	P	SE	S	SE	Cl	SE	K	SE
108	Lion Stone	1.28	0.23	5.31	0.09	3.29	0.06	17.4	0.18	0.443	0.038	9.15	0.09	0.913	0.021	0.486	0.051
122	Barberton	1.31	0.25	8.92	0.14	3.28	0.09	20.7	0.24	0.289	0.038	2.23	0.04	0.599	0.022	0.242	0.051
381	Russett	1.37	0.15	4.31	0.06	3.60	0.05	18.0	0.17	0.459	0.035	8.34	0.08	0.944	0.020	0.476	0.051
552	Arkansas	1.46	0.12	4.77	0.05	4.36	0.04	19.9	0.13	0.554	0.033	3.96	0.04	1.314	0.019	0.459	0.049
554	Perseverance	1.12	0.14	4.30	0.06	4.68	0.06	20.6	0.18	0.528	0.036	2.77	0.04	0.949	0.021	0.454	0.052
642	Antistasi	1.87	0.13	4.60	0.05	6.05	0.06	22.1	0.17	0.476	0.032	1.49	0.02	0.532	0.011	0.373	0.048
886	JosephMcCoy	1.76	0.17	4.54	0.07	5.22	0.07	20.9	0.17	0.443	0.038	1.96	0.04	0.674	0.024	0.396	0.054
890	Haiwassee	1.59	0.17	4.34	0.07	4.84	0.07	20.4	0.22	0.443	0.037	2.40	0.04	0.817	0.023	0.389	0.053
1046	Santa Catarina	1.12	0.26	10.88	0.12	2.30	0.05	20.6	0.19	0.265	0.031	2.04	0.03	0.618	0.014	0.119	0.045
1745	Santorini1	1.11	0.24	10.73	0.11	2.35	0.05	20.6	0.20	0.256	0.030	1.56	0.02	0.529	0.012	0.118	0.045
1747	Santorini2	1.06	0.27	11.86	0.13	2.08	0.05	20.9	0.23	0.236	0.030	1.36	0.02	0.507	0.013	0.089	0.044
1880	Kos	0.92	0.20	4.09	0.10	4.52	0.09	20.1	0.24	0.514	0.049	2.90	0.07	0.745	0.037	0.486	0.063
1881	Tilos	0.92	0.20	4.96	0.12	4.43	0.11	20.3	0.28	0.499	0.050	2.46	0.07	0.664	0.035	0.425	0.062
1882	Rhodes	0.99	0.15	4.11	0.07	4.37	0.07	20.0	0.22	0.501	0.039	2.43	0.04	0.702	0.022	0.489	0.055
1886	Kasos	1.18	0.15	11.01	0.09	2.26	0.04	20.4	0.14	0.238	0.029	2.20	0.03	0.428	0.010	0.122	0.045
1974	Vail Beach	1.55	0.13	4.31	0.05	4.60	0.05	20.5	0.19	0.393	0.032	2.10	0.03	0.687	0.014	0.374	0.048

Sol refers to APXS measurement. Concentrations are given in weight% of element or parts per million for Ni, Zn, and Br.
Error (SE) is absolute statistical error (2 sigma error for the precision of the value). Values for Kos, Tilos and Rhodes are preliminary.

Table 5.2 (continued)

Sol	Cobble	Ca	SE	Ti	SE	Cr	SE	Mn	SE	Fe	SE	Ni	SE	Zn	SE	Br	SE
108	Lion Stone	3.60	0.03	0.460	0.046	0.126	0.022	0.224	0.009	11.1	0.08	572	52	415	19	268	20
122	Barberton	3.16	0.04	0.305	0.043	0.342	0.030	0.280	0.015	15.4	0.13	1639	89	207	25	47	21
381	Russett	3.91	0.03	0.482	0.041	0.134	0.022	0.236	0.009	12.0	0.08	628	51	585	21	60	16
552	Arkansas	5.18	0.03	0.567	0.039	0.178	0.021	0.254	0.007	13.5	0.06	539	45	418	15	110	16
554	Perseverance	4.89	0.04	0.560	0.043	0.154	0.025	0.237	0.010	15.9	0.09	508	65	327	24	79	19
642	Antistasi	4.95	0.03	0.650	0.040	0.166	0.021	0.233	0.007	12.9	0.06	899	49	189	12	35	14
886	JosephMcCoy	4.78	0.05	0.622	0.049	0.196	0.028	0.238	0.013	15.6	0.09	807	81	263	29	37	20
890	Haiwassee	4.81	0.05	0.570	0.047	0.159	0.027	0.238	0.013	16.5	0.13	566	69	282	25	64	21
1046	Santa Catarina	2.45	0.02	0.142	0.035	0.420	0.025	0.292	0.009	16.0	0.10	3207	76	164	13	59	16
1745	Santorini1	2.33	0.02	0.184	0.035	0.415	0.024	0.290	0.009	17.2	0.11	3255	76	128	12	22	15
1747	Santorini2	2.09	0.02	0.141	0.035	0.423	0.024	0.304	0.009	16.3	0.11	4979	91	120	12	20	15
1880	Kos	5.15	0.08	0.675	0.059	0.212	0.038	0.309	0.025	16.8	0.15	485	119	437	53	47	27
1881	Tilos	5.16	0.08	0.629	0.060	0.325	0.042	0.315	0.024	16.3	0.18	465	122	299	51	35	36
1882	Rhodes	4.98	0.05	0.672	0.053	0.193	0.029	0.267	0.014	18.3	0.14	435	80	335	30	65	22
1886	Kasos	2.14	0.02	0.137	0.034	0.375	0.022	0.304	0.008	16.3	0.06	2722	65	88	9	99	15
1974	Vail Beach	4.88	0.04	0.575	0.040	0.270	0.022	0.292	0.008	17.3	0.11	505	47	305	14	75	16

5.2.1 Outcrop Fragments

Lion Stone sits on the rim of Endurance crater and measures 30 by 10 cm. It is one of many similar rocks encountered on the rims of craters. Undisturbed and abraded spots of the rock's surface were measured and imaged between sols 105 and 108. *Russett* (~13 cm by 15 cm) was encountered on the plains ~800 m south of Endurance crater. Only the undisturbed surface of the rock was investigated on sols 380 and 381. In false-color Pancam images, both rocks appear bright and red compared to other material in the field of view, including soil, darker cobbles and spherules with a bluish appearance. Pancam spectral parameters of this set of cobbles are also consistent with those of outcrop in terms of their having higher blue-to-red slopes and 535 nm band depths [*Farrand et al.* 2007; *Weitz et al.*, 2010]. Spherules were also observed, contained within the bulk of each rock, as shown in Figure 5.7 for the undisturbed surface of *Russett*. Spherules are typically observed in outcrop rocks, and their occurrence in *Russett* and *Lion Stone* is another indication for their connection to outcrop rocks. Both cobbles are indistinguishable from outcrop for practically all elements (Figure 5.5 and Figure 5.6). Compared to other cobbles, their sulfur content is especially high. Their Mössbauer spectra are also typical for outcrop rocks. Figure 5.8a shows a direct comparison of outcrop fragment spectra and a typical outcrop spectrum, Figure 5.8b shows the content of Iron-bearing phases derived from them. Fits yield relative subspectral areas of ~15 % divided between olivine and pyroxene, ~25 % Fe3D3 (an unassigned ferric phase, cf. [*Morris et al.*, 2006b]), ~30 % jarosite and ~30 % hematite. Based on these findings, the *Lion Stone* and *Russett* cobbles are identified as outcrop fragments with high confidence. *Russett* is the only fragment of Meridiani outcrop that Opportunity investigated far from any crater.
Outcrop fragments are larger (>10 cm) than other cobbles (cf. Table 5.1), perhaps because smaller fragments of the comparably soft outcrop rocks are not as long-lasting as the other cobble types consisting of harder material.

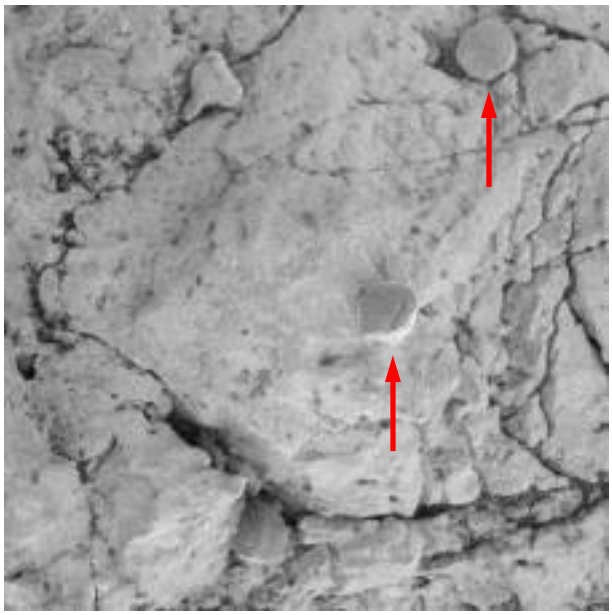

Figure 5.7: Merge of 4 radiometrically-calibrated MI images of target *Eye* on the undisturbed surface of outcrop fragment *Russett*, taken on Sol 381 when the target was fully shadowed. Area shown is ~3 cm². Embedded spherules (arrows) are clearly visible. Image credit: NASA/JPL/MI.

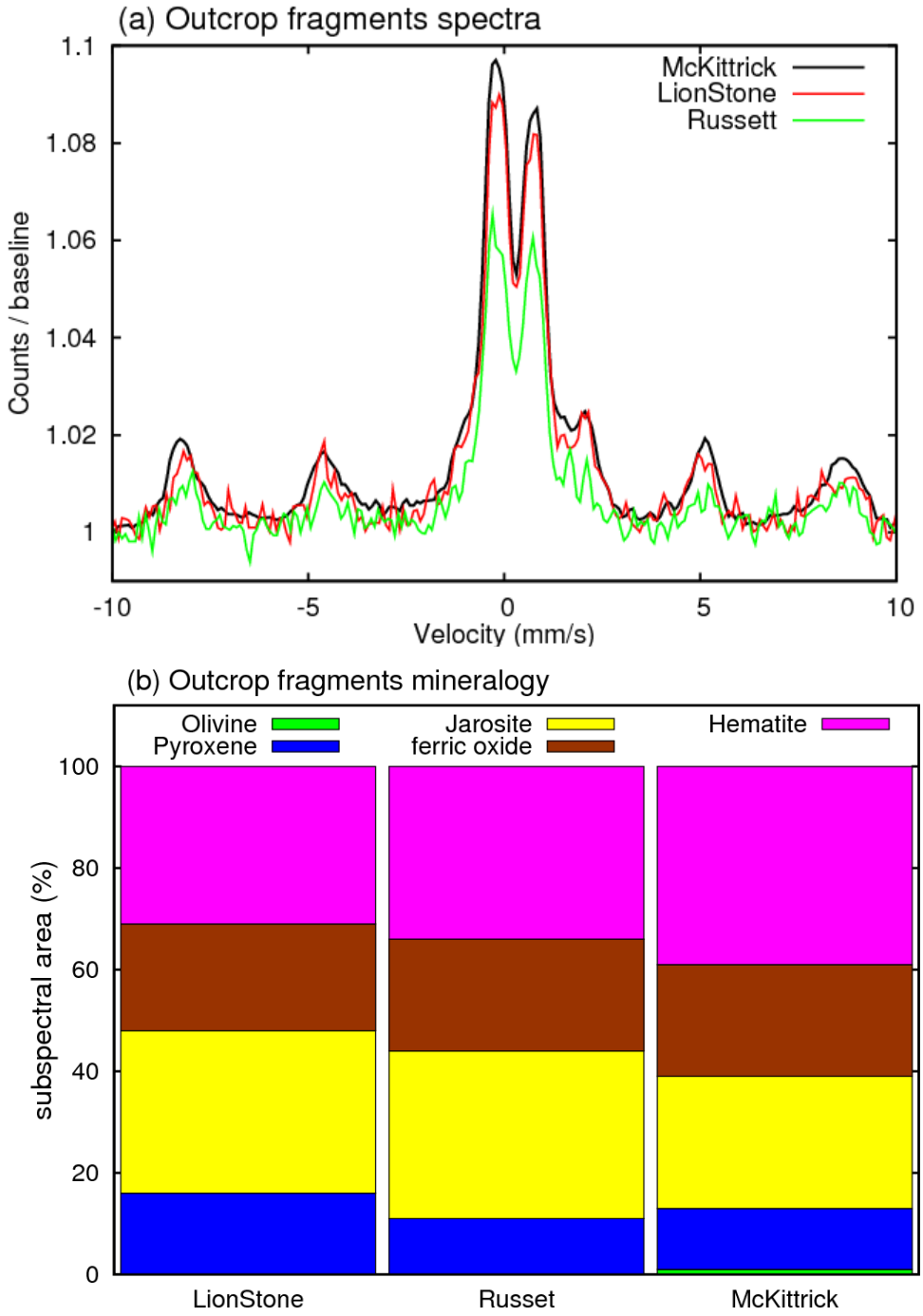

Figure 5.8: Mössbauer spectra of the two outcrop fragments *Lion Stone* and *Russett* are practically identical to a typical outcrop spectrum (*McKittrick*).

5.2.2 Barberton Group

Barberton (~4 cm) was encountered on the southern rim of Endurance crater on sol 121. Seven kilometers further south, *Santa Catarina* (14 by 11 cm) was found in a cobble field close to the northern rim of Victoria crater. Between sols 1045-1048, MI images, APXS, and Mössbauer spectra were obtained on the undisturbed, but relatively dust-free surface of the *Santa Catarina*. *Schröder et al.* [2008] have provided a detailed description of *Barberton* and *Santa Catarina*. From sol 1713 to sol 1749, ~800 m south of Victoria crater, the ~10 cm cobble *Santorini* was analysed [*Schröder et al.,* 2009]. *Kasos* (~8 cm) was encountered ~1.5 km south of Victoria crater, in close proximity to the Arkansas group cobbles *Tilos, Kos*, and *Rhodes*. The undisturbed surface of *Kasos* was investigated between sols 1886 and 1890. None of the Barberton group cobbles were brushed or abraded with the RAT because of their small size and unfavorable geometry. In true and false color Pancam images, all these cobbles appear dark compared to outcrop and soil in the field of view (Figure 5.1b, Figure 5.1c and Figure 5.1d). Figure 5.9 shows MI images of the two Barberton group cobbles *Santa Catarina* and *Santorini*. *Santa Catarina* MI images clearly show several clasts, suggesting a brecciated nature (compare also *Schröder et al*., [2008], Fig. 11). Compared to *Santa Catarina, Santorini* does not look brecciated; its surface appears to be clean from dust and partly glassy and lustrous. *Barberton* is partly coated by dust masking diagnostic textures, and the surface is somewhat pitted. The surface of *Kasos* is cleaner, showing a clastic texture with mostly sub-rounded clasts. Glints of sunlight suggest a glassy luster, perhaps resulting from a coating.

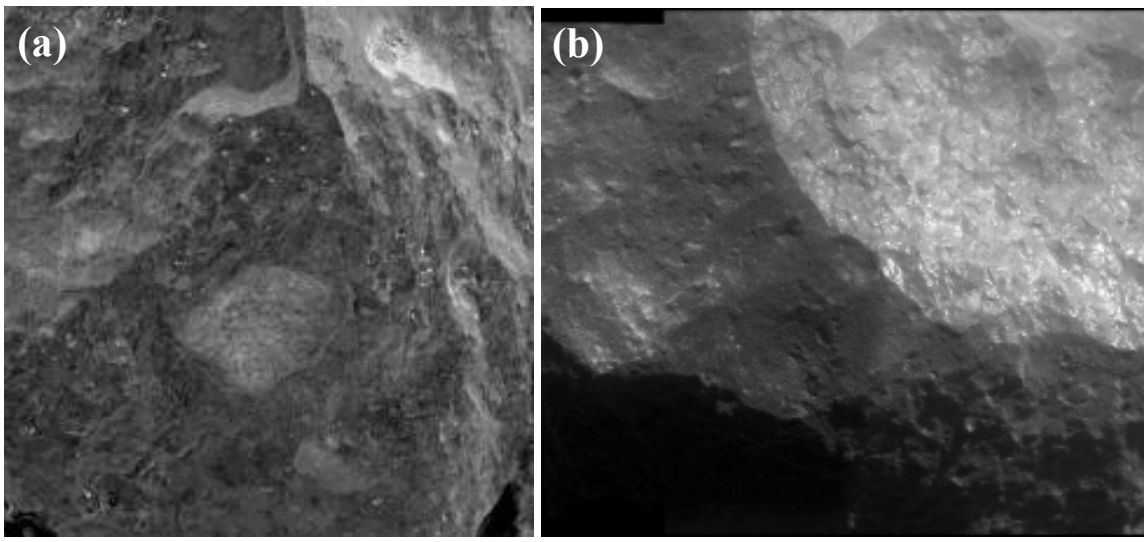

Figure 5.9: (a) Merge of 7 radiometrically-calibrated MI images of *Santa Catarina* taken on Sol 1055 when target was fully shadowed. Area shown is ~3 cm². Clasts are clearly visible. (b) MI mosaic of *Santorini* taken on Sol 1747. Area shown is ~3 cm high, illumination from upper right. The surface appears partly lustrous.

APXS spectra were obtained on one spot each on *Barberton, Santa Catarina* and *Kasos*, and two spots on *Santorini*. Elemental trends are shown in Figure 5.5 and Figure 5.6 in comparison with Meridiani soils, outcrop rocks, other cobbles, and SNC meteorites. SNC meteorites are inferred to have originated from Mars [e.g., *McSween et al.,* 1979; *Nyquist et al.,* 1979; *Walker et al.,* 1979; *Wasson and Wetherill,* 1979; *Bogard and Johnson,* 1983; *Treiman et al.*, 2000]. They are included in all these plots because they provide a possibility to compare all Meridiani cobbles to Martian materials excavated by impact events.

The P/Al ratio is characteristic for most SNCs. These elements are both incompatible in mafic igneous systems, and their correlation in SNC meteorites is a result of igneous

fractionation in martian magmas. Meridiani soils and outcrops depart from the P-Al trend line indicating chemical weathering and/or physical transport have separated the mineral hosts – phosphates and feldspars – from the original igneous parents. The Barberton group cobbles follow the SNC P-Al trend. The Meridiani soils and outcrops show a strong trend in the Ca–Al plot that is distinct from that of SNC meteorites. Barberton group cobbles plot close to the Ca–Al trend line defined by Meridiani samples, and distinct from the SNC meteorites. SNC meteorites show a good correlation for Ti and Al, which can also be observed for all Meridiani outcrops. The Barberton group Ti and Al concentrations plot below the correlation line. The SNCs span a wide field in the Mg/Si vs. Al/Si diagram shown in Figure 5.5. Some SNCs follow the Mars mantle-crust fractionation line (bold line) [e.g., *Dreibus et al*., 2003]. Other SNCs seem to follow a different evolution line (dashed line). Barberton group cobbles plot close to the fractionation line. In the Ca-K plot, Barberton group cobbles span the concentrations between the SNCs and the Meridiani samples. The *Barberton* specimen plots closest to other Meridiani materials, probably due to soil in the field of view. Cl and S concentrations are similar for soils and most cobbles, with the lowest values for Barberton group cobbles. The concentrations of both elements are significantly higher in outcrop rocks, and significantly lower in SNC meteorites. Barberton group cobbles are among the samples with the highest Cr contents observed at Meridiani Planum and plot on the Mg-Cr correlation line for SNCs (Figure 5.6). SNCs have variable olivine contents, with very high contents for chassignites [e.g., *Meyer*, 2010] and Ni can be incorporated in olivine during crystallization, which is the cause of the high Ni-Mg-ratios observed for SNC meteorites. The overall Ni and Mg concentrations are tightly clustered for Meridiani Planum materials except for the Barberton group cobbles. Their Ni concentrations range between ~1500 and 5000 µg/g and their Mg concentrations are about twice that of soils and outcrops. The extremely high Ni contents of the Barberton group cobbles and their deviations from SNC compositions point to a meteoritic (i.e., non-Martian) origin. The overall chemical composition of Barberton group cobbles is most consistent with mesosiderite silicate clasts [*Schröder et al.*, 2008].

A direct comparison of the four Barberton group Mössbauer spectra is shown in Figure 5.10a, the similarities between the spectra are evident. Figure 5.10b shows a comparison of the contents of Iron-bearing phases in the rocks, fits are shown in Figure 5.11. The plots are derived from simultaneous fits with the *MERFit* program described in chapter 4 [*Agresti and Gerakines*, 2009] to establish parameter relations between separate spectra. Mössbauer parameters for any given mineral phase can be set equal for all spectra of the data set. Each individual spectrum is preserved in the fit. The fits for Barberton group cobbles are derived from a model including olivine, pyroxene, kamacite (α-Fe,Ni), troilite (FeS) and nanophase ferric oxide (npOx, a generic name for Iron oxides or oxyhydroxides with particle sizes in the nanometer range that are superparamagnetic at the temperature of observation, e.g. hematite (α-Fe_2O_3), maghemite (γ-Fe_2O_3) or goethite (α-FeOOH)) [e.g., *Morris et al.,* 2006a]. Kamacite and troilite are typically detected in meteorites. Their Mössbauer parameters were constrained because of the comparably small subspectral area of both phases. Parameters for kamacite and troilite were obtained from a specimen of the *Mundrabilla* meteorite measured at a temperature of ~235 K (described in detail in chapter 6). Mössbauer parameters and subspectral areas are given in Table 5.3.

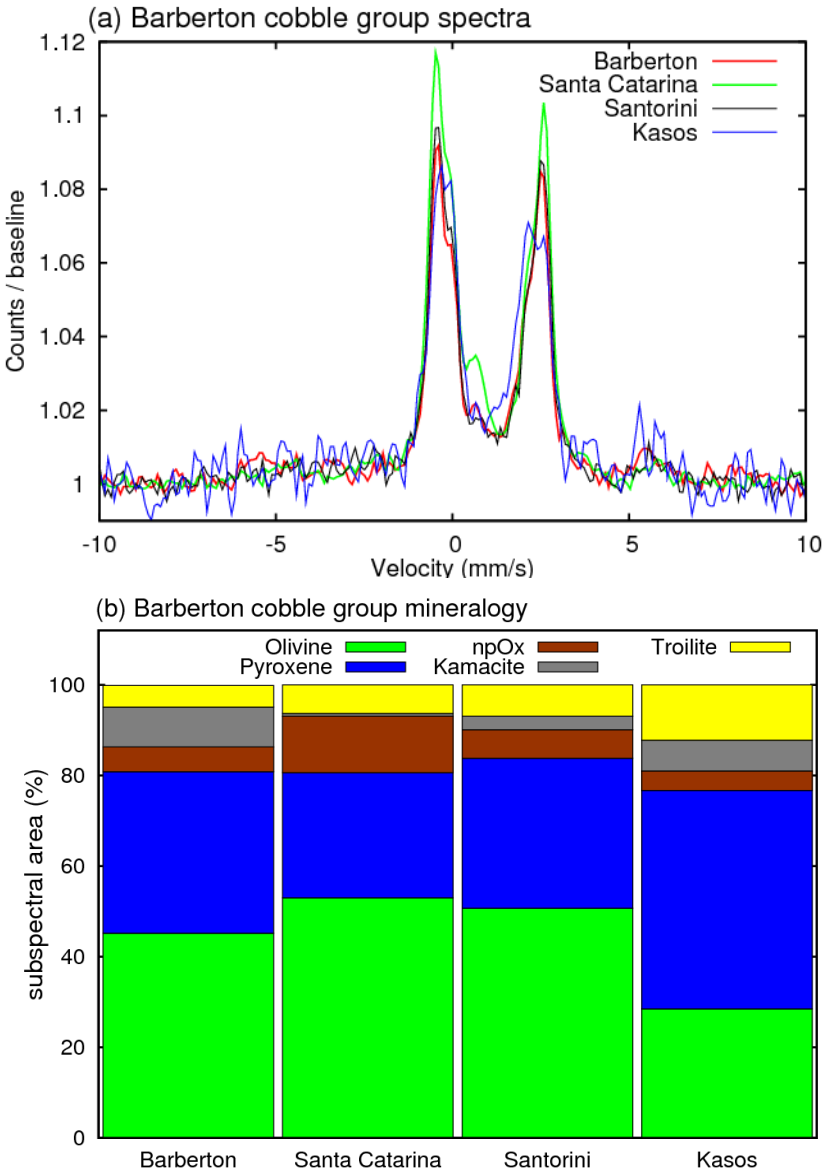

Figure 5.10: The "Barberton group cobbles" *Barberton, Santa Catarina, Santorini* and *Kasos* show very similar Mössbauer spectra dominated by the basaltic minerals olivine and pyroxene. Additional contributions from kamacite and troilite are present.

Barberton, Santa Catarina and *Santorini* have spectra with more Fe from olivine than from pyroxene, with the opposite for *Kasos*. The simultaneous fit demonstrates that the spectra obtained on *Barberton* and *Santorini* show the presence of kamacite and troilite, while the *Santa Catarina* spectrum shows almost exclusively troilite. These results are consistent with previous publications by *Morris et al.* [2006b] and *Schröder et al.* [2008]. The *Kasos* spectrum is characterized by poorer counting statistics compared to the other cobbles because of decreased activity of the Mössbauer source at the time of the measurement (sol ~1890), but it is in agreement with the presence of both kamacite and troilite.
These results show that Barberton group cobbles are fundamentally different from all other materials investigated at Meridiani Planum. Genetic associations of *Santa Catarina* with additional cobbles in its vicinity are implied by Mini-TES data [Ashley et al., 2009b]. A detailed discussion of possible pairing of the Barberton group cobbles and resulting implications is provided by *Schröder et al.* [2010b].

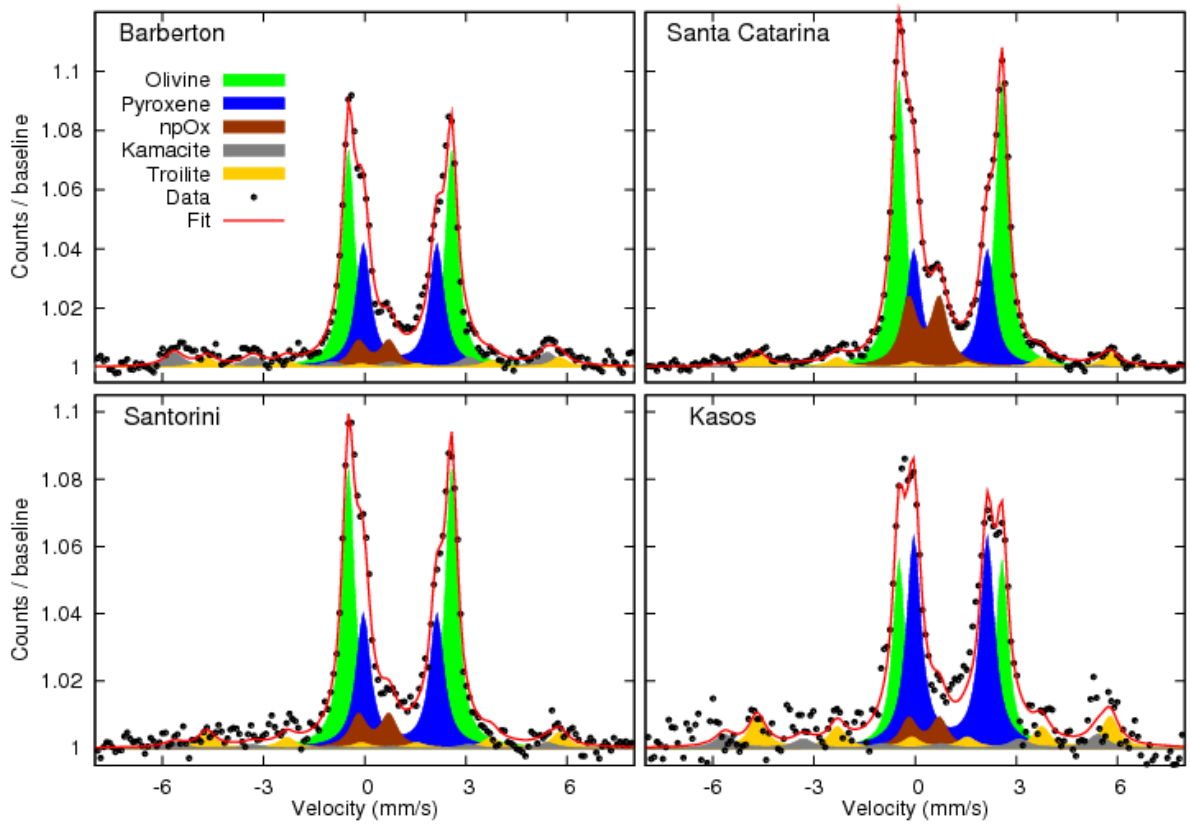

Figure 5.11: Barberton group spectra with components derived from a simultaneous fit of all spectra.

Table 5.3: Mössbauer parameters and subspectral areas for Barberton group cobbles.

Mineral Phase	δ[a] (mm/s)	ΔE_Q (mm/s)	B_{hf} (T)	Subspectral Area[b] (%)			
				Barberton	Santa Catarina	Santorini	Kasos
Olivine	1.16	3.06	-	48	52	53	32
Pyroxene	1.16	2.18	-	32	26	28	41
npOx[c]	0.37	0.91	-	6	14	8	8
Kamacite[d]	0.01	-0.03	34.3	11	1	2	5
Troilite[d]	0.75	-0.17	31.3	3	6	9	14

[a]The Mössbauer center shift δ is given relative to α-Iron.
[b]Uncertainties for subspectral areas for *Barberton*, *Santa Catarina* and *Santorini* are ±2 % (absolute) and ±4 % for *Kasos*.
[c]npOx: nanophase ferric oxide.
[d]Kamacite and Troilite parameters were constrained to values obtained from a specimen of the *Mundrabilla* meteorite measured at ~235 K.

5.2.3 Arkansas Group

Three cobbles were investigated close to Erebus crater (Figure 5.2). *Arkansas* (~5 cm) and *Perseverance* (~3 cm) were investigated between sols 551 and 554, and *Antistasi* (~5 cm) between sols 641 and 645. *JosephMcCoy* and *Haiwassee* (sol 886 - 890) are both small (<2 cm) cobbles encountered in the "Jesse Chisholm area", a dark mound close to Beagle crater (~1.5 km south of Erebus crater). *Tilos, Kos* and *Rhodes* were encountered ~1.5 km south of Victoria crater between sols 1880 and 1882, just a few meters from the Barberton group cobble *Kasos*. The small (~2 cm) cobble *Vail Beach* was investigated on sol 1974, ~4 km south-southwest of Victoria crater. In false- and true color Pancam images, Arkansas group cobbles appear dark (comparable to Barberton group cobbles) with irregular shapes. Microscopic images show nearly dust-free surfaces with heterogeneous textures. Two representative MI images obtained on *JosephMcCoy* and *Perseverance* are shown in Figure 5.12. Brighter and darker areas are clearly visible. Both cobbles appear to consist of large, subangular grains in a darker matrix [*Herkenhoff et al.*, 2008]. It is also possible that the brighter areas result from a discontinuous coating on their surfaces, rather than internal textural differences.

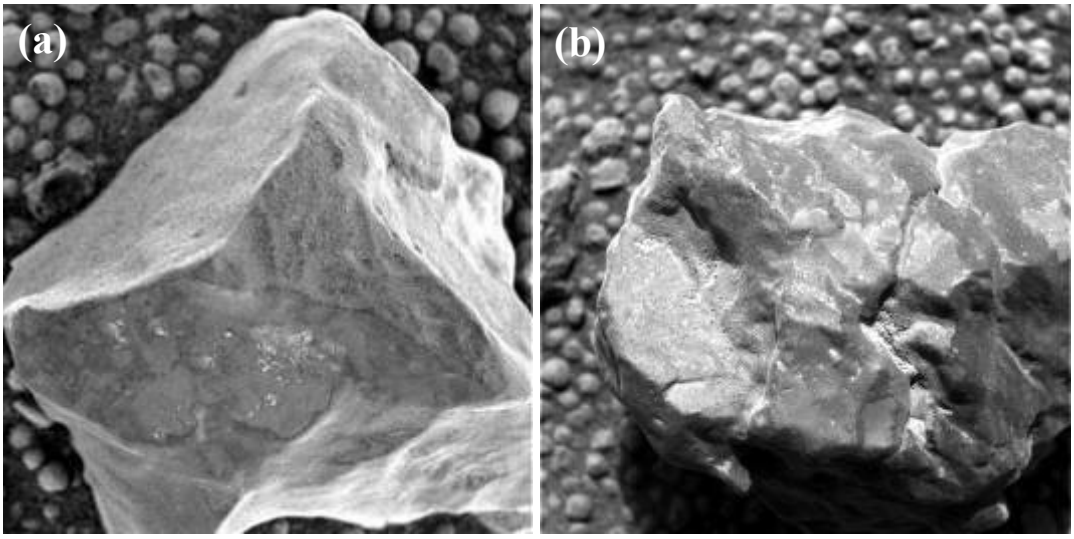

Figure 5.12: (a) MI mosaic obtained on *JosephMcCoy*. (b) Merge of 6 MI images of *Perseverance* acquired on sol 554. Area shown is ~3 cm². Both images show darker and brighter areas.

Compared to Barberton group cobbles, Arkansas group cobbles are generally high in Al, P, K, Ca and Ti; and low in Ni, Mg and Cr. The plots shown in Figure 5.5 and Figure 5.6 indicate that there is a close relationship between basaltic soils and the Arkansas group cobbles. Compared to outcrop and other cobbles, Ti and Al concentrations are high for soils and Arkansas group cobbles. Arkansas group cobbles have Ca and Al concentrations very similar to those of Meridiani soils; and the Ni and Mg contents are also in a similar range. The Mg/Si vs. Al/Si plot also emphasizes the similarity between soils and Arkansas group cobbles compared to outcrop rocks. SNC meteorites cover a wider range. The Ca-K plot shows that, in contrast to the SNCs, the incompatible element K is enriched in all soils, outcrops, and the Arkansas group cobbles. For P, some Arkansas group cobbles are more similar to those of outcrop rocks. This fact points to different P mobilities and thus to different formation processes of basaltic soil and cobbles. Outcrop rocks have high concentrations of Cl and S. For these two elements, cobbles generally plot close to the soil field. The *Arkansas* cobble is an exception; it is more similar to outcrop, likely because of a significant contribution from outcrop material. Cr concentrations of Arkansas group cobbles are intermediate between those of soils and outcrops.

The cobbles *Tilos*, *Kos* and *Rhodes* did not completely fill the APXS field of view, so that underlying outcrop or soil in the instrument field of view may have contributed to the elemental concentrations. However, with their comparably low concentrations of Ni, Cr, and Mg, these cobbles are clearly not specimens of the Barberton group. The comparably high concentrations of Al, P, K, Ca and Ti are characteristic for Arkansas group cobbles.
Mössbauer spectra were measured on *Arkansas*, *Antistasi*, and *JosephMcCoy*. The *Antistasi* and *JosephMcCoy* Mössbauer spectra are very similar to each other. The *Arkansas* spectrum has a larger ferric component and also shows similarities to typical Meridiani outcrop spectra, with the obvious exception that the hematite sextet signature is less pronounced in the *Arkansas* spectrum. A direct comparison of the spectra is shown in Figure 5.13a, along with contents of Iron-bearing minerals in the rocks shown in Figure 5.13b.
Satisfactory fits of all spectra were obtained by using a model with three ferrous doublets corresponding to the basaltic minerals olivine, pyroxene and ilmenite, one ferric doublet representing nanophase ferric oxide (npOx) and one sextet assigned to hematite. All three spectra, with phases derived from a simultaneous fit, are shown in Figure 5.14. Mössbauer parameters and subspectral areas are given in Table 5.4. Ilmenite parameters were fixed to values from [*Morris et al.*, 2006a], reported for ilmenite-bearing rocks encountered by the MER Spirit in Gusev crater. The hematite center shift was fixed to 0.37 mm/s because of the low subspectral area of hematite.
Olivine and pyroxene occur in all basaltic soils and most rocks at both landing sites; and dominate the spectra of *Antistasi* and *JosephMcCoy*. Ilmenite has previously not been reported at Meridiani. While the subspectral areas for ilmenite are within uncertainty of zero, the presence of ilmenite in Arkansas group cobbles is consistent with the Ti concentrations in these rocks (Figure 5.5). These are equivalent to Ti values determined for typical Martian basaltic soils, which contain titanomagnetite [*Morris et al.*, 2008]. A spectral signature consistent with titanomagnetite is not observed in spectra from Arkansas group cobbles. Hematite, a constituent of Meridiani outcrop, is clearly present in the *Arkansas* spectrum and potentially also in the *JosephMcCoy* spectrum, with poorer counting statistics. The quadrupole splitting of the ferric doublet from Arkansas group spectra is larger compared to npOx from soil and most other rocks from both MER landing sites [*Morris et al.*, 2006a, 2006b], and smaller compared to that of jarosite in Meridiani outcrop spectra. Similar Mössbauer parameters were derived for npOx from spectra obtained on rocks encountered by Opportunity's twin rover Spirit in the Columbia Hills [*Morris et al.*, 2006a, 2008]. The assignment of npOx therefore appears reasonable for the ferric doublet observed in Arkansas group spectra, although the history of both rock groups is entirely different. The large quadrupole splitting may also reflect a contribution from jarosite in addition to npOx. However, it is not possible to resolve two ferric doublets in a consistent way for all Arkansas group spectra. The general texture and dark color of all Arkansas group cobbles show that they are clearly not rocks dominated by unaltered outcrop fragments. The high S content measured in *Arkansas* suggests a relation to outcrop, such as the presence of small outcrop fragments in a darker matrix.
The differences of the npOx Mössbauer parameters between spectra from Arkansas group cobbles on the one hand, and spectra from soil or dust on the other hand exclude the possibility that the npOx signature stems from dust coatings on the cobble surface.

The Mössbauer spectra of Arkansas group cobbles show substantially greater variability than those of the other cobble groups. This variability may result in part from the cm-scale mineralogical heterogeneity in Arkansas group cobbles. The field of view of the APXS is ~2.5 cm in diameter, while that of the Mössbauer spectrometer is smaller (1.5 cm). The clear clast-in-matrix texture of these rocks, as seen in MI images (Figure 5.12), hints at significant cm-scale compositional heterogeneity. Both instruments may have incompletely sampled this heterogeneity and hence show significant sample-to-sample variability, where APXS spectra may be at least somewhat more representative of the true average composition.

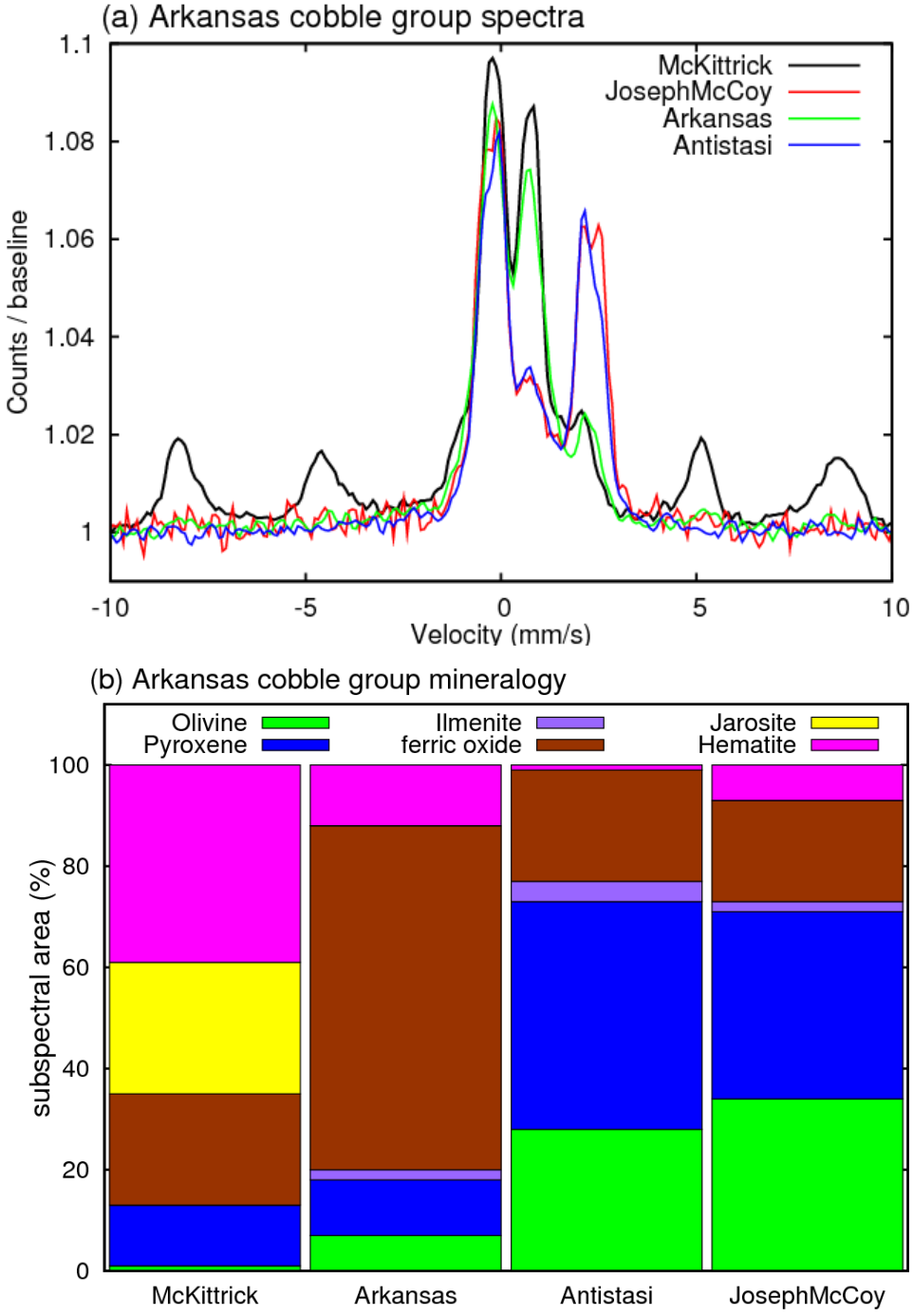

Figure 5.13: Arkansas group cobbles share Mössbauer spectral features with typical outcrop. Compared to other cobble groups, a greater diversity is observed among this group. "Ferric oxide" refers to npOx for cobbles and to Fe3D3 for outcrop.

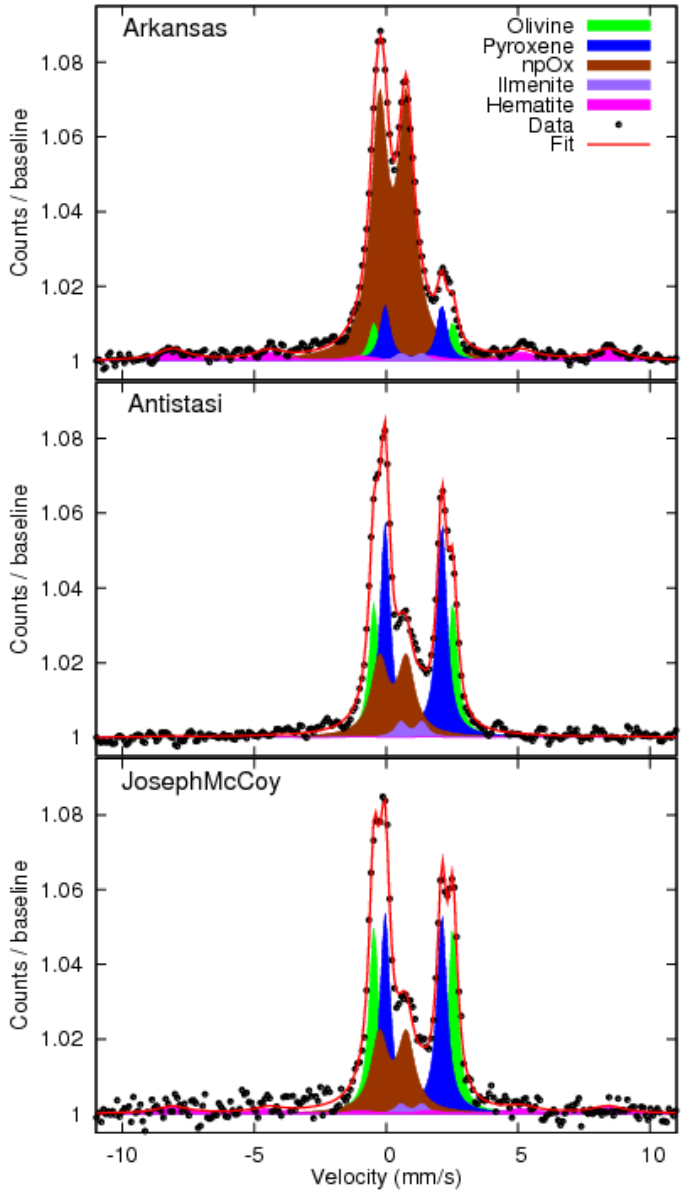

Figure 5.14: Mössbauer spectra for Arkansas group cobbles with components derived from a simultaneous fit of all spectra.

Table 5.4: Mössbauer parameters and subspectral areas for Arkansas group cobbles.

Mineral Phase	δ[a] (mm/s)	ΔE_Q (mm/s)	B_{hf} (T)	Subspectral Area[b] (%)		
				Arkansas	Antistasi	JosephMcCoy
Olivine	1.14	3.00	-	7	26	39
Pyroxene	1.15	2.15	-	11	48	34
npOx[c]	0.37	1.02	-	72	23	20
Ilmenite[d]	[1.07]	[0.80]	-	2	2	2
Hematite[d]	0.37	-0.18	51.2	8	0	5

[a]The Mössbauer center shift δ is given relative to α-Iron.
[b]Uncertainties for subspectral areas are ±2 % (absolute).
[c]npOx: nanophase ferric oxide.
[d]Mössbauer parameters for ilmenite and the center shift for hematite were held constant during the fits.

5.2.4 Classification based on Principal Component Analysis of APXS Data

Principal Component Analysis (PCA) of APXS data brings insight regarding the classification of the cobbles on the basis of their chemical compositions. Through a change of reference frame, from the initial basis of elemental abundances to the new basis of the Principal Components (PC), PCA allows the data to be plotted with fewer axes in the new PC space. This highlights the compositional variance in a way that is not necessarily apparent on simpler binary element-element or oxide variation diagrams. The approach is described in detail in [*Tréguier et al.*, 2008]. A PCA was performed using chemical compositions based on the 16 chemical elements usually measured by APXS [cf. Table 5.2], including all Meridiani outcrop rocks, soils (including spherule-rich targets) and 13 cobbles (including *Bounce Rock*). The cobbles *Tilos*, *Kos* and *Rhodes* were not plotted because of their small size and therefore unknown proportion of soil in the field of view.

In this analysis, all abundances were standardized to a mean of 0 and a standard deviation of 1 in order to place greater weight on relative variations in concentration rather than absolute values of abundance. The scatterplot in Figure 5.15 shows data in the plane of the two first principal components; this projection representing 54.5 % of total data variance.

This analysis clearly supports the interpretation of *Lion Stone* and *Russett* as outcrop fragments as they plot within the bulk of Meridiani abraded outcrop measurements. *Arkansas* and Perseverance appear compositionally similar to regular undisturbed outcrop, which represents a mixture of basaltic soil, dust and outcrop with surface coatings. The other Arkansas group cobbles seem to differ a bit from the bulk of outcrop samples. The three cobbles *Vail Beach*, *Haiwassee* and *JosephMcCoy* look compositionally close to each other, while *Antistasi* appears compositionally different from other Arkansas group cobbles. The spherule-rich target Berry Bowl plots close to Arkansas group cobbles, consistent with the detection of hematite in *Arkansas* and Joseph McCoy. Barberton group cobbles are all different from the rest of Meridiani samples (rocks or soils). *Santa Catarina*, *Kasos* and *Santorini* form a relatively compact cluster. The *Barberton* cobble is the smallest rock piece of the group and probably did not completely fill the field of view of the APXS instrument This is likely the reason that in all elemental plots (Figure 5.5 and Figure 5.6) *Barberton* is closer to soils than other Barberton group cobbles. This could indicate that *Barberton* is a mixture of *Santa Catarina*-like material with some amount of soil. A subtraction of a soil component as was done by *Schröder et al.* [2008] moves *Barberton* towards the other three cobbles of that group in PC space. Three cobbles of the Arkansas Group have a diameter of less than 2 cm, while the field of view of the APXS is 2.5 cm. These three, *JosephMcCoy*, *Haiwassee*, and *Vail Beach*, fall clearly in the field of the soils in the scatterplot (Figure 5.15) pointing to a contribution of the underlying soil to the APXS analysis. *Antistasi*, which is somewhat larger (6 cm in diameter), seems to have a soil contribution, too. Results from PCA of APXS data support the interpretations and cobble classification based on Mössbauer mineralogical data and APXS elemental weight ratios.

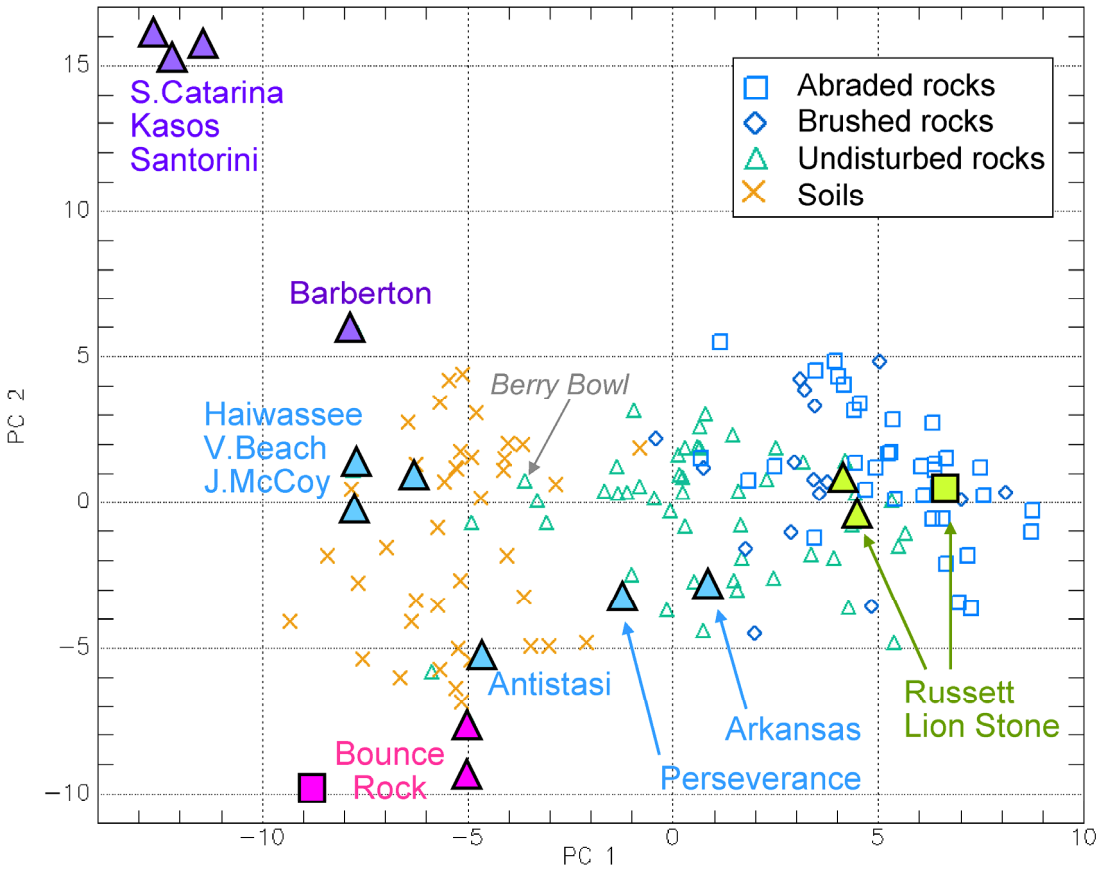

Figure 5.15: Scatterplot of the data points in the plane of the first two principal axes of the PCA performed for chemical compositions of Meridiani samples. Cobbles and *Bounce Rock* are indicated with larger symbols. The spherule-rich target "Berry Bowl" was also labeled as a reference point. Triangles are undisturbed and squares are abraded samples. (Figure provided by E. Tréguier).

5.3 Possible Origins of Barberton and Arkansas Group Cobbles

Cobbles have been observed along Opportunity's traverse since Eagle crater. Cobbles that appear related based on Mössbauer-determined mineralogy and APXS-determined composition are separated by several kilometers. Cobbles appear more concentrated near impact craters and in some cases, a direct connection between dark cobbles and craters can also be inferred [*Golombek et al.*, 2010a; 2010b]. Several options for cobble origins have been identified by *Jolliff et al.* [2006]. Cobbles may be:

(1) Fragments of meteorites.
(2) Fragments of ejecta from impacts elsewhere on Mars delivered to the local region, many of which may have formed secondary craters.
(3) Locally derived ejecta from outcrop rocks.
(4) Resistant material eroded from the sulfate-rich outcrop, e.g., rinds and fracture fillings.
(5) Erosional remnants of a layer that once lay above the presently exposed outcrops.
(6) Erosional remnants of a deeper layer within the underlying but local stratigraphy, brought to the surface as impact ejecta.
(7) Impact melts of the outcrop lithology or a mixture of the outcrop lithology and underlying strata.

The clear enrichment of Ni in all Barberton group cobbles along with the detection of kamacite and troilite and the clast-in-matrix-texture suggests a meteoritic origin of this cobble group (option 1). The overall chemistry and mineralogy is consistent with a mesosiderite silicate clast composition, as discussed in more detail by *Schröder et al.* [2008, 2009]. Compared to other meteorites, mesosiderites are uncommon, at least on Earth, where they make up <1 % of observed falls. This supports the idea that the Barberton group cobbles have a common source.
The similarity in composition of Barberton group cobbles raises the possibility that they are derived from a single impactor that dispersed fragments over a 7 km area. Their compositional relations make it unlikely that they were delivered to the Martian surface in several impact events [*Schröder et al.,* 2010b]. A delivery as secondary impact ejecta to its current location (option 2) is very plausible for the boulder *Bounce Rock*, which is of Martian origin (similar to SNC meteorites) and clearly not related to the site or other cobbles [*Zipfel et al.*, 2010]. A similar scenario appears likely for *Marquette Island* [*Mittlefehldt et al*., 2010]. *Russett* and *Lion Stone* are interpreted to be derived from local outcrop and distinctly different from any other cobbles (option 3).
The origin of the Arkansas group cobbles is more difficult to determine. Most meteorite types contain kamacite and/or troilite, and typically have enrichments in Ni over planetary crustal materials. The compositions of Arkansas group cobbles show strong similarities to rocks and especially soils at Meridiani Planum (Figure 5.5 and Figure 5.6). Therefore, we can confidently eliminate a meteoritic origin for this group. The compositional similarities of Arkansas group cobbles to locally derived materials also suggests that they are not ejecta from an area on Mars with distinctly different geology (origin 2). Their compositions do not match those of outcrop interiors (Figure 5.5 and Figure 5.6), eliminating origin 3.
Material eroded from the outcrop (origin 4) includes rinds, fracture fillings and fins (probable erosional remnants of some type of fracture filling). One such target, a protruding fin of rock (*Dorsal_Fin*), was measured in Victoria crater and was found to be similar to outcrop material, but with a substantial hematite content (~50 % Mössbauer subspectral area), a clear difference from any of the Arkansas group cobbles. Material eroded from outcrop would be expected to accumulate preferentially in association with outcrop exposures, which is not consistent with the observed cobble clustering close to

craters. Also, all rinds and fracture fills that were observed in situ have a distinctive planar geometry, inconsistent with the shapes of Arkansas group cobbles. Similarly, remnants of a resistant layer that once lay above the presently exposed outcrop would be expected to be more evenly and commonly distributed across the plains.

Remnants of a deeper layer brought to the surface by an impact would be expected to be more abundant across the plains. They should also be concentrated near craters large enough to excavate such a layer. This fits with the observed cobble clusters close to impact craters. However, it would be expected to observe this layer deep in the crater's stratigraphy. A layer with different chemical, mineralogical or spectral properties than the outcrop has not been observed at any location along the 20 km rover traverse or at any impact crater investigated by Opportunity, including the two largest investigated craters Victoria and Endurance. This is not surprising; because even Victoria would have excavated only to a depth of ~200 m, and the layered sulfate-rich sediments in which it formed are substantially thicker than that [*Arvidson et al.,* 2003]. If the Arkansas group cobbles are ejecta from a deeper layer, the crater from which they were excavated must be at least tens of km from where Opportunity has traversed.

With their clast-in-matrix textures (Figure 5.12), Arkansas group cobbles appear consistent with being impact-derived breccias and/or melts. If the clast-in-matrix texture is a correct interpretation, then there is little differential weathering between clasts and matrix, suggesting similar hardness. Unlike outcrop rocks, spherules are not observed in the Arkansas group cobbles. Compositionally, these cobbles appear to be compositionally similar to soils or mixtures of soils and outcrop, as can be observed on all elemental plots (Figure 5.5 and Figure 5.6). It is unlikely that this observation is made only due to soil in the APXS field of view, since at least some cobbles are large enough to fill the instrument field of view completely. MI images indicate that their surfaces are not contaminated by dust or soil. Thus, the soil-like composition of the Arkansas group cobbles is that of the cobbles, not "contaminants" in the APXS FOV.

Arkansas group cobbles have Ni contents comparable to soil and outcrop (Figure 5.5). However, the two Arkansas group cobbles with the highest Ni content – *Antistasi* and *JosephMcCoy* (Table 5.2) – are distinct in composition from soils with similar Ni contents. The latter are all soils rich in hematite-bearing spherules, and have much higher Fe contents than *Antistasi* or *JosephMcCoy*.

The amounts of Ni in basaltic soils and Meridiani outcrop rocks were found to be consistent with a contribution of 1 % to 3 % chondritic input [*Yen et al.*, 2006]. An additional meteoritic component in Arkansas group cobbles from an impactor would lead to higher Ni contents (cf. Barberton group cobbles). Thus, most Arkansas group cobbles were formed from soil and/or outcrop with very little meteoritic component added during the impact that formed them. *Antistasi* and *JosephMcCoy* are possible exceptions; their higher Ni contents would allow for the addition of meteoritic material during impact melting.

Most Arkansas group cobbles have Cl and S contents comparable to soil, with higher values for the *Arkansas* cobble. *Arkansas* also has Mössbauer spectra with similarities to those of outcrop (Figure 5.13), and together with the high S and Cl in *Arkansas*, this suggests that this cobble was formed from a mixture of soil and outcrop. These results suggest that Arkansas group cobbles may represent mixtures of Meridiani outcrop and soil, consistent with impact melt, which is derived dominantly from the target material rather than the impactor [e.g., *French,* 1998]. Several authors have speculated about the presence of impact melt [e.g., *Jolliff et al.,* 2006; *Weitz et al*., 2006], which would be a possible explanation for the lustrous appearance of some cobble surfaces, and also the clasts observed, which exceed the grain sizes observed in soil. Finally, because the cobbles are generally very similar to soil in composition, soil must be the major component of the

cobbles. Melting during impact would be required to produce a coherent rock from loose soil.

Different cobble groups may or may not be related to each other and to observed craters. It is noteworthy that the three Arkansas group cobbles *Tilos*, *Kos* and *Rhodes* were found in close association with the Barberton group cobble *Kasos*. The physical proximity of cobble specimens belonging to different groups at this site suggests that there may indeed be a relationship between Barberton group and Arkansas group cobbles; for example, they could represent impactor fragments and impact-derived breccias from the same impact event. Cobbles from both groups may represent a lag of impact derived material (fragments and impact-melt breccias) that has accumulated through time [e.g., *Golombek et al*., 2006], owing to the fact that they are harder than the Meridiani outcrop rocks.

5.4 Conclusions

Cobbles were encountered along Opportunity's entire ~20 km traverse. On the basis of APXS elemental chemistry and Iron mineralogy from Mössbauer spectra, three different groups of cobbles are distinguished. The first group comprises bright cobbles, which are texturally similar to, and chemically and mineralogically indistinguishable from outcrop and thus identified as outcrop fragments. All other cobbles appear dark in true- and false-color Pancam images. The Barberton group cobbles have an ultramafic composition. Their unusually high Ni content and the presence of the Iron-bearing minerals troilite and kamacite implicate a meteoritic origin, and their overall chemistry and mineralogy is consistent with a mesosiderite silicate clast composition.

The Arkansas group cobbles appear to be related to Meridiani outcrop, with an additional basaltic – or basaltic soil – component. These cobbles have textures consistent with brecciation, pointing to an impact-related origin during which local bedrock and basaltic material from local soil were mixed (e.g., impact melt and/or breccia). The presence of many craters, some of them comparably young, is evidence for multiple impact events involved in the formation process of cobbles. Apparently, they invoke the same processes forming cobbles of similar composition as a result, independent of the composition of the impactor.

6 The Meridiani Planum Iron Meteorites

This chapter is partly based on the following publication:
I. Fleischer, C. Schröder, G. Klingelhöfer, J. Zipfel, R. V. Morris, J. W. Ashley, R. Gellert, S. Wehrheim and S. Ebert (2010), *New insights into the mineralogy of the Meridiani Planum Meteorite, Mars: Identification of kamacite, taenite, schreibersite, and Iron oxides.* Meteoritics and Planetary Science (submitted).

6.1 Introduction

Meteorites found on Earth are generally of interest for studies addressing their parent bodies or processes occurring in the (early) solar system. On Mars, meteorites can be regarded as artificial, highly sensitive probes of known character inserted into the surface environment. They contain metallic Iron and are thus highly susceptible to the presence of even trace amounts of water. In the dry Martian environment, they are preserved over large time scales. From their weathering state, information can be inferred about atmospheric and weathering conditions at their impact sites. Meteorites on Earth with practically identical compositions are available for laboratory studies. A detailed discussion of the scientific value of meteorites on the surface of Mars is given by *Ashley et al.* [2010b].
With a meteorite flux to the surface comparable or larger than on Earth, meteorites can be expected to accumulate in the preserving Martian environment at a larger rate than at any place on Earth [*Bland and Smith*, 2000]. Meteorites and meteorite candidates were encountered at both MER landing sites. Opportunity encountered four iron-nickel meteorites, three of which were investigated with the rover's instrument suite. Two potential iron-nickel meteorites were identified by Spirit, but these were not investigated with the contact instruments [*Ashley et al.*, 2010b].

6.2 Description of Meridiani Planum Iron Meteorites

On sol 350 (January 2005), almost one year after landing at Meridiani Planum, Opportunity investigated the heat shield that had been dropped during landing. Just a few meters from it, an intriguing rock with a pitted surface and a maximum dimension of ~30 cm was discovered. Informally named *Heat Shield Rock* [*Schröder et al.*, 2008], it is the first approved meteorite on the surface of Mars with the official name *Meridiani Planum* after the location of its find [*Connolly et al.*, 2006]. Here, it will be referred to as *Heat Shield Rock* to avoid confusion with the site. *Heat Shield Rock* appears relatively pristine, with minimal signs of alteration. Its surface is covered with cavities, which may be regmaglypts formed during the descent through the atmosphere.
Between July and October 2009, separated ~10 km from *Heat Shield Rock*, three other Iron meteorites were encountered less than 1 km from each other, informally named *Block Island*, *Shelter Island* and *Mackinac Island*. The four Iron meteorites are shown in Figure 6.1.
Block Island was first encountered on sol 1961 and target of an extensive investigation over a period of six weeks. With ~60 cm diameter along its longest axis and a calculated hemispherical mass of ~425 kg, it is the largest meteorite yet observed on Mars. A large part of its pitted surface (approximately three quarters) appears smooth and rounded. The remaining quarter of the exposed upper surface appears rougher. Within this rougher side, a large pit (~20 cm diameter) is present, rimmed by delicate metal structures. This pit may have formed by removal of a porphyritic inclusive mass and/or by a corrosive process. The meteorite surface is partly covered by a discontinuous coating. Sand and spherules are

present in hollows up to ~14 cm above the ground surface, indicating that one or several sand ripples migrated over the meteorite up to this height. Spherules, which are too large to saltate, were left behind [*Golombek et al.*, 2010a, 2010b].
Shelter Island was first encountered on sol 2022. With a size of ~50 cm by 20 cm, it likely has a mass close to ~120 kg. At least one inclusion or resistant mass is weathering out of the groundmass. *Shelter Island* appears more weathered than *Block Island*, with large scale excavations penetrating deep into its interior and large spires of metal. Other portions of the meteorite appear relatively fresh with smooth surfaces and hollows suggesting those portions were ablated by the atmosphere during entry and descent, and were subsequently protected from erosion. A discontinuous surface coating is also present on this meteorite. Most of the hollows on *Shelter Island* contain sand and spherules, including those near the top. One surface target was investigated with the APXS and MI instruments, but Mössbauer spectra were not obtained.

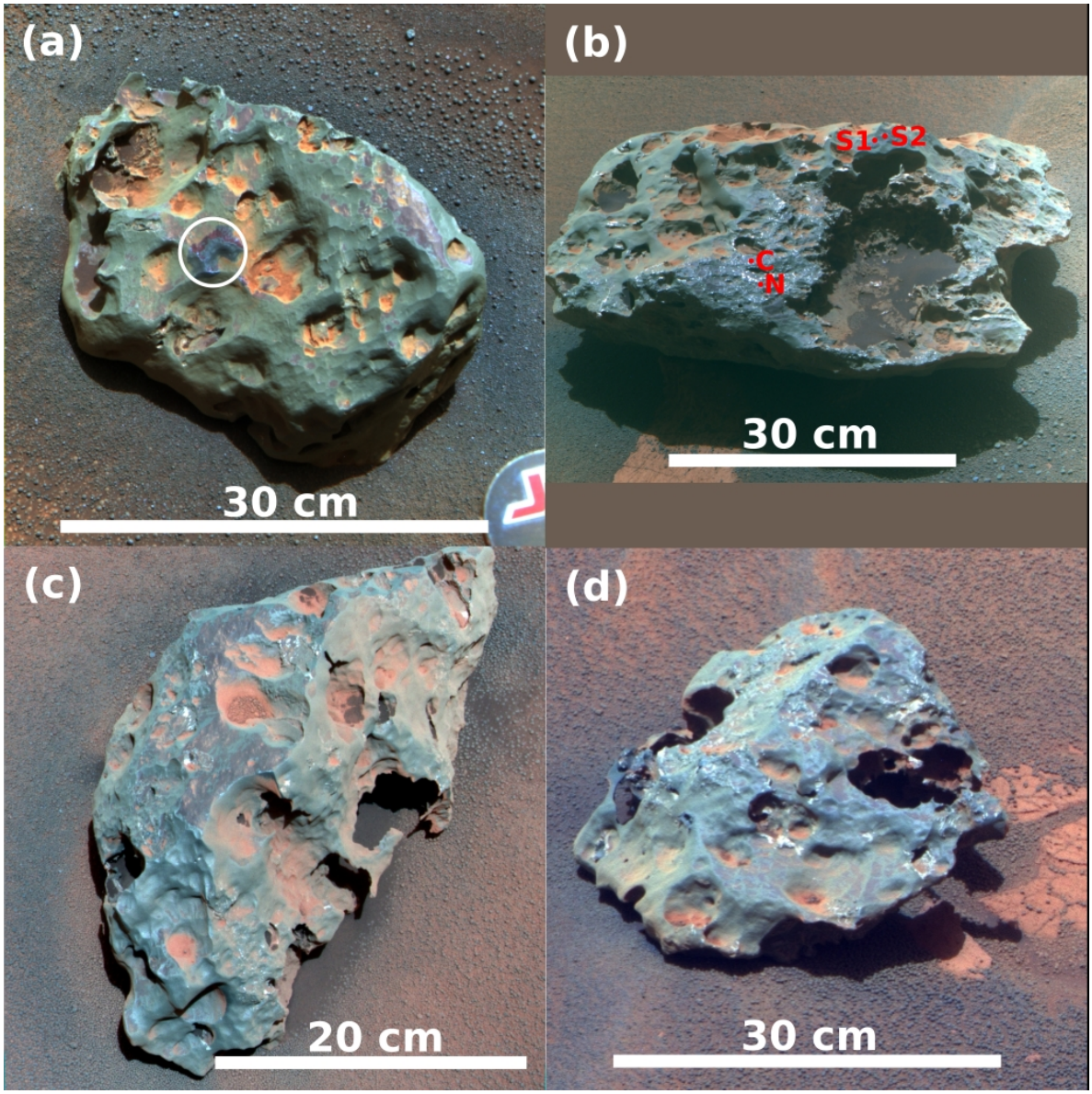

Figure 6.1: False color Pancam images of the four Meridiani Iron meteorite finds. (a) *Heat Shield Rock*, the brushed area is marked with a circle. (b) *Block Island* with a large surface pit, the four measured spots are indicated (N = *New Shoreham*, C = *Clayhead Swamp*, S1 = *Siah's Swamp*, S2 = *Siah's Swamp 2*). *Shelter Island* (c) and *Mackinac Island* (d) exhibit weathered hollows.

Mackinac Island was encountered on sol 2034, but not targeted with any IDD measurements. It is comparable to *Heat Shield Rock* in size (~30 cm across), but likely has a smaller mass due to severe mass removal. A metal lacework is all that remains of the former bulk mass in some regions. The surface of *Mackinac Island* is partly covered with rounded hollows partially filled with sand and spherules, suggesting it too was buried temporarily by one or more ripples.
The surfaces of all four meteorites show variable degrees of dust contamination. Discontinuous coatings were observed on *Heat Shield Rock*, and across much of the surface of *Block Island*. On *Shelter Island*, the coating appears somewhat more continuous in the target area than on *Block Island*.

6.3 Classification of Meridiani Planum Iron Meteorites

A detailed introduction to the classification of Iron meteorites is provided in several textbooks [e.g., *Hutchison,* 2004; *Davis,* 2005; *McFadden,* 2007]. Here, a brief overview will be given.
Iron meteorites represent material from differentiated parent bodies formed from melted precursors. During melting, high-density Iron sank to form pools or a core below the lower density parent magma. Most Iron meteorites consist mainly of lamellae of iron-rich kamacite (α-Fe-Ni with body-centered cubic structure, 0.2-50 mm thick) bound by thinner, Ni-rich taenite lamellae (γ-Fe-Ni with face-centered cubic structure). An interstitial mixture of taenite with kamacite (termed plessite) may also be present. The Ni concentration in the melt determines the crystallization temperature and this establishes kamacite orientation in the final meteorite. These orientations are revealed by etching of polished cut meteorite surfaces with nitric acid in alcohol, which preferentially affects the more susceptible kamacite. The etched structure is called “Widmanstätten pattern” after its discoverer. Meteorites containing <6 % Ni are called hexahedrites because they yield a hexahedral etch pattern of large, centimeter-thick kamacite lamellae. Iron meteorites with 6 – 16 % Ni crystallize in an octahedral pattern and are called octahedrites. Meteorites with a lower Ni content have the thickest kamacite lamellae (>3.3 mm) and yield the coarsest Widmanstätten pattern, while those highest in Ni are composed of very thin (<0.2 mm) kamacite lamellae and are very fine octahedrites. Iron meteorites containing >16 % Ni lack a Widmanstätten pattern and are called Ni-rich ataxites. Ni-poor ataxites are hexahedrites or octahedrites that were reheated in massive impacts or artificially. Iron meteorites can be further classified based on the contents of Ga and Ge. Both elements correlate with Ni (and thus the Widmanstätten pattern). Many Iron meteorites are derived from five parent bodies represented by five iron meteorite groups termed IAB, IIAB, IIIABCD, IVA and IVB.
Elemental compositions of the Meridiani finds were determined by APXS measurements for *Heat Shield Rock*, *Block Island* and *Shelter Island*. The chemical composition of all three of them is very similar, with ~93 % Fe, ~7 % Ni, ~400 ppm Ge and <200 ppm Ga [*R. Gellert*, personal communication]. The abundance of P was found to be elevated in the *New Shoreham* spot on *Block Island* compared to other investigated spots [*R. Gellert*, personal communication]. *Mackinac Island* was not investigated with either the APXS or MIMOS II. It is therefore unknown whether it has a composition similar to the other three Iron meteorites.
The Ni, Ge and Ga contents of *Heat Shield Rock, Block Island* and *Shelter Island* are nearly identical. As shown in Figure 6.2, they are similar to the range of compositions for IAB and IIICD Iron meteorites found on Earth, such as *Canyon Diablo* [*Wasson and Kallemeyn,* 2002; *Wasson,* 1970; *Scott and Wasson,* 1976; *Wasson and Ouyang,* 1990]. The IAB and IIICD groups form the IAB Iron meteorite complex [e.g., *Wasson and Kallemeyn,* 2002].

The IAB complex Iron meteorite group shows a wide range in compositions. With ~1 % of all meteorite falls on Earth, they make up a significant portion of all terrestrial Iron meteorite finds [*Wasson and Kallemeyn,* 2002].
Their similar compositions suggest that the Meridiani finds may be fragments from the same meteorite rather than separate falls. On the other hand, this would require fragmentation of the original meteorite in the thin Martian atmosphere, which appears quite unlikely [e.g., *Chappelow and Golombek,* 2010].

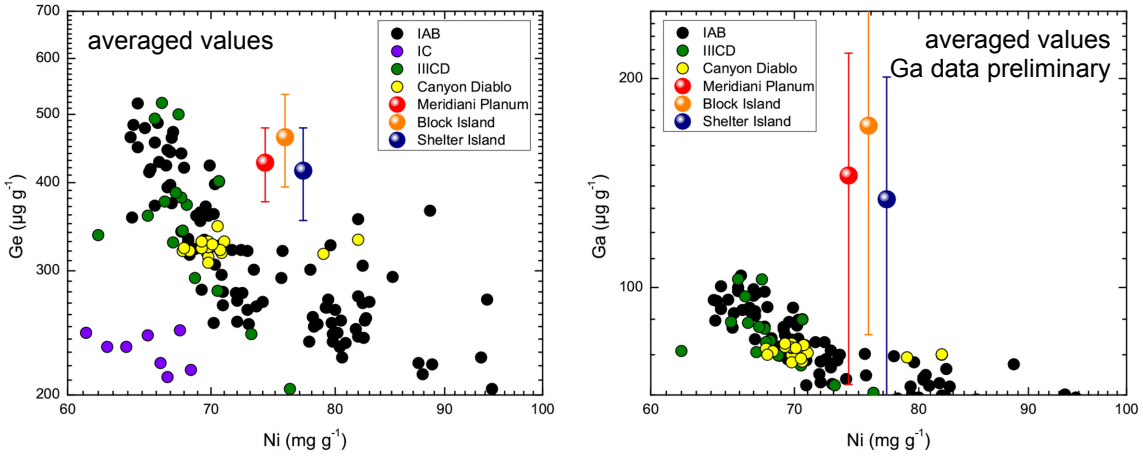

Figure 6.2: The compositions of three of the four Meridiani Iron meteorites are close to compositions form the IAB Iron meteorite complex, comprising the IAB and IIICD groups (Figure from [*Fleischer et al.*, 2010b], provided by D. Mittlefehldt).

6.4 Mössbauer Spectroscopic Analysis of Analogue Samples

For a detailed analysis of Mössbauer spectra from Meridiani Iron meteorites, knowledge of the Mössbauer parameters of candidate mineral phases is required, either from analogue measurements or from other studies. Five meteorite specimens, shown in Figure 6.3, were investigated as analogues. Representative spectra are shown in Figure 6.4, Mössbauer parameters for typical meteorite mineral phases are listed in Table 6.1.
A 10 cm by 5 cm disc of the *Mundrabilla* IAB-ungrouped octahedrite was measured at room temperature and over a range of low temperatures equivalent to the range on Mars. The chemical composition of the *Mundrabilla* metal phase was reported as 91.2 % Fe, 7.9 % Ni, 0.5 % Co, 0.3 % P, 67 ppm Ga and 173 ppm Ge [*Weinke,* 1977]. On average, taenite and plessite cover 15 – 20 % by area in *Mundrabilla* [*Buchwald,* 1975]. Three spots on the unetched specimen were measured separately, as indicated in Figure 6.3a, one on the metallic matrix, one on a troilite inclusion and one on a schreibersite-rich spot. The troilite and schreibersite spots did not fill the field of view completely, leading to contributions of kamacite or kamacite and troilite, respectively, in the spectra (Figure 6.4). 10 K-wide temperature windows in the range from 190 K to 300 K were evaluated separately for the metallic matrix and troilite. For schreibersite, room temperature data and the sum of spectra obtained in the range from 200 K to 240 K were analysed. Parameters from the temperature-dependent analysis are listed in Table A7 in the appendix.
A 4.5 cm by 4 cm disc of the *North Chile* IIAB hexahedrite, shown in Figure 6.3b, was measured at room temperature. It was not etched, shows one troilite inclusion (~5 mm diameter) close to one rim and a number of straight, thin inclusions and/or corrosion features. One rim is rugged with small metal ridges, between which it is covered with a brownish crust. Twelve North Chilean hexahedrites were found in a region 125 km wide and 400 km long. They have very similar concentrations of most elements, with Ni ranging from 5.27 % to 5.6 5%, Ga ranging from 57 ppm to 62 ppm and Ge ranging from 170 ppm to 190 ppm. Other elements, such as Re, Os and Ir, show larger variations, indicating that

the North Chilean hexahedrites originate from at least five separate falls [*Wasson and Goldstein,* 1967]. Four spots were measured, one on the metallic matrix, one on the inclusion and two on the rugged rim of the disc.

The 12 cm by 7 cm disc of the *Canyon Diablo* IAB octahedrite (Figure 6.3c) shows two large adjacent brownish inclusions (~20 mm and ~7 mm diameter) with bright rims with a metallic shine, as well as numerous small, elongated, bright inclusions. The surface also shows some signs of corrosion. The rim is covered by a dark red-brown crust. Five spots were measured at room temperature, three on the Widmanstätten pattern, one on the large inclusion, and one on a smaller inclusion, as indicated in Figure 6.3c. The *Canyon Diablo* impactor is associated with Barringer Meteor Crater in Arizona, USA. Its total mass of ~30 tons [e.g. *Vdovykin,* 1972] has been divided into numerous specimens. *Wasson and Ouyang,* [1990] analysed 15 specimens and measured Ni contents between 6.8 % and 7 %, Ge contents between 280 ppm and 360 ppm and Ga contents between 78 ppm and 85 ppm. *Vdovykin* [1972] reports a low abundance of taenite and plessite (up to 3 vol%) and abundances of up to 8 vol% for cohenite, 1 % for schreibersite and 2 % for troilite as the most abundant accessory minerals.

A 9 cm by 2 cm disc of the *Shisr043* IIIAB octahedrite shows some fine cracks, but no inclusions in the metallic matrix. The surface was not etched and bears lineations obviously stemming from cutting the sample, but kamacite lamellae are also faintly visible. The meteorite has a partially preserved fusion crust that is partly covered by a dark surface layer (Figure 6.3d). Five spots were measured at room temperature, three on the metallic matrix and two on the surface layer. The meteorite has a bulk Ni content of 8.1 %, a Ga content of 18.8 ppm and a Ge content of 36.2 ppm [*Al-Kathiri et al.*, 2006].

The 4.5 cm by 3 cm disc of the *Bear Creek* IIIAB octahedrite shows a well-defined Widmanstätten pattern with some inclusions with a metallic shine (Figure 6.3e). The rim of the sample is covered with a red-brown layer, apparently from corrosion. The metallic surface also shows some signs of corrosion. Three spots were measured on the metallic matrix, two on inclusions and two on the corroded rim. *Lovering et al.* [1956] report a Ni content of 10.14 %, a Ga content of 15 ppm and a Ge content of 25 ppm.

Subspectra corresponding to kamacite, troilite and cohenite were in all cases fitted with one sextet each. At some spots, an additional singlet was detected in spectra from the metallic matrix, corresponding to paramagnetic taenite (also referred to as "antitaenite" [e.g., *de Grave et al*., 1992; *Rancourt et al.*, 1999]. The identification of kamacite and magnetically ordered taenite is discussed in more detail in section 6.6.

Schreibersite has three crystallographic sites for metal atoms, and schreibersite spectra have been described with three sextets corresponding to these crystallographic sites [*Bailey and Duncan*, 1967; *Ouseph et al.*, 1979]. Although a detailed study of the magnetic structure of Fe_3P [*Lisher et al.,* 1974] revealed that the spectra can be fitted with up to six sextets (two for each site), a satisfactory fit of *Mundrabilla* schreibersite could be obtained with three sextets.

Iron oxides are detected in spectra from the corroded rims of the specimens in the form of a ferric doublet and a sextet with broad lines, reflecting that it likely represents a composite of several overlapping sextets with similar parameters which arise from different Iron oxides such as hematite (α-Fe_2O_3), maghemite (γ-Fe_2O_3) and potentially magnetite (Fe_3O_4). The sextet and the attributed magnetically ordered phases will be referred to as "magOx". The ferric doublet may be attributed to Iron oxides or oxyhydroxides with particle sizes in the nanometer range that are superparamagnetic at the temperature of observation (e.g. hematite, goethite (α-FeOOH), akaganéite (β–FeO(OH, Cl)) or lepidocrocite (γ-FeOOH)) and that are referred to as "npOx"[*Morris et al.*, 2006a]. Both spectral features are related to meteorite weathering, discussed in more detail in section 6.7.

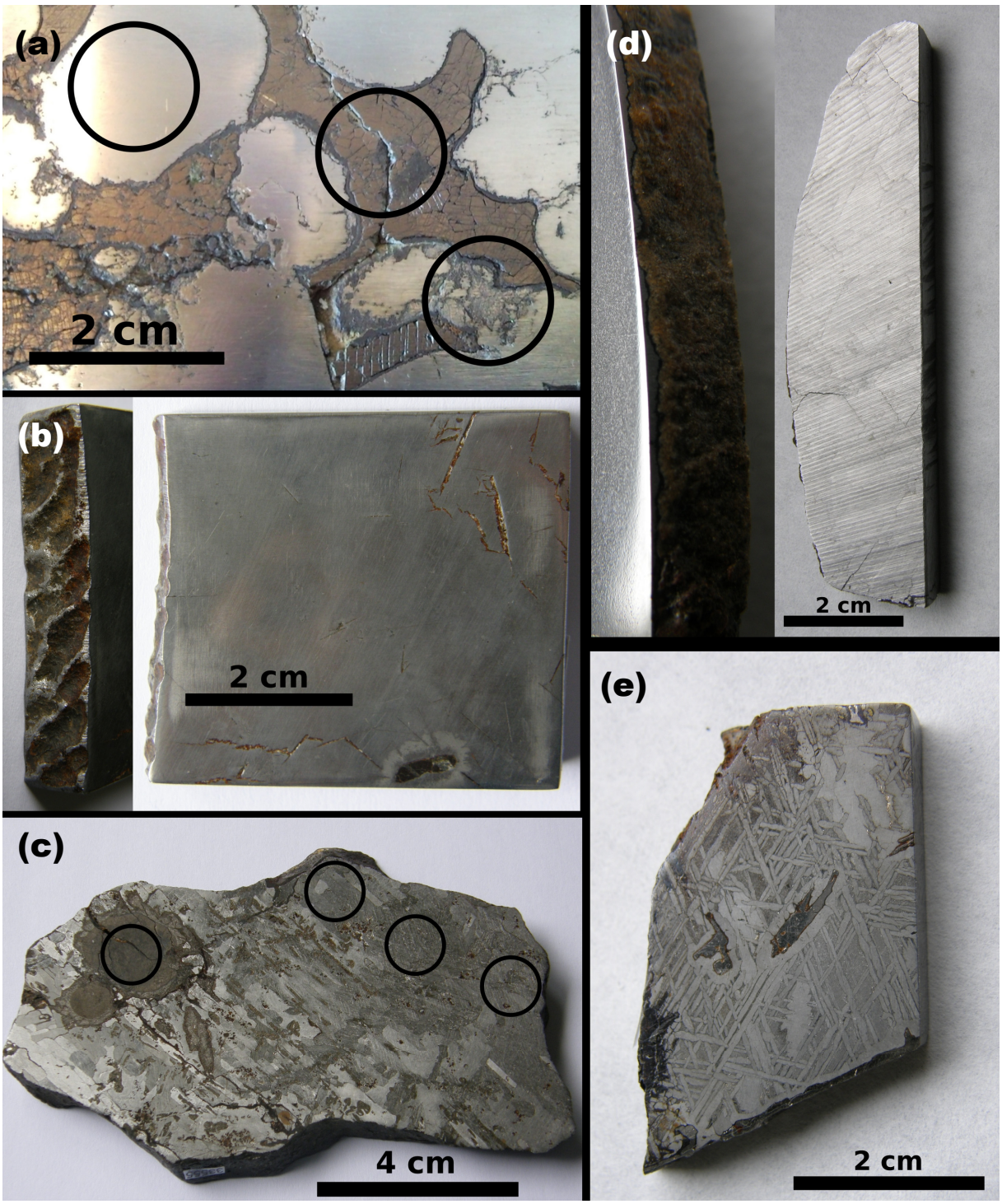

Figure 6.3: (a) Mundrabilla (not etched) with troilite and schreibersite inclusions. (b) North Chile, the inset (left) shows the corroded rim. (c) Canyon Diablo with larger troilite and numerous smaller inclusions, mainly troilite and cohenite. (d) Shisr043 with a part of the rim covered by fusion crust and weathering rind (inset). (e) Bear Creek with a clear Widmanstätten pattern and some inclusions. The circles are representative for the instrument field of view (~1.5 cm).

Table 6.1: Representative Mössbauer parameters from analogue measurements and other studies (relative to α-Iron; measured at room temperature unless indicated otherwise)

Mineral Phase	**δ** (mm/s)	**ΔE_Q** (mm/s)	**B_{hf}** (T)	**Meteorite**	**Reference**
Chalcopyrite $CuFeS_2$	~ 0.30	~ 0.08	~ 35		Stevens et al., 2002
Chromite $FeCr_2O_4$	2 or 3 doublets covering a range of parameters				Stevens et al., 2002
Cohenite $(Fe,Ni,Co)_3C$	0.20	0.65	21.0		Wojnarowska et al., 2008
	0.20	0	20.9		Ouseph et al., 1979
	0.22	0.03	20.7	Canyon Diablo	this work
Daubreelite $FeCr_2S_4$	0.71	0.14	19.4		Stevens et al., 2002
Kamacite	0.08	-0.05	33.1	Torino	Ortalli et al., 1990
	0.02	0	33.6	New Halfa	Abdu et al., 1997
	0.01	0.02	33.4	Abee (Enstatite)	Dunlap, 1997
	0.02	0	33.6	Morasko	Wojnarowska et al., 2008
	0.01	0	33.6	Canyon Diablo	this work
	0.02	0	34.4	Bear Creek	
	0.02	0	33.4	Shisr043	
	0.01	0.01	33.9	Mundrabilla (205 K)	
Mackinawite $(Fe,Ni)S_{0.9}$	0.91	0.09	29.8		Stevens et al., 2002
	0.85	0.06	26.2		
	0.88	0.09	22.8		
Pentlandite $(Fe,Ni)_9S_8$	~ 0.35	~ 0.35	-		Stevens et al., 2002
	~0.6	-	-		
magOx[a]	0.32	-0.2	48.6	Canyon Diablo	this work
	0.34	-0.1	49.7	Bear Creek	
npOx[b]	0.35	0.70	-	Shisr043	this work
	0.34	0.77	-	Bear Creek	
Schreibersite $(Fe,Ni)_3P$	0.29	0.02	24.4	Mundrabilla (200-230 K)	this work
	0.16	0.01	21.2		
	0.49	0.2	15.2		
Pyrrhotite $Fe_{1-x}S$	~0.7	~0.15	~30		Stevens et al., 2002
	~0.7	~0.15	~28		
	~0.7	~0.15	~25		
Taenite (paramagnetic)	-0.02	0	-	Santa Catharina (180 K)	de Grave et al., 1992
	-0.10	0	-	Santa Catharina (300 K)	
	-0.08	0	-	Morasko	Wojnarowska et al., 2008
	-0.17	0	-	Morasko	
	0.10	0	-	Canyon Diablo	this work
	0	0	-	Canyon Diablo	
Taenite (magnetically ordered)	-0.05	0.09	32.8	Torino	Ortalli et al., 1990
	0.12	0.12	30.3	New Halfa	Abdu et al., 1997
	0.01	0.02	31.1	Abee (Enstatite)	Dunlap, 1997
	0	0	31.0	Morasko	Wojnarowska et al., 2008
Troilite FeS	0.75	-0.16	31.7	Mundrabilla (205 K)	this work

[a]magnetically ordered iron oxides
[b]nanophase iron oxides
Uncertainties are ±0.02 mm/s for δ and ΔE_Q and ±0.2 T for B_{hf}.

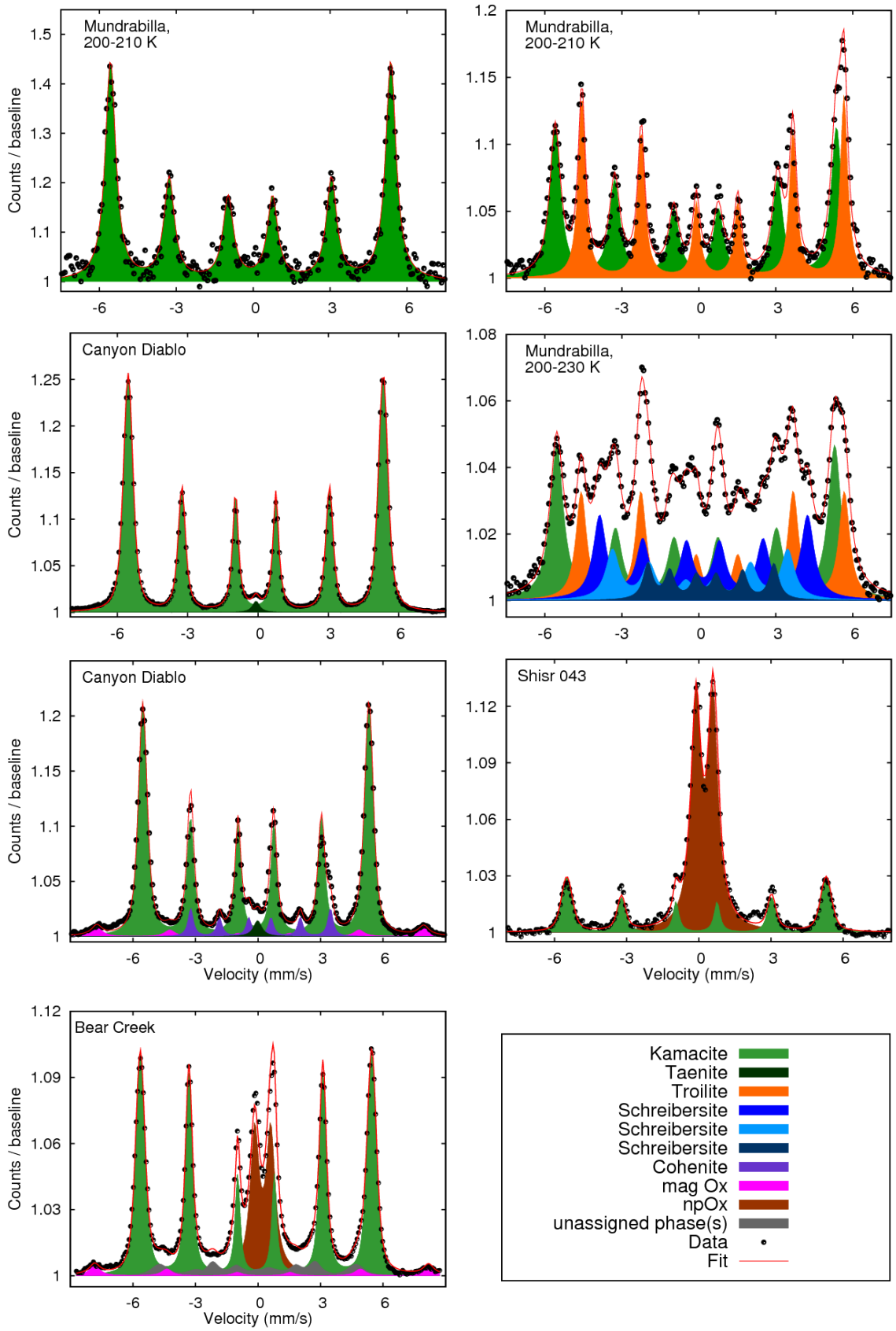

Figure 6.4: Example spectra obtained on analogue meteorite samples. a) Metallic matrix; *Mundrabilla*. b) Troilite and kamacite; *Mundrabilla*. c) Kamacite, troilite and schreibersite; *Mundrabilla*. d) Kamacite and paramagnetic taenite; *Canyon Diablo*. e) Kamacite, paramagnetic taenite, cohenite and ferric oxides; *Canyon Diablo*. f) corroded surface of *Shisr043* with kamacite and nanophase ferric oxide (npOx). g) corroded surface of *Bear Creek* with kamacite and ferric oxides.

6.5 Mössbauer Spectroscopic Analysis of Heat Shield Rock and Block Island

At Meridiani Planum, Mössbauer spectra were obtained on *Heat Shield Rock* and *Block Island*. Figure 6.5a shows Mössbauer spectra obtained on *Heat Shield Rock* and the two *Block Island* targets *New Shoreham* and *Siah's Swamp 2* in comparison. Integration times were limited due to mission constraints, so that the two *Block Island* spectra are not as well resolved as the *Heat Shield Rock* spectrum: more than 5 half lives of the Mössbauer source have passed between the measurements.
All spectra are dominated by a Mössbauer sextet corresponding to kamacite. The presence of other phases is clearly indicated in both *Block Island* spectra, and additional minor phases may be present with low abundances in the range of a few percent.

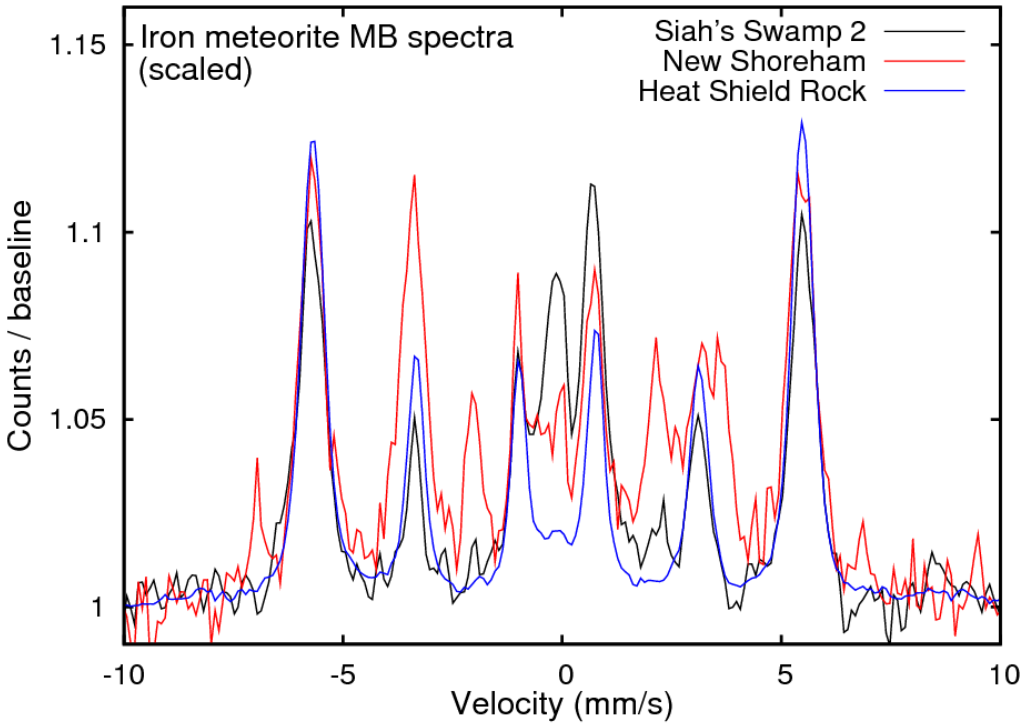

Figure 6.5: Comparison of spectra obtained on *Heat Shield Rock* and two spots on *Block Island*. The spectra are generally similar (*New Shoreham* and *Siah's Swamp 2*). Additional features are indicated for the *New Shoreham* spectrum. The *Heat Shield Rock* spectrum is better resolved because it was measured earlier in the mission with a higher source strength.

One spot on the surface of *Heat Shield Rock* was investigated before and after RAT-brushing. Mössbauer spectra were obtained in the temperature range between 200 K and 270 K. Spectra obtained on the undisturbed and brushed surface are practically identical. Four spots were measured on the undisturbed surface of *Block Island*, two spots each were located close to each other and measured from the same rover position, *New Shoreham* and *Clayhead Swamp* to the left of the surface pit; *Siah's Swamp* and *Siah's Swamp 2* right above the pit on an apparently coated spot, as indicated in Figure 6.1. On *Block Island*, all spectra were obtained over a similar temperature range (200-270 K for *New Shoreham*; 200-280 K for the other three spots). The collection of all spectra is shown in Figure 6.6. Mössbauer parameters are given in Table 6.2.
The two *Block Island* spectra from the adjacent spots *Siah's Swamp* and *Siah's Swamp 2* and the *Heat Shield Rock* spectra are very similar. Reasonable fits can be obtained with two phases; a sextet corresponding to kamacite and a ferric doublet which may be

attributed to Iron oxides or oxyhydroxides that are in a paramagnetic state over the measured temperature range and will be referred to as nanophase ferric oxide (npOx; e.g., nanocrystalline hematite (α-Fe_2O_3), maghemite (γ-Fe_2O_3), goethite (α-FeOOH), akaganéite (*β*–FeO(OH, Cl)) and/or lepidocrocite (γ-FeOOH)) [*Morris et al.*, 2006a; *van Cromphaut et al.*, 2007].

The npOx phase corresponds most likely to a discontinuous coating observed on both meteorites. Pancam false-color images (using 432 nm, 535 nm, and 753 nm filters) show intermittent patches of smooth material with purple hues. Pancam spectral features for this material are consistent with a more oxidized surface compared to uncoated meteorite surface spots. MI images indicate that the purple material coats the meteorite surface [*Johnson et al.*, 2010]. The spot *Siah's Swamp 2* was selected in particular because it had the largest amount of the "purple coating" for the field of view of the instruments. The Mössbauer spectrum shows the largest fraction of npOx with a subspectral area of 27 % (compared to less than 10 % for *Siah's Swamp* and *Heat Shield Rock*).

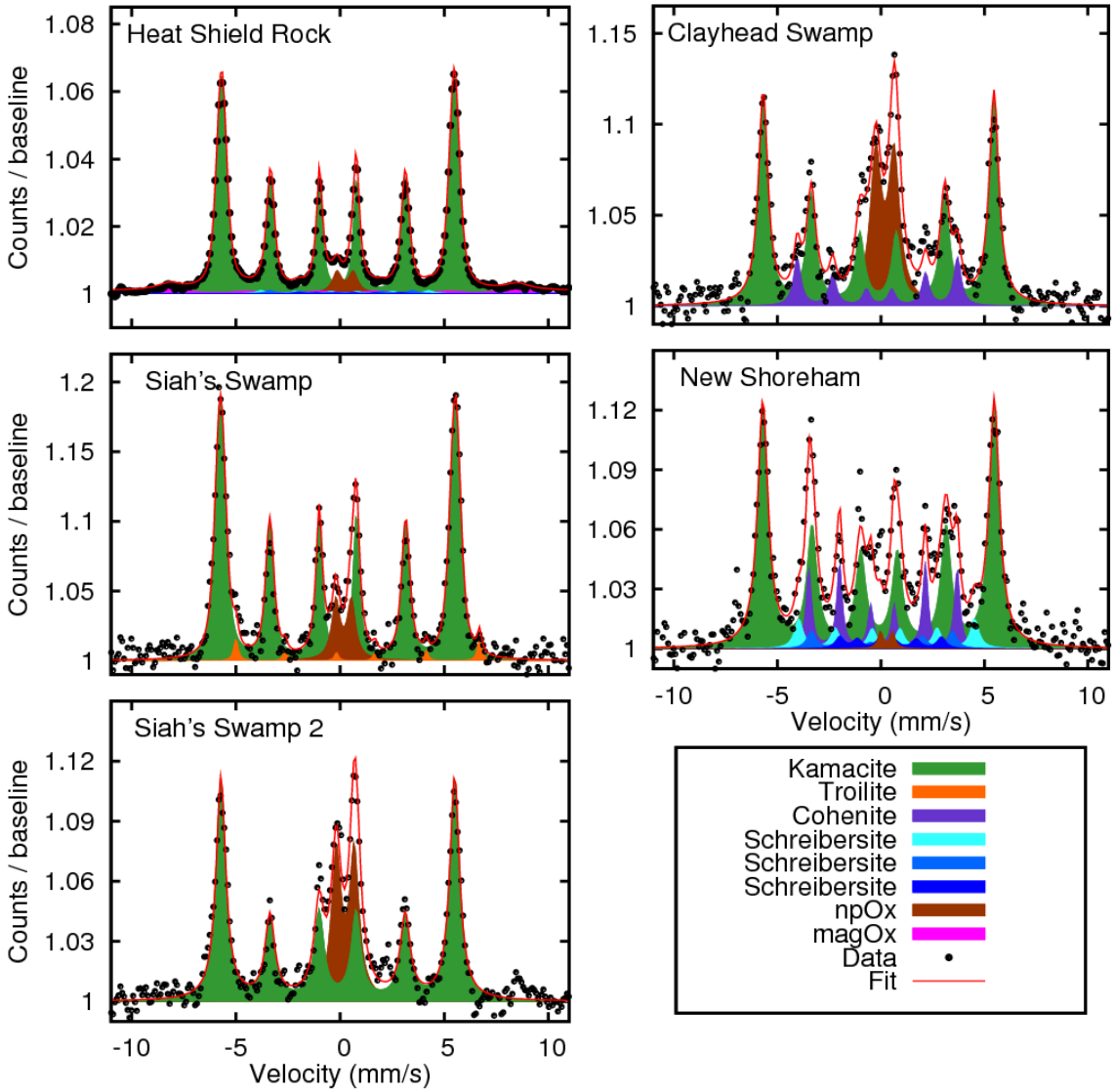

Figure 6.6: The collection of spectra obtained on the Meridiani finds *Heat Shield Rock* and *Block Island*. All spectra are dominated by a sextet corresponding to kamacite. The ferric doublet indicates surface weathering, likely related to a coating of varying thickness on the spots. Cohenite, schreibersite and a sulfide (potentially troilite) were detected in some spots.

The spectrum from *Siah's swamp* is also consistent with a minor amount (~2 %) of troilite (FeS) or a comparable sulfide, identified by its large center shift. Parameter deviations compared to analogue measurements are likely a consequence of the low signal-to-noise ratio of the spectrum. Additional spectral features are also indicated for spectra from *Heat Shield Rock*. Although just above the limit of background counts, they appear consistently in many single temperature window spectra and thus deserve further consideration. For the investigation of minor phases, sums of all available spectra from integrations on the undisturbed and brushed surface, respectively, were considered. Separate fits were performed with the sums of 6.4 keV spectra obtained on the undisturbed and on the brushed surface, respectively; with the sums of 14.4 keV spectra obtained on the undisturbed and on the brushed surface, respectively; and with the sum of all spectra obtained on the brushed surface (14.4 keV plus 6.4 keV), because minor features were most apparent in this case.

Table 6.2: Mössbauer parameters for Meridiani Planum Iron meteorites (temperature range 200 – 280 K)

Mineral Phase	**δ** (mm/s)	**ΔE_Q** (mm/s)	**B_{hf}** (T)	**Meteorite**
Kamacite (Fe,Ni)	0.01	0.02	34.6	Heat Shield Rock
	-0.01	0.02	34.6	Block Island Clayhead Swamp
	0.01	-0.01	34.7	Block Island New Shoreham
	0	0.01	34.9	Block Island Siah's Swamp
	0	0.01	34.8	Block Island Siah's Swamp 2
Cohenite $(Fe,Ni,Co)_3C$	-0.02	-0.08	24.0	Block Island Clayhead Swamp
	0.20	0.03	22.2	Block Island New Shoreham
Troilite FeS	0.91	0.12	36.2	Block Island Siah's Swamp
magOx	0.39	-0.2	51.7	Heat Shield Rock
npOx	0.39	0.81	-	Heat Shield Rock
	0.31	0.88	-	Block Island Clayhead Swamp
	0.36	0.86	-	Block Island Siah's Swamp 2
Uncertainties for Heat Shield Rock are ±0.02 mm/s for δ and ΔE_Q and ±0.2 T for B_{hf}. Uncertainties for Block Island are ±0.03 mm/s for δ and ΔE_Q and ±0.5 T for B_{hf}.				

The most pronounced minor features occur at ~ -8 mm/s and +8.5 mm/s, pointing to one or more sextets with rather large B_{hf}, which is characteristic for Iron oxides. A fit yields a sextet with broad lines, reflecting that it likely represents a composite of several overlapping sextets with similar parameters which arise from different Iron oxides such as hematite (α-Fe_2O_3), maghemite (γ-Fe_2O_3) and potentially magnetite (Fe_3O_4). As has been done for the analogue samples, the sextet and the attributed phases will be referred to as "magOx". The parameters of the sextet were obtained from the sum of all spectra obtained on the brushed surface and constrained to these values for all other fits. After adding the magOx sextet, unexplained features remain at -4 mm/s, -2 mm/s, +2 mm/s and +4.5 mm/s, indicative for one or more sextets with B_{hf} significantly smaller than that for any Iron oxide or oxyhydroxide. A number of other phases commonly found in Iron meteorites were considered to explain these remaining features, which are listed in Table 6.1. Based on their Mössbauer parameters, chromite and pentlandite can be excluded because their spectra are exclusively composed of doublet patterns. Chalcopyrite, Daubreelite, Mackinawite, pyrrhotite and troilite do not match the observed features because of their large isomer shifts δ and/or large magnetic hyperfine fields B_{hf}.

The cohenite parameters are in a suitable range, but do not match the exact position and shape of the spectral features. Only the schreibersite MB spectrum, composed of three

sextets, matches the additional spectral features with good consistency [*Wojnarowska et al.*, 2008, *Ouseph et al.*, 1979, *Stevens et al.*, 2002]. Because of the low intensity of the schreibersite lines in the Mössbauer spectrum of *Heat Shield Rock*, the parameters for the three schreibersite sextets were constrained to values obtained from low temperature (200 K - 240 K) measurements on the *Mundrabilla* specimen. For *Mundrabilla*, the schreibersite sextet with the largest splitting shows the largest subspectral area. For *Heat Shield Rock*, on the contrary, the intermediate schreibersite sextet shows the largest subspectral area. Its parameters are similar to those of cohenite (Table 6.1), which may indicate that cohenite is present in addition to schreibersite, but cannot be resolved separately. With Opportunity's APXS, a higher concentration of P, Cl and S relative to Martian soil was detected in *Heat Shield Rock* [*R..Gellert*, personal communication]. APXS spectra obtained on the undisturbed and brushed surface are very similar, suggesting that the enhanced concentrations of P, Cl and S do not stem from dust on the rock surface. Enrichment in P at least supports indications for the presence of schreibersite. Cl could be present in the nanophase ferric oxide, e.g. in the form of akaganéite. Troilite inclusions may have melted during the descent through the atmosphere, leading to the deposition of S on the surface [*Schröder et al.*, 2008]. With subspectral areas in the range of less than ~5 %, schreibersite and magOx are just above the limit of background counts. However, the spectra obtained on *Heat Shield Rock* are of good statistical quality due to the high Iron content of the meteorite. Thus, the line positions of minor spectral features can be compared between many single temperature windows. The spectra obtained on the undisturbed surface show the smallest subspectral areas of schreibersite (2 %) and magOx (3 – 5 %) compared to 3 – 4 % schreibersite and 6 – 7 % magOx for any other spectrum. Potential soil on the meteorite surface would have the greatest influence on the spectra obtained on the undisturbed surface, masking the spectral signatures from schreibersite and magOx.

The remaining two *Block Island* spectra are more complex. In addition to Fe-Ni-phases and npOx, the *Clayhead Swamp* spectrum shows indications for cohenite ($(Fe,Ni,Co)_3C$, ~12 %). Parameter deviations compared to analogue measurements may result from both the low statistical quality of the spectrum and from the presence of other phases (e.g., minor amounts of schreibersite) that cannot be resolved separately. A direct comparison of the *New Shoreham* and *Clayhead Swamp* spectra shows that the *New Shoreham* spectrum is even more complex. A fit is consistent with the presence of both cohenite and schreibersite (~16 % each). The presence of schreibersite would also be consistent with high phosphorous concentrations inferred from APXS spectra. The low statistical quality of the *Block Island* spectra does not allow the detection of any other phases, such as magnetically ordered Iron oxides.

For *Heat Shield Rock*, the good statistical quality of spectra from single temperature windows allows an extrapolation of kamacite B_{hf} values to room temperature (Figure 6.7) for a direct comparison to values from analogue samples. Low-temperature hyperfine parameters are compiled in Table A8 in the appendix. The extrapolation yields 33.7 T for the undisturbed as well as for the brushed surface, in good agreement with values from analogue measurements and other studies summarized in Table 6.1.

Laboratory measurements on meteorites are often carried out on polished meteorite slides. On the Meridiani Iron meteorites, however, the exposed surfaces were measured that have been affected by heating during the fall through the Martian atmosphere, followed by cooling and exposure to Martian weathering processes on the surface (further discussed in section 6.7). The fall of a meteorite through Earth's atmosphere may lead to the formation of a fusion crust [e.g., *El Goresy and Fechtig,* 1967] or surface layer through ablation and melting [e.g., *Maringer,* 1960]. *Buchwald* [1977] describes the occurrence of metastable α_2-Iron with a hatched kamacite structure in the heat affected surface zone of uncorroded Iron meteorites. This zone may affect the outer 2-4 mm of the meteorite surface [*Al-Kathiri*

et al., 2006]. The effect of the Martian atmosphere may be less significant, but the affected surface layer may well be in the range of the sampling depth of the Mössbauer radiation (~50 µm), providing a further explanation for differences between Mössbauer parameters from Meridiani Iron meteorites and analogue samples.

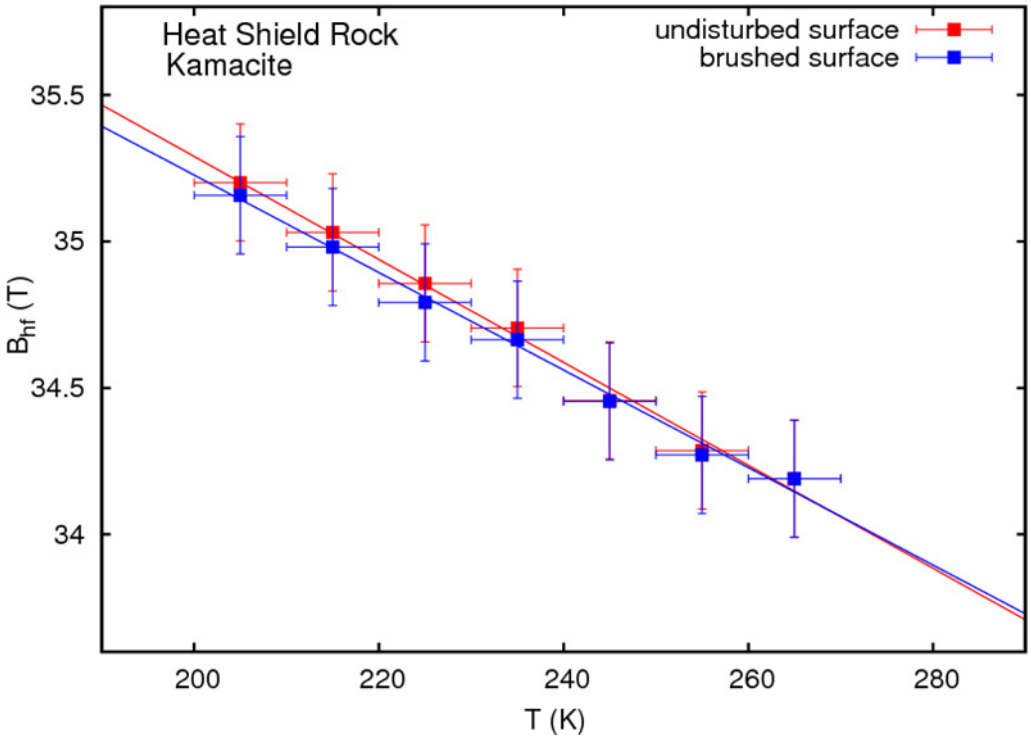

Figure 6.7: Temperature dependence of B_{hf} from kamacite from *Heat Shield Rock* for the undisturbed and brushed surface. Linear extrapolation yields a room temperature value of 33.7 T.

6.6 Kamacite and Taenite

The dominating metallic phase from all meteorite spectra discussed so far can be modeled with a single sextet attributed to kamacite, as has been done in sections 6.4 and 6.5. A single sextet, however, does not represent the spectral line shape very well, which may be a consequence of line broadening due to geometry- and thickness-effects (section 2.1.4) or due to the presence of taenite. As indicated in Table 6.1, Mössbauer parameters very similar to those of the kamacite sextet have been reported for magnetically ordered taenite [cf. *de Grave et al.*, 1992, *Abdu et al.*, 1997, *Dunlap*, 1997, *Ortalli et al.*, 1990, *Wojnarowska et al.*, 2008]. In all these studies, B_{hf} of taenite was found to be slightly smaller than B_{hf} of kamacite. With bulk Ni contents ranging from ~5.5 % (*North Chile*) to ~10 % (*Bear Creek*), the presence of both kamacite and taenite is strongly expected in the Meridiani Iron meteorites and analogue samples [e.g., based on the Fe-Ni phase diagram [*Reisener and Goldstein,* 2003]. Taenite contents have been reported to be rather low for *Canyon Diablo* (3 vol%, [*Vdovykin,* 1972]) and comparably high for *Mundrabilla* (15 – 20 % by area [*Buchwald,* 1975]). Clear evidence for the presence of taenite is the presence of a Widmanstätten pattern on the etched analogue samples from *Canyon Diablo* (Figure 6.3c) and *Bear Creek* (Figure 6.3e). Evidence for a Widmanstätten pattern on the Meridiani Iron meteorites is implied by differentially wind-eroded lamellae visible in microscopic images [*Ashley et al.,* 2010b].

The kamacite and taenite sextets cannot be directly resolved in spectra from the Meridiani Iron meteorites or analogue samples. To investigate possible line broadening due to the presence of taenite, 13 spots were measured on the metallic matrices of analogue samples;

three spots each on *Canyon Diablo*, *Bear Creek* and *Mundrabilla*, and two spots each on *North Chile* and *Shisr043*. For comparison, a stack of metallic α-Fe foils (with a total thickness of ~200 µm) was also measured with two different MIMOS II sensor heads. The Fe foil measurements allow studying of line broadening with just one phase involved, with a magnetic hyperfine field similar to that of meteoritic Fe-Ni phases (i.e., Fe foil and meteorite spectra are affected by line broadening in a similar manner). Line widths of these spectra were evaluated pair wise; lines 1 and 6, lines 2 and 5, and lines 3 and 4 were set to have equal widths and heights. The ratio of the widths of the outer two line pairs (lines 1 and 6 vs. lines 2 and 5) was calculated, the innermost line pair (lines 3 and 4) was neglected because it has a strong overlap with the npOx doublet and/or other phases for Meridiani Iron meteorites, which increases the uncertainty of determining line widths. Widths and width ratios are listed in Table 6.3.

Table 6.3: Widths and width ratios determined from Meridiani Iron meteorites, analogue samples and a stack of metallic α-Fe foils.

Sample	**Width (mm/s) lines 1 & 6**	**Width (mm/s) lines 2 & 5**	**Ratio**
Canyon Diablo	0.218	0.166	1.31
	0.221	0.163	1.36
	0.218	0.167	1.31
Bear Creek	0.239	0.186	1.29
	0.236	0.192	1.23
	0.237	0.188	1.26
Mundrabilla	0.244	0.193	1.26
	0.240	0.183	1.31
	0.238	0.183	1.30
North Chile	0.223	0.175	1.27
	0.223	0.177	1.26
Shisr043	0.225	0.171	1.32
	0.234	0.175	1.34
Fe foil	0.200	0.165	1.21
	0.197	0.161	1.22
HSR as is	0.275	0.209	1.32
HSR brushed	0.273	0.204	1.34
Block Island Siah's Swamp	0.291	0.197	1.48
Block Island Siah's Swamp 2	0.299	0.193	1.55
Uncertainties for line widths are ±0.02 mm/s.			

The width ratios cover the range from 1.21 to 1.55. The two measurements on Fe foils show the smallest width ratio. The largest width ratio is observed for *Block Island*, which may also be related to the low statistical quality of *Block Island* spectra. With one exception for *Bear Creek*, all meteorite width ratios are larger than 1.25. If taenite has a noteworthy influence on line broadening, large width ratios would be expected for those meteorites with considerable taenite or plessite contents (e.g., *Mundrabilla*), while the effect would be expected to be smaller for meteorites with low taenite or plessite contents (e.g., *Canyon Diablo*). However, the width ratios for both meteorites are in a similar range and even slightly larger for *Canyon Diablo*.

The larger line broadening observed in meteorite spectra is an indication that line broadening is not only related to geometry- and thickness- effects and likely reflects the more complex metallographic structure compared to Fe foil, but the presence of magnetically ordered taenite in addition to kamacite cannot be inferred from line

broadening. Paramagnetic taenite, characterized by a singlet (Table 6.1), cannot be detected in spectra of Meridiani Iron meteorites because it strongly overlaps with the npOx-doublet or because the statistical quality of the spectra does not allow to resolve a Mössbauer singlet.

6.7 Physical and Chemical Weathering

Among the four Meridiani Iron meteorites, *Heat Shield Rock* appears most pristine, with a smooth surface covered with small pits, likely regmaglypts formed by ablation during the descent through the atmosphere (Figure 6.1a). Portions of the other meteorites appear similarly fresh, but other surface features are suggestive of both physical and chemical weathering. The large pit on the surface of *Block Island* is rimmed by delicate metal spires, which are unlikely to have survived the meteorite's descent through the atmosphere. They are likely remnants of mass removal, potentially of a large inclusion [Figure 6.1b, Figure 6.8a and Figure 6.8b; *Ashley et al.*, 2010b]. Their formation and the associated mass removal may have involved aqueous and eolian processes.

Shelter Island and *Mackinac Island* show large hollows with metal spires, indicating extensive, probably eolian, erosion (Figure 6.1c, Figure 6.1d and Figure 6.8d). Hematite spherules and sand grains are residing in some of the lower hollows on *Block Island* and most of the hollows on *Shelter Island* and *Mackinac Island* (Figure 6.8a, Figure 6.8c and Figure 6.8d). Spherules are too large to saltate and their presence thus indicates that the meteorites were at least partially buried by migrating sand ripples. Therefore, the meteorites must have been present on the surface since before the last episode of ripple migration, i.e., more than 10^5 years ago, but they may also have landed much earlier [*Golombek et al.*, 2010a, 2010b; *Ashley et al.*, 2010b].

As described in sections 6.2 and 6.5, a discontinuous coating (purple-hued in false-color Pancam images; Figure 6.1) is present on all four meteorites. Mössbauer spectra and multi-filter Pancam spectra demonstrate that the coating contains Iron oxides and/or oxyhydroxides [section 6.5, *Johnson et al.*, 2010; *Ashley et al.*, 2010a, 2010b]. MI images obtained on the surface of *Block Island* show indications for differentially wind-eroded kamacite and taenite lamellae. Cross-cutting relationships between apparently wind-eroded features and the coating indicate that the coating has formed post-fall. It must then have formed by chemical weathering and is unlikely to be a fusion crust [*Ashley et al.*, 2010a]. The interpretation that the coating is not a fusion crust, but has rather formed through weathering is also supported by APXS measurements on the *Block Island* coating, which reveal elevated abundances of Mg and Zn relative to the uncoated surface [*R. Gellert*, personal communication]. A fusion crust would also be more similar in composition to the substrate.

The coating appears to be more continuous on *Shelter Island* than on any other Meridiani Iron meteorite, suggesting a more weathered state. Similarly, larger subspectral areas of npOx were detected in spectra from *Block Island* compared to *Heat Shield Rock*. Overall, this indicates a more weathered state for *Block Island*, consistent with the presence of the large surface pit.

Iron oxides and oxyhydroxides, particularly maghemite, occur as weathering products on Iron meteorites found on Earth [*White et al.*, 1967, *Bender Koch and Buchwald*, 1994; *Morris et al.*, 2000a; *Al-Kathiri et al.*, 2006]. Spectra obtained on the corroded rims of analogue samples exhibit spectral features comparable to those observed for Meridiani Iron meteorites: a sextet characteristic for Iron oxides and a doublet characteristic for paramagnetic Iron oxides and/or oxyhydroxides, as shown in Figure 6.4 and Figure 6.6. The spectral similarities are also another indication that the coatings on Meridiani Iron meteorites are a result of chemical weathering rather than remnant fusion crusts.

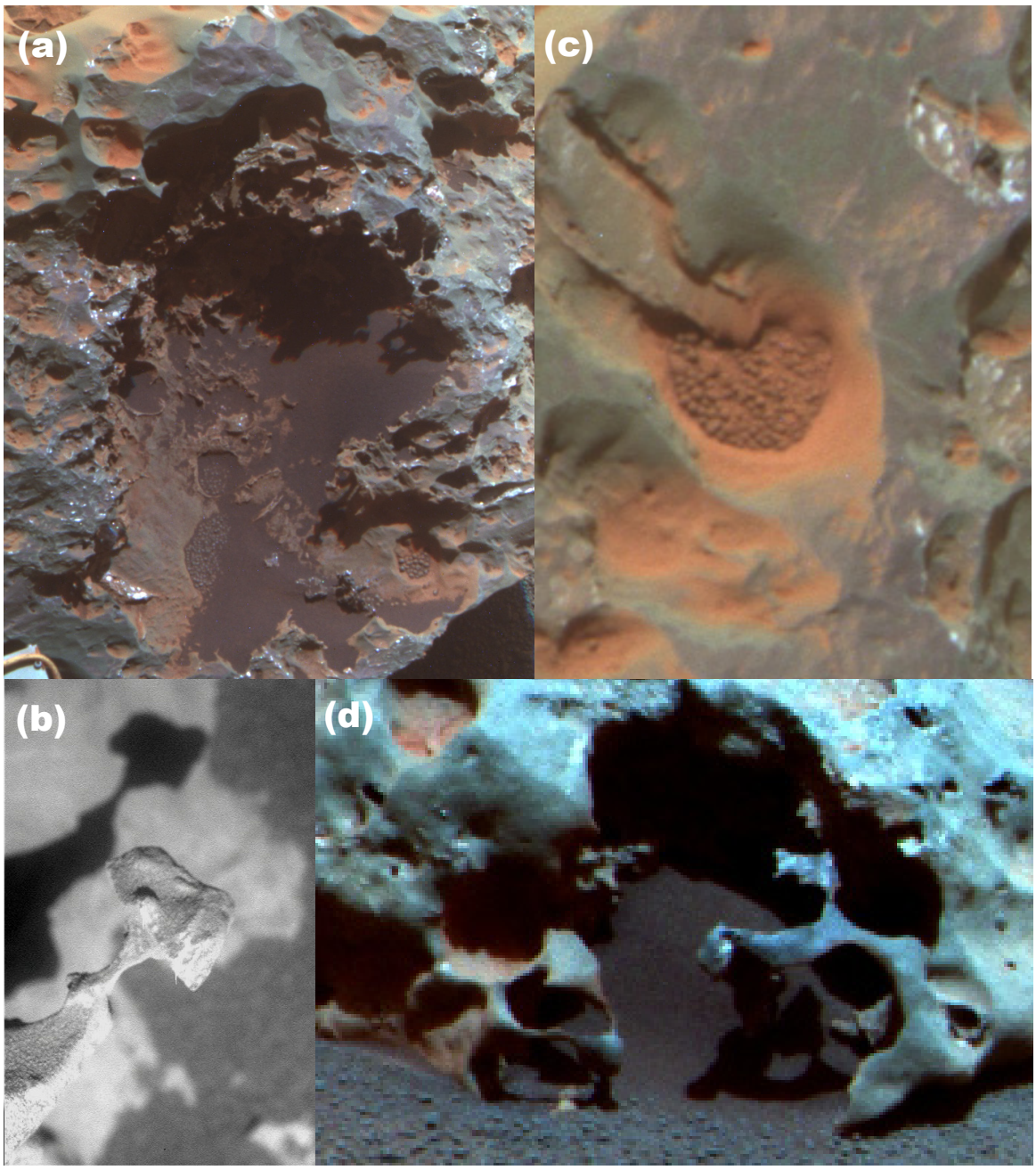

Figure 6.8: (a) Close-up of the pit on *Block Island* surrounded by metal spires and partly filled with spherules and sand. The "purple coating" is visible above the pit. (b) MI image of a metal spire from the pit on *Block Island*. (c) Spherules residing in a hollow on top of *Shelter Island*. (d) Hollow with large metal spires in *Mackinac Island*.

The high quality of *Heat Shield Rock* spectra allows for a separate analysis of both 14.4 keV and 6.4 keV spectra to estimate the thickness of the "purple coating" from a simulation of both spectra, as described in section 3. Both the 14.4 keV and 6.4 keV post-brush spectra have very similar subspectral areas; 5 % for npOx and 6 % (14.4 keV) or 8 % (6.4 keV) for magOx (the complete set of subspectral areas is given in Table A9 in the appendix). These similar numbers suggest that the coating must be thin compared to the ~50 µm penetration depths of both radiations. Iron oxides and oxyhydroxides are possible candidates for the observed npOx doublet, so that a composition of 50 % np-Fe_2O_3 and 50 % np-FeOOH is assumed. Pure Fe_2O_3 is assumed for the phase characterized by the sextet. This assumption is one of many possibilities. The thickness of the layer depends only slightly on the exact composition; it would be well in the range of possibilities that the

layer consists purely of Fe_2O_3. The simulations suggest an average thickness of less than 1 µm. The coating may be thicker if non-Iron-bearing phases are present. It has to be taken into account that the field of view contained coated and uncoated portions of the surface, thus reducing the effect of the surface layer on the spectra. The presence of an oxyhydroxide would strongly suggest interaction with water at some time in the surface or near-surface exposure history of the rock, be it as liquid water, frost or gas. A purely oxidic layer may have formed through interaction with atmospheric O_2, but oxidation through the presence of water appears at least as plausible.
Overall, a low degree of chemical weathering is indicated for the Meridiani Iron meteorites by the presence of thin, discontinuous oxide-bearing coatings. Larger parts of the meteorites, especially *Shelter Island* and *Mackinac Island*, are affected by physical weathering that led to the formation of sand-blasted hollows and metal spires (e.g., Figure 6.8c and Figure 6.8d). Different degrees of (physical) weathering argue against a possible pairing of the four Meridiani Iron meteorites [*Ashley et al.*, 2010a, 2010b; *Schröder et al.*, 2010b].

6.8 Conclusions

Three of the four Iron meteorites encountered by Opportunity at Meridiani Planum have very similar elemental compositions; the composition of the fourth is unknown. Mössbauer spectra obtained on *Heat Shield Rock* and *Block Island* were interpreted based on measurements on five analogue meteorite specimens and found to be dominated by kamacite with minor contributions from schreibersite and cohenite. Taenite is expected to be present based on their Ni contents, but cannot be distinguished from kamacite. A low degree of chemical weathering is indicated by the presence of nanophase ferric oxide and magnetically ordered Iron oxides (hematite, maghemite and potentially magnetite) attributed to a discontinuous coating detected on the meteorites. Simulations of *Heat Shield Rock* spectra suggest a thickness of less than 1 µm. Thicker coatings with similar spectral signatures are also present on the corroded surfaces of analogue meteorite specimens. Based on the amounts of ferric oxide detected in Mössbauer spectra, *Block Island* appears to be more weathered than *Heat Shield Rock*, in agreement with the large pit on *Block Island* that is surrounded by metal spires and most likely originated from physical weathering. Hollows and metal spires are also present on *Shelter Island* and *Mackinac Island* and thus indicate a more weathered state than for *Heat Shield Rock*.

7 Analogue in-situ studies at Rio Tinto, Spain

This chapter is partly based on the following publication: I. Fleischer, G. Klingelhöfer, F. Rull, S. Wehrheim, S. Ebert, M. Panthöfer, M. Blumers, D. Schmanke, J. Maul and C. Schröder (2010), *In-situ Mössbauer Spectroscopy with MIMOS II at Rio Tinto, Spain.* Journal of Physics: Conference Series 217, 012062.

7.1 Introduction

The Rio Tinto rises in the core of the Iberian Pyrite Belt and reaches the Atlantic Ocean at Huelva after its ~100 km long course (Figure 7.1). The Iberian Pyritic belt is of hydrothermal origin, one of the biggest sulfide deposits in the world, 250 km long and between 25 km and 70 km wide [e.g. *Leistel et al.*, 1998]. The Rio Tinto basin can be divided into three environmental domains on the basis of geological and geochemical characteristics. The northern region is dominated by highlands up to ~600 m above sea level and water with a low pH of ~2.3. Ferric Iron is maintained in solution in the acidic waters, causing the dark red color of the river (shown in Figure 7.2) and serving as a buffer on the pH [e.g., *Fernandez-Remolar et al.*, 2003]. The geological substrate includes greywackes, shales and hydrothermally influenced volcanic materials. Three acidic springs downhill from the *Pena the Hierro* mine pit crater are apparently the source of the Rio Tinto. The transitional region is characterized by a weak marine influence, the pH value increases downstream to values higher than 3. Its position depends on seasonal changes and the tidal regimen. This area has a lower altitude (less than 100 m) and a smooth relief, with the substrate varying from shales to sandstones and carbonates. In the estuary region, the Rio Tinto merges with the Odiel river and experiences a strong marine influence. The river becomes less acidic (pH ~5) and oversaturated with oxyhydroxides, which precipitate [e.g., *Fernandez-Remolar et al.*, 2003, 2004, 2005].

The sulfide ores of the Rio Tinto basin have been exploited for several thousand years and mining for gold, zinc and copper continues today. The acidic waters were believed to have originated from acid mine drainage. However, a natural origin for the region's unusual mineralogy, clearly predating human activity, has been confirmed from the existence of at least three Iron oxide bearing terraces, up to 60 m above the current water level and up to 20 km away from the river [e.g., *Fernandez-Remolar et al.*, 2004, 2005].

The high concentrations of ferric Iron and sulfate in the Rio Tinto water are products of the biooxidation of pyrite by an underground chemolithotrophic bacterial community using sulfide minerals as an energy source [e.g., *Fernandez-Remolar et al.*, 2005; *Amils et al.*, 2007]. Sulfate minerals form through aqueous alteration of iron-rich sulfide minerals and precipitate in sediments in the acidic water and as evaporite salts close to the water margin.

The occurrence of sulfate minerals makes the Rio Tinto basin an analogue site for Meridiani Planum, where the sulfate mineral jarosite ($(K,Na)Fe^{3+}_3(SO_4)_2(OH)_6$) was detected with Opportunity's Mössbauer spectrometer [e.g., *Klingelhöfer et al.*, 2004; *Morris et al.*, 2006]. The identification of sulfates and in particular jarosite provides clear mineralogical evidence for past water activity and acidic conditions at Meridiani Planum. Rio Tinto provides a setting where the occurrence and formation of sulfates and associated minerals can be investigated in situ.

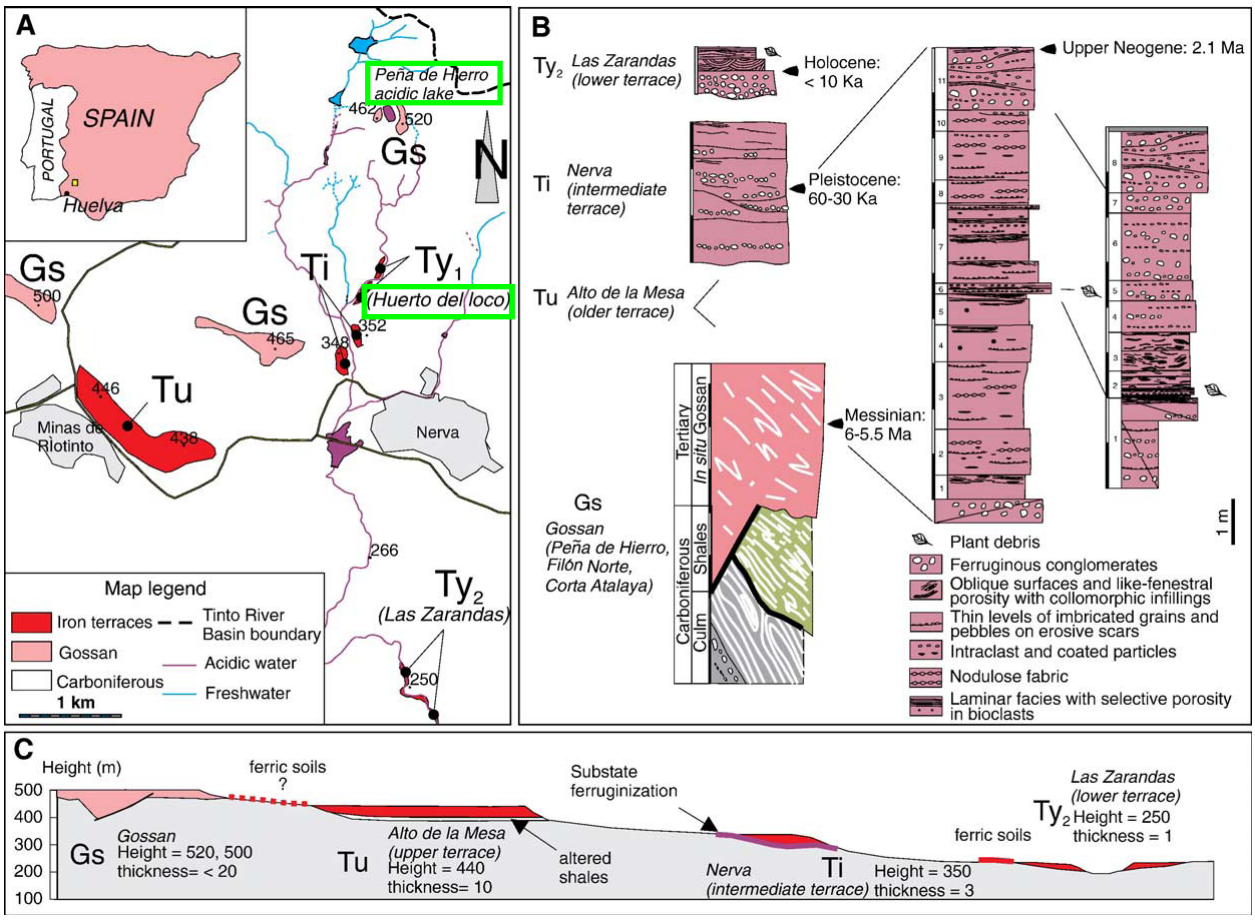

Figure 7.1: Rio Tinto geologic setting. The two field campaign sites *Pena de Hierro* and *Huerto del Loco* are marked green (from *Fernandez-Remolar et al.*, 2005).

Figure 7.2: The Rio Tinto water exhibits a dark red color. Image obtained at the *Huerto del Loco* site, June 2008.

7.2 Campaign Overview and Instrumentation

In the course of the two field campaigns in June 2008 and September 2009, five different sampling sites were studied with the aim of investigating the Rio Tinto rock sequence, including primary volcanic rocks, different stages of weathering due to hydrothermal transformation and evaporite minerals as the direct product of the acidic water evaporation mediated by acidophilic bacterial activity. The sampling sites include *Huerto del Loco* and *Pena de Hierro* (marked green in Figure 7.1) as well as the Rio Tinto source and *Anabel's Garden*, both located downhill from *Pena de Hierro*. *Dique de la Pena* is located a few kilometers from the river. Micro-Raman and Mössbauer spectroscopy are among the instrumentation available or under development for in-situ analyses on the Martian surface. Both instruments can be mounted on the robotic arm of a rover, constituting the contact-analytical forefront for surface mineral analysis. On a Mars mission, the combination of these techniques will provide definitive mineralogical and chemical identification of a great number of surface minerals and in particular of sulfates on Mars. The capabilities of both instruments in combination were investigated by in situ analyses performed during both field campaigns. In situ measurements were performed on evaporative precipitates and bedrock, Raman and Mössbauer spectra were taken on spots in close proximity to each other. For the in situ Mössbauer setup, two MIMOS II sensor heads were equipped with ^{57}Co-sources (~30 mCi intensity). Spectra of good quality were obtained within less than two hours and at ambient temperatures of ~35 °C. Raman spectra were obtained in-situ with a portable i-Raman from B&W TEC Inc., adapted to work under field conditions. The optical head was positioned in front of the samples using a mechanical device which allows mapping the surface at near the mineral grain scale. A baffle was used to minimize the solar light background. The excitation used was a 532 nm wavelength laser with ~15 mW power on the sample and a spot diameter of 100 µm. Spectral resolution was 5 cm^{-1}. In situ XRD and XRF measurements were recorded with the CheMin instrument, part of the payload of the Mars Science Laboratory mission scheduled for launch in 2011 (http://mslscicorner.jpl.nasa.gov/Instruments/CheMin).

In addition to the in-situ measurements, representative samples from all sampling sites were analysed in detail after the field trip with the laboratory instrument setups. In support of laboratory Mössbauer analyses, XRD measurements were recorded on finely ground samples using a Bruker AXS D8 Advance diffractometer with Mo Kα radiation and a SolX energy-dispersive detector in Bragg-Brentano mode. Phase analysis was performed using the program Bruker AXS EVA 10.0, based on the PDF-2 data base.

A representative data set will be discussed in the following sections, with a special focus on the Mössbauer data set. Detailed descriptions of results from Raman and CheMin investigations are given elsewhere [e.g., *Sobron et al.*, 2008; *Rull et al.*, 2009a; *Rull et al.*, 2009b; 2010]. Mössbauer parameters and uncertainties are listed in Table A10 in the appendix for representative Rio Tinto samples.

7.3 Primary Volcanic Rocks

Outcrops of primary volcanic rocks were investigated a few kilometers from the river, at *Dique de la Pena*. These show signs of weathering on the surface and, due to water circulation, along minor cracks. Spectra were obtained on a drill core, which included surface material and a crack. Raman measurements reveal the silicate phases quartz (SiO_2) and muscovite ($KAl_2(Si_3Al)O_{10}(OH,F)_2$), which do not contain Iron and are therefore not detectable in Mössbauer spectra. Because of the apparently low Iron content of these rocks, integration times had to be extended to several days per measurement. Mössbauer spectra show a ferrous doublet, a ferric doublet and a sextet (Figure 7.3). The ferrous doublet, with a center shift (δ) of 1.14 mm/s and a quadrupole splitting (ΔE_Q) of 2.73 mm/s can be attributed to chlorite crystals in the sample. The sextet, with δ = 0.37 mm/s, a magnetic hyperfine field (B_{hf}) of 51.5 T and a quadrupole disturbance (ΔE_Q) of -0.2 mm/s, is characteristic hematite. The ferric doublet, with δ = 0.36 mm/s and ΔE_Q = 0.69 mm/s, can be attributed to superparamagnetic occurrences of both hematite and goethite. The presence of both phases is confirmed by Raman measurements. Hematite and goethite are present in larger amounts in the red colored sample parts apparently affected by weathering.

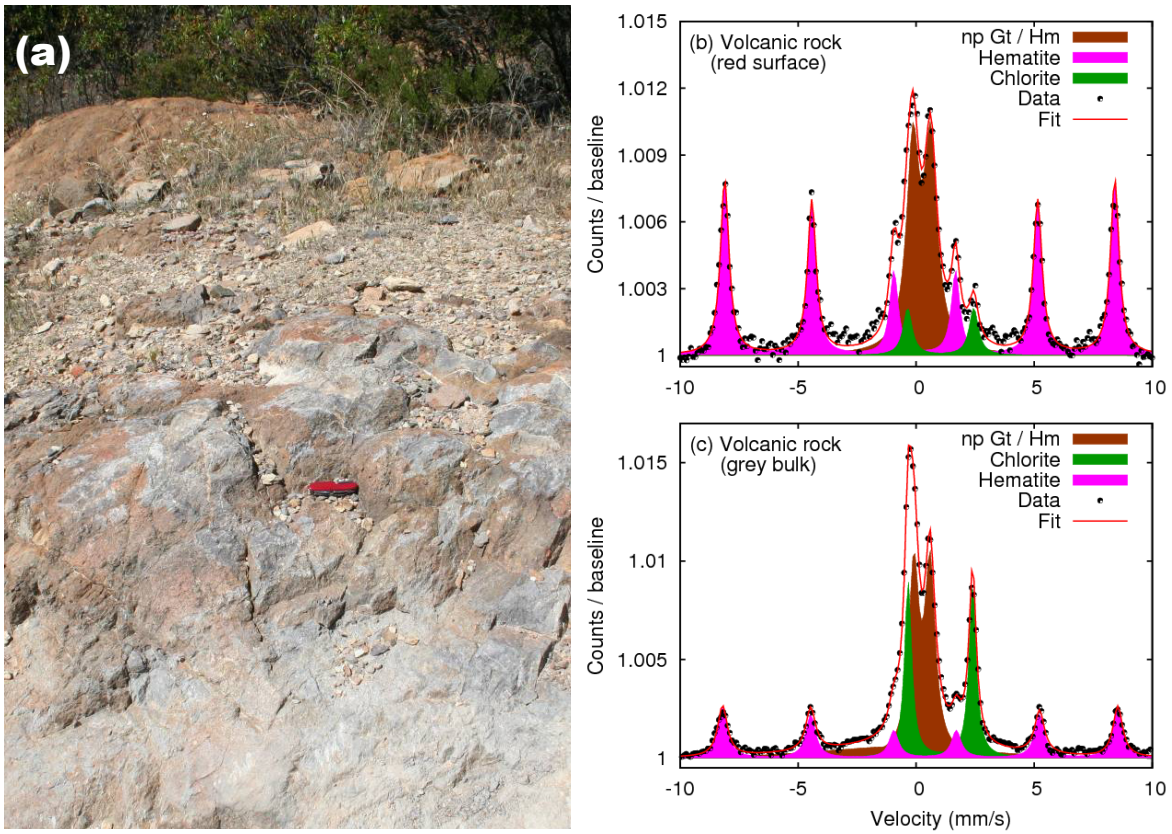

Figure 7.3: (a) Outcrop of primary volcanic rocks at *Dique de la Pena* (knife for scale). (b) Hematite and goethite were detected, particularly in red colored spots. (c) Chlorite was detected in the grey colored parts of the rocks.

7.4 Gossan Rocks

Porous volcanosedimentary materials originally constituted the rock complex at the *Pena de Hierro* site (Figure 7.1) before they were affected by hydrothermal fluids, forming rocks rich in quartz, other silicates and pyrite. Acidic weathering driven by microbial activity then led to the replacement of the sulfide ore body by gossan [e.g., *Leistel et al.*, 1998]. The resulting rocks contain black, hard material intermixed with softer material colored in shades of red and yellow (Figure 7.5). Hematite is detected in all spectra, with average Mössbauer parameters δ = 0.37 mm/s, ΔE_Q = -0.21 mm/s and B_{hf} = 50.7 T. Some samples contain hematite with different degrees of crystallinity, characterized by two separate sextets, where well-crystalline hematite shows a larger magnetic hyperfine field and smaller line widths. In almost all spectra, hematite is detected in association with both crystalline goethite characterized by Mössbauer sextets with a distribution of magnetic hyperfine fields ranging from ~26 T to ~38 T and superparamagnetic Iron oxides characterized by a ferric doublet with average δ = 0.37 mm/s and average ΔE_Q = 0.64 mm/s. Representative spectra are shown in Figure 7.5. XRD analyses confirm the presence of goethite and hematite in these samples instead of other superparamagnetic phases which would be consistent with the Mössbauer parameters (Figure 7.4).
The presence of hematite with different degrees of crystallinity and goethite were confirmed by Raman analyses. In addition to iron-bearing minerals, epsomite ($Mg(SO_4)\cdot 7(H_2O)$) and quartz were detected through Raman and XRD measurements, respectively.

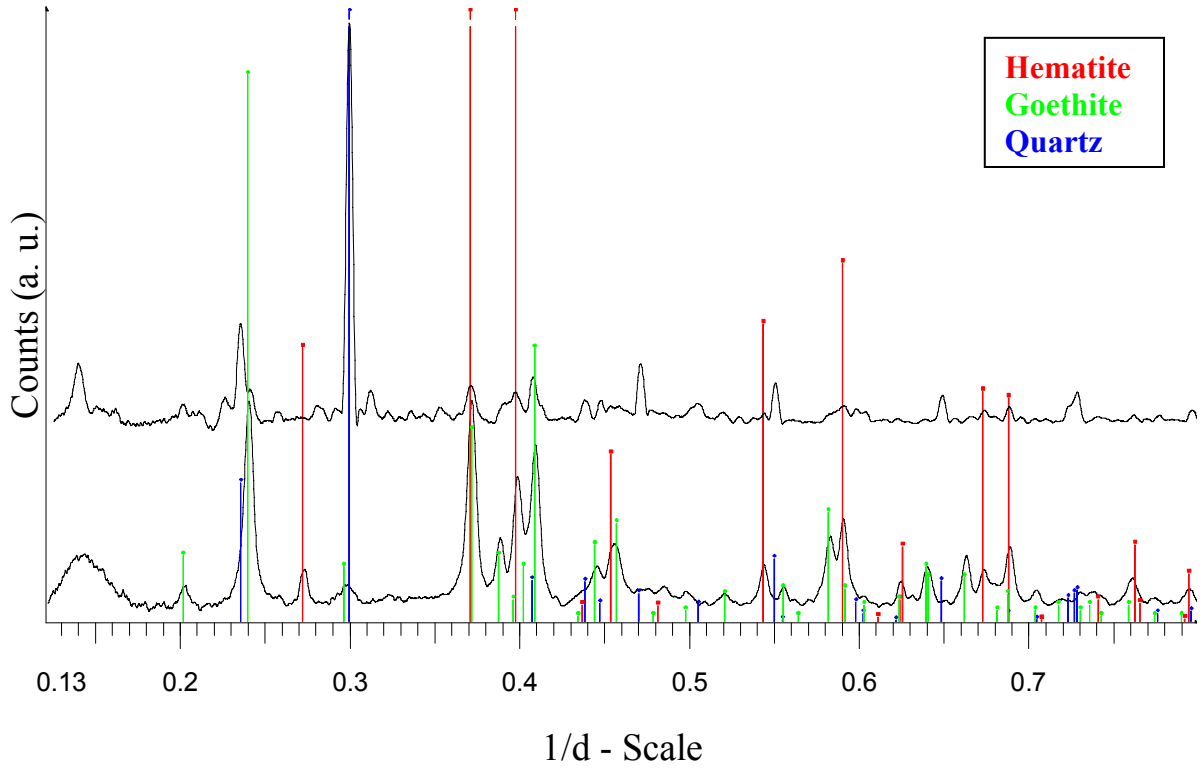

Figure 7.4: XRD analyses confirm the presence of goethite and hematite in *Pena de Hierro* Gossan rocks.

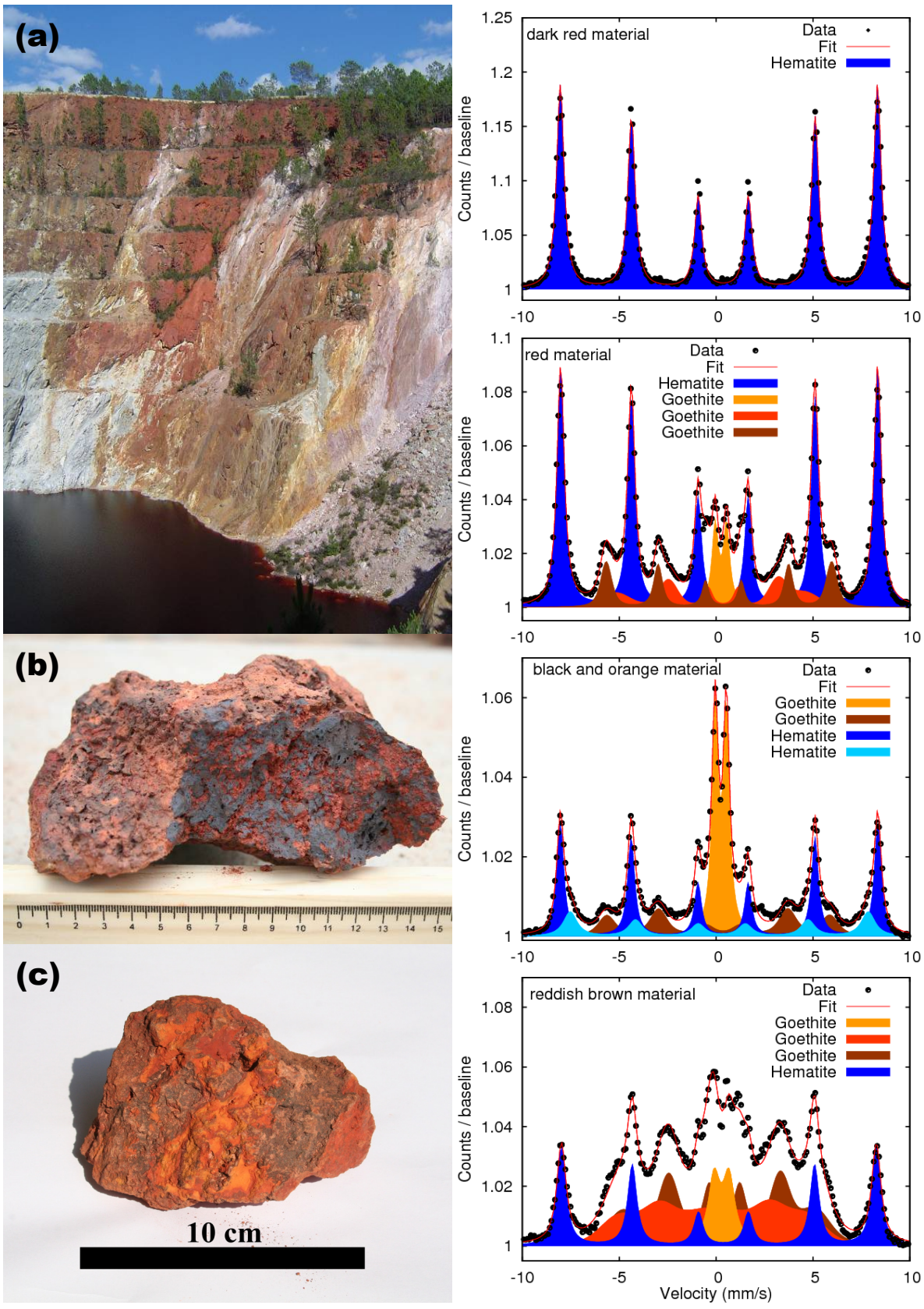

Figure 7.5: Gossan rocks at the *Pena de Hierro* site (a, red part; the light grey part represents a sulfide lens). In close up, gossan rocks show black material intermixed with red, orange, brown and yellow material (b and c). Spectra show mixtures of hematite and goethite.

7.5 River Bedrock

The lithified sedimentary deposits at the *Huerto del Loco* area (Figure 7.1) were found to be conglomeratic, cemented materials with clast sizes in the range up to ~3 cm. The surface of the rocks is in many cases visibly affected by the acidic water and exhibits a dark crust. Several samples from the river bedrock and a drill core were taken for laboratory analyses. Mössbauer spectra (Figure 7.6) show a prominent ferric doublet with average δ = 0.37 mm/s and average ΔE_Q = 0.54 mm/s. XRD analyses confirm the assignment to superparamagnetic goethite rather than other nanophase Iron oxides (Figure 7.7). Minor amounts of hematite are also present. Some clasts show ferrous doublets due to silicate phases. Raman spectra confirm the presence of goethite and hematite and identify quartz as the main silicate phase in the matrix.

Portions of the river bedrock are covered with a red crust, in which jarosite ($KFe_3(SO_4)_2(OH)_6$) was detected with the Mössbauer and the Raman spectrometer. A spectrum was obtained on red crust on top of black substrate. It shows pyrite from the substrate layer, with δ = 0.33 mm/s and ΔE_Q = 0.59 mm/s, and jarosite from the red crust with δ = 0.37mm/s and ΔE_Q = 1.18 mm/s (Figure 7.8). At some locations, an additional, thin, white or yellow crust covers the red crust. A spectrum obtained on bright crust on top of red crust is shown in Figure 7.8. Jarosite from the red crust and copiapite with coquimbite from the bright crust were clearly detected. In this spectrum, jarosite and copiapite have similar center shifts of δ ~0.38 mm/s, but different quadrupole splittings of ΔE_Q = 1.15 mm/s and ΔE_Q = 0.55 mm/s, respectively. Raman spectra obtained on several spots of this sample show mostly copiapite or coquimbite, jarosite was detected at some spots. In this case, the detection of two phases in Mössbauer spectra demonstrates again the ability of MIMOS II to perform depth-selective measurements.

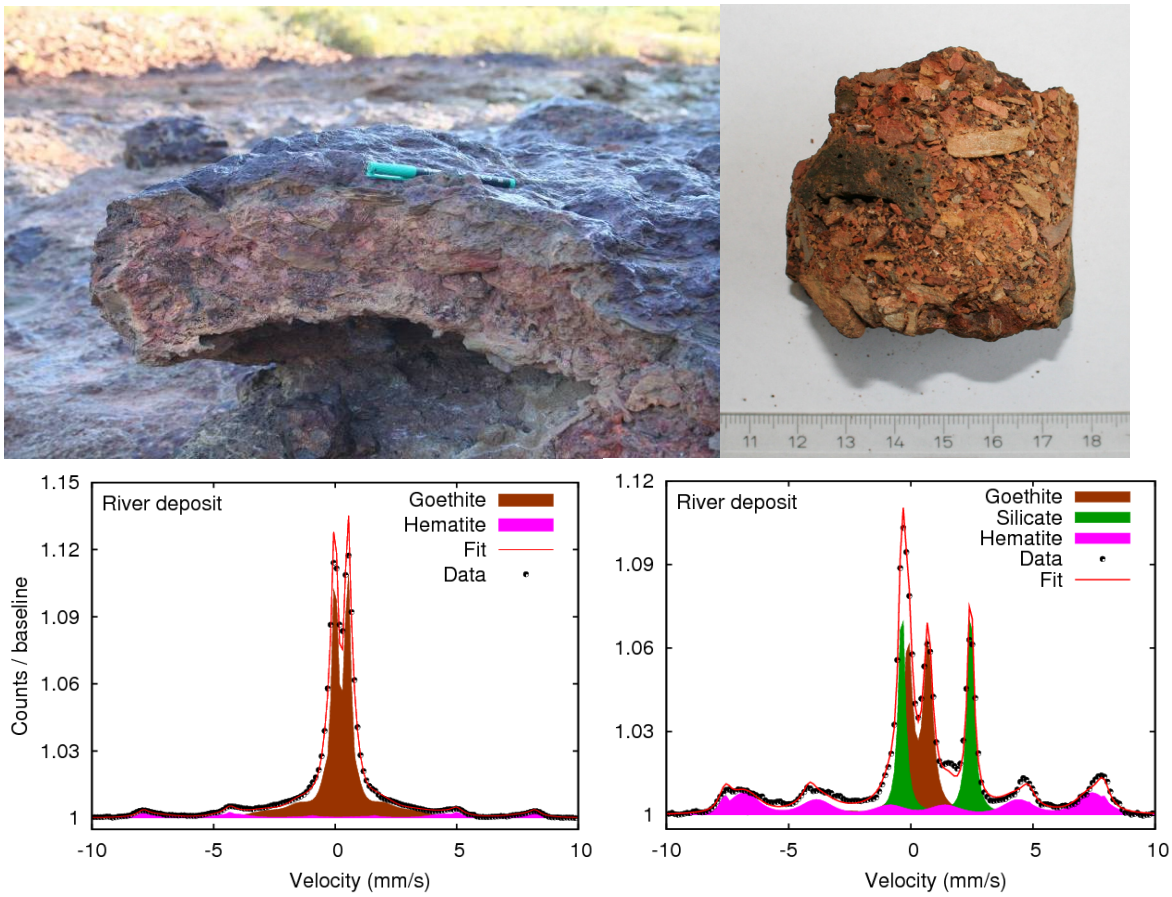

Figure 7.6: Conglomeratic river deposits are dominated by nanophase goethite and hematite. Ferrous doublets due to silicate clasts are also observed.

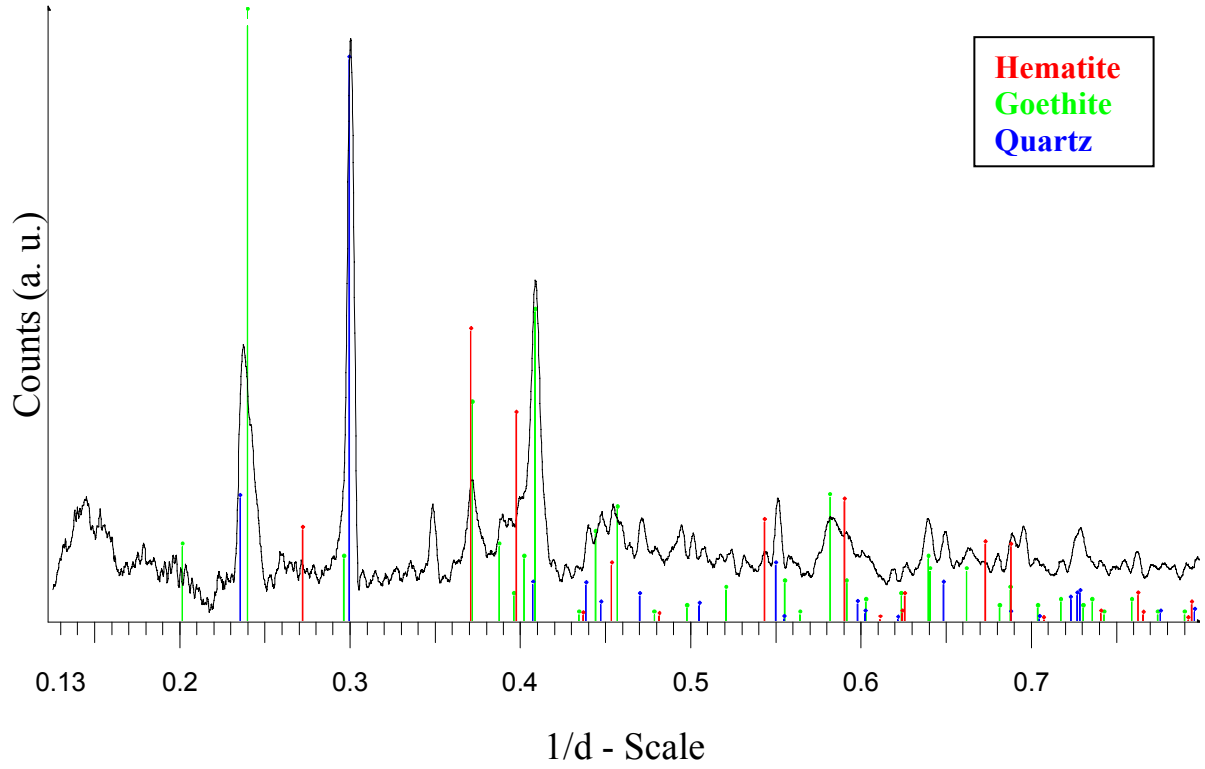

Figure 7.7: XRD analyses of river bedrock samples clearly confirm the presence of goethite. Small amounts of hematite are also indicated.

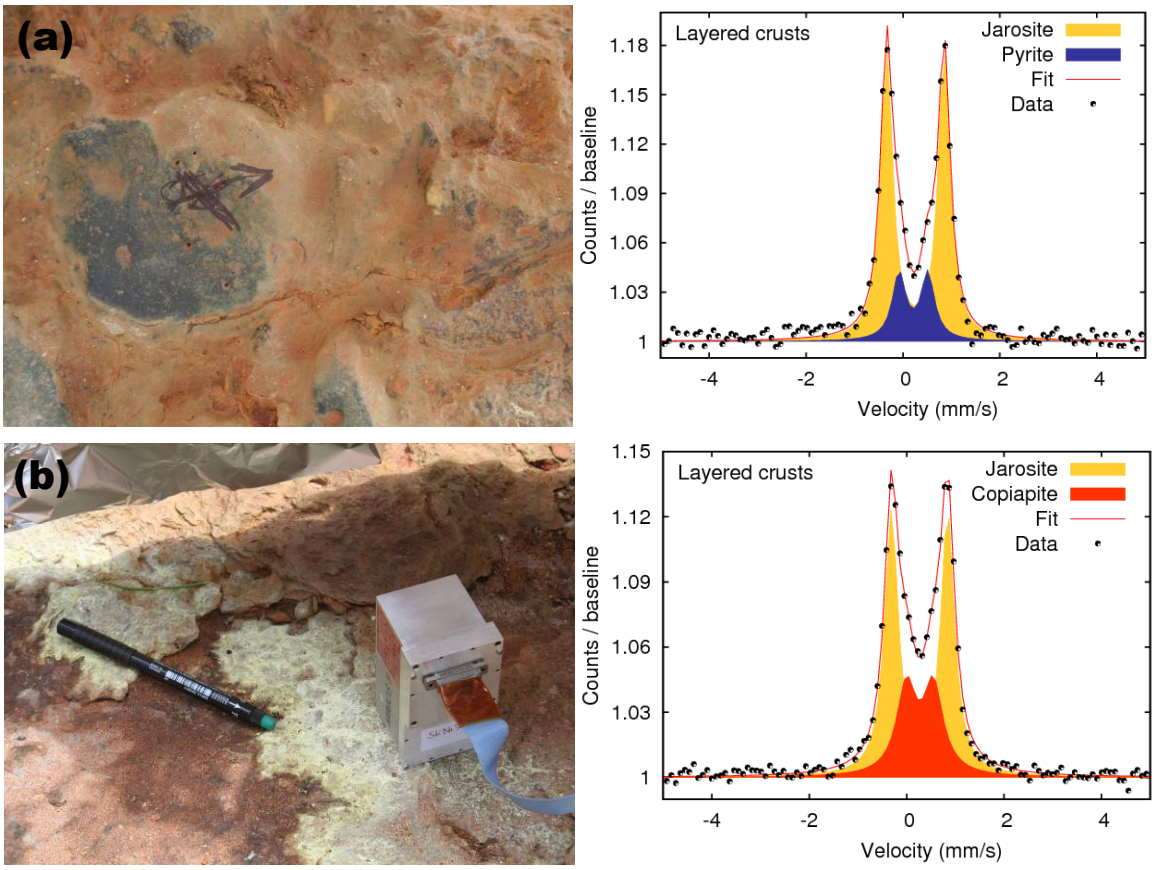

Figure 7.8: (a) A layered sample of red crust on top of black substrate shows jarosite from the crust and pyrite from the substrate. (b) Bright crust on top of red crust shows copiapite from the bright crust and jarosite from the red crust.

7.6 Evaporites and Sediments

Efflorescent precipitates and evaporite crusts can be observed as seasonal deposits in a number of locations close to the stream margin. During the field campaigns, precipitates with "popcorn"-like texture a few centimeters in diameter were most common, their main colors were white and different shades of yellow, sometimes mixed with small amounts of red or grey. Loose crusts up to ~5 mm thick and up to ~3 cm in diameter were encountered on some rocks close to the water surface, exhibiting a variety of colors including white and different shades of green and blue. Crusts with different colors and from different locations were sampled for laboratory analyses. As evaporite minerals may easily be altered by a change of their environment (e.g., temperature and humidity), representative samples were analysed in situ. Typical integration times in the field were between 30 minutes and two hours. The samples studied in situ were again analysed with laboratory equipment after ~8 weeks, mineralogical changes could not be detected.

The Mössbauer spectra of "popcorn-texture" evaporites exhibit a single ferric doublet, with average δ = 0.42 mm/s and average ΔE_Q = 0.55 mm/s (Figure 7.9). This doublet results from a mixture of ferric sulfates, mainly copiapite ($Fe^{2+}Fe_4^{3+}(SO_4)(OH)_2{\cdot}20H_2O$) and coquimbite ($Fe_2(SO_4)_3{\cdot}9H_2O$), which can be distinguished in Raman and XRD measurements (Figure 7.10). XRD measurements also reveal the additional presence of minor amounts of rhomboclase ($((H_5O_2)^+Fe^{3+}(SO_4)_2{\cdot}2(H_2O))$). In addition to the ferric doublet, some Mössbauer spectra show minor amounts (~5 %) of a ferrous doublet with δ ~1.6 mm/s and QS ~2.6 mm/s. In accordance with XRD measurements, this phase can be assigned to szomolnokite ($Fe^{2+}(SO_4){\cdot}H_2O$).

Mössbauer spectra obtained on white, green and blue crusts show a single ferrous doublet with average δ =1.25 mm/s and average ΔE_Q = 3.19 mm/s (Figure 7.9), resulting from the ferrous sulfates melanterite ($Fe^{2+}(SO_4){\cdot}7(H_2O)$) and rozenite ($Fe^{2+}(SO_4){\cdot}4(H_2O)$). As shown in Figure 7.11, these ferrous sulfates can be distinguished in XRD analyses.

Sediments were sampled at two sites. A thick deposit of sediment was sampled at the water margin of a small artificial lake a few kilometers downstream from the *Pena de Hierro* site. Samples were obtained from dried and wet sediment. Mössbauer spectra show the presence of two doublets, which were identified as jarosite (δ = 0.38 mm/s; ΔE_Q = 1.14 mm/s) and superparamagnetic goethite (δ = 0.35 mm/s; ΔE_Q = 0.54 mm/s) (Figure 7.9). While jarosite was also detected by in-situ Raman and XRD measurements, the goethite could only be detected in Mössbauer spectra.

Close to the Rio Tinto source, ochre colored sediment was sampled from a stream with a comparably high pH-value (~3.5) running parallel to the source stream. Sediment was sampled directly from the stream and dried for laboratory analyses. With δ = 0.36 mm/s and ΔE_Q = 0.61 mm/s, it was identified as schwertmannite ($Fe^{3+}{}_{16}O_{16}(OH)_{12}(SO_4)_2$). The spectrum (Figure 7.9) shows a slight asymmetry, as has been reported for schwertmannite previously [*Murad and Cashion,* 2004].

Figure 7.12a shows a comparison of Mössbauer parameters (ΔE_Q vs. δ) obtained on a suite of samples, Figure 7.12b represents a close-up of the ferric doublet phases. Generally, the mineral phases discussed above form distinct clusters on these plots. Schwertmannite and np-Gt have similar Mössbauer parameters, but were sampled in different settings and can therefore be easily distinguished.

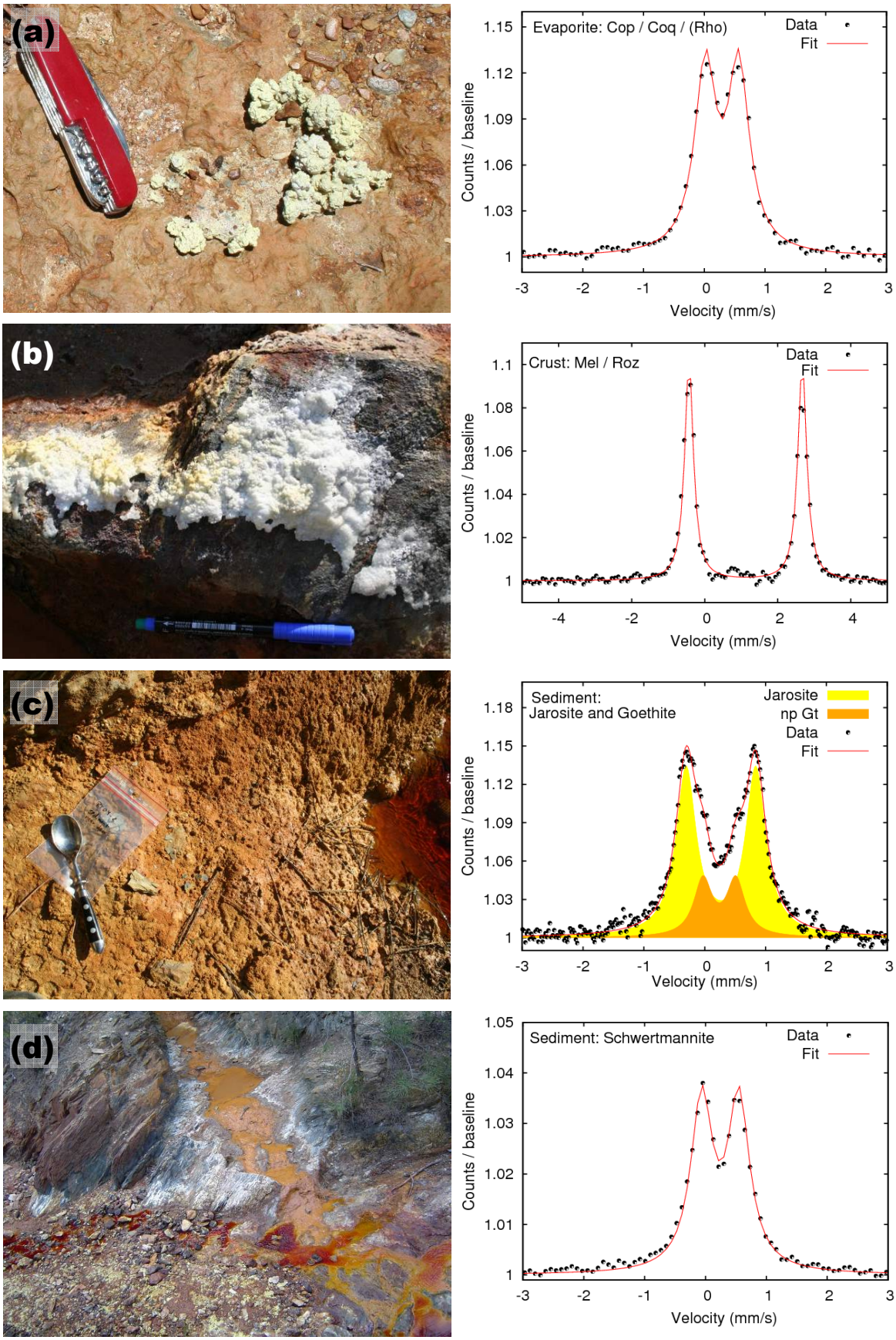

Figure 7.9: Context images and Mössbauer parameters for representative samples. (a) The common popcorn texture evaporites are dominated by copiapite (Cop) and coquimbite (Coq) with minor amounts of rhomboclase (Rho). (b) The ferrous sulfates melanterite (Mel) and rozenite (Roz) were identified in crust precipitates. (c) Jarosite and nanophase goethite (np-Gt) were detected in Rio Tinto sediment. (d) Schwertmannite was identified in sediment from a less acidic stream (ochre colored, to the right).

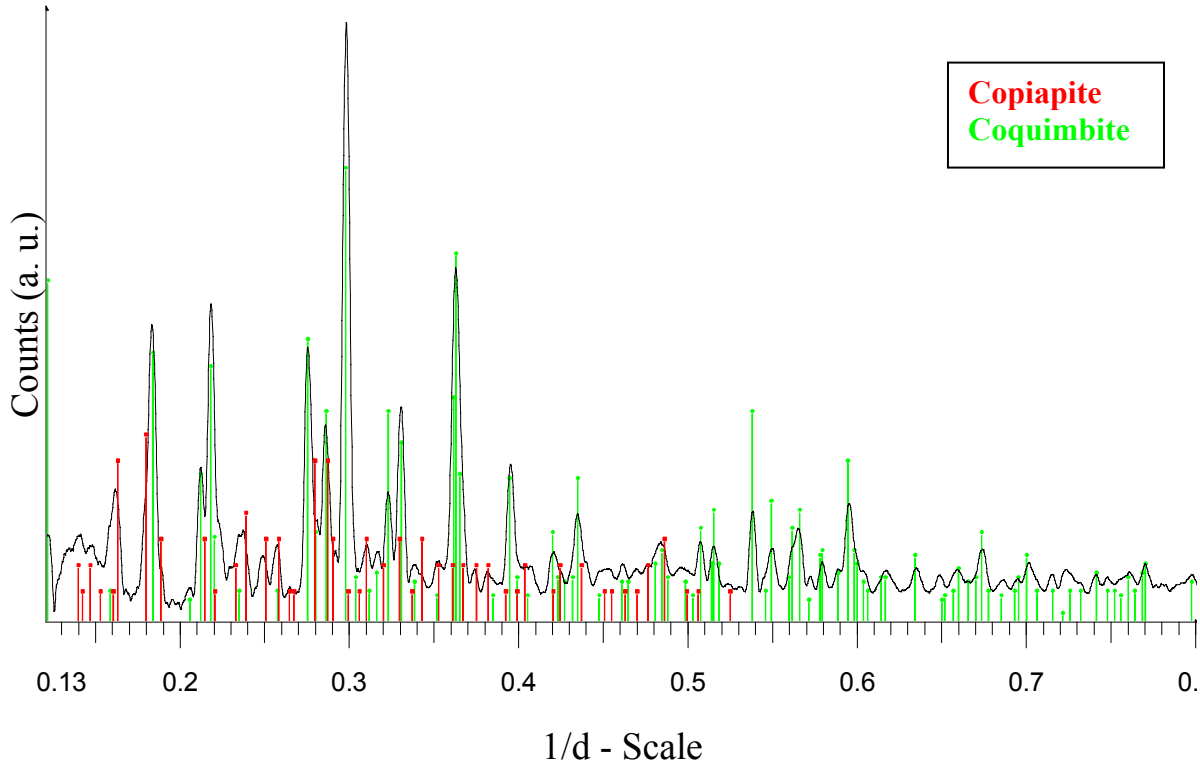

Figure 7.10: The ferric sulfates copiapite and coquimbite can be distinguished through XRD measurements. In this case, coquimbite and minor amounts of copiapite were detected in the same sample.

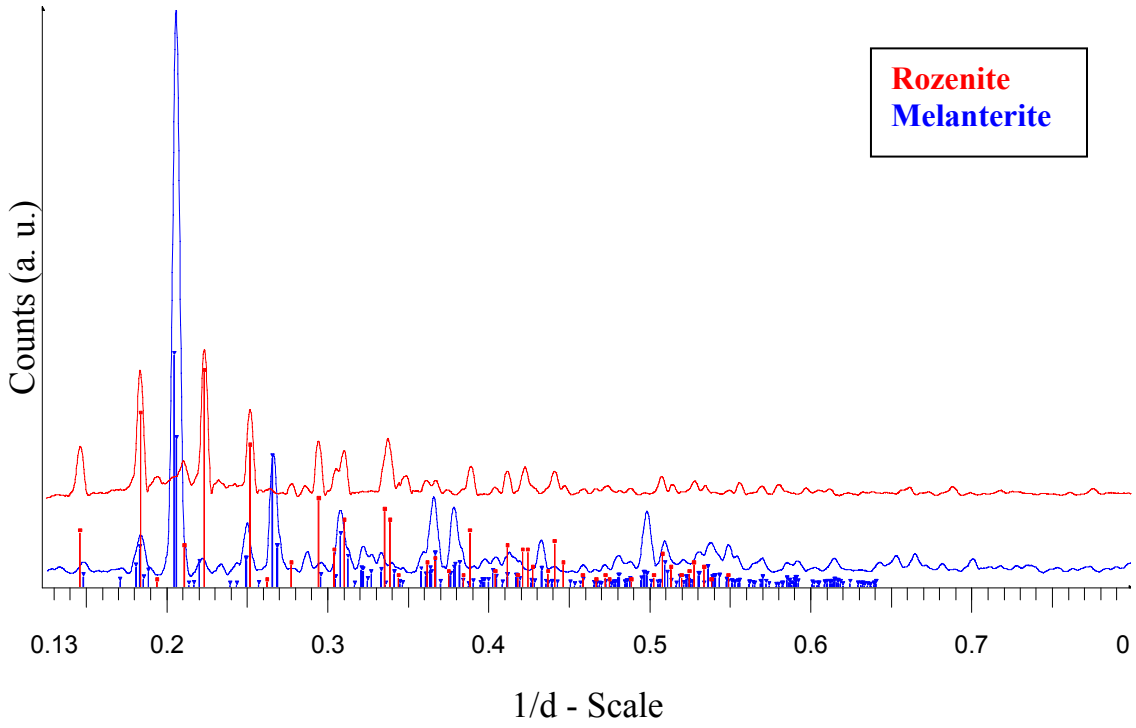

Figure 7.11: The ferrous sulfates rozenite and melanterite can be distinguished through XRD measurements. Data from two separate samples are shown in comparison.

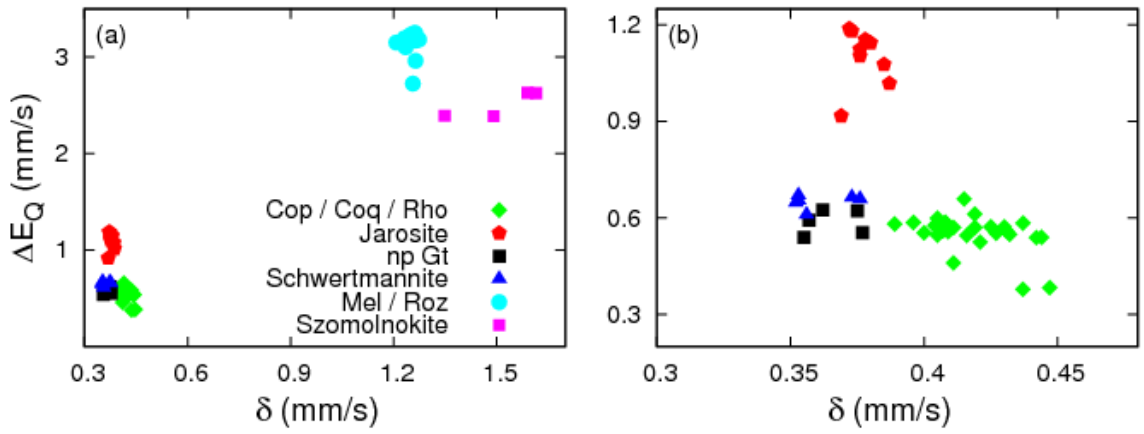

Figure 7.12: ΔE_Q versus δ plot for minerals from evaporites and sediments (a) and a close-up on ferric sulfates (b). Cop = Copiapite; Coq = Coquimbite; Rho = Rhomboclase; np Gt = nanophase Goethite; Mel = Melanterite; Roz = Rozenite. Different minerals form distinct clusters. Schwertmannite and goethite have similar parameters, but occur in different settings.

7.7 Lessons from Rio Tinto for future Mars Exploration

The rock formations of the Rio Tinto basin and Meridiani Planum clearly have differences and similarities, which must be considered when applying lessons from Rio Tinto to the exploration of Meridiani Planum and Mars. Liquid water is abundant in the Rio Tinto basin, and Rio Tinto sediments precipitate in seasonally arid stream beds. In contrast, only small amounts of water exist as solid or vapor under the harsh and dry conditions of present-day Mars. However, the Meridiani rock formation provides evidence for a formation via eolian and aqueous processes in an arid environment.

The detection of jarosite is considered one of the important discoveries of the MER mission [*Klingelhöfer et al.*, 2004; *Amils et al.*, 2007]. Jarosite forms in acidic conditions and its presence suggests a formation scenario for the sedimentary rocks at Meridiani Planum involving processes that are active in the Rio Tinto basin today or preserved in the rock record. In addition to jarosite, Mössbauer spectra of Meridiani outcrops show hematite and an unidentified ferric phase (Fe3D3). At Rio Tinto, jarosite was detected in association with other sulfates and nanophase ferric oxides, particularly nanophase goethite (np-Gt). Hematite was found to occur in the river bedrock and in hydrothermally altered volcanic rocks ("Gossan"), in association with goethite.

Within this context, the Rio Tinto basin provides not only an analogue site for Meridiani Planum, but also a test bed for instrumentation for future Mars missions. The combined Mössbauer- and Raman spectroscopic in-situ studies demonstrate that the two instruments provide complementary information about a sample: Raman spectroscopy is sensitive to the very surface, and the Raman field of view is small enough (~100 µm) to perform measurements at the scale of single mineral grains. MIMOS II, with its field of view of ~1.5 cm and sampling depth of ~200 µm, provides mineralogical context information about a larger volume and depth selective information from the comparison of 14.4 keV γ-ray and 6.4 keV X-ray backscatter spectra. The two instruments also provide complementary mineralogical information: While Raman spectroscopy is sensitive to a large number of minerals and organic phases, Mössbauer spectroscopy provides detailed information about Iron-bearing mineral phases, Fe oxidation states and the distribution of Fe among them.

Future Mars missions such as the combined NASA / ESA effort ExoMars [e.g., *Pacros et al.*, 2009] and Mars Astrobiology Explorer – Cacher (MAX-C) [e.g., *Beaty et al.*, 2010]

will specifically address astrobiological questions. As an extreme terrestrial habitat, Rio Tinto is also relevant to framing biological expectations. Despite low pH conditions and high metal concentrations, Rio Tinto waters support a microbial diversity, including acidophile microorganisms, which appear to play an essential role in maintaining the peculiar characteristics of the ecosystem, especially via subsurface bioleaching of the metallic massif [e.g., *Fernandez-Remolar et al.*, 2005, *Amils et al.*, 2007]. Acidophile microorganisms generate mineral signatures which may facilitate the detection of (extinct) occurrences of life [*Amils et al.*, 2007]. The combination of Raman and Mössbauer spectroscopy may prove valuable to determine organic phases and Fe oxidation states to search for past or present traces of life on Mars.

8 Summary and Outlook

In this work, Mössbauer spectroscopy is used to characterize different iron-bearing lithologic components at Meridiani Planum, encountered by the Mars Exploration Rover Opportunity. The analysis of Mössbauer spectra obtained on Mars is complemented by laboratory investigations and analogue in-situ studies at the Rio Tinto basin in southwestern Spain.

Opportunity's landing site at Meridiani Planum is characterized by bright, sulfate-rich outcrop rocks that contain hematite and jarosite as iron-bearing phases overlain by basaltic sand and a lag deposit of mm-sized spherules that have weathered from the outcrop. Occasional occurrences of loose rock fragments are scattered across the area and provide the only access to material not originally from Meridiani Planum. Larger fragments are rare and include Iron meteorites and impact ejecta delivered from distant regions on Mars. The remaining fragments, cm-sized "cobbles", occur along the traverse, preferentially in clusters associated with impact craters.

One central aim of the MER mission was to assess whether water may once have been present on the Martian surface. Under the influence of small amounts of water, rocks may experience weathering, leading to the formation of thin weathering layers on their surfaces. Depth-selective Mössbauer spectroscopy is introduced as a tool to characterize surface layers like these. The ability of the method is illustrated through its application to two suitable rock targets encountered during the mission. In both cases, an enhanced concentration of Iron oxides at the rock surface was detected, consistent with a low degree of aqueous alteration.

Hematite is present in the matrix of Meridiani outcrop rocks and in spherules that have formed in these sedimentary rocks. A detailed analysis of the hematite component in both target types, based on simultaneous fitting (simfitting), provides insights into the nature of the hematite and the history of the Meridiani outcrop formation. In contrast to previous analyses, simfitting reveals that two different hematite populations are present in both the outcrop matrix and in spherules. Separate hematite populations may arise from either a distribution of particle sizes, compositional impurities, different degrees of crystallinity, or a combination thereof. Based on the temperature dependence of their Morin transition, no hematite population is well-crystalline and chemically pure at the same time; hematite with a higher degree of crystallinity and/or purity is present in the outcrop matrix. The occurrence of separate hematite populations in the outcrop matrix and in spherules may reflect distinct hematite formation episodes under different environmental conditions.
The investigation of hematite at Meridiani Planum has also demonstrated that simfitting is a suitable and useful method to evaluate a large, correlated set of Mössbauer spectra.

Postdating the formation episode of Meridiani outcrop rocks, impacts have also shaped the area. Cobbles deposited through impact events can be divided into three different groups, according to APXS-determined chemical compositions and iron-bearing mineral phases determined from Mössbauer spectra. The first cobble group comprises outcrop fragments, which are bright, contain spherules and represent unaltered fragments from local outcrop rock, delivered to their current site as locally derived ejecta. All other cobbles are dark. The second cobble group consists of cobbles of meteoritic origin, which contain the minerals kamacite and troilite and exhibit high Ni contents. Their overall chemical and phase composition is closest to mesosiderite silicate clasts. Cobbles from the third group bear compositional similarities to local outcrop rocks and basaltic soil, with a phase composition and texture pointing to a formation scenario involving partial melting and

inclusion of small, bright outcrop clasts. These cobbles are thus interpreted as melt-bearing impact breccias.

Iron meteorites on the Martian surface are highly sensitive to weathering conditions at their impact site. At Meridiani Planum, they provide information on the more recent history of water activity and atmospheric conditions (i.e., postdating the episode of outcrop formation and possibly extending to the present time). Opportunity encountered four Iron meteorites, which exhibit evidence for physical and chemical weathering. Large excavated hollows and remnant metal spires are evidence for physical weathering by eolian abrasion. Discontinuous coatings cover the meteorites' surfaces. Mössbauer spectra obtained on the coatings reveal enhanced concentrations of Iron oxides compared to uncoated surface spots, indicating a low degree of aqueous alteration.

With its sulfate-rich mineralogy, the Rio Tinto basin provides a terrestrial analogue site for Meridiani Planum and constitutes a terrestrial habitat with unconventional extreme conditions. In-situ Mössbauer spectroscopic studies at Rio Tinto contribute to the understanding of the formation of sulfate minerals from primary volcanic rocks under acidic aqueous conditions and driven by acidophile microorganisms. In addition, in-situ studies at Rio Tinto provide a test bed for recent and ongoing developments in instrumentation for future Mars missions. Combined in-situ investigations with MIMOS II and a field-portable Raman spectrometer demonstrate that the two instruments provide complementary information about investigated samples.

After more than six years of operations, the two Mars Exploration Rovers Spirit and Opportunity are about to enter their 7th extended mission on the Martian surface. Both rovers have already returned an overwhelming data set that has so far only partly been analysed in detail. In the course of the mission, the available detailed studies have made the materials at the landing site familiar and facilitate the interpretation of newly observed lithologic changes. Within this context, results presented in this work may also serve as a starting point for further detailed studies:

- The experience gained with simfitting of a set of Mössbauer spectra may also be applied to the characterisation of other target types. Comparable studies could involve hematite and goethite from rocks encountered by Spirit in the Columbia Hills, or hematite and magnetite in Martian soil.
- Further cobble investigations are planned as Opportunity continues its journey towards Endeavour crater. As an extended cobble data set becomes available, the existing classification may be refined and further cobble groups may be identified.
- Iron meteorites are expected to be preserved over long time scales in the dry, cold Martian climate and are thus likely to be encountered elsewhere on Mars during future Mars missions. The characterisation of their weathering states and comparison to the Meridiani Iron meteorites will contribute to the overall understanding of aqueous and eolian weathering processes on the Martian surface.

The advanced miniaturised Mössbauer spectrometer MIMOS II A is currently under development for future missions. The increased sensitivity of the instrument and enhanced quality of spectra, in particular those corresponding to the 6.4 keV transition, will considerably facilitate depth-selective investigations for terrestrial studies and during future space missions.
Both a MIMOS II A instrument and a Raman spectrometer may be part of the payload of a future Mars mission. In combination, these two techniques open up the field of observation of a broader range of compounds, including organic substances as remnants of possible extraterrestrial biological activity.

Bibliography

Abdu, Y. A., and T. Ericsson (1997), Mössbauer spectroscopy, X-ray diffraction, and electron microprobe analysis of the New Halfa meteorite*, Meteoritics & Planetary Science,* 32, 373–375.

Agresti, D. G., E. Kankeleit, and B. Persson (1967), Hyperfine interaction and isomer shift in 195Pt*, Phys. Rev.,* 155, 1339–1341.

Agresti, D. G., M. Bent, and B. Persson (1969), A versatile computer program for analysis of Mössbauer spectra*, Nuclear Instruments and Methods,* 72, 2, 235–236.

Agresti, D. G., M. D. Dyar, and M. W. Schaefer (2005), MERView: A New Computer Program for Easy Display of MER-acquired Mössbauer Data*, Lunar and Planetary Science Conference,* 36, Abstract 1941.

Agresti, D. G., M. D. Dyar, and M. W. Schaefer (2006a), Derivation of Velocity Scales for Mars Mössbauer Data*, Lunar and Planetary Science Conference,* 37, Abstract 1517.

Agresti, D. G., M. D. Dyar and M. W. Schaefer (2006b), Velocity calibration for in-situ Mössbauer data from Mars*, Hyperfine Interactions,* 167, 845–850. DOI: 10.1007/s10751-006-9370-x.

Agresti, D. G., M. D. Dyar, and M. W. Schaefer (2006c), Velocity scales for Mars Mössbauer data*, Hyperfine Interactions,* 170, 67–74. DOI: 10.1007/s10751-006-9472-5.

Agresti, D. G., and P. A. Gerakines (2008), Simfitting: A new approach to MER Mössbauer data analysis*, Lunar and Planetary Science Conference,* 39, Abstract 2118.

Agresti, D. G., and P. A. Gerakines (2009), Simultaneous fitting of Mars Mössbauer data*, Hyperfine Interactions,* 188, 113–120. DOI: 10.1007/s10751-008-9896-1.

Agresti, D. G., I. Fleischer, G. Klingelhöfer, and R. V. Morris (2010), On simfitting MER Mössbauer data to characterize Martian hematite*, Journal of Physics: Conference Series,* 217, 12063.

Ahrens, T. J. (Ed.) (1995), Mineral Physics and Crystallography: A Handbook of Physical Constants. Washington, D.C., USA: AGU (2).

Al-Kathiri, A., B. A. Hofmann, E. Gnos, O. Eugster, K. C. Welten, and U. Krähenbühl (2006), Shisr 043 (IIIAB medium octahedrite): The first iron meteorite from the Oman desert*, Meteoritics and Planetary Science Supplement,* 41, 217–230.

Amils, R., E. González-Toril, D. Fernández-Remolar, F. Gómez, Á. Aguilera, M. RodrMalki, A. G. GarcFairén, V. de La Fuente, and J. Luis Sanz (2007), Extreme environments as Mars terrestrial analogs: The Rio Tinto case*, Planetary and Space Science,* 55, 370–381.

Amin N. and S. Arajs (1987), Morin temperature of annealed submicronic α-Fe2O3 particles*, Physical Review B,* 35, 10.

Aramu, F. and V. Maxia (1970), Shift and broadening of Mössbauer peaks by lack of collimation*, Nuclear Instruments and Methods,* 80, 35–39.

Arvidson, R. E., F. P. Seelos, K. S. Deal, W. C. Koeppen, N. O. Snider, J. M. Kieniewicz, B. M. Hynek, M. T. Mellon, and J. B. Garvin (2003), Mantled and exhumed terrains in Terra Meridiani, Mars*, Journal of Geophysical Research (Planets),* 108, 8073.

Ashley, J. W., S. W. Ruff, P. R. Christensen, L. A. Leshin (2008), Effects of dust on thermal infrared reflectivity of iron meteorite candidates found by the Mars Exploration Rovers*, Meteoritics & Planetary Science,* 43, 7.

Ashley, J. W., M. D. Fries, G. R. Huss, J. E. Chappelow, M. Golombek, M. A. Velbel, S. W. Ruff, C. Schröder, W. H. Farrand, D. D. Durda, P. A. Bland, I. Fleischer, A. C. McAdam, S. P. Wright, A. T. Knudson, L. A. Leshin, and A. Steele (2009a), The Scientific Rationale for Studying Meteorites found on Other Worlds. *2013-2022 Planetary Science Decadal Survey.* http://www8.nationalacademies.org/ssbsurvey/publicview.aspx.

Ashley, J. W., S. W. Ruff, A. T. Knudson, and P. R. Christensen (2009b), Mini-TES measurements of Santa Catarina-type, stony-iron meteorite candidates by the Opportunity rover*, Lunar and Planetary Science Conference,* 40, Abstract 2468.

Ashley, J. W., M. P. Golombek, C. Schröder, I. Fleischer, T. J. McCoy, P. R. Christensen, T. J. Parker, and Athena Science Team (2010a), Morphologic Evidence for Mechanical and Chemical Weathering of Three New Iron-Nickel Meteorites on Mars: Process Insights for Meridiani Planum*, Lunar and Planetary Science Conference,* 41, Abstract 2208.

Ashley, J. W., M. P. Golombek, P. R. Christensen, S. W. Squyres, T. J. McCoy, C. Schröder, I. Fleischer, J. R. Johnson, K. E. Herkenhoff, T. J. Parker (2010b): Evidence for Mechanical and Chemical Alteration of Iron-Nickel Meteorites on Mars — Process Insights for Meridiani Planum, manuscript in review for publication in *Journal of Geophysical Research – Planets*.

Bailey, R. E., and J. F. Duncan (1967), Moessbauer and nuclear magnetic resonance studies of several iron phosphides*, Inorganic chemistry,* 6, 8, 1444–1447.

Bancroft, G. M. (1973), Mössbauer Spectroscopy - An Introduction for Inorganic Chemists and Geochemists. London: Wiley.

Beaty, D. W., C. C. Allen, and the MEPAG Mid-range Rover science analysis group (2010), The proposed Mars astrobiology Explorer - Cacher (MAX-C) Rover: First step in a potential sample return campaign*, Lunar and Planetary Science Conference,* 41, Abstract 2571.

Bell, J. F., S. W. Squyres, K. E. Herkenhoff, J. N. Maki, H. M. Arneson, D. Brown, S. A. Collins, A. Dingizian, S. T. Elliot, E. C. Hagerott, A. G. Hayes, M. J. Johnson, Johnson, JR, J. Joseph, K. Kinch, M. T. Lemmon, R. V. Morris, L. Scherr, M. Schwochert, M. K. Shepard, G. H. Smith, J. N. Sohl-Dickstein, R. J. Sullivan, W. T. Sullivan, and M. Wadsworth (2003), Mars Exploration Rover Athena Panoramic Camera (Pancam) investigation*, Journal of Geophysical Research - Planets,* 108, E12.

Bell, J. F., J. Joseph, J. N. Sohl-Dickstein, H. M. Arneson, M. J. Johnson, M. T. Lemmon, and D. Savransky (2006), In-flight calibration and performance of the Mars Exploration

Rover Panoramic Camera (Pancam) instruments, *Journal of Geophysical Research (Planets),* 111, E02S03.

Bender Koch, C., and V. F. Buchwald (1994), Weathering of iron meteorites from Monuraqui, Chile., *Meteoritics,* 29, 4.

Bent, M. F., B. I. Persson, and D. G. Agresti (1969), Versatile program for analysis of Mössbauer spectra, *Computer Physics Communications,* 1, 2, 67–87.

Berger, M. J. (2010), X-COM: Photon cross sections database. http://physics.nist.gov/PhysRefData/Xcom/html/xcom1.html.

Bland, P. A., and T. B. Smith (2000), Meteorite Accumulation on Mars, I*carus,* 144, 21–26.

Blumers, M., B. Bernhardt, P. Lechner, G. Klingelhöfer, C. d'Uston, H. Soltau, L. Strüder, R. Eckhardt, J. Brückner, H. Henkel, J.Girones Lopez, and J.Maul (2010), The miniaturised Mössbauer spectrometer MIMOSIIA: Increased sensitivity and new capability for elemental analysis, *Nuclear Instruments and Methods in Physics Research A*, doi:10.1016/j.nima.2010.04.007

Bogard, D. D., and P. Johnson (1983), Martian gases in an Antarctic meteorite?, *Science,* 221, 651–654.

Buchwald, V. F. (1975), Handbook of iron meteorites: Their history, distribution, composition and structure. Berkeley, Calif.: Univ. of California Press.

Brückner, J., G. Dreibus, R. Gellert, S. W. Squyres, H. Wänke, A. Yen and J. Zipfel (2008), Mars Exploration Rovers: chemical composition by the APXS. in: Bell, J. (Ed.), The Martian Surface: Composition, Mineralogy, and Physical Properties, Cambridge University Press, Cambridge, UK.

Burns, R. G. (1993), Mössbauer Spectral Chracterization of Iron in Planetary surface Materials. In: Pieters, C. M.; Englert, P. A. J. (Ed.): Remote Geochemical Analysis: Elemental and Mineralogical Composition. Cambridge, UK: Cambridge University Press, 539–556.

Calvin, W. M., J. D. Shoffner, J. R. Johnson, A. H. Knoll, J. M. Pocock, S. W. Squyres, C. M. Weitz, R. E. Arvidson, J. F. Bell, P. R. Christensen, P. A. de Souza, W. H. Farrand, T. D. Glotch, K. E. Herkenhoff, B. L. Jolliff, A. T. Knudson, S. M. McLennan, A. D. Rogers, and S. D. Thompson (2008), Hematite spherules at Meridiani: Results from MI, Mini-TES, and Pancam, *Journal of Geophysical Research - Planets, 113.* DOI: 10.1029/2007JE003048.

Chappelow, J. E., and M. P. Golombek (2010), Can Mars' Current Atmosphere Land Block Island Sized Meteorites?, *Lunar and Planetary Science Conference,* 41, Abstract 2351.

Christensen, P. R., J. L. Bandfield, R. N. Clark, K. S. Edgett, V. E. Hamilton, T. Hoefen, H. H. Kieffer, R. O. Kuzmin, M. D. Lane, M. C. Malin, R. V. Morris, J. C. Pearl, R. Pearson, T. L. Roush, S. W. Ruff, and M. D. Smith (2000), Detection of crystalline hematite mineralization on Mars by the Thermal Emission Spectrometer: Evidence for

near-surface water, *Journal of Geophysical Research, 105, 9623–9642*. DOI: 10.1029/1999JE001093.

Christensen, P. R., G. L. Mehall, S. H. Silverman, S. Anwar, G. Cannon, N. Gorelick, R. Kheen, T. Tourville, D. Bates, S. Ferry, T. Fortuna, J. Jeffryes, W. O'Donnell, R. Peralta, T. Wolverton, D. Blaney, R. Denise, J. Rademacher, R. V. Morris, and S. Squyres (2003), Miniature Thermal Emission Spectrometer for the Mars Exploration Rovers*, Journal of Geophysical Research - Planets,* 108, E12, 8064. DOI: 10.1029/2003JE002117.

Clark, B. C., R. V. Morris, S. M. McLennan, R. Gellert, B. Jolliff, A. H. Knoll, S. W. Squyres, T. K. Lowenstein, D. W. Ming, N. J. Tosca, A. Yen, P. R. Christensen, S. Gorevan, J. Brückner, W. Calvin, G. Dreibus, W. Farrand, G. Klingelhöfer, H. Waenke, J. Zipfel, J. F. Bell, J. Grotzinger, H. Y. McSween, and R. Rieder (2005), Chemistry and mineralogy of outcrops at Meridiani Planum, 240, 73–94. DOI: 10.1016/j.epsl.2005.09.040.

Connolly, H. C., J. Zipfel, J. Grossman, L. Folco, C. Smith, R. H. Jones, K. Righter, M. Zolensky, S. S. Russell, G. K. Benedix, A. Yamaguchi, and B. A. Cohen (2006), The Meteoritical Bulletin, No. 90, 2006 September*, Meteoritics & Planetary Science,* 41, 9, 1383–1418.

Cornell, R. M., and U. Schwertmann (1996), The iron oxides, Structure, properties, reactions, occurence and uses. Weinheim: VCH Verlagsges.

Dang, M. Z., D. G. Rancourt, J. E. Dutrizac, G. Lamarche, and R. Provencher (1998), Interplay of surface conditions, particle size, stoichiometry, cell parameters, and magnetism in synthetic hematite-like minerals*, Hyperfine Interactions,* 117, 271–319.

Davis, A. M. (2005), Meteorites, comets and planets. 1. ed. Amsterdam: Elsevier.

de Coster, M., H. Pollak, and S. Amelinckx (1963), A Study of Mössbauer Absorption in Iron Silicates*, Physica Status Solidi,* 3, 283–288.

de Grave, E., L. H. Bowen, and S. B. Weed (1982), Mössbauer study of Aluminum-substituted Hematites*, Journal of Magnetism and Magnetic Materials,* 27, 98–108.

de Grave, E., D. Chambaere, and L. H. Bowen (1983), Nature of the Morin transition in Al-substituted Hematite*, Journal of Magnetism and Magnetic Materials,* 30, 349–354.

de Grave, E., and R. E. Vandenberghe (1990), Mössbauer Effect Study of the Spin Structure in Natural Hematites*, Physics and Chemistry of Minerals,* 17, 344–352.

de Grave, E., and A. van Alboom (1991), Evaluation of ferrous and ferric Mössbauer fractions*, Physics and Chemistry of Minerals,* 18, 337–342.

de Grave, E., R. E. Vandenberghe, P. M. A. de Bakker, A. van Alboom, R. Vochten, and R. van Tassel (1992), Temperature dependence of the Mössbauer parameters of the Fe-Ni phases in the Santa Catharina meteorite*, Hyperfine Interactions,* 70, 1009–1012.

de Grave, E., R. E. Vandenberghe, and C. Dauwe (2005), ILEEMS: Methodology and Applications to Iron Oxides*, Hyperfine Interactions,* 161, 147–160.

de Souza, P. A. J., R. de Queiroz, T. Morimoto, A. Guimarães, and V. Garg (2000), Air Pollution Investigation in Vitória Metropolitan Region, ES, Brazil*, Journal of Radioanalytical and Nuclear Chemistry,* 246, 1, 85–90.

de Souza, P. A. J., B. Bernhardt, G. Klingelhöfer, and P. Gütlich (2003), Surface Analysis in Archaeology Using the Miniaturized Mössbauer Spectrometer MIMOS II*., Hyperfine Interactions,* 151/152, 125–130.

de Souza, P. A. J. (2004), Extraterrestrial and Terrestrial Outdoor Applications of Mössbauer Spectroscopy. Dissertation, Mainz, Johannes-Gutenberg-Universität.

Dreibus, G., B. Huisl, B. Spettel, and R. Haubold (2003), Comparison of the chemistry of Y-000593 and Y-000749 with other Nakhlites*, Lunar and Planetary Science Conference, 34,* Abstract 1586.

Dunlap, R. A. (1997), A Mössbauer effect investigation of the enstatite chondrite from Abee, Canada*, Hyperfine Interactions,* 110, 209–215.
Dyar, M. D., D. G. Agresti, M. W. Schaefer, C. A. Grant, and E. C. Sklute (2006), Mössbauer spectroscopy of Earth and planetary materials*, Annu. Rev. Earth Planet. Sci.,* 34, 38–125.

El Goresy, A., and H. Fechtig (1967), Fusion crust of iron meteorites and mesosiderites and production of cosmic spherules*, Smithsonian Contributions to Astrophysics,* 11, 391–397.

Farrand, W. H., J. F. Bell, Johnson, JR, B. L. Jolliff, A. H. Knoll, S. M. McLennan, S. W. Squyres, W. M. Calvin, J. P. Grotzinger, R. V. Morris, J. Soderblom, S. D. Thompson, W. A. Watters, and A. S. Yen (2007), Visible and near-infrared multispectral analysis of rocks at Meridiani Planum, Mars, by the Mars Exploration Rover Opportunity*, Journal of Geophysical Research - Planets,* 112, E6, E06S02.

Farrand, W. H., J. F. Bell III, J. R. Johnson, R. E. Arvidson, L. S. Crumpler, J. A. Hurowitz, and C. Schröder (2008), Rock spectral classes observed by the Spirit Rover's Pancam on the Gusev Crater Plains and in the Columbia Hills*, Journal of Geophysical Research,* 113, E12S38, doi:10.1029/2008JE003237.

Fegley, J. B., G. Klingelhöfer, R. A. Brackett, N. Izenberg, D. T. Kremser, and K. Lodders (1995), Basalt oxidation and the formation of hematite on the surface of Venus*, Icarus,* 118, 373–383.

Fernández-Remolar, D. C., N. Rodriguez, F. Gómez, and R. Amils (2003), Geological record of an acidic environment driven by iron hydrochemistry: The Tinto River system*, Journal of Geophysical Research - Planets,* 108, E7, 5080.

Fernandez-Remolar, D., J. Gomez-Elvira, F. Gomez, E. Sebastian, J. Martiin, J. A. Manfredi, J. Torres, C. Gonzalez Kesler, and R. Amils (2004), The Tinto River, an extreme acidic environment under control of iron, as an analog of the Terra Meridiani hematite site of Mars*, Planetary and Space Science,* 52, 239–248.

Fernández-Remolar, D. C., R. V. Morris, J. E. Gruener, R. Amils, and A. H. Knoll (2005), The R\io Tinto Basin, Spain: Mineralogy, sedimentary geobiology, and implications for

interpretation of outcrop rocks at Meridiani Planum, Mars*, Earth and Planetary Science Letters,* 240, 149–167.

Flanders, P. J., and J. P. Remeika (1965), Magnetic Properties of Hematite Single Crystals*, Philosophical Magazine,* 11, 114, 1271–1288. DOI: 10.1080/14786436508224935.

Fleischer, I. (2006), Quantifizierung der Tiefenselektivität von 14,4 -keV- und 6,4-keV-Strahlung in Mössbauer-Spektren Diploma thesis. Mainz. Johannes-Gutenberg-Universität.

Fleischer, I., G. Klingelhöfer, R. V. Morris, C. Schröder, D. Rodionov, and P. de Souza (2008a), Analysis of 6.4 keV Mössbauer spectra obtained with MIMOS II on MER on cobbles at Meridiani Planum, Mars and considerations on penetration depths*., Lunar and Planetary Science Conference,* 39, Abstract 1618.

Fleischer, I., G. Klingelhöfer, C. Schröder, R. V. Morris, M. Hahn, D. Rodionov, R. Gellert, and P. A. de Souza (2008b), Depth selective Mossbauer spectroscopy: Analysis and simulation of 6.4 keV and 14.4 keV spectra obtained from rocks at Gusev Crater, Mars, and layered laboratory samples*, Journal of Geophysical Research - Planets,* 113, E06S21.

Fleischer, I., D. Agresti, and G. Klingelhöfer (2009), Mössbauer Hematite Temperature Study on Samples from the MER Landing Sites*, Lunar and Planetary Science Conference,* 40, Abstract 1832.

Fleischer, I., G. Klingelhöfer, F. Rull, S. Wehrheim, S. Ebert, M. Panthöfer, M. Blumers, D. Schmanke, J. Maul and C. Schröder (2010a), In-situ Mössbauer Spectroscopy with MIMOS II at Rio Tinto, Spain, *Journal of Physics: Conference Series*, 217, 012062.

Fleischer, I., G. Klingelhöfer, C. Schröder, D. W. Mittlefehldt, R. V. Morris, M. Golombek, and J. W. Ashley (2010b), In Situ Investigation of Iron Meteorites at Meridiani Planum, Mars*, Lunar and Planetary Science Conference,* 41, Abstract 1791.

Fleischer I., C. Schröder, G. Klingelhöfer, J. Zipfel, R. V. Morris, J. W. Ashley, R. Gellert, S. Wehrheim, S. Ebert (2010c), New insights into the mineralogy of the Meridiani Planum Meteorite, Mars, manuscript in review for publication in *Meteoritics & Planetary Science*.

French, B. M. (1998), Traces of Catastrophe: A Handbook of Shock-Metamorphic Effects in Terrestrial Meteorite Impact Structures. Houston, Texas.

Fysh, S. A., and P. E. Clark (1982), Aluminous hematite: A mössbauer study*, Physics and Chemistry of Minerals,* 8, 6, 257–267.

Gangas, N. H. J., T. Bakas, and A. Moukarika (1985), Mössbauer study of the Morin transition*, Hyperfine Interactions,* 23, 245–258.

Gellert, R., O. Geiss, G. Klingelhöfer, H. Ladstätter, B. Stahl, G. Walter, and E. Kankeleit (1993), Depth selective CEMS in the energy range 0 to 20 keV*, Nuclear Instruments and Methods in Physics Research B,* 76, 381–382.

Gellert, R., R. Rieder, R. C. Anderson, J. Brückner, B. C. Clark, G. Dreibus, T. Economou, G. Klingelhöfer, G. W. Lugmair, D. W. Ming, S. W. Squyres, C. d'Uston, H. Wänke, A.

Yen, and J. Zipfel (2004), Chemistry of Rocks and Soils in Gusev Crater from the Alpha Particle X-ray Spectrometer*, Science,* 305, 829–833.

Gellert, R., R. Rieder, J. Brückner, B. C. Clark, G. Dreibus, G. Klingelhöfer, G. Lugmair, D. W. Ming, H. Wänke, A. Yen, J. Zipfel, and S. W. Squyres (2006), Alpha Particle X-Ray Spectrometer (APXS): Results from Gusev crater and calibration report*, Journal of Geophysical Research - Planets,* 111, E10.

Golden, D. C., D. W. Ming, R. V. Morris, H. V. Lauer, and S. R. Yang (1993), Mineralogy of three slightly palagonitized tephra samples from the summit of Mauna Kea, Hawaii*, Journal of Geophysical Research,* 98, 3401–3411.

Golden, D. C., D. W. Ming, R. V. Morris, and T. G. Graff (2008), Hydrothermal synthesis of hematite spherules and jarosite: Implications for diagenesis and hematite spherule formation in sulfate outcrops at Meridiani Planum, Mars*, American Mineralogist,* 93, 1201–1214. DOI: 10.2138/am.2008.2737.

Golombek, M. P., J. A. Grant, L. S. Crumpler, R. Greeley, R. E. Arvidson, J. F. Bell, C. M. Weitz, R. Sullivan, P. R. Christensen, L. A. Soderblom, and S. W. Squyres (2006), Erosion rates at the Mars Exploration Rover landing sites and long-term climate change on Mars*, Journal of Geophysical Research - Planets,* 111, E12S10.

Golombek, M., K. Robinson, A. McEwen, N. Bridges, B. Ivanov, L. Tornabene, and R. Sullivan (2010a), Constraints on Ripple Migration at Meridiani Planum from Observations of Fresh Craters by Opportunity and HiRISE*, Lunar and Planetary Science Conference, 41,* Abstract 2373.

Golombek, M., K. Robinson, A. McEwen, N. Bridges, B. Ivanov, L. Tornabene, R. Sullivan (2010b), Constraints on ripple migration at Meridiani Planum from Opportunity and HiRISE observations of fresh craters, manuscript in review for publication in *Journal of Geophysical Research – Planets*.

Gonser, U. (1975), Mössbauer spectroscopy. Berlin, Heidelberg, New York: Springer (Topics in applied physics, Vol. 5).

Gorevan, S. P., T. Myrick, K. Davis, J. J. Chau, P. Bartlett, S. Mukherjee, R. Anderson, S. W. Squyres, R. E. Arvidson, M. B. Madsen, P. Bertelsen, W. Goetz, C. S. Binau, and L. Richter (2003), Rock Abrasion Tool: Mars Exploration Rover mission*, Journal of Geophysical Research - Planets,* 108, E12, 8068.

Greenwood, N. N., and T. C. Gibb (1971), Mössbauer spectroscopy. London: Chapman and Hall.

Grokhovsky, V. I., O. B. Milder, and V. A. a. O. M. I. Semionkin (2003), Comparative study of meteorites Bilibino and Sikhote-Alin by Mössbauer spectroscopy*., Annual Meteoritical Society Meeting,* 66, Abstract 5284.

Grokhovsky, V. I., E. V. Zhiganova, M. Y. Larionov, K. A. Uymina, and M. I. Oshtrakh (2008), Mössbauer Spectroscopy with High Velocity Resolution in the Meteorites Study*, The Physics of Metals and Metallography,* 105, 2, 177–187.

Gunnlaugsson, H. P., Ö. Helgason, L. Kristjánsson, P. Nørnberg, H. Rasmussen, and G. SteinWeyer (2006), Magnetic properties of olivine basalt: Application to Mars, *Physics of the Earth and Planetary Interiors,* 154, 276–289.

Gütlich, P., R. Link, A. Trautwein, P. Gütlich, R. Link, A. Trautwein, and Gütlich-Link-Trautwein (1978), Mössbauer Spctroscopy and Transition Metal Chemistry. Berlin, Heidelberg, New York / Berlin: Springer (Inorganic chemistry concepts, 3).

Hamilton, V. E., R. V. Morris, J. E. Gruener, and S. A. Mertzman (2008), Visible, near-infrared, and middle infrared spectroscopy of altered basaltic tephras: Spectral signatures of phyllosilicates, sulfates, and other aqueous alteration products with application to the mineralogy of the Columbia Hills of Gusev Crater, Mars, *Journal of Geophysical Research (Planets),* 113, E12S43.

Hawthorne, F. C. (1988), Mössbauer Spectroscopy. In: Hawthorne, F. C. (Ed.): Spectroscopic Methods in Mineralogy. Washington, D.C., USA (Reviews in Mineralogy, 18), 255–340.

Herkenhoff, K. E., S. W. Squyres, J. F. Bell, J. N. Maki, H. M. Arneson, P. Bertelsen, D. I. Brown, S. A. Collins, A. Dingizian, S. T. Elliott, W. Goetz, E. C. Hagerott, A. G. Hayes, M. J. Johnson, R. L. Kirk, S. McLennan, R. V. Morris, L. M. Scherr, M. A. Schwochert, L. R. Shiraishi, G. H. Smith, L. A. Soderblom, J. N. Sohl-Dickstein, and M. V. Wadsworth (2003), Athena Microscopic Imager investigation, *Journal of Geophysical Research - Planets,* 108, E12, 8065. DOI: 10.1029/2003JE002076.

Herkenhoff, K. E., S. W. Squyres, R. Anderson, B. A. Archinal, R. E. Arvidson, J. M. Barrett, K. J. Becker, J. F. Bell, C. Budney, N. A. Cabrol, M. G. Chapman, D. Cook, B. L. Ehlmann, J. Farmer, B. Franklin, L. R. Gaddis, D. M. Galuszka, P. A. Garcia, T. M. Hare, E. Howington-Kraus, J. R. Johnson, S. Johnson, K. Kinch, R. L. Kirk, E. M. Lee, C. Leff, M. Lemmon, M. B. Madsen, J. N. Maki, K. F. Mullins, B. L. Redding, L. Richter, M. R. Rosiek, M. H. Sims, L. A. Soderblom, N. Spanovich, R. Springer, R. M. Sucharski, T. Sucharski, R. Sullivan, J. M. Torson, and A. Yen (2006), Overview of the Microscopic Imager Investigation during Spirit's first 450 sols in Gusev crater, *Journal of Geophysical Research - Planets,* 111, E02S04. DOI: 10.1029/2005JE002574.

Herkenhoff, K. E., J. Grotzinger, A. H. Knoll, S. M. McLennan, C. Weitz, A. Yingst, R. Anderson, B. A. Archinal, R. E. Arvidson, J. M. Barrett, K. J. Becker, J. F. Bell, C. Budney, M. G. Chapman, D. Cook, B. Ehlmann, B. Franklin, L. R. Gaddis, D. M. Galuszka, P. A. Garcia, P. Geissler, T. M. Hare, E. Howington-Kraus, J. R. Johnson, L. Keszthelyi, R. L. Kirk, P. Lanagan, E. M. Lee, C. Leff, J. N. Maki, K. F. Mullins, T. J. Parker, B. L. Redding, M. R. Rosiek, M. H. Sims, L. A. Soderblom, N. Spanovich, R. Springer, S. W. Squyres, D. Stolper, R. M. Sucharski, T. Sucharski, R. Sullivan, and J. M. Torson (2008), Surface processes recorded by rocks and soils on Meridiani Planum, Mars: Microscopic Imager observations during Opportunity's first three extended missions, *Journal of Geophysical Research - Planets,* 113. E12. DOI: 10.1029/2008JE003100.

Hutchison, R. (2006), Meteorites, A petrologic, chemical, and isotopic synthesis. Cambridge: Cambridge University Press (Cambridge planetary science, 2).

Johnson, J. R., K. E. Herkenhoff, J. F. Bell, W. H. Farrand, J. Ashley, C. Weitz, and S. W. Squyres (2010), Pancam Visible/Near-Infrared Spectra of Large Fe-Ni Meteorites at Meridiani Planum, Mars, *Lunar and Planetary Science Conference,* 41, Abstract 1974.

Jolliff, B. L., W. H. Farrand, J. R. Johnson, C. Schröder, and C. M. Weitz (2006), Origin of rocks and cobbles on the Meridiani Plains as seen by Opportunity, *Lunar and Planetary Science Conference, 37,* Abstract 2401.

Jolliff, B. L., R. Gellert, D. W. Mittlefehldt, and Athena Science Team (2007), More on the possible composition of the Meridiani hematite-rich concretions, *Lunar and Planetary Science Conference,* 38, Abstract 2279.

Klingelhöfer, G., and E. Kankeleit (1990), Conversion electron Mössbauerspectroscopy with very low energy (0 to 15 eV) electrons, *Hyperfine Interactions,* 57, 1905–1910.

Klingelhöfer, G., U. Imkeller, E. Kankeleit, and B. Stahl (1992), Remarks on depth selective CEMS Backscattering measurements, *Hyperfine Interactions,* 71, 1445–1448.

Klingelhöfer, G., P. Held, B. Bernhardt, J. Foh, R. Teucher, and E. Kankeleit (1998), In-situ phase analysis by a versatile miniaturized Mössbauer spectrometer, *Hyperfine Interactions,* 111, 1, 331–334.

Klingelhöfer, G., B. Bernhardt, J. Foh, U. Bonnes, D. Rodionov, P. A. de Souza, C. Schröder, R. Gellert, S. Kane, P. Gütlich, and E. Kankeleit (2002a), The Miniaturized Mössbauer Spectrometer MIMOS II for Extraterrestrial and Outdoor Terrestrial Applications: A Status Report, *Hyperfine Interactions,* 144, 371–379.

Klingelhöfer, G., G. M. da Costa, A. Prous, and B. Bernhardt (2002b), Rock paintings from Minas Gerais, Brasil, investigated by in-situ Mössbauer spectroscopy., *Hyperfine Interactions,* C 5, 423–426.

Klingelhöfer, G., R. V. Morris, B. Bernhardt, D. Rodionov, P. A. de Souza, S. W. Squyres, J. Foh, E. Kankeleit, U. Bonnes, R. Gellert, C. Schröder, S. Linkin, E. Evlanov, B. Zubkov, and O. Prilutski (2003), Athena MIMOS II Mössbauer spectrometer investigation, *Journal of Geophysical Research - Planets,* 108, E12, 8067.

Klingelhöfer, G., R. V. Morris, B. Bernhardt, C. Schröder, D. S. Rodionov, P. A. de Souza, A. Yen, R. Gellert, E. N. Evlanov, B. Zubkov, J. Foh, U. Bonnes, E. Kankeleit, P. Gütlich, D. W. Ming, F. Renz, T. Wdowiak, S. W. Squyres, and R. E. Arvidson (2004), Jarosite and Hematite at Meridiani Planum from Opportunity‘s Mössbauer Spectrometer, *Science*, 306, 1740–1745.

Klingelhöfer, G., E. de Grave, R. V. Morris, A. van Alboom, V. G. de Resende, P. A. de Souza, D. Rodionov, C. Schröder, D. W. Ming, and A. Yen (2005), Mössbauer spectroscopy on Mars: goethite in the Columbia Hills at Gusev crater, Hyperfine Interactions, 166, 549–554.

Klingelhöfer, G., M. Blumers, B. Bernhardt, P. Lechner, J. Gironés-Lopez, J. Maul, H. Soltau, L. Strüder, H. Henkel (2010), The improved miniaturised Mössbauer spectrometer MIMOS IIA with elemental analysis capability and increased sensitivity, *Lunar and Planetary Science Conference,* 41, Abstract 2423.

Krumbein, W. C., and L. L. Sloss (1963), Stratigraphy and Sedimentation. 2nd edition. San Francisco: Freeman.

Kündig, W., and H. Bömmel (1965), Some Properties of Supported Small α-Fe2O3 particles Determined with the Mössbauer Effect*, Physical Review,* 142, 2, 327–333.

Lane, M. D., R. V. Morris, S. A. Mertzman, and P. R. Christensen (2002), Evidence for platy hematite grains in Sinus Meridiani, Mars*, Journal of Geophysical Research - Planets,* 107, 5126. DOI: 10.1029/2001JE001832.

Leistel, J. M., E. Marcoux, D. Thiéblemont, C. Quesada, A. Sánchez, G. R. Almodóvar, E. Pacual, and R. Sáez (1998), The volcanic-hosted massive sulphide deposits of the Iberian Pyrite Belt, Review and preface to the Thematic Issue*, Mineralium Deposita,* 33, 2–30.

Lisher, E. J., C. Wilkinson, T. Ericsson, Häggström L., Lundgren L., and Wäppling R. (1974), Studies of magnetic structure of Fe3P*, J. Phys. C: Solid State Phys.,* 7, 1344–1352.

Lodders, K., and B. Fegley, JR. (1998), Planetary Scientist's Companion, p. 300-308. New York / Oxford: Oxford University Press.

Long, G. J. (1986), Industrial applications of the Mössbauer effect. New York: Plenum press.

Lovering, J. F., W. Nichiporuk, A. Chodos, and H. Brown (1957), The distribution of gallium, germanium, chromium, and copper in iron and stony-iron meteorites in relation to nickel content and structure*, Geochimica et Cosmochimica Acta,* 11, 263–278.

Margulies, S., and Ehrmann J. R. (1961), Transmission and line broadening of resonance radiation on a resonance absorber*, Nuclear Instruments and Methods,* 12, 131–137.

Maringer, R. E. (1960), Ablation deposits on iron meteorites*, Geochimica et Cosmochimica Acta,* 19, 1, 5–6.

McCammon, C. (1995), Mössbauer Spectroscopy of Minerals. In: Ahrens, T. J. (Ed.): Mineral Physics and Crystallography: A Handbook of Physical Constants. Washington, D.C., USA: AGU (2), 332–347.

McFadden, L.-A. (2007), Encyclopedia of the solar system. 2. ed. Amsterdam: Elsevier.

McLennan, S. M., J. F. Bell III, W. M. Calvin, P. R. Christensen, B. C. Clark, P. A. de Souza, J. Farmer, W. H. Farrand, D. A. Fike, R. Gellert, A. Ghosh, T. D. Glotch, J. P. Grotzinger, B. Hahn, K. E. Herkenhoff, J. A. Hurowitz, J. R. Johnson, S. S. Johnson, B. Jolliff, G. Klingelhöfer, A. H. Knoll, Z. Learner, M. C. Malin, H. Y. McSween Jr., J. Pocock, S. W. Ruff, L. A. Soderblom, S. W. Squyres, N. J. Tosca, W. A. Watters, M. B. Wyatt, and A. Yen (2005), Provenance and diagenesis of the Burns formation, Meridiani Planum, Mars, *Earth Planet. Sci. Lett.*, 240, 95-121. doi:10.1016/j.epsl.2005.09.041.

McSween, H.Y. Jr., E.M. Stolper, L.A. Taylor, R.A. Muntean, G.D.O'Kelley, J.S. Eldridge, S. Biswas, H.T. Ngo and M.E. Lipschutz (1979) Petrogenetic relationship between Allan Hills 77005 and other achondrites, *Earth Planet. Sci. Lett.*, 45, 275-284.

McSween, H. Y., S. W. Ruff, R. V. Morris, R. Gellert, G. Klingelhöfer, P. R. Christensen, T. J. McCoy, A. Ghosh, J. M. Moersch, B. A. Cohen, A. D. Rogers, C. Schröder, S. W. Squyres, J. Crisp, and A. Yen (2008), Mineralogy of volcanic rocks in Gusev crater, Mars:

Reconciling Mössbauer, Alpha Particle X-ray Spectrometer, and Miniature Thermal Emission Spectrometer spectra, *Journal of Geophysical Research - Planets,* 113, E6.

Meyer, C. (2010), Mars Meteorite Compendium. http://curator.jsc.nasa.gov/antmet/mmc; last accessed on August 18, 2010.

Mitra, S. (1992), Applied Mössbauer Spectroscopy: Theory and Practice for geochemists and Archaeologists. Oxford, New York, Seoul, Tokyo: Pergamon Press.

Mittlefehldt, D. W., R. Gellert, K. E. Herkenhoff, R. V. Morris, B. C. Clark, B. A. Cohen, I. Fleischer, B. L. Jolliff, G. Klingelhöfer, D. W. Ming, and R. A. Yingst (2010), Marquette Island: A distinct mafic lithology discovered by Oppportunity, *Lunar and Planetary Science Conference,* 41, Abstract 2109.

Morris, R. V., D. G. Agresti, H. V. Lauer, J. A. Newcomb, T. D. Shelfer, and A. V. Murali (1989), Evidence for pigmentary hematite on Mars based on optical, magnetic, and Moessbauer studies of superparamagnetic (nanocrystalline) hematite, *Journal of Geophysical Research,* 94, 2760–2778. DOI: 10.1029/JB094iB03p02760.

Morris, R. V., D. C. Golden, and J. F. Bell, III (1997), Low-temperature reflectivity spectra of red hematite and the color of Mars, *Journal of Geophysical Research,* 102, 9125–9133.

Morris, R. V., D. C. Golden, J. F. Bell, T. D. Shelfer, A. C. Scheinost, N. W. Hinman, G. Furniss, S. A. Mertzman, J. L. Bishop, D. W. Ming, C. A. Allen, and T. Britt (2000a), Mineralogy, composition and alteration of Mars Pathfinder rocks and soils: Evidence from multispectral, elemental, and magnetic data on terrestrial analogue, SNC meteorite, and Pathfinder samples, *Journal of Geophysical Research,* 105, E1, 1757–1817. DOI: 10.1029/1999JE001059.

Morris, R. V., M. D. Lane, S. Mertzman, T. D. Shelfer, and P. R. Christensen (2000b), Chemical and Mineralogical Purity of Sinus Meridiani Hematite, *Lunar and Planetary Science Conference,* 31, Abstract 1618.

Morris, R. V., G. Klingelhöfer, B. Bernhardt, C. Schröder, D. S. Rodionov, P. A. de Souza, A. Yen, R. Gellert, E. N. Evlanov, J. Foh, E. Kankeleit, P. Gütlich, D. W. Ming, F. Renz, T. Wdowiak, S. W. Squyres, and R. E. Arvidson (2004), Mineralogy at Gusev Crater from the Mössbauer Spectrometer on the Spirit Rover, *Science,* 305, 833–837.

Morris, R. V., D. W. Ming, T. G. Graff, R. E. Arvidson, J. F. Bell, S. W. Squyres, S. A. Mertzman, J. E. Gruener, D. C. Golden, L. Le, and G. A. Robinson (2005), Hematite spherules in basaltic tephra altered under aqueous, acid-sulfate conditions on Mauna Kea volcano, Hawaii: Possible clues for the occurrence of hematite-rich spherules in the Burns formation at Meridiani Planum, Mars, *Earth and Planetary Science Letters,* 240, 168–178. DOI: 10.1016/j.epsl.2005.09.044.

Morris, R. V., G. Klingelhöfer, C. Schröder, D. S. Rodionov, A. Yen, D. W. Ming, P. A. de Souza, I. Fleischer, T. Wdowiak, R. Gellert, B. Bernhardt, E. N. Evlanov, B. Zubkov, J. Foh, U. Bonnes, E. Kankeleit, P. Gutlich, F. Renz, S. W. Squyres, and R. E. Arvidson (2006a), Mossbauer mineralogy of rock, soil, and dust at Gusev crater, Mars: Spirit's journey through weakly altered olivine basalt on the plains and pervasively altered basalt in the Columbia Hills, *Journal of Geophysical Research - Planets,* 111, E02S13.

Morris, R. V., G. Klingelhöfer, C. Schröder, D. S. Rodionov, A. Yen, D. W. Ming, P. A. de Souza, T. Wdowiak, I. Fleischer, R. Gellert, B. Bernhardt, U. Bonnes, B. A. Cohen, E. N. Evlanov, J. Foh, P. Gutlich, E. Kankeleit, T. Mccoy, D. W. Mittlefehldt, F. Renz, M. E. Schmidt, B. Zubkov, S. W. Squyres, and R. E. Arvidson (2006b), Mossbauer mineralogy of rock, soil, and dust at Meridiani Planum, Mars: Opportunity's journey across sulfate-rich outcrop, basaltic sand and dust, and hematite lag deposits*, Journal of Geophysical Research - Planets,* 111, E12S15.

Morris, R. V., G. Klingelhöfer, C. Schröder, I. Fleischer, D. W. Ming, A. S. Yen, R. Gellert, R. E. Arvidson, D. S. Rodionov, L. S. Crumpler, B. C. Clark, B. A. Cohen, T. J. McCoy, D. W. Mittlefehldt, M. E. Schmidt, P. A. de Souza, and S. W. Squyres (2008), Iron mineralogy and aqueous alteration from Husband Hill through Home Plate at Gusev Crater, Mars: Results from the Mossbauer instrument on the Spirit Mars Exploration Rover*, Journal of Geophysical Research - Planets,* 113, E12, E12S42.

Mössbauer, R. L. (1958a), Kernresonanzfluoreszenz von Gammatrahung in Ir191*, Zeitschrift für Physik,* 151, 124–143.

Mössbauer, R. L. (1958b), Kernresonanzfluoreszenz von Gammastrahlung in Ir191*, Naturwissenschaften,* 45, 538–539.

Mössbauer, R. L. (2000), The discovery of the Mössbauer effect*, Hyperfine Interactions,* 126, 1–12.

Murad, E. (1984), High-precision determination of magnetic hyperfine fields by Mössbauer spectroscopy using an internal standard*, J. Phys. E: Sci. Instrum.,* 17, 736–737.

Murad, E., and J. Cashion (2004), Mössbauer Spectroscopy of Environmental Materials and their Industrial Utilization. Dordrecht / Berlin: Kluwer Academic Publishers Group; Springer US.

Nagata, T. (1961), Rock Magnetism. Tokyo: Maruzen Company Ltd.

Nininger, R. C., and D. Schroeer (1978), Mössbauer studies of the Morin transition in bulk and microcrystalline α-Fe2O3*, J. Phys. Chem. Solids,* 39, 137–144.

Nuding, D. L., and B. A. Cohen (2009), Characterization of rock types at Meridiani Planum, Mars using MER 13-filter Pancam spectra*, 40th Lunar and Planetary Science Conference,* Abstract #2023.

Nyquist, L.E., D.D. Bogard, J.L. Wooden, H. Wiesmann, C.-Y. Shih, B.M. Bansal, and G.A. McKay (1979) Early differentiation, late magmatism, and recent bombardment on the shergottite parent planet, *Meteoritics*, 14,502.

Ortalli, I., and G. Pedrazzi (1990), Study of the Torino Meteorite*, Hyperfine Interactions,* 57, 2275–2278.

Oshtrakh, M. I., O. B. Milder, V. I. Grokhovsky, and V. A. Semionkin (2004), Hyperfine Interactions in Iron Meteorites: Comparative Study by Mössbauer spectroscopy*., Hyperfine Interactions,* 158, 365–370.

Oshtrakh, M. I., E. V. Petrova, I. Grokhovsky, and V. A. Semionkin (2008), A study of ordinary chondrites by Mössbauer spectroscopy with high-velocity resolution, *Meteoritics and Planetary Science,* 43, 941–958.

Ouseph, P. J., H. E. Groskeutz, and A. A. Johnson (1979), Mossbauer spectra for iron-bearing phases in the meteorite Toluca, *Meteoritics & Planetary Science,* 14, 1, 97–108.

Pacros, A., A. F. Haldemann, and J. Vago (2009), Overview of the ExoMars Payload, *EPSC Abstracts,* Vol. 4, EPSC2009-776.

Paliwal, B. S., R. P. Tripathi, H. C. Verma, and S. K. Sharma (2000), Classification of the Didwana-Rajod meteorite: A Mössbauer spectroscopic study, *Meteoritics & Planetary Science,* 35, 639–642.

Pollak, H., M. de Coster, and S. Amelinckx (1962), Mössbauer Effect in Biotite, *Physica Status Solidi,* 2, 1653–1659.

Rancourt, D. G., K. Lagarec, A. Densmore, R. A. Dunlap, J. I. Goldstein, R. J. Reisener, and R. B. Scorzelli (1999), Experimental proof of the distinct electronic structure of a new meteoritic Fe-Ni alloy phase, *Journal of Magnetism and Magnetic Materials,* 191, L255-L260.

Reisener, R. J., and J. I. Goldstein, Ordinary chondrite metallography: Part 1. Fe-Ni taenite cooling experiments, *Meteoritics & Planetary Science,* 38, 1669–1678.

Rieder, R., R. Gellert, J. Brückner, G. Klingelhöfer, G. Dreibus, A. Yen, and S. W. Squyres (2003), The new Athena alpha particle X-ray spectrometer for the Mars Exploration Rovers, *Journal of Geophysical Research - Planets,* 108, E12.

Riesenman, R., J. Steger, and E. Kostiner (1969), Cosine Effect in Mössbauer spectroscopy involving a source of non-zero radius, *Nuclear Instruments and Methods,* 72, 109–110.

Rodionov, D., G. Klingelhöfer, B. Bernhardt, C. Schröder, M. Blumers, S. Kane, F. Trolard, G. Bourrie, and J. M. Génin (2006), Automated Mössbauer spectroscopy in the field and monitoring of fougerite, *Hyperfine Interactions,* 167, 1, 869–873.

Ruff, S. W., P. R. Christensen, T. D. Glotch, D. L. Blaney, J. E. Moersch, and M. B. Wyatt (2008), The mineralogy of Gusev crater and Meridiani Planum derived from the Miniature Thermal Emission spectrometers on the Spirit and Opportunity rovers. In: Bell, Jim F. (Ed.): The Martian surface. Composition, mineralogy and physical properties. Cambridge: Cambridge Univ. Press (Cambridge planetary science, 9), 315–338.

Rull, F., A. Sansano, P. Sobron, B. Lafuente, P. Sarrazin, M. Gailhanou, and D. Blake (2009a), Raman and XRD field characterisation of sulfate efflorescences at Rio Tinto (Spain), *Lunar and Planetary Science Conference,* 40, 1974.

Rull, F., G. Klingelhöfer, A. Sansano, I. Fleischer, P. Sobron, M. Blumers, A. Lafuente, D. Schmanke, and J. Maul (2009b), In-situ Micro-Raman and Mössbauer spectroscopic study of evaporate minerals in Rio Tinto (Spain): Applications for planetary exploration, *Conference on Micro-Raman Spectroscopy and Luminescence Studies in the Earth and Planetary Sciences*.

Rull, F., G. Klingelhöfer, J. Martinez-Frias, I. Fleischer, J. Medina, and A. Sansano (2010), In-situ Raman, LIBS and Mössbauer spectroscopy of surface minerals at Jaroso Ravine and related areas in Sierra Almagrera (Almeria-Spain)*, Lunar and Planetary Science Conference,* 41, 2736.

Salvat, F., and J. Parellada (1984), Theory of conversion electron Mössbauer spectroscopy (CEMS)*, Nuclear Instruments and Methods in Physics Research B,* 1, 70–84.

Saragovi, C., J. Arpe, E. Sileo, R. Zysler, L. C. Sanchez, and C. A. Barrero, Changes in the structural and magnetic properties of Ni-substituted hematite prepared from metal oxinates*, Physics and Chemistry of Minerals,* 31, 625–632. DOI 10.1007/s00269-004-0422-y.

Schröder, C. (2003), Catalogue of Athena Reference (AREF) samples; unpublished.

Schröder, C. (2006), Weathering of Iron-bearing Minerals Under Extraterrestrial Conditions, Investigated by Mössbauer Spectroscopy Dissertation. Mainz. Johannes-Gutenberg-Universität.

Schröder, C., D. S. Rodionov, T. J. McCoy, B. L. Jolliff, R. Gellert, L. R. Nittler, W. H. Farrand, Johnson, JR, S. W. Ruff, J. W. Ashley, D. W. Mittlefehldt, K. E. Herkenhoff, I. Fleischer, A. F. Haldemann, G. Klingelhöfer, D. W. Ming, R. V. Morris, P. A. de Souza, S. W. Squyres, C. Weitz, A. S. Yen, J. Zipfel, and T. Economou (2008), Meteorites on Mars observed with the Mars Exploration Rovers*, Journal of Geophysical Research - Planets,* 113, E06S22.

Schröder, C., J. W. Ashley, M. G. Chapman, B. A. Cohen, W. H. Farrand, I. Fleischer, R. Gellert, K. E. Herkenhoff, J. R. Johnson, B. L. Jolliff, J. Joseph, G. Klingelhöfer, R. V. Morris, S. W. Squyres, S. P. Wright, and the Athena Science Team. (2009), Santorini, another meteorite on Mars and third of a kind*, Lunar and Planetary Science Conference,* 40, Abstract 1665.

Schröder, C., G. Klingelhöfer, R. V. Morris, B. Bernhardt, M. Blumers, I. Fleischer, D. Rodionov, J. Girones Lopez, and P. A. de Souza Jr. (2010a), Field-portable Mössbauer Spectroscopy on Earth, the Moon, Mars, and Beyond. *Geochemistry: Exploration, Environment, Analysis*, proceedings of the International Applied Geochemistry Symposium.

Schröder, C., K. E. Herkenhoff, W. H. Farrand, J. E. Chappelow, W. Wang, L. R. Nittler, J. W. Ashley, I. Fleischer, R. Gellert , M. P. Golombek, J. R. Johnson, G. Klingelhöfer, R. Li, R. V. Morris and Steven W. Squyres (2010b), Properties and distribution of paired stony meteorite candidate rocks at Meridiani Planum, Mars, manuscript in print for publication in *Journal of Geophysical Research – Planets*.

Schroeer, D., and R. C. Nininger (1967), Morin Transition in α-Fe2O3 Microcrystals*, Physical Review Letters,* 19, 11, 632–634.

Scott, E. R. and J. T. Wasson (1976), Chemical classification of iron meteorites. VIII - Groups IC, IIE, IIIF and 97 other irons*, Geochimica et Cosmochimica Acta,* 40, 103–115.

Sobron, P., A. Sanz, T. Acosta, and F. Rull (2009), A Raman spectral study of stream waters and efflorescent salts in Rio Tinto, Spain, *Spectrochimica Acta Part A: Molecular and Biomolecular Spectroscopy*, 71, 5, 1678–1682.

Soderblom, L. A., R. C. Anderson, R. E. Arvidson, J. F. Bell, N. A. Cabrol, W. Calvin, P. R. Christensen, B. C. Clark, T. Economou, B. L. Ehlmann, W. H. Farrand, D. Fike, R. Gellert, T. D. Glotch, M. P. Golombek, R. Greeley, J. P. Grotzinger, K. E. Herkenhoff, D. J. Jerolmack, J. R. Johnson, B. Jolliff, G. Klingelhöfer, A. H. Knoll, Z. A. Learner, R. Li, M. C. Malin, S. M. McLennan, H. Y. McSween, D. W. Ming, R. V. Morris, J. W. Rice, L. Richter, R. Rieder, D. Rodionov, C. Schröder, F. P. Seelos, J. M. Soderblom, S. W. Squyres, R. Sullivan, W. A. Watters, C. M. Weitz, M. B. Wyatt, A. Yen, and J. Zipfel (2004), Soils of Eagle Crater and Meridiani Planum at the Opportunity Rover Landing Site, *Science*, 306, 1723–1726.

Sprenkel-Segel, E. L., and S. S. Hanna (1964), Mössbauer analysis of iron in stone meteorites, *Geochimica et Cosmochimica Acta*, 28, 1913–1931.

Squyres, S. W., R. E. Arvidson, E. T. Baumgartner, J. F. Bell, P. R. Christensen, S. Gorevan, K. E. Herkenhoff, G. Klingelhöfer, M. B. Madsen, R. V. Morris, R. Rieder, and R. A. Romero (2003), Athena Mars rover science investigation, *Journal of Geophysical Research - Planets*, 108, E12, 8062.

Squyres, S. W., R. E. Arvidson, D. Bollen, J. F. Bell, J. Brückner, N. A. Cabrol, W. M. Calvin, M. H. Carr, P. R. Christensen, B. C. Clark, L. Crumpler, D. J. Des Marais, C. d'Uston, T. Economou, J. Farmer, W. H. Farrand, W. Folkner, R. Gellert, T. D. Glotch, M. Golombek, S. Gorevan, J. A. Grant, R. Greeley, J. Grotzinger, K. E. Herkenhoff, S. Hviid, Johnson, JR, G. Klingelhöfer, A. H. Knoll, G. Landis, M. Lemmon, R. Li, M. B. Madsen, M. C. Malin, S. M. McLennan, H. Y. McSween, D. W. Ming, J. Moersch, R. V. Morris, T. Parker, J. W. Rice, L. Richter, R. Rieder, C. Schröder, M. Sims, M. Smith, P. Smith, La Soderblom, R. Sullivan, N. J. Tosca, H. Wanke, T. Wdowiak, M. Wolff, and A. Yen (2006), Overview of the Opportunity Mars Exploration Rover mission to Meridiani Planum: Eagle crater to Purgatory ripple*, Journal of Geophysical Research - Planets,* 111, E12S12.

Squyres, S. W., A. H. Knoll, R. E. Arvidson, J. W. Ashley, J. F. Bell, III, W. M. Calvin, P. R. Christensen, B. C. Clark, B. A. Cohen, P. A. de Souza, JR., L. Edgar, W. H. Farrand, I. Fleischer, R. Gellert, M. P. Golombek, J. Grant, J. Grotzinger, A. Hayes, K. E. Herkenhoff, J. R. Johnson, B. Jolliff, G. Klingelhöfer, A. Knudson, R. Li, T. J. McCoy, S. M. McLennan, D. W. Ming, D. W. Mittlefehldt, R. V. Morris, J. W. Rice, JR., C. Schröder, R. J. Sullivan, A. Yen, and R. A. Yingst (2009), Exploration of Victoria Crater by the Mars Rover Opportunity*, Science,* 324, 5930, 1058–1061.

Squyres, S. W., and Athena Science Team (2010), Recent Scientific Results from Opportunity‘s Traverse Toward Endeavour Crater, Meridiani Planum, Mars*, Lunar and Planetary Science Conference,* 41, 1757.

Srivastava, J. K., and R. P. Sharma (1972), Magnetic Dilution Effects on Morin Phase Transition in Hematite*, Phys. Stat. Sol. (b),* 49, 135–146.

Stevens, J. G., A. M. Khasanov, J. W. Miller, H. Pollak, and Z. Li (2002), Mössbauer Mineral Handbook. Asheville, North Carolina: Mössbauer Effect Data Center.

Treguier, E., C. d'Uston, P. C. Pinet, G. Berger, M. J. Toplis, T. J. McCoy, R. Gellert, and J. Brückner (2008), Overview of Mars surface geochemical diversity through Alpha Particle X-Ray Spectrometer data multidimensional analysis: First attempt at modeling

rock alteration, *Journal of Geophysical Research - Planets,* 113. DOI: 10.1029/2007JE003010.

Treiman, A. H., J. D. Gleason, and D. D. Bogard (2000), The SNC meteorites are from Mars, *Planetary and Space Science,* 48, 1213–1230.

van Cromphaut, C., V. G. de Resende, E. de Grave, and R. E. Vandenberghe (2007), Mössbauer study of Meridiani Planum, the first iron-nickel meteorite found on the surface of Mars by the MER Opportunity, *Meteoritics & Planetary Science,* 42, 12, 2119–2123.

Vandenberghe, R. E., E. de Grave, E. van San, M. A. Ahmed, and C. Dauwe (1998), Integrated low energy electron Mössbauer spectroscopy (ILEEMS), *Phys. Mag.,* 20, 339–353.

Vandenberghe, R. E., C. A. Barrero, G. M. da Costa, Van San E., and E. de Grave (2000), Mössbauer characterization of iron oxides and (oxy)hydroxides: the present state of the art, *Hyperfine Interactions,* 126, 247–259.

Vdovykin, G. P. (1973), The Canyon Diablo meteorite, *Space Science Reviews,* 14, 758–831.

Verbeeck, A. E., E. de Grave, and R. E. Vandenberghe (1986), The effect of the particle morphology on the Mössbauer Effect in α-Fe2O3, *Hyperfine Interactions,* 28, 639–642.

Walker, D., E.M. Stolper, and J.F. Hays (1979) Basaltic volcanism: The importance of Planet size, *Proc. Lunar Planet. Sci. Conf. 10th*, 1995-2015.

Wasson, J. T., and J. I. Goldstein (1968), The North Chilean hexahedrites: Variations in composition and structure, *Geochimica et Cosmochimica Acta,* 32, 329–339.

Wasson, J. T. (1970), The Chemical Classification of Iron Meteorites. IV. Irons with Ge concentrations greater than 190 ppm and other Meteorites Associated with Group I, *Icarus,* 12, 407.

Wasson, J. T., and G. W. Wetherill (1979), Dynamical chemical and isotopic evidence regarding the formation locations of asteroids and meteorites. In: Gehrels, T. (Ed.): Asteroids, 926–974.

Wasson, J. T., and X. Ouyang (1990), Compositional range in the Canyon Diablo meteoroid, *Geochimica et Cosmochimica Acta,* 54, 3175–3183.

Wasson, J. T., and G. W. Kallemeyn (2002), the IAB iron-meteorite complex: A group, five subgroups, numerous grouplets, closely related, mainly formed by crystal segregation in rapidly cooling melts, *Geochimica et Cosmochimica Acta,* 66, 2445–2473.

Wegener, H. (1966), Der Mössbauer-Effekt und seine Anwendungen in Physik und Chemie. Mannheim: Bibliographisches Institut Hochschultaschenbücher-Verlag.

Weinke, H. H. (1977), Chemical and mineralogical investigation of a Mundrabilla specimen, *Meteoritics & Planetary Science,* 12, 384–386.

Weitz, C. M., R. C. Anderson, J. F. Bell, W. H. Farrand, K. E. Herkenhoff, Johnson, JR, B. L. Jolliff, R. V. Morris, S. W. Squyres, and R. J. Sullivan (2006), Soil grain analyses at Meridiani Planum, Mars*, Journal of Geophysical Research - Planets,* 111, E12S04.

Weitz, C., W. H. Farrand, J. R. Johnson, I. Fleischer, C. Schröder, R. A. Yingst, B. L. Jolliff, R. Gellert, J. F. Bell III, K. E. Herkenhoff, G. Klingelhöfer, B. Cohen, W. Calvin, M. Rutherford, J. W. Ashley (2010), Visible and near-infrared multispectral analysis of geochemically measured rock fragments at the Opportunity landing site in Meridiani Planum, manuscript in review for publication in *Journal of Geophysical Research – Planets.*

White, J. S., E. P. Henderson, and B. Mason (1967), Secondary minerals produced by weathering of the Wolf Creek meteorite*, The American Mineralogist,* 52, 1190–1197.

Wojnarowska, A., T. Dziel, J. Galazka-Friedman, and L. Karwowski (2008), New mineralogical phases identified by Mössbauer measurements in Morasko meteorite*, Hyperfine Interactions,* 186, 167–171.

Yen, A. S., R. Gellert, C. Schröder, R. V. Morris, J. F. Bell, A. T. Knudson, B. C. Clark, D. W. Ming, J. A. Crisp, R. E. Arvidson, D. Blaney, J. Brückner, P. R. Christensen, D. J. Desmarais, P. A. de Souza, T. E. Economou, A. Ghosh, B. C. Hahn, K. E. Herkenhoff, L. A. Haskin, J. A. Hurowitz, B. L. Joliff, J. R. Johnson, G. Klingelhöfer, M. B. Madsen, S. M. McLennan, H. Y. McSween, L. Richter, R. Rieder, D. Rodionov, L. Soderblom, S. W. Squyres, N. J. Tosca, A. Wang, M. Wyatt, and J. Zipfel (2005), An integrated view of the chemistry and mineralogy of martian soils*, Nature,* 436, 49–54. DOI: 10.1038/nature03637.

Yen, A. S., D. W. Mittlefehldt, S. M. McLennan, R. Gellert, J. F. Bell, H. Y. McSween, D. W. Ming, T. J. McCoy, R. V. Morris, M. Golombek, T. Economou, M. B. Madsen, T. Wdowiak, B. C. Clark, B. L. Jolliff, C. Schröder, J. Brückner, J. Zipfel, and S. W. Squyres (2006), Nickel on Mars: Constraints on meteoritic material at the surface*, Journal of Geophysical Research (Planets),* 111, E12S11.

Zipfel, J., C. Schröder, B. L. Jolliff, R. Anderson, J. F. Bell III, J. Brückner, J. A. Crisp, P. R. Christensen, B. C. Clark, P. A. de Souza, G. Dreibus, C. d'Uston, T. Economou, R. Gellert, S. P. Gorevan, B. C. Hahn, K. E. Herkenhoff, G. Klingelhöfer, G. W. Lugmair, H. Y. McSween Jr., D. W. Ming, R. V. Morris, R. Rieder, D. S. Rodionov, S. W. Squyres, H. Wänke, M. B. Wyatt, A. S. Yen (2010), Bounce Rock at Meridiani Planum on Mars – a basaltic shergottite on Mars, manuscript in review for publication in *Meteoritics & Planetary Science.*

List of Publications

Articles in peer-reviewed journals

1. Morris, R. V., S. W. Ruff, R. Gellert, D. W. Ming, R. E. Arvidson, B. C. Clark, D. C. Golden, K. Siebach, G. Klingelhöfer, C. Schröder, I. Fleischer, A. S. Yen, and S. W. Squyres, Identification of Carbonate-Rich Outcrops on Mars by the Spirit Rover, *Science*, 329, 421-424. doi: 10.1126/science.1189667.

2. Fleischer, I., G. Klingelhöfer, F. Rull, S. Wehrheim, S. Ebert, M. Panthöfer, M. Blumers, D. Schmanke, J. Maul, and C. Schröder (2010), In-situ Mössbauer Spectroscopy with MIMOS II at Rio Tinto, Spain, *Journal of Physics: Conference Series* 217, 012062, doi:10.1088/1742-6596/217/1/012062.

3. Agresti, D. G., I. Fleischer, G. Klingelhöfer and R. V. Morris (2010), On simfitting MER Mössbauer data to characterize Martian hematite, *Journal of Physics: Conference Series* 217, 012063, doi: 10.1088/1742-6596/217/1/012063.

4. Squyres S. W, A. H. Knoll, R. E. Arvidson, J. W. Ashley, J. F. Bell III, W. M. Calvin, P. R. Christensen, B. C. Clark, B. A. Cohen, P. A. de Souza Jr., L. Edgar, W. H. Farrand, I. Fleischer, R. Gellert, M. P. Golombek, J. Grant, J. Grotzinger, A. Hayes, K. E. Herkenhoff, J. R. Johnson, B. Jolliff, G. Klingelhöfer, A. Knudson, R. Li, T. J. McCoy, S. M. McLennan, D. W. Ming, D. W. Mittlefehldt, R. V. Morris, J. W. Rice Jr., C. Schröder, R. J. Sullivan, A. Yen, R. A. Yingst (2009): Exploration of Victoria Crater by the Mars Rover Opportunity. *Science,* 324, 5930, 1058–1061. doi: 10.1126/science.1170355.

5. Ashley, J. W., M. D. Fries, G. R. Huss, J. E. Chappelow, M. P. Golombek, M. A. Velbel, S. W. Ruff, C. Schröder, W. H. Farrand, D. D. Durda, P. A. Bland, I. Fleischer, A. C. McAdam, S. P. Wright, A. T. Knudson, L. A. Leshin, and A. Steele (2009), The scientific Rationale for Studying Meteorites found on Other Worlds*, 2013-2022 Planetary Science Decadal Survey*.

6. Fleischer, I., G. Klingelhöfer, C. Schröder, R. V. Morris, M. Hahn, D. Rodionov, R. Gellert, and P. A. de Souza (2008), Depth selective Mössbauer spectroscopy: Analysis and simulation of 6.4 keV and 14.4 keV spectra obtained from rocks at Gusev Crater, Mars, and layered laboratory samples, *Journal of Geophysical Research – Planets,* 113, E06S21, doi:10.1029/2007JE003022

7. Fleischer I., G. Klingelhöfer, C. Schröder, D. S. Rodionov (2008), Coatings and weathering rinds at Gusev crater, Mars, investigated by depth selective Mössbauer spectroscopy, *Hyperfine Interactions.* doi 10.1007/s10751-008-9853-z

8. Schröder, C., G. Klingelhöfer, R. V. Morris, D. S. Rodionov, I. Fleischer and M. Blumers (2008), Extraterrestrial Mössbauer spectroscopy: more than 3 years of Mars exploration and developments for future missions, *Hyperfine Interactions*. doi 10.1007/s10751-008-9719-4

9. Schröder, C., D.S. Rodionov, T.J. McCoy, B. L. Jolliff, R. Gellert, L. R. Nittler, W. H. Farrand, J. R. Johnson, S. W. Ruff, J. W. Ashley, D. W. Mittlefehldt, K. E.

Herkenhoff, I. Fleischer, A. F. S. Haldemann, G. Klingelhöfer, D. W. Ming, R. V. Morris, P. A. de Souza Jr., S. W. Squyres, C. Weitz, A. S. Yen, J. Zipfel and T. Economou (2008), Meteorites on Mars observed with the Mars Exploration Rovers, *Journal of Geophysical Research – Planets*, 113, E06S22, doi:10.1029/2007JE002990.

10. Ming, D. W., R. Gellert, R. V. Morris, R. E. Arvidson, J. Brückner, B. C. Clark, B. A. Cohen, C. d'Uston, T. Economou, I. Fleischer, G. Klingelhöfer, T. J. McCoy, D. W. Mittlefehldt, M. E. Schmidt, C. Schröder, S. W. Squyres, E. Tréguier, A. S. Yen and J. Zipfel (2008), Geochemical properties of rocks and soils in Gusev Crater, Mars: Results of the Alpha Particle X-Ray Spectrometer from Cumberland Ridge to Home Plate, *Journal of Geophysical Research – Planets*, 113, E12S39, doi:10.1029/2008JE003195

11. Morris, R. V., G. Klingelhöfer, C. Schröder, I. Fleischer, D. W. Ming, A. S. Yen, R. Gellert, R. E. Arvidson, D. S. Rodionov, L. S. Crumpler, B. C. Clark, B. A. Cohen, T. J. McCoy, D. W. Mittlefehldt, M. E. Schmidt, P. A. de Souza Jr. and S. W. Squyres (2008), Iron mineralogy and aqueous alteration from Husband Hill through Home Plate at Gusev Crater, Mars: Results from the Mössbauer instrument on the Spirit Mars Exploration Rover, *Journal of Geophysical Research – Planets*, 113, E12S42, doi:10.1029/2008JE003201

12. Renz, F., V. Martinez, M. Klein, M. Schott, T. Hoffmann, M. Blumers, I. Fleischer, G. Klingelhöfer, R. Boca and M. Menzel (2008), Chemical tuning by 5-Methyl and N-Methyl-substitution in heptanuclear complexes effects multistability investigated by Mossbauer spectroscopy, *Hyperfine Interactions* 184, 1-3, 259-265

13. Morris R.V., G. Klingelhöfer, C. Schröder, D.S. Rodionov, A. Yen, D.W. Ming, P.A. de Souza Jr., T.Wdowiak, I. Fleischer, R. Gellert, B. Bernhardt, U. Bonnes, B.A. Cohen, E.N. Evlanov, J. Foh, P.Gütlich, E. Kankeleit, T. McCoy, D.W. Mittlefehldt, F. Renz, M.E. Schmidt, B. Zubkov, S.W. Squyres, ad R.E. Arvidson (2006), Mössbauer mineralogy of rock, soil, and dust at Meridiani Planum, Mars: Opportunity's journey across sulfate-rich outcrop, basaltic sand and dust, and hematite lag deposits, *Journal of Geophysical Research – Planets*, 111, E12S15, doi:10.1029/2006JE002791.

14. Morris R.V., G. Klingelhöfer, C. Schröder, D.S. Rodionov, A. Yen, D.W. Ming, P.A. de Souza Jr., I. Fleischer, T. Wdowiak, R. Gellert, B. Bernhardt, E.N. Evlanov, B. Zubkov, J. Foh, U. Bonnes, E. Kankeleit, P. Gütlich, F. Renz, S.W. Squyres, and R.E. Arvidson (2006), Mössbauer mineralogy of rock, soil, and dust at Gusev crater, Mars: Spirit's journey through weakly altered olivine basalt on the plains and pervasively altered basalt in the Columbia Hills, *Journal of Geophysical Research – Planets* 111, E02S13, doi:10.1029/2005JE002584

Articles in print

15. Schröder, C., K. E. Herkenhoff, W. H. Farrand, J. E. Chappelow, W. Wang, L. R. Nittler, J. W. Ashley, I. Fleischer, R. Gellert , M. P. Golombek, J. R. Johnson, G. Klingelhöfer, R. Li, R. V. Morris and Steven W. Squyres (2010), Properties and distribution of paired stony meteorite candidate rocks at Meridiani Planum, Mars. *Journal of Geophysical Research – Planets*.

16. Fleischer, I., J. Brückner, C. Schröder, W. Farrand, E. Tréguier, R.V. Morris, G. Klingelhöfer, K. Herkenhoff, D. Mittlefehldt, J. Ashley, M. Golombek, J. R. Johnson, B. Jolliff, S. W. Squyres, C. Weitz, R. Gellert and P. A. de Souza (2010) : Mineralogy and Chemistry of Cobbles at Meridiani Planum, Mars, investigated by the Mars Exploration Rover Opportunity. *Journal of Geophysical Research – Planets*

17. Schröder, C., G. Klingelhöfer, R. V. Morris, B. Bernhardt, M. Blumers, I. Fleischer, D. Rodionov, J. Girones Lopez, and P. A. de Souza Jr. (2010), Field-portable Mössbauer Spectroscopy on Earth, the Moon, Mars, and Beyond. *Geochemistry: Exploration, Environment, Analysis*, proceedings of the International Applied Geochemistry Symposium.

18. Fleischer, I., Agresti, D. G., G. Klingelhöfer and R. V. Morris (2010): Distinct hematite populations from simultaneous fitting of Mössbauer spectra from Meridiani Planum, Mars. *Journal of Geophysical Research – Planets*

19. Klingelhöfer G. and I. Fleischer (2010), Mobile Mössbauer Spectroscopy with MIMOS II in Space and on Earth, in: Gütlich, P., Bill, E. and Trautwein, A. X. (Ed), Mössbauer spectroscopy and Transition Metal Chemistry. Heidelberg, Dordrecht, London, New York: Springer.

20. Rodionov, D., G. Klingelhöfer, E. Evlanov, M. Blumers, B. Bernhardt, J. Girones, J. Maul, I. Fleischer, O. Prilutskii, A. Shlyk and C. d'Uston (2010), Miniaturised Mössbauer spectrometer MIMOS II for project Phobos Grunt, *Solar System Research 44.*

Articles in review

21. Fleischer I., C. Schröder, G. Klingelhöfer, J. Zipfel, R. V. Morris, J. W. Ashley, R. Gellert (2010), New insights into the mineralogy of the Meridiani Planum Meteorite, Mars. *Meteoritics & Planetary Science*.

22. Ashley, J. W., M. P. Golombek, P. R. Christensen, S. W. Squyres, T. J. McCoy, C. Schröder, I. Fleischer, J. R. Johnson, K. E. Herkenhoff, T. J. Parker (2010): Evidence for Mechanical and Chemical Alteration of Iron-Nickel Meteorites on Mars — Process Insights for Meridiani Planum. *Journal of Geophysical Research – Planets*.

23. Weitz, C., W. H. Farrand, J. R. Johnson, I. Fleischer, C. Schröder, R. A. Yingst, B. L. Jolliff, R. Gellert, J. F. Bell III, K. E. Herkenhoff, G. Klingelhöfer, B. Cohen, W. Calvin, M. Rutherford, J. W. Ashley (2010), Visible and near-infrared multispectral analysis of geochemically measured rock fragments at the Opportunity landing site in Meridiani Planum. *Journal of Geophysical Research – Planets.*

Conference contributions (selection)

1. Fleischer, I. G. Klingelhöfer, C. Schröder, J. Ashley (2010), Cobbles and Meteorites at Meridiani Planum, Mars; 38th COSPAR Scientific Assembly, abstract B02-0010-10.

2. Johnson, J. R., J. Ashley, J. F. Bell III, W. Farrand, I. Fleischer, B. Jolliff, K. Herkenhoff, and A. Yen (2010), Surface alteration of Fe-Ni meteorites analyzed by the Opportunity Mars Exploration Rover, Goldschmidt Conference, Knoxville, Tennessee, USA.

3. Fleischer, I., D. G. Agresti, G. Klingelhöfer, and R. V. Morris (2010), Hematite at Meridiani Planum, Mars, investigated by simultaneous fitting of Mössbauer spectra. L*unar and Planetary Science Conference*, 41, Abstract 1805.

4. Fleischer, I., G. Klingelhöfer, C. Schröder, D. W. Mittlefehldt, R. V. Morris, M. Golombek, and J. W. Ashley (2010), In Situ Investigation of Iron Meteorites at Meridiani Planum, Mars, *Lunar and Planetary Science Conference*, 41, Abstract 1791.

5. Ashley, J. W., M. P. Golombek, C. Schröder, I. Fleischer, T. J. McCoy, P. R. Christensen, T. J. Parker, and the Athena Science Team (2010), Morphologic Evidence for Mechanical and Chemical Weathering of Three New Iron-Nickel Meteorites on Mars — Process Insights for Meridiani Planum, *Lunar and Planetary Science Conference, 41, A*bstract 2208.

6. Rodionov, D., G. Klingelhöfer, M. Blumers, B. Bernhardt, I. Fleischer, J. Gironés, M. Maul, E. Evlanov, A. Shlyk, C. d'Uston (2010), In Situ Analysis of Iron Mineralogy on Phobos Surface by Moessbauer Spectroscopy, *Lunar and Planetary Science Conference, 41, A*bstract 2261.

7. Rull, F., G. Klingelhöfer, J. Martinez-Frias, I. Fleischer, J. Medina, A. Sansano (2010), In-Situ Raman, LIBS and Mössbauer Spectroscopy of Surface Minerals at Jaroso Ravine and Related Areas in Sierra Almagrera (Almeria-Spain), *Lunar and Planetary Science Conference, 41,* Abstract 2736.

8. Mittlefehldt, D. W., R. Gellert, K. E. Herkenhoff, R. V. Morris, B. C. Clark, B. A. Cohen, I. Fleischer, B. L. Jolliff, G. Klingelhöfer, D. W. Ming, R. A. Yingst, Athena Science Team (2010), Marquette Island: A Distinct Mafic Lithology Discovered by Opportunity, *Lunar and Planetary Science Conference, 41,* Abstract 2109.

9. Rull, F., G. Klingelhöfer, P. Sarrazin, J. Medina, I. Fleischer, D. Blake, J. D. Martin Ramos (2010), Combined Raman-LIBS, Moessbauer and XRD In-Situ Mineral Analysis of Evaporite Minerals at Rio Tinto (Spain), *Astrobiology Science Conference 2010: Evolution and Life: Surviving Catastrophes and Extremes on Earth and Beyond,* Abstract 5472.

10. Fleischer , I., F. Rull, G. Klingelhöfer, A. Sanz, A. Sansano, S. Wehrheim, S. Ebert, M. Blumers, J. Maul, D. Schmanke, and C. Schröder (2009), Primary and secondary minerals of the Rio Tinto area investigated with Raman and Mössbauer

spectroscopy in preparation for the ESA "ExoMars" mission, European Planetary Science Conference, Abstract EPSC2009-517.

11. Fleischer, I., W. Farrand, C. Schröder, B. Jolliff, J. Ashley, G. Klingelhöfer and R. Gellert (2009), Cobbles at Meridiani Planum, Mars, European Planetary Science Conference, Abstract EPSC2009-512.

12. Klingelhöfer, G., I. Fleischer, M. Blumers, J. Maul, D. Schmanke, and C. Schröder (2009), In-situ Mössbauer spectroscopy with MIMOS II at Rio Tinto, Spain, International Conference on the Applications of the Mössbauer Effect, Vienna, Austria.

13. Agresti, D. G., I.Fleischer, G.Klingelhöfer, and R.V.Morris (2009), On simfitting MER Mössbauer data, International Conference on the Applications of the Mössbauer Effect, Vienna, Austria.

14. Schröder, C., J. W. Ashley, I. Fleischer, R. Gellert, G. Klingelhöfer, P. A. de Souza Jr. and the Athena Science Team (2009), Meteorites on Mars: Implications from three probably paired meteorite candidates at Meridiani Planum. 72nd Annual Meteoritical Society Meeting, Abstract 5246.

15. Fleischer, I., C. Schröder, G. Klingelhöfer, and R. Gellert (2009), Identification of schreibersite in the Meridiani Planum meteorite, 72nd Annual Meteoritical Society Meeting, Abstract 5238.

16. Schröder, C., J. W. Ashley, M. G. Chapman, B. A. Cohen, W.H. Farrand, I. Fleischer, R. Gellert, K. E. Herkenhoff, J. R Johnson, B. L. Jolliff, J. Joseph, G. Klingelhöfer, R. V. Morris, S. W. Squyres, S. P. Wright, and the Athena Science Team (2009), Santorini, another meteorite on Mars and third of a kind. *Lunar and Planetary Science Conference,* 40, Abstract 1665.

17. Fleischer I., D. Agresti, and G. Klingelhöfer (2009), Mössbauer Hematite temperature study on samples from the MER landing sites, *Lunar and Planetary Science Conference*, 40, Abstract 1832.

18. Klingelhöfer G., I. Fleischer, M. Blumers, D. Rodionov , J. Maul, J. Gironés López, D. Schmanke, J. Brückner, B. Bernhardt, H. Henkel (2009), In-situ mineralogical analysis of lunar rocks and soil, resource prospection and ore process monitoring with the miniaturized Mössbauer spectrometer MIMOS II, Symposium "Lunar Base – Bauen für ein Leben auf dem Mond", Kaiserslautern, Germany.

19. Rull, F., G. Klingelhöfer, A. Sansano, I. Fleischer, P. Sobrón, M. Blumers, A. Lafuente, D.Schmanke, J. Maul (2009), In-situ Micro-Raman and Mössbauer spectroscopic study of evaporite minerals in Rio Tinto (Spain): Applications for Planetary exploration, Conference on Micro-Raman Spectroscopy and Luminescence Studies of the Earth and Planetary Sciences (Corals I), Mainz, Germany.

20. Fleischer, I., G. Klingelhöfer, R.V. Morris, C. Schröder, D. Rodionov (2008), Analysis of 6.4 keV Mössbauer Spectra obtained with MIMOS II on MER on Cobbles at Meridiani Planum, Mars, Geophysical Research Abstracts, Vol. 10, EGU2008-A-11463.

21. Klingelhöfer, G., I. Fleischer, C. Schröder and W. Tremel (2008), Weathering of Iron-bearing minerals on Mars. Concluding colloquium of DFG program "Mars and the terrestrial planets".

22. Fleischer, I., G. Klingelhöfer, C. Schröder, D. Rodionov, M. Blumers, J. Girones Lopez, J. Maul, G. Studlek, D. Schmanke, M. Hahn, and J. Fernandez Sanchez (2008), Home Plate und der Krater Victoria - neue Mössbauer-Ergebnisse vom Mars, Frühjahrstagung der Deutschen Physikalischen Gesellschaft, Freiburg, Germany, EP3.5.

23. Fleischer, I., G. Klingelhöfer, F. Rull, M. Blumers, D. Rodionov, C. Schröder, A. Sansano, J. Medina, D. Schmanke, J. Maul (2008), Sulfate minerals from two Mars analogue sites Rio Tinto and Jaroso Ravine, Spain, investigated by Mössbauer and Raman spectroscopy, European Planetary Science Conference, Abstract EPSC2008-A-00530.

24. Fleischer, I., G. Klingelhöfer, D. Rodionov (2008), Depth-selective Mössbauer spectroscopy from the two MER landing sites, European Planetary Science Conference, Abstract EPSC2008-A-00533.

25. Fleischer, I., G. Klingelhöfer, R.V. Morris, D. Rodionov, M. Blumers, B. Bernhardt, C. Schröder, D.W. Ming, A.S. Yen, B.A. Cohen, T.J. McCoy, D.W. Mittlefehldt, M.E. Schmidt, J. Girones Lopez, G. Studlek, J. Brückner, R. Gellert, and C. d'Uston (2008), The miniaturised Mössbauer spectrometers MIMOS II on MER: four years of operation – a summary. *Lunar and Planetary Science Conference*, 39, Abstract 2323.

26. Ming, D. W., R. Gellert, R. V. Morris, A. S. Yen, R. E. Arvidson, J. Brückner, B. C. Clark, B. A. Cohen, I. Fleischer, G. Klingelhöfer, T. J. McCoy, D. W. Mittlefehldt, M. E. Schmidt, C. Schröder, S. W. Squyres, and J. Zipfel (2008), Geochemical properties of rocks and soils in Gusev crater, Mars: APXS results from Cumberland Ridge to Home Plate. *Lunar and Planetary Science Conference 39,* Abstract 1068.

27. Klingelhöfer, G., D. Rodionov, M. Blumers, L. Strüder, P. Lechner, B. Bernhardt, H. Henkel, I. Fleischer, C. Schröder, J. Girones Lopez, G. Studlek, J. Maul, J. Fernandez-Sanchez, C. d'Uston (2008), The advanced miniaturised Mössbauer spectrometer MIMOS IIA: Increased sensitivity and new capability of elemental analysis. *Lunar and Planetary Science Conference,* 39, Abstract 2379.

28. Fleischer, I., G. Klingelhöfer, R.V. Morris, C. Schröder, D. Rodionov, and P. de Souza (2008), Analysis of 6.4 keV Mössbauer spectra obtained with MIMOS II on MER on cobbles at Meridiani Planum, Mars, and considerations on penetration depths. *Lunar and Planetary Science Conference,* 39, Abstract 1618.

29. Rull1, F., I. Fleischer, J. Martinez-Frias, A. Sanz, C. Upadhyay and G. Klingelhöfer (2008), Raman and Mössbauer spectroscopic characterisation of sulfate minerals from the Mars analogue sites at Rio Tinto and Jaroso Ravine, Spain. *Lunar and Planetary Science Conference,* 39, Abstract 1616.

30. Fleischer, I., C. Schröder, D. Rodionov, M. Blumers, J. Gironés López, J. Fernández Sánchez, M. Hahn, C. Upadhyay and G. Klingelhöfer, Ergebnisse der

Mars-Exploration-Rover Mössbauer-Spektrometer aus dem Jahr 2006, DPG-Frühjahstagung Regenburg März 2007.

31. Upadhyay, C., G. Klingelhöfer, I. Fleischer, C. Schröder, D. Rodionov, M. Panthöfer, R. Jung-Pothmann, N. Tahir, T. Hager and W. Tremel, Classification of Martian jarosite, 38th *Lunar and Planetary Science Conference*, Abstract 1835

32. Fleischer, G. Klingelhöfer, C. Schröder, D. Rodionov, Weathering rinds on Gusev crater rocks: simulation of 6.4 keV and 14.4 keV backscatter Mössbauer spectra and implications on depth selectivity, *Lunar and Planetary Science Conference*, 38, Abstract 1701.

33. Klingelhöfer, G., C. Schröder, W. Tremel, I. Fleischer, and C. Upadhyay (2007), Weathering of iron-bearing minerals and rocks under extraterrestrial conditions investigated by Mössbauer spectroscopy, XRD, XRF, and other methods, 4th Colloquium of the SPP 1115 "Mars and the Terrestrial Planets", 19-20 February 2007 Berlin, Germany.

34. Klingelhöfer, G., D. Rodionov, M. Blumers, B. Bernhardt, I. Fleischer, C. Schroeder, R. V. Morris, J. Girones Lopez (2007), The miniaturised Mössbauer spectrometer MIMOS II: Application for the Phobos Grunt" mission, Workshop on the Exploration of Phobos and Deimos, Abstract 7038.

35. Fleischer, I., G. Klingelhöfer, C. Schröder, D. Rodionov (2007), Depth selectivity in MER Mössbauer spectra and possible surface layers on Gusev crater rocks, 7th International Conference on Mars, Abstract 3198.

36. Fleischer, I., D. Rodionov, C. Schröder, R. V. Morris, A. Yen, D. Ming, D. Mittlefehldt, R. Gellert, B. Cohen, and G. Klingelhöfer (2007), The MER Mössbauer spectrometers: 40 months of operation on the Martian surface, European Planetary Science Conference 2007.

37. Klingelhöfer, G, I. Fleischer, C. Upadhyay, D. Rodionov, C. Schröder, R.V. Morris, M. Blumers, M. Panthöfer, R. Jung-Pothmann, N. Tahir, T. Hager and W. Tremel Jarosite at Meridiani Planum and Weathering rinds at Gusev crater: Interpretation of Mössbauer spectra obtained during the Mars Exploration Rover Mission, International Conference for the Applications of the Mössbauer Effect, Kanpur, India.

38. Klingelhöfer, G., D. Rodionov, I. Fleischer, C. Schröder, and R. V. Morris (2007), More than Three Years of Mars Surface Exploration with the Mösssbauer Spectrometer Mimos II on MER, European Mars Science & Exploration Conference: Mars Express and ExoMars ESTEC, The Netherlands.

39. Klingelhöfer, G., R.V. Morris, D.S. Rodionov, C. Schröder, I. Fleischer, D.W. Ming, and A. Yen (2006), The Iron Mineralogy at Meridiani Planum as determined by the Mössbauer Spectrometer MIMOS II on the Mars Exploration Rover Opportunity, Program and Abstracts, I-34, Sixth Seeheim Workshop on Mössbauer Spectroscopy, June 2006, Seeheim, Germany.

40. Blumers, M., D.S. Rodionov, C. Ruby, U. Bonnes, J. Foh, I. Fleischer, J.-M. Genin, E. Kankeleit, J.G. López, R.V. Morris, J.F. Sánchez, C. Schröder, C. Upadhyay,

and G. Klingelhöfer (2006), The Miniaturized Mössbauer Spectrometer MIMOS II: A Status Report and further Improvements, Program and Abstracts, P-60, Sixth Seeheim Workshop on Mössbauer Spectroscopy, June 2006, Seeheim, Germany.

41. Fleischer, I., G. Klingelhöfer, D.S. Rodionov, C. Schröder, R.V. Morris, and M. Blumers (2006), Quantification of Depth Selectivity in Backscatter Mössbauer Spectra obtained by the Spectrometer MIMOS II on Mars, Program and Abstracts, P-72, Sixth Seeheim Workshop on Mössbauer Spectroscopy, June 2006, Seeheim, Germany.

42. Schröder, C., G. Klingelhöfer, D.S. Rodionov, R.V. Morris, I. Fleischer, and A. Yen (2006), Mössbauer Spectroscopy with MIMOS II on Mars: A status report of data obtained so far, and how to work with them, Program and Abstracts, C-73, Sixth Seeheim Workshop on Mössbauer Spectroscopy, June 2006, Seeheim, Germany.

43. Rodionov, D., C. Schröder, C. Upadhyay, I. Fleischer, M. Blumers, J. Fernandez, J. Gorones, M. Hahn, P. Gütlich, W. Tremel, and G. Klingelhöfer (2006), Jarosite and other Fe-S-Compounds on the Planet Mars identified with the Mössbauer Spectrometer MIMOS II; MWFZ annual meeting.

44. Schröder, C., D. Rodionov, I. Fleischer, M.Blumers, J. Girones, J.F. Sanchez, M. Hahn, and G. Klingelhöfer (2006), Neue Ergebnisse der MER Mössbauer-Spektrometer, Verhandlungen der Deutschen Physikalischen Gesellschaft, DPG Frühjahrstagung, Heidelberg, 13.-16.3. 2006, EP21.1, p. 32.

45. Klingelhöfer, G., R.V. Morris, C. Schröder, D.S. Rodionov, A. Yen, D.W. Ming, and I. Fleischer (2006), Iron mineralogy on Mars at Gusev Crater and Meridiani Planum by the Mössbauer spectrometers MIMOS II on the Mars Exploration Rovers Spirit and Opportunity, 43rd Annual Meeting of the Clay Mineral Society, 3-7 June 2006, Ile d'Oléron, France.

46. Klingelhöfer, G., R.V. Morris, D. Rodionov, C. Schröder, A. Yen, D.W. Ming, and I. Fleischer (2006), Mineralogy at Meridiani Planum, Mars, from the MER Opportunity Mössbauer spectrometer, Committee on Space Research, 36th COSPAR Scientific Assembly, Beijing, China, 16 - 23 July, COSPAR-2006-A-03411.

47. Klingelhöfer, G., R. V. Morris, C. Schröder, D. S. Rodionov, A. S. Yen, D. W. Ming, B. Cohen, I. Fleischer, D. W. Mittlefehldt, T. McCoy, P. de Souza Jr., and the Athena Science team (2006), Two Martian Winters at Gusev Crater and Meridiani Planum: New Results From the MER Mössbauer Spectrometers, AGU Fall 2006 Assembly.

48. Fleischer, I. (2006), Quantifizierung der Tiefenselektivität von 14,4-keV- und 6,4-keV-Strahlung in Mössbauer-Spektren, Diploma thesis, Johannes Gutenberg-Universität Mainz.

49. Klingelhöfer, G., D. S. Rodionov, R. V. Morris, C. Schröder, P. A. de Souza Jr., D. W. Ming, A. S. Yen, B. Bernhardt, F. Renz, I. Fleischer, T. Wdowiak, S. W. Squyres, and The Athena Science Team (2005): MIMOS II on MER – One Year of Mössbauer Spectroscopy on the Surface of Mars: From Jarosite at Meridiani

Planum to Goethite at Gusev Crater. *Lunar and Planetary Science Conference*, 36, Abstract 2349.

50. Klingelhöfer, G., C. Schröder, D. Rodionov, B. Bernhardt, I. Fleischer, J. Foh, E. Kankeleit, U. Bonnes, P.Gütlich, F. Renz, P. de Souza Jr., R. Gellert, and R.V. Morris, Mineralogy at the Mars-Exploration-Rover landing sites determined by the Mössbauer Spectrometer MIMOS II, Verhandlungen der Deutschen Physikalische Gesellschaft, "Physik seit Einstein", March 2005, Berlin, Germany, EP 14.6.

51. Klingelhöfer, G., R. V. Morris, D. Rodionov, C. Schröder, P. de Souza, B. Bernhardt, U. Bonnes, E. Evlanov, J. Foh, R. Gellert, P. Gütlich, I. Fleischer, E. Kankeleit, D. Ming, F. Renz, S. Squyres, T. Wdowiak, and A. Yen (2005), MER Mössbauer Investigations of the Mineralogy of Soils and Rocks at Meridiani Planum and Gusev Crater, 1st Mars Express Science Conference, 21-25 February 2005, Abstract Book, p. 50, ESA-ESTEC, Nordwijk, Netherlands.

52. Klingelhöfer, G., R.V. Morris, D.S. Rodionov, C. Schröder, P.A. de Souza Jr., D.W. Ming, A.S. Yen, B. Bernhardt, I. Fleischer, and S.W. Squyres (2005), One year of Mössbauer spectroscopy on Mars: Highlights and experiences, Geophysical Research Abstracts 7, EGU05-A-10731.

Education and Public Outreach

Vorlesung „Die Erforschung des Sonnensystems“, Veranstaltungsreihe „Physik am Samstag Morgen“ für ca. 100 Oberstufenschüler, Juni 2009

Vortrag „Hämatit-Kügelchen an Opportunity’s Landestelle in Meridiani Planum“ zur Jubiläumsfeier “2 Rover, 4 Instrumente, 5 Jahre auf dem Mars“, Januar 2009

Vortrag „MIMOS II: Mössbauer-Spektrometer auf den Mars Exploration Rovern“ Bergsträßer Weltraumtage, Februar 2008

„Die Mars Exploration Rover Mission als Brettspiel“, Wissenschaftsmarkt der Universität Mainz, September 2006

Vortrag „Mössbauer-Spektroskopie mit den Mars-Exploration-Rovern“, Astronomisches Sommerlager 2006

„Memory-Spiel zur Mars Exploration Rover Mission“, Wissenschaftsmarkt der Universität Mainz, September 2005

Impressions from ILC6 Udaipur Lunar Conference from a youth perspective, November 2004 (http://sci.esa.int/science-e/www/object/ index.cfm?fobjectid=36267&fbodylongid=1713)

Appendix

Table A1: Mössbauer parameters for Meridiani spherules and analogues.

Sample	Olivine		Pyroxene		npOx/Fe^{3+}		Hematite		
	δ	ΔE_Q	δ	ΔE_Q	δ	ΔE_Q	δ	ΔE_Q	B_{hf}
	mm/s		mm/s		mm/s		mm/s		T
Hema2	1.15	2.97	1.13	2.13	0.41	0.87	0.39	-0.16	54.3
							0.35	-0.22	52.1
BerryBowl	1.15	3.00	1.14	2.12	0.37	0.91	0.40	0.17	53.8
							0.35	-0.28	53.4
Panaluu	1.15	3.03	1.14	2.12	0.37	0.85	0.37	-0.20	52.7
							0.35	-0.05	50.1
AegeanCrest	1.15	3.03	1.15	2.17	0.37	0.85	0.40	0.05	52.2
							0.35	-0.39	52.1
LeahsChoice	1.15	3.03	1.15	2.17	0.37	0.85	0.40	0.00	53.1
							0.35	-0.40	52.8
BerrySurvey	1.15	3.03	1.15	2.17	0.37	0.85	0.40	0.19	53.9
							0.35	-0.25	53.6
RippleCrest	1.15	3.03	1.15	2.17	0.37	0.85	0.39	-0.16	53.0
							0.37	-0.19	51.3
Mobarak	1.15	3.03	1.15	2.17	0.37	0.85	0.37	-0.10	53.8
							0.36	-0.21	51.6
MayBeRooz	1.15	3.03	1.15	2.17	0.37	0.85	0.38	-0.17	53.4
							0.36	-0.20	51.4
Cure	1.15	3.03	1.15	2.17	0.37	0.85	0.37	-0.32	55.0
							0.37	-0.17	52.6
Laboratory analogue setups	1.15	2.94	1.02	2.23	0.51	0.65	0.37	-0.18	51.4

Table A1 (continued)

Sample	Magnetite (tetrahedrally coordinated Fe^{3+})			Magnetite (octahedrally coordinated Fe^{3+}/Fe^{2+})			Maghemite		
	δ	ΔE_Q	B_{hf}	δ	ΔE_Q	B_{hf}	δ	ΔE_Q	B_{hf}
	mm/s		T	mm/s		T	mm/s		T
Laboratory analogue setups	0.60	-0.48	49.7	0.51	0.27	48.5	0.37	0.02	45.7

Table A2: Mössbauer parameters for basaltic samples.

Sample	Olivine		Pyroxene		npOx/Fe^{3+}		Ilmenite	
	δ	ΔE_Q	δ	ΔE_Q	δ	ΔE_Q	δ	ΔE_Q
	mm/s		mm/s		mm/s		mm/s	
Martian soil (average)	1.15	3.00	1.16	2.14	0.37	0.90	-	-
Gusev Adirondack class (average)	1.16	3.01	1.16	2.08	0.38	0.99	-	-
Rhoen basalt	1.14	2.96	1.03	2.19	0.58	0.65	-	-
Ortenberg basalt	1.15	2.96	1.13 1.13	2.53 1.84	0.54	0.66	1.05	0.75
AREF 108	1.14	2.87	1.14	2.03	0.40	0.79	-	-
AREF 135	1.14	2.91	1.08	2.18	0.45	0.64	-	-
AREF 149	1.15	2.85	1.14	1.98	-	-	1.05	0.66
Kremer basalt	1.15	2.94	1.02	2.23	0.51	0.65	-	-

Table A2 (continued)

Sample	Magnetite (tetrahedrally coordinated Fe^{3+})			Magnetite (octahedrally coordinated Fe^{3+}/Fe^{2+})			Hematite/Oxides		
	δ	ΔE_Q	B_{hf}	δ	ΔE_Q	B_{hf}	δ	ΔE_Q	B_{hf}
Martian soil (average)	0.31	0.01	50.0	0.66	-0.01	46.7	0.37	-0.16	51.7
Gusev Adirondack class (average)	0.31	0.01	50.0	0.66	-0.01	46.7	0.37	-0.16	51.7
AREF 108	-	-	-	-	-	-	0.46	0.06	45.3
AREF 135	-	-	-	-	-	-	0.70	0.45	50.7
Kremer basalt	-	-	-	-	-	-	0.33	-0.02	49.2

Table A3: Mössbauer parameters for hematite from analogue samples showing a Morin transition.					
Sample	**T (K)**	**δ (mm/s)**	**ΔE_Q (mm/s)**	**B (T)**	**Γ (mm/s)**
HMCM1	205	0.35	0.26	52.45	0.57
	215	0.35	0.21	52.40	0.68
	225	0.36	0.14	52.18	0.62
	235	0.37	0.10	52.06	0.66
	245	0.37	0.02	51.85	0.75
	255	0.38	-0.11	51.51	0.62
	265	0.37	-0.18	51.08	0.47
	275	0.37	-0.18	51.19	0.47
	285	0.37	-0.18	51.12	0.43
HMMG1	205	0.35	0.46	52.73	0.42
	215	0.37	0.42	52.62	0.40
	225	0.36	0.45	52.45	0.44
	235	0.37	0.39	52.53	0.45
	245	0.37	0.43	52.44	0.44
	255	0.35	-0.12	51.93	0.62
	265	0.37	-0.20	51.31	0.36
	275	0.37	-0.20	51.16	0.40
	285	0.36	-0.20	51.14	0.36
HMMG1-FP	205	0.34	0.34	52.58	0.48
	215	0.34	0.35	52.39	0.46
	225	0.36	0.35	52.47	0.47
	235	0.36	0.35	52.33	0.52
	245	0.35	0.28	52.17	0.49
	255	0.36	-0.10	51.58	0.47
	265	0.37	-0.14	51.42	0.45
	275	0.36	-0.17	51.20	0.45
	285	0.37	-0.20	51.17	0.39
HWMK30	205	0.37	0.16	52.33	0.44
	215	0.37	0.03	51.82	0.48
	225	0.37	-0.01	51.67	0.47
	235	0.36	-0.06	51.61	0.38
	245	0.37	-0.12	51.30	0.43
	255	0.36	-0.14	51.22	0.38
	265	0.36	-0.19	51.22	0.39
	275	0.38	-0.21	50.89	0.38
	285	0.38	-0.16	50.80	0.36

Table A4: Mössbauer parameters for hematite from analogue samples not showing a Morin transition.

Sample	T (K)	δ (mm/s)	ΔE_Q (mm/s)	B (T)	Γ (mm/s)
HMRE2	205	0.36	-0.21	51.65	0.43
	215	0.36	-0.21	51.68	0.42
	225	0.37	-0.20	51.52	0.42
	235	0.38	-0.22	51.40	0.39
	245	0.36	-0.23	51.16	0.42
	255	0.37	-0.20	51.08	0.49
	265	0.35	-0.22	51.21	0.41
	275	0.38	-0.20	50.86	0.38
	285	0.37	-0.23	50.78	0.40
HWMK11	205	0.34	-0.17	51.44	0.53
	215	0.36	-0.18	51.12	0.48
	225	0.35	-0.18	50.99	0.51
	235	0.37	-0.20	50.94	0.50
	245	0.33	-0.19	50.80	0.39
	255	0.36	-0.17	50.63	0.49
	265	0.38	-0.19	50.69	0.46
	275	0.38	-0.14	50.27	0.53
	285	0.37	-0.21	50.25	0.43
HWMK20	205	0.33	-0.18	50.98	0.53
	215	0.34	-0.25	50.86	0.44
	225	0.41	-0.19	50.61	0.61
	235	0.35	-0.25	51.14	0.46
	245	0.35	-0.24	50.47	0.52
	255	0.34	-0.20	50.10	0.59
	265	0.38	-0.25	49.93	0.74
	275	0.33	-0.20	50.07	0.54
	285	0.35	-0.20	49.74	0.55
HWMK745R	205	0.36	-0.14	51.31	0.67
	215	0.34	-0.11	51.46	0.61
	225	0.35	-0.20	51.15	0.60
	235	0.36	-0.19	51.02	0.31
	245	0.38	-0.22	51.19	0.45
	255	0.38	-0.19	50.78	0.57
	265	0.37	-0.21	50.78	0.51
	275	0.37	-0.16	50.96	0.43
	285	0.34	-0.14	50.27	0.47

Table A5: Mössbauer parameters for hematite from Meridiani outcrop determined from simfits with different models. The isomer shift δ was fixed to 0.37 mm/s for all fits.

Model		S1			S2				
	T (K)	ΔE_Q (mm/s)	B (T)	Γ_{16} (mm/s)	ΔE_Q (mm/s)	B (T)	Γ_{16} (mm/s)	Γ_{25} (mm/s)	Skew
S1eS2e	205	0.22	53.90	0.27	0.00	51.96	0.67	-	-
	215	0.17	53.80	0.28	-0.05	51.76	0.73	-	-
	225	0.12	53.53	0.30	-0.04	51.64	0.69	-	-
	235	0.13	53.64	0.36	-0.07	51.59	0.67	-	-
	245	0.05	53.59	0.29	-0.06	51.37	0.70	-	-
	255	0.05	53.51	0.31	-0.08	51.38	0.70	-	-
	265	-0.09	52.62	0.30	-0.12	51.21	0.80	-	-
	275	-0.15	53.14	0.27	-0.11	51.41	0.66	-	-
S1eS2b	205	0.26	53.75	0.28	-0.01	52.00	0.78	0.64	-
	215	0.19	53.68	0.29	-0.06	51.76	0.83	0.69	-
	225	0.14	53.39	0.32	-0.04	51.65	0.81	0.65	-
	235	0.14	53.31	0.39	-0.08	51.60	0.81	0.64	-
	245	0.05	53.51	0.31	-0.06	51.34	0.78	0.69	-
	255	0.07	53.25	0.34	-0.09	51.37	0.86	0.67	-
	265	-0.09	52.55	0.32	-0.12	51.21	0.89	0.75	-
	275	-0.17	52.87	0.29	-0.09	51.46	0.80	0.62	-
S1eS2ek	205	0.22	53.91	0.26	0.00	52.14	0.67	-	0.09
	215	0.18	53.85	0.28	-0.05	52.07	0.74	-	0.14
	225	0.12	53.58	0.29	-0.04	51.89	0.69	-	0.12
	235	0.13	53.86	0.36	-0.06	51.98	0.67	-	0.19
	245	0.05	53.77	0.29	-0.06	51.86	0.70	-	0.25
	255	0.05	53.83	0.31	-0.08	51.96	0.68	-	0.28
	265	-0.08	52.82	0.36	-0.13	51.73	0.77	-	0.21
	275	-0.15	53.33	0.28	-0.11	51.83	0.64	-	0.20
S1eS2bk	205	0.27	53.71	0.28	-0.02	52.15	0.80	0.65	0.06
	215	0.21	53.69	0.30	-0.06	52.07	0.84	0.69	0.11
	225	0.15	53.44	0.33	-0.04	51.89	0.80	0.64	0.09
	235	0.19	53.51	0.41	-0.08	52.00	0.80	0.63	0.16
	245	0.06	53.72	0.31	-0.06	51.84	0.75	0.68	0.23
	255	0.09	53.48	0.36	-0.09	51.88	0.83	0.66	0.21
	265	-0.08	52.63	0.38	-0.13	51.73	0.85	0.72	0.18
	275	-0.19	52.90	0.31	-0.08	51.79	0.80	0.62	0.13

Table A6: Mössbauer parameters for hematite from Meridiani outcrop determined from simfits with different models. The isomer shift δ was fixed to 0.37 mm/s for all fits.

Model		S1				S2			
	T (K)	ΔE_Q (mm/s)	B (T)	Γ_{16} (mm/s)	Γ_{25} (mm/s)	ΔE_Q (mm/s)	B (T)	Γ_{16} (mm/s)	Γ_{25} (mm/s)
S1eS2e	195	0.01	54.55	0.58	-	-0.08	52.52	0.43	-
	205	0.03	54.08	0.55	-	-0.04	52.17	0.44	-
	215	0.01	54.06	0.54	-	-0.10	52.14	0.40	-
	225	-0.03	53.99	0.52	-	-0.09	52.06	0.36	-
	235	-0.06	53.92	0.49	-	-0.07	52.15	0.34	-
	245	-0.10	53.72	0.44	-	-0.12	51.90	0.34	-
	255	-0.13	53.22	0.46	-	-0.19	51.38	0.36	-
	265	-0.16	52.98	0.49	-	-0.21	51.12	0.41	-
	275	-0.16	52.98	0.47	-	-0.19	51.29	0.38	-
	285	-0.23	53.14	0.52	-	-0.22	51.28	0.37	-
S1eS2b	195	0.01	54.43	0.59	-	-0.09	52.45	0.51	0.44
	205	0.03	54.00	0.57	-	-0.05	52.17	0.55	0.47
	215	0.02	53.98	0.57	-	-0.12	52.18	0.54	0.43
	225	-0.02	53.95	0.55	-	-0.10	52.09	0.47	0.38
	235	-0.05	53.69	0.55	-	-0.08	52.35	0.57	0.42
	245	-0.09	53.66	0.48	-	-0.13	51.95	0.47	0.37
	255	-0.12	53.11	0.51	-	-0.20	51.52	0.54	0.40
	265	-0.14	52.86	0.53	-	-0.22	51.26	0.59	0.43
	275	-0.13	52.65	0.53	-	-0.24	51.73	0.65	0.45
	285	-0.22	52.99	0.55	-	-0.23	51.28	0.55	0.42
S1bS2e	195	0.00	54.22	0.67	0.59	-0.11	52.25	0.46	-
	205	0.03	53.94	0.62	0.54	-0.06	52.17	0.53	-
	215	0.01	53.97	0.61	0.51	-0.13	52.20	0.49	-
	225	-0.03	53.88	0.60	0.51	-0.10	52.05	0.43	-
	235	-0.06	53.81	0.59	0.47	-0.07	52.25	0.43	-
	245	-0.10	53.55	0.55	0.44	-0.13	51.90	0.41	-
	255	-0.13	53.10	0.56	0.44	-0.20	51.47	0.47	-
	265	-0.16	52.93	0.59	0.45	-0.20	51.33	0.55	-
	275	-0.17	52.93	0.59	0.44	-0.18	51.55	0.50	-
	285	-0.23	52.90	0.62	0.50	-0.21	51.24	0.49	-
S1bS2b	195	0.01	54.18	0.66	0.61	-0.12	52.23	0.51	0.43
	205	0.03	53.91	0.62	0.55	-0.07	52.16	0.56	0.52
	215	0.03	53.88	0.61	0.54	-0.15	52.27	0.58	0.48
	225	-0.02	53.84	0.61	0.53	-0.11	52.09	0.49	0.42
	235	-0.06	53.73	0.59	0.48	-0.08	52.28	0.50	0.44
	245	-0.10	53.51	0.56	0.45	-0.14	51.92	0.48	0.42
	255	-0.12	53.05	0.56	0.46	-0.21	51.51	0.53	0.44
	265	-0.15	52.84	0.58	0.47	-0.21	51.34	0.65	0.54
	275	-0.17	52.88	0.57	0.44	-0.19	51.52	0.55	0.50
	285	-0.22	52.85	0.62	0.52	-0.22	51.21	0.56	0.48

Table A7. Temperature dependent Mössbauer parameters for kamacite, troilite and schreibersite from *Mundrabilla*.

Mineral phase	**T**	**δ**	**ΔE_Q**	**Γ**	**B_{hf}**
	(K)	**(mm/s)**			**(T)**
Kamacite	195	0.00	0.00	0.47	33.9
	205	0.01	0.01	0.49	33.9
	215	0.01	0.00	0.46	33.8
	225	0.01	0.00	0.47	33.7
	235	0.01	0.00	0.46	33.6
	245	0.01	0.00	0.46	33.6
	255	0.01	0.02	0.45	33.5
	265	0.01	0.00	0.45	33.5
	275	0.02	0.00	0.46	33.4
	285	0.02	0.00	0.44	33.4
	295	0.02	0.00	0.43	33.3
Troilite	205	0.74	-0.16	0.34	31.7
	215	0.74	-0.16	0.35	31.6
	225	0.74	-0.16	0.36	31.5
	235	0.75	-0.17	0.33	31.3
	245	0.75	-0.16	0.33	31.4
	255	0.75	-0.17	0.34	31.2
	265	0.75	-0.14	0.36	31.1
	275	0.75	-0.17	0.32	31.1
	285	0.74	-0.16	0.33	30.9
	295	0.75	-0.16	0.33	30.9
Schreibersite	200-240	0.29	0.03	0.61	25.1
		0.16	0.02	0.64	21.2
		0.49	0.19	0.44	15.2
	295	0.30	0.01	0.44	24.1
		0.26	0.00	0.60	21.2
		0.45	0.31	0.30	16.2

Values of δ are given relative to metallic Fe foil at the same temperature as the sample. Parameter uncertainties are ±0.02 mm/s for δ and ΔE_Q and ±0.2 T for B_{hf}.

Table A8. Temperature dependent Mössbauer parameters for kamacite, nanophase ferric oxide (npOx) and magnetically ordered Iron oxides (magOx) from *Heat Shield Rock*.

Mineral phase	**T (K)**	**δ (mm/s)**	**ΔE_Q (mm/s)**	**Γ (mm/s)**	**B_{hf} (T)**	**δ (mm/s)**	**ΔE_Q (mm/s)**	**Γ (mm/s)**	**B_{hf} (T)**
		undisturbed surface				**brushed surface**			
Kamacite	205	0.00	0.00	0.29	35.2	-0.01	0.00	0.35	35.2
	215	0.00	0.00	0.31	35.0	0.00	0.00	0.35	35.0
	225	0.00	0.00	0.33	34.9	0.00	0.00	0.35	34.8
	235	0.01	0.00	0.34	34.7	0.00	-0.01	0.34	34.7
	245	0.02	0.00	0.32	34.5	0.02	0.00	0.29	34.5
	255	0.02	0.00	0.33	34.3	0.03	0.00	0.33	34.3
	265	0.02	0.00	0.33	34.2	0.03	0.00	0.37	34.2
		average value							
npOx	200-270	0.40	0.81		-	0.40	0.81		
magOx	200-270	0.39	-0.16		51.7	0.39	-0.16		51.7

Values of δ are given relative to metallic Fe foil at the same temperature as the sample.
Parameter uncertainties are ±0.02 mm/s for δ and ΔE_Q and ±0.2 T for B_{hf}.

Table A9. Subspectral areas for 6.4 keV and 14.4 keV spectra obtained on the undisturbed and brushed surface of *Heat Shield Rock*.

	Mineral phase	**Subspectral area (%)**		
		14.4 keV	**6.4 keV**	**6.4 keV + 14.4 keV**
undisturbed surface	Kamacite	90	88	
	npOx	5	5	
	Schreibersite	2	2	
	magOx	3	5	
brushed surface	Kamacite	84	84	86
	npOx	6	5	5
	Schreibersite	3	4	3
	magOx	7	7	6

The uncertainties of subspectral areas are ±2 % (absolute subspectral area) for npOx, schreibersite and magOx.
Mössbauer parameters for schreibersite were constrained to the values obtained from *Mundrabilla*. For all other phases, Mössbauer parameters were contrained to values obtained from the fit of summed 14.4 keV plus 6.4 keV spectra obtained on the brushed surface of *Heat Shield Rock*. The sum of spectra obtained on the undisturbed surface was not fitted.

Table A10. Representative Mössbauer parameters for Rio Tinto samples, corresponding to spectra shown in chapter 7.

Target type	Mineral phase	δ (mm/s)	ΔE_Q (mm/s)	B_{hf} (T)
Volcanic rock	Chlorite	1.14	2.73	-
	Hematite	0.37	-0.21	51.2
	Nanophase Gt / Hm	0.36	0.69	-
Gossan	Hematite	0.37	-0.23	50.8
		0.37	-0.21	50.8
	Goethite	0.35	-0.25	35.7
		0.38	-0.22	36.1
	Nanophase Goethite	0.35	0.58	-
		0.36	0.59	-
River Bedrock	Hematite	0.35	-0.19	48.0
	Nanophase Goethite	0.37	0.53	-
Crusts	Jarosite	0.37	1.19	-
	Pyrite	0.33	0.59	-
	Copiapite	0.38	0.55	-
Evaporites	Cop/Coq/(Rho) average	0.42	0.55	-
	Mel/Roz average	1.24	3.19	-
	Jarosite average	0.38	1.17	-
	Nanophase Goethite	0.37	0.60	-
Sediment	Schwertmannite	0.36	0.61	-

Cop = Copiapite; Coq = Coquimbite; Rho = Rhomboclase; np Gt = nanophase Goethite; Mel = Melanterite; Roz = Rozenite. Uncertainties are ±0.02 mm/s for δ and ΔE_Q and ±0.5 T for B_{hf}.